Energy dissipation on quantum systems and 2D materials

-An Atomic Force Microscopy Study-

Inauguraldissertation

zur

Erlangung der Würde eines Doktors der Philosophie

vorgelegt der

Philosophisch-Naturwissenschaftlichen Fakultät

der Universität Basel

von

Alexina Ollier

Basel, 2023

Genehmigt von der Philosophisch-Naturwissenschaftlichen Fakultät
auf Antrag von:

Prof. Dr. Ernst Meyer
Prof. Dr. Martino Poggio
Prof. Dr. Peter Grütter

Basel, 18. October 2022

Prof. Dr. Marcel Mayor, Dekan

"*A method is more important than a discovery, since the right method will lead to new and even more important discoveries.*"
Lev Landau

To my mom, who always believe in me.

Abstract

Understanding the nanoscale energy dissipation is nowadays among few priorities particularly in solid state systems. Breakdown of topological protection, loss of quantum information and disorder-assisted hot electrons scattering in graphene are few examples, where the presence of energy dissipation has a great impact on the studied object. It is therefore critical to know, how and where the energy leaks.

The aim of this project is to address this issue by using a highly sensitive pendulum geometry Atomic Force Microscope (p-AFM), oscillating like a tiny pendulum over the sample surface. The microscope is perfectly suited to measure tiny amounts of dissipation, the tip position is controlled with atomic accuracy owing to a tunnelling current and the enhanced sensitivity allows to distinguish between electronic, phononic or van der Waals type of dissipation. The measurements can be performed in a wide range of temperatures from $T = 5\ K$ to room temperature and in magnetic fields spanning from $B = 0\ T$ to $B = \pm 7\ T$. The design of the sample holder allows to perform dissipation measurements while passing electric current in the plane as well as to apply in-plane voltage to the the sample surface as well as adding two contact wires.

The experiments showed that the mechanical oscillations of the cantilever and the sample surface can sense the quantum effects of 2D materials or quantum systems. Indeed, quantum dot-like behaviour is reported on free-standing graphene monolayer where electrons charging and discharging events are observed and dissipation maps show Coulomb rings. In addition to that, the band filling of twisted bilayer graphene at the magic angle twist and a signature of potential orbital ferromagnetic behaviour for the band filling equal to $3n_s/4$ was investigated. Last, the transition between ferromagnetic to paramagnetic phase in a molybdenum disulfate monolayer was investigated and revealed a linear dependence of the magnetic susceptibility as suggested by theoretical studies.

Acknowledgements

I wanted to start this thesis by acknowledging everyone involved in this work.

My first thanks are addressed to Prof. Dr. Ernst Meyer and Dr. Marcin Kisiel for giving me the opportunity to work on this project. You provided me all the necessary and the best work environment that I didn't even dream of before. All the help in the lab, science understanding and all the patience. It enables me to gain more confidence and it was a great pleasure for me to come to work.

The second thanks are going to the thesis committee that allow me to defend as well as the chairman. I wanted to thank you all separately, Prof. Dr. Martino Poggio for the short but very interesting annual meetings with every time very good comments. You also made my journey in my PhD life easier by providing me the twisted bilayer graphene that revealed very interesting results. Prof. Dr. Peter Grütter for kindly accepting my request for the external expert, our small conversation during NC AFM was very interesting. And last, Prof. Dr. Christian Schönenberger for chairing my defence. I am especially happy to have you as the chairman since you also had a big impact on my PhD journey. First, as the SNI director and second as a collaborator in the MoS_2 samples, you allowed me to enter a little bit in the conductance physics and opened me a lot of opportunity especially this year with two very interesting events, the Capri Spring School, and the Graphene workshop in Budapest. I feel very honoured that you thought about me for those two events.

The third thanks go to the SNI. I have so many things to say about how I am grateful to be part of the SNI PhD students program, but I will try to make it short. First, I want to thank all the members of SNI especially Claudia, Michèle and Christel for their presence and kindness. I also want to thank Dr. Andreas Baumgartner for organizing the Nano in the Snow Winter School and always try to provide us interesting workshops where we can develop ourselves more. Second, all the other PhD students that provide a very enjoyable environment and good feelings all along those four years. And last, I want to thank all the organisation (even those that I haven't met) for providing a

very good PhD environment but also studying programme that brings together very different disciplines and space for improvement and not only funding.

The fourth thanks are addressed to my co-workers, present and past, I hope I wasn't too annoying with all my emails. I really liked working with you all. All the different conversations and events that we organized together will stay in my memory. You helped me a lot to gain more confidence and open myself more to people. I also want to thank Prof. Dr. Alexis Baratof, Prof. Dr. Erio Tosatti, Ali Khosravi and all the SISSA members for their help in the project, the zoom meetings, and their kind welcome during the ICTP conference.

During this PhD I got to meet a lot of different people that helped me to feel good and comfortable when I just moved in, to make it short I will just thank Dr. Sara Freund and Dr. Olha Popova for taking me with them and introduce me gently to this new adventure when I just arrived.

Finally, I want to give a big thank to my family. Since they don't speak english, I will make it short. Even if they didn't really understand my choice of doing a PhD, they were always supportive.

Contents

List of Figures

List of Tables

Nomenclature

Symbols

Latin letters

A	Oscillation amplitude
a	Graphene lattice
a_s	Graphene interatomic lattice
A_{exc}	Excitation amplitude
A_{osc}	Oscillation amplitude
A_L	Lateral amplitude
A_N	Normal amplitude
A_H	Hamaker constant
B	Magnetic field
B_c	Critical magnetic field
c	Constant
C	Capacitance of plate capacitor
C_{dot}	Quantum dot capacitance
C_{pp}	Atom-atom pair potential
c_P	Specific heat capacity
C_{PAR}	Parasitic capacitance
C_{sub}	Substrate capacitance
C_{tip}	Tip capacitance
C_Q	Quantum capacitance
C_Σ	Total capacitance
D	Displacement current
d	Tip-sample distance
E	Energy
E_{2D}	2D elastic Young modulus
E_C	Charging energy
E_F	Fermi energy
E_{flex}	Flexural phonon modulus
E_{latt}	Lattice modulus
E_n	Quantization energy
E_{wrink}	Wrinkle modulus
E_Y	Young modulus
F	Force
f_0	Resonance frequency
f_i	Cantilver interaction frequency
F_C	Coulomb force

$F_{capacitor}$	Force between two plate capacitors
F_{Chem}	Chemical force between tip and sample
F_{elec}	Electrostatic force
F_{ext}	External forces
F_{fric}	Friction force
F_i	Interaction force
F_L	Lateral force
F_{min}	Minimum detectable force
F_N	Normal force
F_{Pauli}	Pauli-repulsion forces
F_{TOT}	Total tip-sample force
F_{vdW}	Van der Waals force
$F(x)$	Lateral force
$F(z(t)$	Distance dependent interaction force
f	Frequency
h	Height
$HWHM$	Half width at half maximum
$\hbar$	Reduced Planck constant
K	Momentum at the K points of the Brillouin zone
k	Spring constant
k_B	Boltzman constant
k_{eff}	Effective spring constant
k_f	Fermi wave vector
k_v	Wave vector
j	Local current
I	Tunneling current
M	Magnetization
m	Electron mass
m_{eff}	Effective mass
M_L	Lateral momentum
M_N	Normal Momentum
M_s	Tip magnetization
m_{tip}	Magnetic moment of the tip
N	External attractive axial force
n	Doping
n_D	Disorder density
n_s	Density to fill the mini Brillouin zone
$n_s/2$	Half filling
$n_s/4$	One quarter filling
$3n_s/4$	Three quarter filling
l_B	Magnetic lenght
L, l	Cantilever lenght
L_x	Lenght accross the quantum dot
l_{eff}	Effective lenght
L_y	Length along the quantum dot
$P(\phi)$	Probability density
P_i	Cantilever dissipated power

P_0	Free cantilever driven power loss
p	Vacuum pressure
p_i	Dipole moment of atoms
Q	Quality factor
Q_i	Electric charge of bodies
q	Electron charge
R	Radius of curvature of the tip
r_C	Cyclotron radius
R_{sys}	Sytem resistance
r	Distance between two bodies
S	Effective area of the quantum dot
T	Temperature
t	Thickness
U	Bias voltage
U_{CPD}	CPD bias voltage
U_{el}	Electrostatic potential
V / V_S	Bias voltage
v	Velocity
V_0	Potential barrier
V_{BIAS}	Bias voltage
V_{BG}	Backgate voltage
V_{CH}	Chemical potential
V_{CPD}	Voltage compensating the contact potential difference
V_{DC}	Direct current voltage
v_F	Fermi velocity
V_{max}	Maximun bias voltage
V_{vdW}	van der Waals potential energy
W	Width
w	Interlayer hopping
$x(t)$	Equilibirum fluctuations
x	Coordinate of one horizontal axis in the sample surface place
x_0	Cantilever driven oscillations
x_{rms}	Rms amplitude
y	Coordinate of one horizontal axis in the sample surface plane
z	Coordinate of the vertical axis between tip and sample
$z(t)$	Time dependent tip position

Greek letters

α	Lever arm
α_i	Polarizability of atom
Γ	Friction coefficient
Γ_0	Cantilever internal friction
Γ_{ph}	Phononic friction coefficient
γ	Tunneling rate
δ	Cantilever deflection
δf	Frequency shift
δf_L	Lateral frequency shift
δf_N	Normal frequency shift
ϵ	Dispertion energy
ϵ_0	Vacuum permittivity
ϵ_T	Energy loss factor
κ	Compressiblity
$\Theta(...)$	Heaviside unit step function
θ	Angle
μ	Static friction coefficient
μ_0	Vacuum permeability
μ_B	Bohr magnetron
μ_i	Moment of atom
μ_{Ec}	Kinetic friction coefficient
ρ	Density of states
ρ_i	Number of atom par unit volume
ρ_m	Mass density
σ	Distance that brings the intermolecular potential to zero
σ_0	Pre-tension
σ_p	Standard deviation of the momentum
σ_{phi}	Phase noise
σ_x	Standard deviation of the particule position
τ	Decay/Relaxation time
τ_{AM}	Amplitude modulation decay time
τ_{FM}	Frequency modulation decay time
ϕ	Work function
$\phi(t)$	Fluctuating phase
Φ_B	Peierls phase
ϕ_i	Phase
ϕ_{samp}	Sample work function
ϕ_{tip}	Tip work function
χ	Magnetic susceptibility
ψ	Electron wave function
ω_0	Angular resonance frequency
ω	Frequency of the sensor
ζ	constant

Abbreviations

Å	Angstrom 10^{-10} m
aF	AttoFarade 10^{-18} F
AC	Alternative current
AFM	Atomic force microscopy/microscope
AM	Amplitude-modulation
ATEC-Cont	Advanced tip at the end of the cantilever for contact mode
BS	Bohr-Sommerfeld
BW	Backward
BZ	Brillouin zone
CNP	Charge neutrality point
CPD	Contact potential difference
CR	Coulomb rings
Cu	Copper
DOS	Density of states
fA	FemtoAmpere 10^{-15} A
FF	Filling factor
FFT	Fast Fourier transform
FM	Frequency-modulation
FP	Ferromagnetic phase
FW	Forward
GPa	GigaPascal
hBN	Hexagonal boron nitride
LDOS	Local density of states
LT	Low temperature
MoS_2	Molybdenum disulfite
MHz	MegaHertz 10^6 Hz
NC	Non-contact
nm	Nanometer 10^{-9} m
nF	NanoFarade
p-AFM	Pendulum atomic force microscope
PLL	Phase locked loop
pm	Picometer 10^{-12} m
PMMA	Polymethyl methacrylate
PP	Paramagnetic phase
PSD	Position sensitive detector
qbits	Quantum bits
QD	Quantum dot
RT	Room temperature
SiO_2	Silicon dioxide
mBZ	mini Brillouin zone

0D	Zero-dimentional
1D	One-dimentional
2D	Two-dimensional
MATBG	Magic angle twisted bilayer graphene
SPM	Scanning probe microscopy/microscope
STM	Scanning tunneling microscopy/microscope
STS	Scanning tunneling spectroscopy
SICM	Scanning ionic conductance microscopy
SNOM	Scanning near optical microscopy
TBG	Twisted bilayer graphene
TMDs	Transition metal dichalcogenides
UHV	Ultra-high vacuum

Introduction

"Nothing in life is to be feared; it is only to be understood."
Marie Sklodowska-Curie

The studies on Two-Dimensional materials (2D materials) and the understanding of their physical characteristics especially their electronic properties represent a major technological improvement. Indeed, the understanding of their nanoscale properties in the short and long scale at different conditions enable to optimize their functionalities.

Moreover, the evolution of synthesis and characterization techniques enabled the realisation and studies of 2D materials. The first to be investigated was graphene and it opened new possibilities. Even after two intensive decades of observations and different kind of experimentations, graphene seems to not have given all its secrets. Recently, superconductivity has been observed on Twisted Bilayer Graphene (TBG) at very low temperature. Graphene like other 2D materials exhibits very interesting features. Another material of great interest is Molybdenum Disulfate (MoS_2). Its electronic properties show interesting spin-orbit coupling. With that, it can be understood that the future of technology relies on our understanding of such new materials that could reveal more than it seems.

Technology has developed since the XX^{th} century and has reached the nanoscale domain. 2D materials are very promising materials in the advancement of new technologies. Although the electronic, mechanical or even optical properties are heavily studied, their energy dissipation mechanisms are on the other hand less investigated.

The energy loss mechanisms are not trivial. The understanding of how and where the energy is lost in a material is very crucial. The energy loss is responsible of the aging and the performance of materials of every device that is being used nowadays. In fact, the improvement of nanotechnology is based on increasing the density of devices that can be put in a small area. Such nanoscale objects are not necessarily in direct contact with each other. However, the intrinsic energy loss of each additional object and the interactions between them due to their small distance can lead to a non negligible energy loss. Indeed, at this scale, quantum size effects might happen and induce some

unexpected effects affecting the material properties. Sometimes, these quantum effects are the targeted effects like in quantum computing for example.

Addressing the energy loss in such systems represent an important topic and is one of the keys of the new challenges that have to be understood and solved. Dissipation losses can also help to understand the origins or the mechanisms of the new quantum phenomena. It is therefore not delusional to think that it can be an alternative way to investigate quantum effects on 2D materials or quantum systems.

The development of Scanning Probe Microscopy (SPM) permits the investigation of the surface with nanoscale size. The different technological advancement of this technique allowed to improve the surface investigations. Nowadays, a wide range of studies are possible due to the development of different SPM based techniques. The possibility to do experiments under Ultra High Vacuum (UHV) at very low temperature while applying magnetic field is another improvement made. The UHV environment enables to investigate very clean surfaces without any pollutants on the sample surface. This represents a big advantage for the observation of quantum phenomena.

The Atomic Force Microscopy (AFM) exists in a large number of variations and the pendulum AFM (p-AFM) is one of the multiple AFM based techniques. The conventional AFM geometry has been changed in order to increase dissipation and force sensitivity. It is operating in non-contact way, in the dynamic mode regime. The cantilever oscillations might be affected by different kind of damping effects, classical effects like Joule dissipation, phononic friction or quantum effects like single electron charging in quantum dots.

In the Thesis I addressed the energy loss (or energy dissipation) mechanisms of graphene and MoS_2 using the p-AFM.

The first part consists of the 'State of the Art' on friction and 2D materials. Its goal is to introduce the different topics that are discussed through the Thesis. The second part is composed of three chapters that discussed the materials and the methods used, namely: the AFM, the non-contact friction and the p-AFM. The last part referred the different experimental results and it is divided in three chapters: energy dissipation of the free-standing nanodrum graphene, the twisted bilayer graphene and the magnetic energy loss in MoS_2 monolayer. The manuscript will end with a conclusion.

1

State Of The Art: Friction And 2D Materials

The twenty first century marks the beginning of the age of nanotechnology. It represents a turnover for the overall technology development and one of the reasons comes from the prefix 'nano-'. It comes from a Greek world '$\nu\alpha\nu o\varsigma$ or nanos' meaning '*dwarf*', in science this word is used as the unit for one billionth of a meter noted 'nm' or '10^{-9} m' [5]. This is a very important notion because this nanometric scale is in the same order of magnitude as atoms. In other words, we are able to use, modify, study and start to understand via experiments the atomic structure and properties of matter. This advancement was made possible thanks to the improvement of computational science, engineering (with the development of instruments allowing to investigate materials at the nanometric scale), modern physics and the production of atomic crystals.

Their properties are heavily studied and their internal and external losses became a hot topic. The improvement of friction and the corresponding dissipated energy represents a non-negligible part of the performance of a device. Progress can only be made by understanding the material properties and finding the proper parameters to tune their frictional response and dissipated energy.

The goal of this chapter is to give a brief introduction about friction and 2D materials, especially graphene and MoS_2. These two materials are the scope of this Thesis. The understanding of their frictional response is discussed here.

1.1 History Of Friction

Friction is a common physical phenomenon but also one of the least understood. Already at the beginning of humanity, friction played a huge role in the evolution on humankind. Making fire relies on sliding two rocks together in order to create a flame.

In our everyday life we also encounter friction for instance by walking and biking. In science, the study of friction at the macroscopic scale is called tribology [6].

Nowadays, we are living in a heavily industrialized society that needs tremendous amounts of machines. In this world, friction and all its related phenomena can have a big impact on the working properties of devices. Indeed, friction is the main mechanism in the ageing process and energy/power loss. These losses could be drastically diminished if we understood them better. This is only possible by means of scientific investigations.

The first reported experiment about friction were performed by from Leonardo da Vinci [7]. Experiments consisted of sliding blocks, rolling weights and other materials. Those experiments lead him to two conclusions:

1. *"Friction produces double the amount of effort if the weight be doubled."*
2. *"The friction made by the same weight will be of equal resistance at the beginning of the movement although the contact may be of different breadths or lengths."*

Meaning that the friction force of a the sliding resistance was proportional to the load and independent of the apparent contact area between the sliding body and the surface.

Those observations were confirmed a few centuries later by the French scientist Guillaume Amontons in the $XVII^{th}$ century. He studied in more details the friction encountered by two bodies and came out with the dry friction law:

$$F_{fric} = \mu F \tag{1.1}$$

where μ the static friction coefficient and F the loading force. This law was then confirmed one century later by Charles-Augustin Coulomb with his studies on friction and he completed da Vinci's and Amontons's observations by introducing a third law:

3. *" The kinetic friction is independent of the sliding velocity."*

The kinetic friction μ_{Ec} is generally smaller than the static friction μ.

During the industrialization time, XIX^{th} and XX^{th} century, the tribology research progressed by investigating a wide range of materials. They were able to understand why the visible contact area had a small effect. They found out that all the phenomena happen at a smaller scale, micrometer scale. In fact, the true contact between the

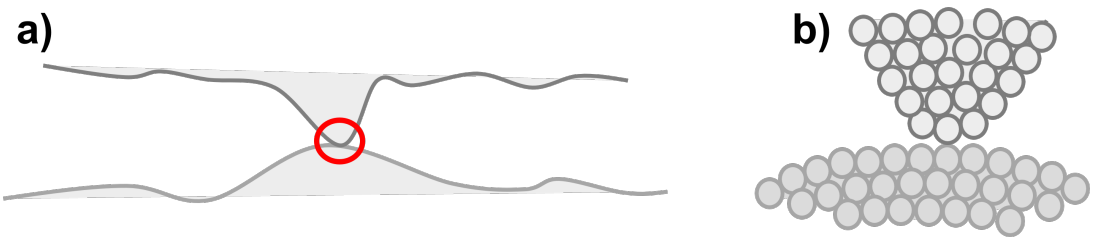

Figure 1.1: — *Schematics of the contact area.* ***a)*** *random asperities of materials at the microscale, where the red circle shows a contact area.* ***b)*** *zoom at the atomic scale contact marked with red circle on a). Only few atoms are really in contact.*

materials is comprised by the number of asperities (roughness of the surface), see figure 1.1 a). The friction dependence is the result of those random (in size and shape) asperities combined with interface effects. Those investigations were made by engineers to implement their lubrication methods, hence no atomic scale investigations were made. In addition to that, no instruments at that time were able to perform such experiments.

The second half of the XX^{th} century saw the emergence of new technologies and the advancement of computational power and theoretical techniques. The atomic scale studies became possible and the nanotribology field started.

1.2 Non-Contact Friction

The friction between two bodies produces energy losses or energy dissipation [8,9]. At the nanoscale, it was observed that a tiny friction force is present when objects are separated by a distance of few nanometers [10]. Several non-contact friction mechanisms were established, namely: phononic friction, Joule dissipation, van der Waals friction (stochastic friction). The explanation of the non-contact main mechanisms will be discussed in the following chapter 3.

The definition of contact and non-contact friction can be introduced with the contact area. In the previous section its importance was described and represented an important parameter in the study of friction. It has been demonstrated that the contact area is related to the contact between the asperities of two objects [11], see figure 1.1 a). In fact, the friction force is mainly due to the atoms which are close enough to have chemical interactions (Fig. 1.1 b)) leading to a creation of chemical bonds also known as ionic or covalent bonds. This leads to the definition of contact: *two objects are in contact if they are close enough to interact chemically.* Hence, non-contact can be defined as: any distance larger than the chemical interaction range.

In order to sense both, contact and non-contact friction at the nanoscale, the AFM [12] revealed itself as an indispensable tool. Indeed, it can work in both regimes and enables the acquisition of the corresponding topography images. This technique is describe in chapter 2.

1.3 2D Materials

The development of 'technologies' always follows our understanding of the materials around us. This word is interesting because it is the contraction of two words, '$\tau\epsilon\chi\nu\eta$, or téchne' meaning art, skills or craft and '$\lambda o\gamma\iota\alpha$, -logia' meaning the study of a branch of a discipline. The most important ages of humanity are also labelled corresponding to the evolution of materials we could use and understand: 'stone age', 'bronze age', 'iron age' and they all show an improvement of our way of living.

Research in materials science is often followed by new technologies. Indeed, the specific materials properties are observed, classified and used regarding their potential

applications. The more we know about the material properties the further we can push technology.

Their properties come from a combination of different factors and they can change depending on their size. Electrical conductivity, chemical reactivity, mechanical or optical properties can change drastically at the nanometer scale. The development of new detection methods and our ability to produce such thin materials opens new possibilities and starts the age of 'technology' and nowadays the age of 'nanotechnology'.

The size of the objects can be used to categorize them in different categories, see figure 1.2:
- bulk, all the three dimensions (x, y and z) are larger than the nanometric scale. It's the material that we all know and deal with most of the time in our life,
- 2D materials, two-dimensions are larger than the nanometric scale. They look like very thin sheets,
- one-dimension objects or 1D objects, one dimension is larger than the nanometric scale. They look like a tube or a wire,
- zero-dimensional object or 0D, all dimensions are at the atomic scale. They look like a dot or a single particle.

Among the last three, 2D materials are the easiest to produce. Indeed, it is often possible to reduce the thickness of material down to a single atom using different methods like mechanical exfoliation or chemical vapour deposition. Most of the interesting physics is happening there. 2D materials investigations have exploded for two decades after the successful separation of a single graphite sheet also called graphene by using the exfoliation method by Prof. Dr. Andre Geim and Prof. Dr. Konstantin Novoselov [13]. In 2010 their research was awarded with Nobel prize.

2D materials are atomically thin crystals. They consist of a stack of different layers connected together by van der Waals forces and with covalent bounds in the intralayer [14]. Different types of 2D materials exist: graphene, hexagonal boron nitride (hBN), various Transition Metal Dichalcogenides (TMD) and emergent monoatomic crystals also called Xenes.

2D materials were first studied theoretically [15–18] and it was concluded that the long-range order cannot exist in two dimensions due to thermodynamic instabilities. Indeed, the contribution of thermal fluctuations in low dimensional materials should

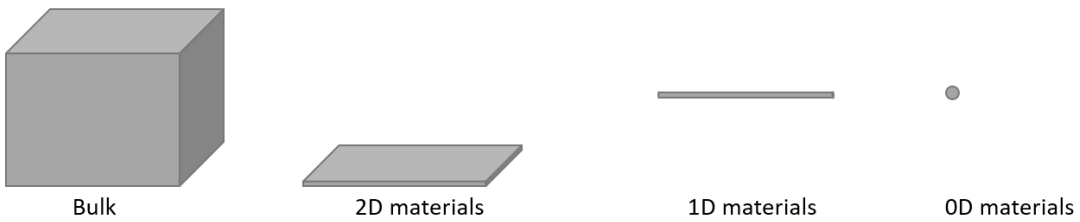

Figure 1.2: — *Schematic of the different material size going from bulk to 0D.*

lead to atomic displacement comparable to the interatomic distance at any finite temperature. Hence, any material made up of interacting particles with harmonic pair potentials cannot exist because they are constrained in the low (- atomic) dimension space where they are defined forbidding out-of plane motion of the particles [16, 19]. The first experiments on growing 2D crystals confirmed this observation [20, 21]. Thin films with a thickness in the atomic range were unstable and were segregating and decomposing. The successful separation of graphene was very surprising, because the layers were separated using exfoliation process but most importantly graphene was stable on a supporting substrate in an ambient environment [13]. The explanation of graphene stability was then heavily demanded and the results concluded that in- and out- plane lattice distortions seem to be essential for the structural stability of graphene [22]. The experiments shows that the out-of-plane motion is not forbidden and plays an important role in the stability of graphene and more generally of 2D materials. The single layer materials out-of-plane vibrational amplitude appear to be much larger than the in-plane vibrational amplitude meaning that the atoms in such materials are not strictly located in the plane [19]. This is the key explanation of their stability.

In general, 2D materials are promising candidates for the development of new technologies. They have interesting mechanical and electronic properties. In the bulk shape, they represent very good lubricant materials due to their van der Waal interbonds and when isolated down to few or one layer, they exhibit a panel of interesting features particularly for electronic and quantum studies. One of their advantages is that they can be investigated separately or stacked on top of each other [23,24], rotated, rolled, stressed or strained. We can induce defects, intercalate ions, study their interface interactions. All that opens a wide range of investigations and different potential applications.

In my work, I studied graphene with two distinct configurations: suspended graphene membranes and Twisted Bilayer Graphene (TBG) and in addition to that, I measured MoS_2 monolayer sheet. All these different materials exhibit different quantum effects and reflect the fascinating and complicated mechanisms of such phenomena.

1.3.1 Graphene

Graphene is the name given to a monolayer of graphite. It is composed of carbon atoms oriented on a two dimensional honeycomb lattice and it forms atomically thin layers as described in figure 1.3 a) and b). The word graphene derivate from the Greek word ' $\gamma\rho\alpha\phi\epsilon\iota\nu$ or graphite' that means "*to write*". Indeed, graphite is widely used in the fabrication of pencils. To write, a friction force is applied to the pencil that deposits few layers of graphite on the paper sheet. The "-ene" at the end of graphene comes from its chemical nature, it is a polycyclic aromatic hydrocarbon (see Fig. 1.3 c)).

Graphene got a lot of attention, since its successful isolation, due to its remarkable electronic and material properties. Moreover, at the atomic level, a single layer of

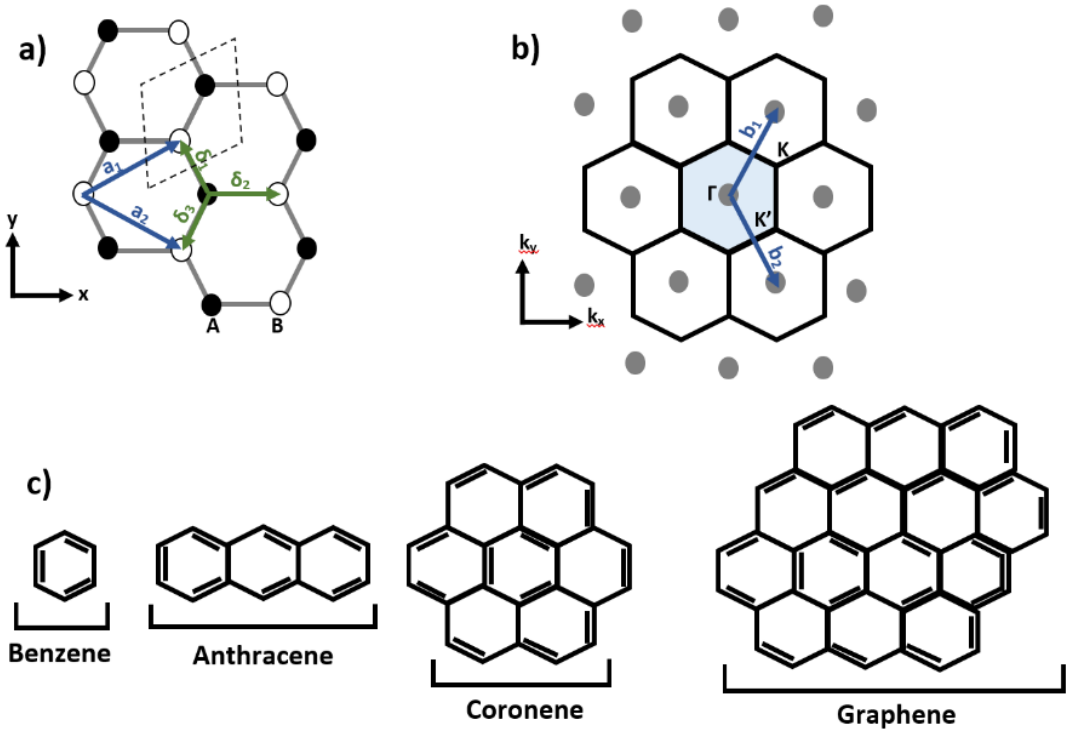

Figure 1.3: — *Schematic of the graphene lattice and chemically familiar derivatives.* ***a)*** *real space crystal structure of graphene, showing its honeycomb lattice structure. A and B are carbon atoms marked in black and white respectively. They both have a triangular sublattice with basis vector a_1 and a_2 in blue and the unit cell is represented by the black dashed diamond. The nearest neighbours are marked by the vectors δ_i in green and they are three in total.* ***b)*** *reciprocal lattice (full line hexagon) with the corresponding reciprocal vectors b_1 and b_2 in blue. The first Brillouin zone is coloured in light blue with the high symmetry point Γ, K and K' points. The gray points correspond to the graphene diffraction points and are surrounded with hexagon accordingly.* ***c)*** *hierarchic schematic of aromatic hydrocarbons from benzene to graphene.*

graphene appears to be optically transparent, it is also electrically conductive and flexible. Its electron mobility is much larger than in silicon. Another particularity of graphene is the nature of its charge carriers, since they reproduce relativistic particle behaviour. In fact, the periodic potential of the honeycomb lattice (Fig. 1.3)) enables the emergence of quasi-particles that can be represented as electrons that lost their mass making its electronic properties widely investigated.

Concerning the free-standing graphene, one of the first experiments was performed by Meyer *et. al.* [25]. They deposited a layer of graphene across a metal supported grid and used electron diffraction to investigate the membranes. A broadening of the diffraction pattern was observed, when changing the diffraction tilt angle. The authors concluded that the membrane was not completely flat, meaning the presence of out-plane corrugations creating ripples on the membranes. The estimated ripples had a size in the range of 5 *nm* to 20 *nm*. Increasing the number of layers from one to two

permits reducing drastically this phenomenon and for more layers, to completely erase it. As a first observation, this indicates that the formation of ripples is intrinsic to monolayer graphene. Further investigations of the ripples using Scanning Transmission Electron Microscopy revealed ripples with amplitudes of $A = 0.5\ nm$ and widths of $W = 5\ nm$.

Those ripples have a strong effect on the graphene properties depending on their size and densities can be cited the mechanical properties [26] and the electronic properties [27].

It is known that electronic properties strongly dependent on the number of layers [28] as well as on multi-layer stacking. The stacking of two or more layers of graphene, or another 2D materials, creates a superlattices structure also called Moiré pattern. This superlattice structure is due to a different stacking sequence of the different graphene layers: AA (simple hexagonal, Fig. 1.4 a)), ABAB (hexagonal also called Bernal stacking, Fig. 1.4 b)) and the ABC (rhombohedral, Fig. 1.4 c)). Those stacking effects are relevant only for thin films graphene (one to ten layers) and impact mechanical [26] and electronic properties [29, 30].

Multi-layer stacking is extremely relevant in case of TBG. In 2018 the group of Prof. Dr. Pablo Harrero-Jarillo *et. al.* were able to experimentally investigate twisted graphene at the so called magic angle twist and observed a drastic change of the electronic density of states [31]. Indeed, the change of the twist angle of the bilayer changes the Moiré pattern and apparently this superlattice change also tunes the electronic properties of the graphene. Previous theoretical studies already predicted that at some special angles (the magic angles) Fermi velocity can drop to zero allowing the presence of flat bands [32–34]. These bands are the nest of exotic quantum phenomena

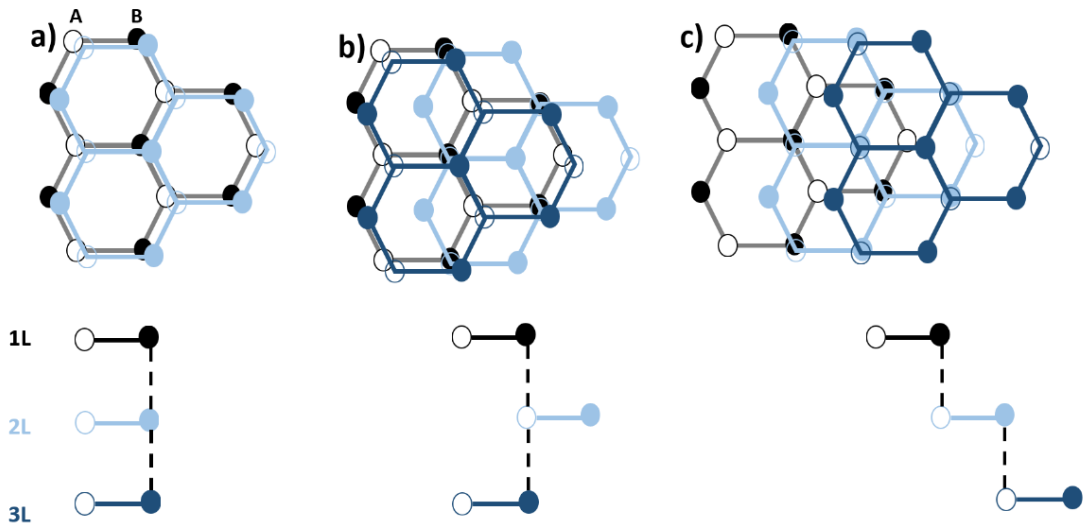

Figure 1.4: — *Schematic of graphene stacking sequences.* ***a)*** *simple AA stacking.* ***b)*** *ABAB stacking sequence.* ***c)*** *ABC stacking sequence.*

such as Mott insulator phase transition which is due to presence of strong correlated electron-electron interactions [35], ferromagnetism [36] where the Hofstadter butterfly spectrum [37] was successfully observed or even superconductivity [31, 38, 39].

The first magic angle corresponds to a twist equal to $\theta = 1.08°$ and it is the most investigated angle where all previously mentioned exotic quantum phenomena were observed. The density of states of this angle revealed high charge density for the AA stacking spot and no density for the other stacking sequences [40].

In my work, dissipation measurements on free-standing graphene and TBG at the magic angle twist are reported in chapter 5 and chapter 6, respectively. Their different properties at low temperature ($T = 5\ K$), under Ultra High Vacuum (UHV) and under magnetic field is investigated.

1.3.2 Molybdenum Disulfate

MoS_2 is part of the TMD family. TMDs consist of layered 2D materials with the type MX_2, where M is a transitional metal atom (Mo, W, V...) and X a chalcogen atom (S, Se or Te) [41]. A monolayer of TMD looks like a sandwich where the M atoms are surrounded by X atoms [42] as illustrated in figure 1.5 for MoS_2. In comparison to graphene their charge carriers are massive and the material is semi-conducting. The energy bandgap is indirect for the bulk, whereas it experiences a transition to direct bandgap when reduced to a monolayer. On the other hand, the honey comb-like structure of MoS_2 (Fig. 1.5 c)) as well as its low-energy-Dirac physics, its spin-orbit coupling [43, 44] and its mobility [45] makes it complementary to graphene. Its electronic and optical properties can be tuned and are now widely investigated.

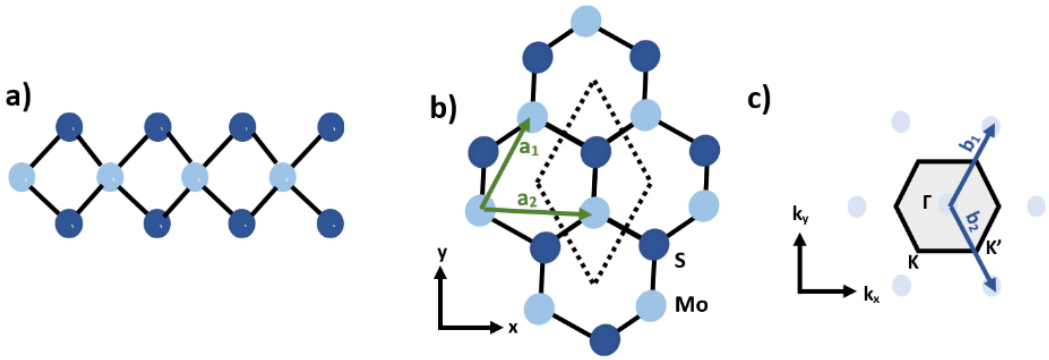

Figure 1.5: — *Schematic of MoS_2 crystal structure.* ***a)*** *side-view of a monolayer showing the internal structure where the Mo atoms are sandwiched between the S atoms.* ***b)*** *top-view of the monolayer showing the honey comb-like lattice structure of MoS_2. Mo and S atoms have a triangular sublattice with basis vector a_1 and a_2 in green and the unit cell is represented by the black dashed diamond.* ***c)*** *corresponding reciprocal space showing the high symmetrical points Γ, K and K' as well as the reciprocal vectors b_1 and b_2. The Brillouin zone is coloured in gray and the blue spots are the diffraction spots.*

In its début in industry, MoS_2 has often been mistaken with graphite due to its similar colour and physical behaviour. It was only in 1927 that it was used as a lubricant, but mixed with other materials such as talc, mica or graphite. In 1939, some patents were considered using it alone as a solid lubricant. And this was started only in 1941. Since that moment, it has been heavily studied in this field [46].

In the beginning of XXI^{th} century, the studies of MoS_2 nanosheets again attracted attention mainly due to their electronic properties and due to the possible applications in nano-electronics. Bulk MoS_2 has an indirect gap of 1.2 eV [47] and by reducing its number of layers, the electronic structure of the material is changed. That way due to quantum confinement [48], the nanosheet of MoS_2 becomes a semiconductor with a direct gap of 1.8 eV [49].

Monolayers TMD have their band gap extrema at the corners of the Brillouin zone (K and K' points) which give an extra degree of freedom. Their spin-orbit coupling in addition to their space broken space inversion symmetry results in the presence of anomalous Landau levels [50]. The presence of the magnetic moment has opened unpredicted, rich and novel physics related to nano-materials. Recent experiments on MoS_2 monolayer enabled investigations of the duality between spin-orbit coupling [51, 52] and strong electron-electron interactions [53].

In my work, dissipation measurements on MoS_2 monolayer are reported in chapter 7. The force and dissipation response of the material to the external magnetic field at low temperature ($T = 5\ K$) and under UHV is investigated.

1.4 Summary

In this chapter a very brief introduction about friction and 2D materials is reported. The need of improving our knowledge about the different friction mechanisms and their link to the size of the objects is still an open research field. The development of nanotechnology increases our need to understand the fundamental effects occurring between the nano-objects. The understanding of those effects will also enable us to improve the development of our technology. To do so, p-AFM is used as a tool to observe energy loss between single asperity tip and graphene and MoS_2 samples.

In my work, I measured non-contact energy dissipation on 2D materials at very low temperatures where quantum effects are observed. The objects do not need to be in contact to exhibit frictional losses, the internal processes like phase transitions or energy level crossing or proximity of the tip itself can also be the reason of potential energy loss.

2

Scanning Probe Microscopy Principle

In the last 40 years, Scanning Probe Microscope (SPM) established itself as one of the most powerful technique to investigate the surface of materials. It is used in many different research fields such as: material science, solid state science as well as biology and chemistry. SPM is a set of different methods that uses a local probe to scan the surfaces and sense the different interactions between the probe and the surface. The first SPM method that has been developed in 1981 is the Scanning Tunnelling Microscopy or STM [54]. Gerd Binnig and Heinrich Rohrer received the noble prize for it in 1986. The same year, they developed the AFM [12]. Since then, SPM developed very widely, sensing different type of interactions that all lead to different techniques. Indeed, the targeted interactions determine the type of SPM - just to cite few of them: the SNOM (Scanning Near Optical Microscopy) that senses the evanescent wave at the surface or the SICM (Scanning Ionic Conductance Microscopy) that measures the ionic current created when a potential difference is applied between the probe and the liquid where the object is immersed. More advanced technologies allow to investigate the surfaces using SPM in different ways. For example one can vary the scanning geometry [55], one can add mechanical induced strain on the device [56], change the sensor geometry [57] or functionalize the tip with single molecules to increase the spatial resolution [58].

The idea to use a very thin tip to scan over the sample surface in an non-invasive way comes from Russell Young ten years before the STM with the invention of the Topografiner [59]. His idea was to use a conducting tip and measure the field emission of electrons between the tip and the sample to image the sample surface. The Topografier did not succeed due to the insensitivity of the field emission. Nevertheless, he suggested that metal-vacuum-metal tunnelling would help to significantly increase the sensitivity but he was not able to verify his theory due to technical issues. A decade later when the engineering processes developed a bit more, Binnig and Rohrer where able to successfully verify this theory by combining metal-vacuum-metal system with probe

scanning and since then the SPM technology developed.

The purpose of this chapter is to give a short introduction to the STM and AFM techniques.

2.1 Scanning Tunnelling Microscopy

STM is the first SPM method that has been developed in 1981 by Binnig and Rohrer [54]. It is also the first scanning probe technique that achieved atomic resolution over a silicon (111) surface in 1982. It measures the tunnelling current between the probe and the surface. The probe as well as the sample has to be a metallic or semi-conducting materials.

The electron tunnelling is a quantum phenomenon. In classical physics, an electron can pass over potential barrier (V_0) if it's energy (E) is larger than the height of the potential barrier ($E > V_0$). Otherwise, for $E < V_0$ the electron cannot pass it, see figure 2.1 a). Quantum mechanics states that there is a non-zero probability for an electron to pass the potential barrier when $E < V_0$ via tunnelling through it (Fig. 2.1 b)). In this case the electron is not described as a particle, but rather as a wave function. In STM case, the barrier is represented by the tip-sample distance that is mainly composed of vacuum gap and a tunnelling current flow can be detected before the tip and the sample comes into contact.

In a first approximation the tunnelling current can be written:

$$I \propto AUe^{-2d\sqrt{\frac{2m}{\hbar^2}\phi}} \tag{2.1}$$

where A is a constant, U is the probe voltage, d the tip-sample distance, $\hbar$ the reduced Planck constant, m the electron mass and ϕ the work function. Equation 2.1 shows that the tunnelling current is exponentially dependent on d, which points out to the high sensitivity in the z-direction since the tunnelling current is changing strongly as a function of the distance.

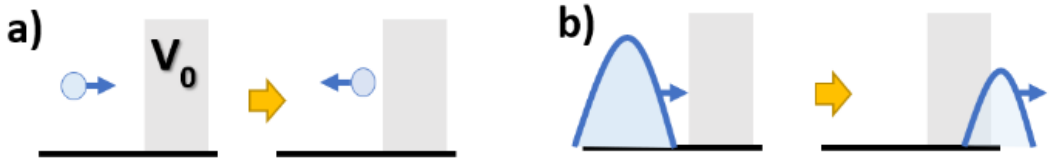

Figure 2.1: — *Comparison between classical physics and quantum physics when $E < V_0$.* ***a)*** *schematic showing the total reflection of the electron when the potential barrier is larger than the electron energy as expected in classical physics.* ***b)*** *quantum physics version of a). The electron is no longer described as a particle, but as a wave function. In this case the electron can pass through the barrier.*

STM has two working modes [60,61], the **constant height mode**, where the probe is moving in the horizontal plane over the sample and the tunnelling current varies with the topography and the electronic density of states of the sample surface. The second mode is **constant current mode**. The probe follows a profile of iso-density electronic states energy at the Fermi level. A feed-back system is used to control the extension of the piezoelectric scanner in the z-direction, in a way to maintain constant tunnelling current between tip and sample. The recorded tip positions during the scan give a tridimensionality map corresponding to the tunnelling iso-current surface of the sample. Both modes allow the acquisition of images with atomic resolution.

2.1.1 Density Of States

The density of states (DOS) or local density of states (LDOS) is pivotal for STM. It is defined as the number of allowed electron states per volume at a given energy [5]. In case of STM, the tunnelling current does not only decay exponentially with d, but it is also strongly affected by the DOS of the sample at the Fermi level, which is described by equation:

$$I \propto V\rho_s(0, E_F)e^{-2d\sqrt{\frac{2m}{\hbar^2}\Phi}} \tag{2.2}$$

where $\rho_s(0, E_F)$ is the DOS (or the LDOS) of the sample surface at the Fermi energy (E_F) and V the applied bias voltage. Equation 2.2 shows that the tunnelling current is proportional to the DOS of the surface underneath the tip. In other words, the tunnelling current does not depend on the total charge density but to the charge density within eV below the Fermi surface. With the equation above, it is visible that STM can be used to investigate of DOS and it gives access to the electronic structure of the studied material.

DOS spectroscopy is typically performed at constant height mode via tip-sample bias voltage sweeps. The experiment consists of varying the tunnelling current with the bias voltage (I-V curve) measured at a fixed tip-sample distance. Thus, different occupied and unoccupied states are contributing to the tunnelling current. The resulting curve shows variations reflecting the presence/absence of electrons at the different bias voltages.

2.1.2 Lock-In Amplifier

The signal to noise ratio in any measurement is very important. In order to optimize it, a lock-in amplifier is used. It allows extracting signals with a small amplitude (very small Alternating Current (AC) signal in the range of few nanovolts) drowned in a big noise signal. It uses a phase sensitive detection method to demodulate the desired signal at a specific frequency and phase. Thus, the noise signal at other frequencies or random phases are getting rejected [62].

2.1.3 STM Spectroscopy

Spectroscopy is used to characterize the local electronic properties of the sample that cannot be resolved by imaging. This method allows a precise analysis of the electronic states as well as the charge state of the quantum entity.

To investigate the DOS of a sample, the I-V measurement is the most widely used spectroscopy method. Measuring directly the I-V curve consists of acquiring the integrated density of states. In order to get the DOS it is mandatory to derivate this quantity. It can be done numerically, however, this approach is too noisy. To avoid this, the derivative is measured directly by using a lock-in amplifier to modulate the tunnelling current with certain frequency and record the data with a reasonable/high signal to noise ratio. The bias voltage is modulated with an AC voltage with a certain dV (few mV) around the interested DC voltage V [63, 64]. The voltage modulation dV enables to record the current modulation dI. The result measurement is the differential conductance ($g(V)$) that is often referred as dI/dV. This quantity is directly proportional to the DOS ($\rho(eV)$) following this equation:

$$g(V) = \frac{dI}{dV} \propto \rho(eV) \tag{2.3}$$

In Scanning Tunnelling Spectroscopy (STS) the differential conductance ($g(V)$ or dI/dV) is recorded versus the bias voltage. Thus, the electronic states of surfaces can be investigated. For conversion of dI/dV into LDOS needs differential conductance division (dI/dV) by conductance (I/V). The transformation permits to obtain LDOS versus the energy.

2.2 Atomic Force Microscopy

STM gives the possibility to record images with atomic resolution, however it is restricted to conducting surfaces due to the fact that insulators do not allow the flow of a current. To overcome this problem, Binning, Gerber and Quate developed a new microscopy technique in 1986, namely AFM [12].

The principle of AFM is based on a very thin tip scanned over a surface. In this case, the measured signal is the interaction force between the tip atoms and the sample's surface atoms. These interactions are complex. The atoms at the extremity of the tip experience short-range interactions, whereas the other atoms of the tip contribute to the long-range forces. The tip is fixed at the end of a cantilever and the acting forces will bend the cantilever: attractive forces will move the cantilever towards the sample surface, while repulsive forces will move the cantilever far from the surface. The cantilever is usually described as a spring and its movements can be described using Hooke's law [65]:

$$F = -k\delta \tag{2.4}$$

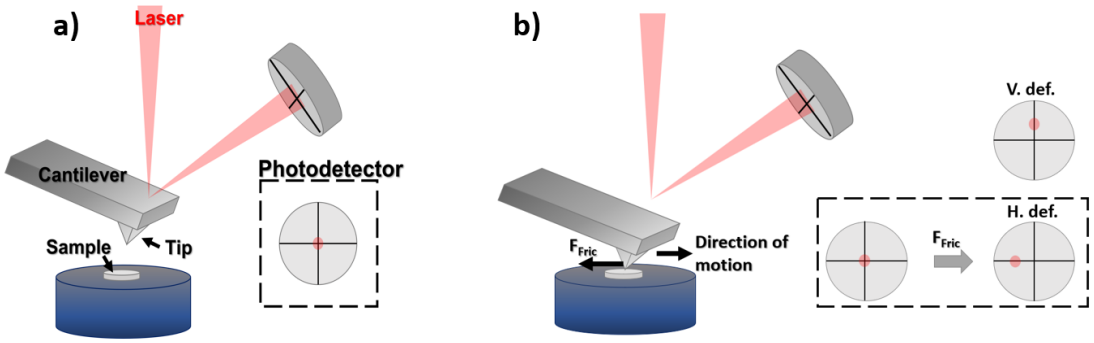

Figure 2.2: — *Schematic of a typical AFM beam deflection setup.* ***a)*** *schematic showing the optimal position of the spot on the photodetector.* ***b)*** *schematic shows the effect of contact frictional forces resulting the horizontal deflection of the spot on the photodetector whereas vertical deflection is due to normal forces (dashed rectangle).*

where F is the force at the edge of the cantilever, k the spring constant and δ the cantilever deflection.

The deflection is measured by a laser beam that is reflected on the back surface of the cantilever. An incident laser light is focused onto the cantilever and is reflected using a set of mirrors. The beam is monitored using a Position Sensitive Detector (PSD). Those are photodetectors which can measure the position of a light spot in one or two dimensions.

In AFM, the typical photodiode used is the quadrant photodiode meaning four detector segments. They enable to obtains few different spatial positions and determine quite precisely the position of the spot light. Such photodiodes are generally based on PIN technology where an undoped intrinsic semiconductor is placed in between comparable heavily doped p and n semiconductors. The intrinsic layer serves to artificially increase the depletion region of the p-n junction. Indeed, when photons enter a depleted (also called charging) region of a p-n junction it induces its absorption by a creation of an electron-hole pair. The induced electron-hole pair is thus dissociated from the depleted region. Indeed, different carriers are induced and pushed to their corresponding p or n respective regions inducing an electric field. The motion of these carriers is the origin of the measured photocurrent.

The spot position and the intensity are very important parameters that have to be well adjusted. This is due to the fact that all informations (image and spectroscopy) are derived from the intensity of the light. Hence, the position of the beam on the cantilever has to be optimized and its reflection on the PSD has to be at the maximum in order not to lose any information nor induce any artefacts, see figure 2.2 a).

Figure 2.2 b) shows a schematic of the typical PSD set up. The distribution of the light intensity between the higher and the lower part of the photodiode gives the vertical position of the spot and indicates the cantilever deflection δ, also called vertical deflection. The lateral distribution of the light gives information on the cantilever torsion, also called horizontal deflection. In contact mode, the friction forces can twist the cantilever torsionally, which will induce a horizontal deflection of the laser beam on

the photodiode. This motion will give extra information about the frictional behaviour in addition to the topography.

Several operating modes are possible depending on the used force domain [66]:
Contact mode, the tip is very close ($d \leq 0.3\ nm$) or in direct contact with the sample surface, see figure 2.3 a). It is a repulsive force domain regime. In this mode there are two operating sub-modes:

- Constant force, the tip-sample interaction forces are detected via the cantilever deflection using the photodiode. A setpoint is fixed for the cantilever deflection and feedback allows the microscope to move vertically the tip over the surface in a way to keep a tip-sample force constant.

- Constant height, in this mode there is no more feedback. The microscope scans the surface without regulating the vertical position of the tip. This mode is used only on very flat and planar samples to avoid the tip crashing (uncontrolled and unexpected contact that leads to surface damage) due to a very big surface corrugation.

Dynamic mode, the tip is oscillating at resonance frequency in the vicinity of the surface. The advantage of this mode is the absence of tip-sample contact frictional forces. Thus, it allows imaging very fragile samples. In this mode cantilever operates in an attractive force domain regime. Similarly to the previous mode, two operating modes are possible:

- Intermittent mode (Fig. 2.3 b)), the tip come in contact with the sample intermittently. This mode is a combination of contact and non-contact mode. The tip oscillates at a mean distance d far enough from the surface ($d = 0.3 - 1\ nm$) with an excitation amplitude A_{exc} big enough, which enables for an intermittent contact.

- Non-contact mode (Fig. 2.3 c)), the tip is oscillating far from the sample ($d = 1 - 100\ nm$) with very low oscillation amplitudes and at frequencies close to the cantilever resonance frequency. In this mode the forces are attractive.

The purpose of this section is to give a short introduction to AFM, focusing mainly on its dynamic mode of operation.

2.2.1 The Cantilever

AFM uses cantilevers where a sharp tip is attached at its end, they are usually made of silicon. The cantilevers can have different geometry: their length, the width and thickness can be modified in order to change their resonance frequency and spring constant. Other modifications can be done, for example the coating of the cantilever with a metallic layer or a magnetic layer to change the nature of the measured interaction forces.

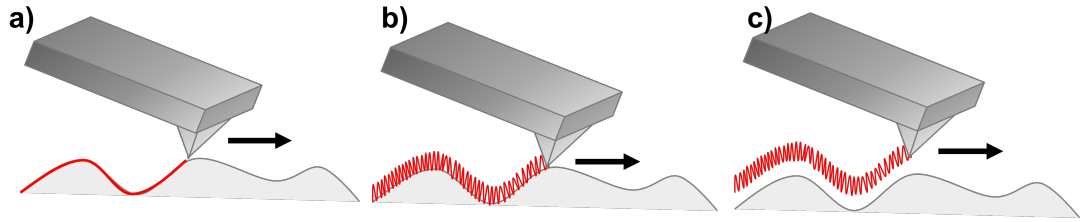

Figure 2.3: — *Schematic of the different AFM modes. The black arrow is referring to the scanning direction.* ***a)*** *contact mode.* ***b)*** *intermittent mode.* ***c)*** *non-contact mode.*

The mechanical characteristics are very important because they enable estimating the minimum detectable forces, described by this formula [67]:

$$F_{min} = \sqrt{\frac{2k_B T k \delta f}{\pi f Q}} \tag{2.5}$$

where k_B is the Boltzmann constant, T the working temperature, f the resonant frequency, δf the measurement bandwidth and $Q = \pi f \tau$ the quality factor with τ the cantilever decay time. Different methods can be used to improve the cantilever sensitivity. The improvement of the sensitivity of the AFM detection will be discussed in chapter 4.

2.2.2 Phase Lock Loop

The Phase Lock Loop (PLL) is an important part of the electronic feedback circuit. Its goal is to synchronize the device output signal with an input signal.

To operate a PLL a phase difference between two signals is needed. In fact, the phase difference between the two signals is used to control the frequency of the loop. The PLL is comparing the phase of the input signal and the internally generated output signal, when these two signals are in a steady state. The PLL will lock this phase difference by adjusting the oscillation frequency of the output signal [68].

In the case of AFM, the input signal is the resonance frequency of the cantilever and the PLL adjusts the excitation voltage and the phase to keep this frequency constant. The oscillation amplitude and frequency are sensitive to the different forces acting between the tip and the sample, hence the PLL adjustment allows obtaining information about the nature of the acting forces.

2.2.3 Dynamic Mode

In dynamic mode, the cantilever is excited at its resonance frequency in order to induce an oscillation. The frequency of the cantilever is controlled via the PLL and the amplitude of the induced oscillation is monitored via an automatic gain controller

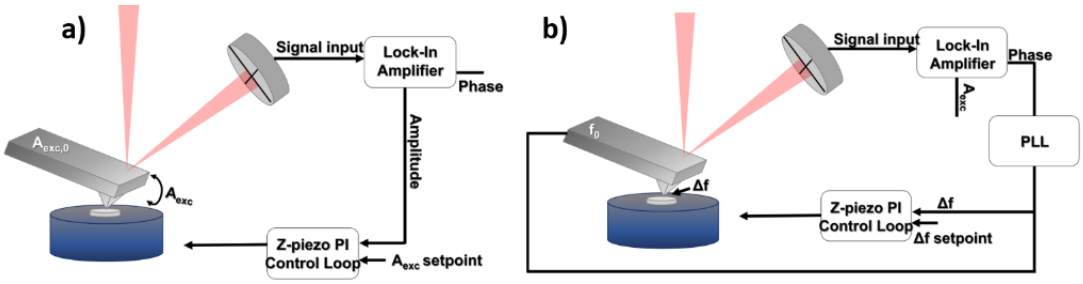

Figure 2.4: — *Schematic of dynamic mode AFM, where the 0 suffix refers to the free system.* ***a)*** *schematic of the AM mode of operation. The oscillation amplitude is recorded by the PSD and tracked by the lock-in amplifier. The AGC feeds the amplitude signal and keeps it constant with respect the original setpoint, by regulating the z position.* ***b)*** *schematic of the FM mode of operation. The input signal is coming from the beam deflection detector, the phase difference between the piezo-excitation and the cantilever oscillation is send to the PLL. The PLL tries to keep the phase shift constant by regulating the frequency of the cantilever. The z-piezo will try to keep the frequency shift constant by adjusting the tip-sample distance.*

(AGC) that keeps the oscillations constant. The oscillation amplitude is influenced by the different acting forces from the sample surface. AFM dynamic method represents a very powerful and versatile technique for atomic and nanometer-scale investigations. It enables the characterisation and manipulation of a wide variety of surfaces, namely metallic, semi-conducting, insulating including molecular networks, very soft materials, and more [66, 69, 70]. One of its best advantages is to offer atomic resolution, while being less invasive than the contact mode since the cantilever is not in direct contact with the sample surface. This mode provides more channels as compared to the contact mode, namely the phase contrast, excitation (or energy dissipation), bimodal phase, etc. This multitude of channels comes in addition to the topography.

There are two basic methods of operation: i) the amplitude modulation (AM) [71,72] and ii) the frequency modulation (FM) [72–74]. The first mode consists of fixing the oscillation amplitude A_{osc} at a fixed frequency that is close to the resonance frequency. When the tip gets close to the sample surface, the force interactions change the phase and the frequency of the cantilever. The lock-in amplifier is using this change in the feedback loop to adjust the amplitude. The electronic circuit of this mode is schematically shown in figure 2.4 a). The problem of this mode is that the changes in the amplitude are not instantaneous but they develop in a time scale also called decay time: $\tau_{AM} \approx 2Q/f_0$, where Q is the quality factor and f_0 the resonance frequency of the cantilever. In a vacuum environment, Q can be very big ($Q \approx 10000$), meaning that the amplitude change is very slow. To overcome this obstacle, the FM mode was developed. It feedbacks the frequency shift between the input and the output signal (see Fig. 2.4 b)). In this mode the eigenfrequency changes within a single oscillation cycle on a time scale of $\tau_{FM} \approx 1/f_0$. Generally, the AM method is used for the intermittent mode in ambient environment and the FM mode is the one used in

vacuum systems.

2.2.4 Contact Potential Compensation

The tip and sample are both usually made of different materials and each material has its own work function noted ϕ_{tip} and ϕ_{samp}, for tip and sample, respectively (see Fig. 2.5 a)). During measurements, the tip is brought into close proximity to the sample surface and the back electrode connection between them leads to electron flow from the material with the higher Fermi energy to the material with the lower Fermi energy until they are both aligned. This difference of work function is commonly called Contact Potential Difference (CPD) and defined as [75, 76]:

$$V_{CPD} = \frac{\phi_{tip} - \phi_{samp}}{e} \tag{2.6}$$

where e is the electron charge. This effect induces an electric field (Fig. 2.5 b)). To suppress this field, the application of a bias voltage equal to V_{CPD} can be done and the procedure leads to CPD compensation as represented in figure 2.5 c).

As we will see in the next section (Sec. 2.2.5.4), the electrostatic potential (U_{el}) between a spherical tip and a conductive planar surface can be modelled by a charged plate capacitor as follow:

$$U_{el} = \frac{1}{2}C(V - V_{CPD})^2 \tag{2.7}$$

where C is a plate capacitor. As a consequence, the frequency shift $\Delta f(V)$ curve has parabolic shape due to the square dependence of the voltage shown in equation 2.7. It

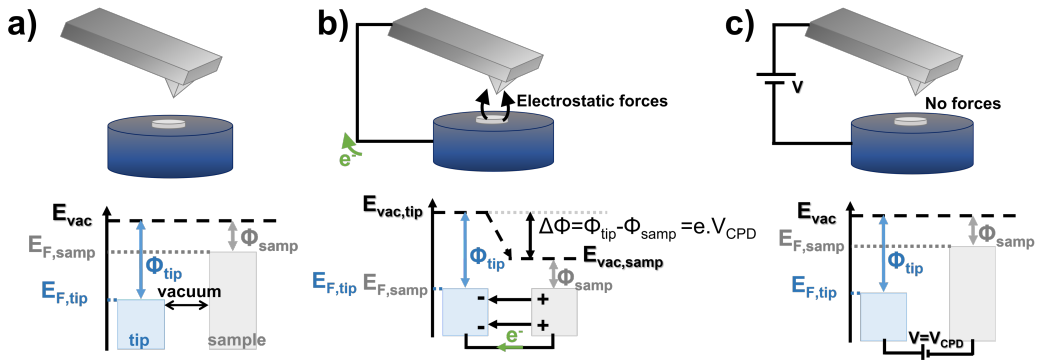

Figure 2.5: — *Schematic of the Contact Potential Difference compensation.* ***a)*** *typical tip-sample system where the tip and the sample have different work functions and are not contacted. The different work functions come from the different materials, labelled as ϕ_{tip} and ϕ_{samp} for the tip and the sample, respectively.* ***b)*** *schematic of the Fermi level equalization of the two work functions when direct contact of two materials leads to emergence of an electric field.* ***c)*** *schematic of the compensation of the CPD by applying a bias voltage $V = V_{CPD}$. Thus, the electric field is compensated and the different work functions can be extracted.*

is related to U_{el} as follows:

$$\Delta f \approx \frac{\partial^2 U_{el}}{\partial^2 z} \approx \frac{1}{2}\frac{\partial^2 C}{\partial^2 z}(V - V_{CPD})^2 \tag{2.8}$$

To extract the CPD from experimental data, Δf curve is fit using a parabolic function. The bias voltage at which Δf curve has a maximum value determines the voltage $V = V_{max} = V_{CPD}$ at which the CPD is compensated.

2.2.5 Main Interactions

AFM measures the interaction forces between tip and sample. These forces might have different nature depending on the environment of the sample, for instance: gas, liquid or vacuum. Two families of forces can be distinguished, the short and the long-range forces.

In vacuum, the measured forces are the composition of several different forces. They are the electrostatic forces (F_{elec}), van der Waals forces (F_{vdW}) and the chemical (F_{Chem}) interactions, as well as Pauli-repulsion force (F_{Pauli}). Magnetic forces (F_B) can be added for measurements with a magnetic tip or in external magnetic field. All the contributions to the total force can be summed together as follow:

$$F_{tot} = F_B + F_{elec} + F_{vdW} + F_{Chem} + F_{Pauli} \tag{2.9}$$

All these forces are attractive except Pauli-repulsion forces that prevent matter from collapsing to a single point. Contributions of each force in equation 2.9 are not equal due to the fact that their strength and interaction length are not the same and interaction varies with tip-sample distance.

It is interesting to note that in AFM, the tip is kept at relatively short distance from the sample. Hence, long range interactions are varying more slowly compared to short range forces. Long range (large d) forces can be regarded as a continuous background interaction.

In this section all the forces will be described in order to understand their influence and thus their importance.

2.2.5.1 Pauli force

The Pauli expulsion principle was established by the Austrian theoretical physicist Wolfgang Ernst Pauli that is one of the pioneers of quantum physics. Pauli principle describes the behaviour of fermions particles (which posses half spin integer). It is a key component of any intermolecular interactions and has its origin in the quantum mechanical nature of electrons. It says that two or more fermions cannot occupy the same quantum states simultaneously in an atom implying a total antisymmetric wave-function. If we consider two electrons of the same spin state trying to intersect in space, their orthogonalized wave function will have to take a larger slope to keep the function overlapping equal zero. This increase of slope leads to an increase of the

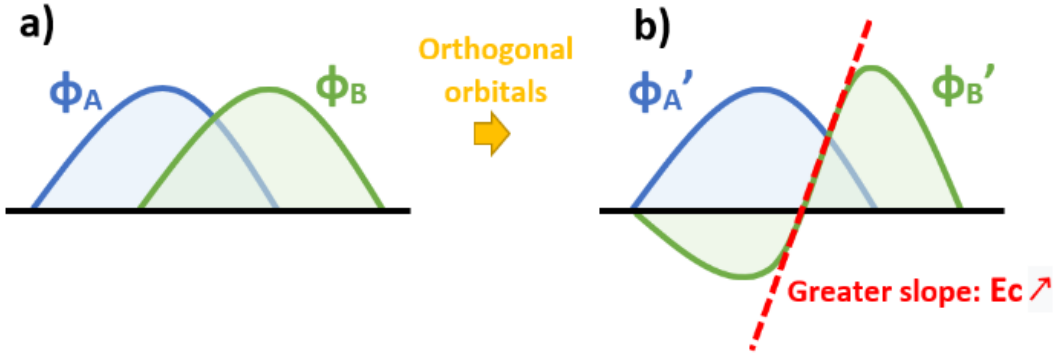

Figure 2.6: — *Schematic of the wave-functions of two fermions experiencing Pauli repulsion principle.* ***a)****, schematic representing the wave-functions before orthogonalization.* ***b)*** *orthogonalized orbital due to Pauli exclusion principle that require an antisymmetrization for fermion system. The slope of the curvature (red dash line) is proportional to the kinetic energy.*

kinetic energy ($E_c \propto E_{Pauli}$) that is mainly originating from the Pauli repulsion effect, as presented in figure 2.6. The corresponding energy can be defined as the energy difference between the orthogonalized and non-orthogonalized wave-functions:

$$E_{Pauli} = E_{int}(\uparrow\downarrow) - E_{int}(\uparrow\uparrow) \tag{2.10}$$

where E_{int} is the interaction energy. It is the dominant interaction at inter- atomic and molecular separations ($< 500\ pm$ [77]) and it is expressed as an repulsion of the fermions. To achieve such distances with a probe is not trivial. The advancement of AFM by functionalizing the tip using a CO molecule was a breakthrough in the AFM field. Indeed, when approaching the probe with a CO tip, the CO wave-function starts to overlap with the surface object (atom, molecule, etc.) wave-function. As a results, the wave-functions starts to minimize their overlap by increasing their slopes thus their E_{int}. The Pauli repulsion gets increased exponentially as the CO molecule approaches the sample surface object. In scanning probe or force probe microscopy the corresponding vertical force (F_z) can be expressed as [78]:

$$F_z(d) = -\frac{\partial E_{int}}{\partial d} \tag{2.11}$$

And the corresponding frequency shift as:

$$\Delta f = -\frac{f_0}{2k_0}\frac{\partial F_z(d)}{\partial d} \tag{2.12}$$

In it important to mention that the use of '*force*' to describe the exclusion principle is controversial [79]. Indeed, it is mostly a geometry consequence of the wave-function symmetrization than a physical effect. Thus, the Pauli exclusion force is considered as a non-conventional force.

2.2.5.2 Chemical Interactions - Lennard-Jones Potential

Lennard Jones potential is named after the British mathematician Sir John Edward Lennard-Jones and describes the interaction between two non-bound bodies. It models the attractive (dipole-dipole, dipole-induced dipole and London interactions) and repulsive forces at play for two neutral bodies separated by the vacuum gap. The potential is given by the following formula [80]:

$$V(r) = 4\epsilon[(\frac{\sigma}{r})^{12} - (\frac{\sigma}{r})^{6}] \tag{2.13}$$

where r is the distance between the two bodies, ϵ is the depth of the potential well (dispersion energy) and a measure of how strong the two bodies attract each other and σ is the distance at which the intermolecular potential between two bodies is zero.

This potential describes the chemical interaction in matter. Sir Lennard-Jones investigated the interaction of molecular crystals of noble gases. He found that the interaction of two noble gases can be described by the van der Waals dipole interaction. Moreover, to prevent the crystal from collapsing, short range repulsive forces have to be present as well. This is due to the repulsion of ion core which determines the equilibrium distance of two atoms.

It can be noted that this force as well as the van der Waals force are conservative interactions, meaning that the gain in the energy process is reversible in a perfectly closed system. However, real systems are not perfectly reversible leading to energy loss.

2.2.5.3 Van Der Waals Interactions

Van de Waals interactions are named after Dutch scientist Johannes Diderik van der Waals that was the first to introduce this interaction effect on the gas equation of state in 1873 and in 1910 he received the Nobel prize for that. These interactions are driven by induced electrical interactions between two or more atoms or molecules that are very close to each other. It is a distance-dependent interaction between atoms or molecules, thus it vanishes quickly at long distances ($d > 0.6\ nm$). It is as well the weakest among the intermolecular forces (0.4 to 4 kJ/mol).

When two or more atoms or molecules are close to each other an induced electrical interaction is created. These interactions lead to the creation of the so-called dipole. It consists of molecules (or atoms) with equal and opposite electrical charges separated by a small distance. In quantum mechanics, the constant movement of an electron is a well established concept. The electron is described as a probabilistic matter waves by the Schrödinger equation:

$$\hat{\mathcal{H}}\psi = E\psi \tag{2.14}$$

where ψ is the wave function. The solution of equation 2.14 for each ψ is associated with an electron binding energy E. It suggests that a particle (here an electron) in a

box (or an orbital) can be found anywhere in the box. This constant electron motion is also emphasized in the Heisenberg's uncertainty principle:

$$\Delta x \Delta p \geq \frac{\hbar}{2} \tag{2.15}$$

$$\Delta t \Delta E \geq \frac{\hbar}{2} \tag{2.16}$$

where Δi is the standard deviation of position (x), momentum (p), time (t) and energy (E). This principle states that having precise information about the energy leads to loose information about the position of the electron. It proposes that the energy of the electron is never zero; therefore, it is constantly moving around it's orbital. These two important concepts of quantum mechanics states that the electron is constantly moving in an atom, thus the probability to create spontaneous dipole is very high. The creation of spontaneous dipole occurs when a group of electrons are moving to one end of the atoms creating a positive and a negative pole.

If now, we consider the interaction of two atoms A and B. Atom A is a polar atom with a moment μ_A and atom B is neutral. As atom A approaches atom B, the electrons of atom B will be attracted to the positive side of atom A. This leads to the creation of an electric field that induces the polarization of the atom B, $p_B = \alpha_B / r^3$, where p is the polarization, α_B is the polarizability and r the distance between them. The polarization of atom B induces a moment μ_B and the interaction of the second dipole with atom A induces a polarization ($p_A = \alpha_A / r^3$) of the atom. The potential energy of an induced dipole interaction can be expressed with the equation [81]:

$$V_{vdW} = \frac{-\mu_A \mu_B}{r^3} = \frac{-\alpha_A \alpha_B}{r^6} \tag{2.17}$$

For macroscopic bodies, this description is not sufficient because:
- it has to take into consideration the interaction of all particles. That is not possible due to the rapid decay of the polarization by a third particle,
- the calculations need to be integrated over the total volume of the objects which makes the calculation dependent on the volume and shape. That leads to different expressions of the force,
- the van der Waals interactions is composed of three types of interactions: interaction between permanent rotating dipole, interaction between a permanent rotating dipole and an induced dipole, and interaction between an instantaneous dipole and an induced dipole.

In the case of AFM, the geometry of the system can be represented as the interaction between a sphere (end of the tip with a radius R) and a plate (sample surface) separated by a distance d. Hamaker [82], calculated the energy of van der Waals interactions by summing the interactions between all the molecular pairs of the two bodies. van der Waals potential energy for AFM configuration is given by:

$$V_{vdW}(d) = \frac{-AR}{6d} \tag{2.18}$$

where $A = \pi^2 C \rho_1 \rho_2$ is the Hamaker constant, C the in the atom-atom pair potential and ρ_i the number of atoms per unit volume in each body. The force can be derived using the potential as follows [83, 84]:

$$F(\overrightarrow{r}) = \frac{-dV(\overrightarrow{r})}{d\overrightarrow{r}} \tag{2.19}$$

where $\overrightarrow{r}$ denotes the tip-sample distance d.

$$F_{vdW}(\overrightarrow{r}) = \frac{-AR}{2\overrightarrow{r}^2} \tag{2.20}$$

Such forces when overcome the static spring constant of the cantilever might cause the snapping of the tip onto the sample surface.

2.2.5.4 Electrostatic Forces

The electric charge is a fundamental property of matter as well as the mass. It has been observed for the first-time during antiquity. They observed that amber after being rubbed against wool acquires the ability to attract certain light bodies. The term of electricity was first used in the $XVII^{th}$ century using the Greek word '$\eta\lambda\epsilon\kappa\tau\rho o\nu$ or elektron' meaning amber.

The phenomenon is easily observable in everyday life and can create high electrification that provokes sparkles or thunder during storms. It is only in the XIX^{th} century that a mathematical theory about electricity emerged. Before that, in the end of $XVIII^{th}$ century, Charles-Augustin Coulomb highlighted the law that now bears his name. This law describes the strength of the electrical interaction between two electrically charged particles and it forms the basis of electrostatics. This law is stated as follow "*the mutual interaction force between two electric objects is inversely proportional to the square of the separation distance*". It can also be written using the formula:

$$F_C = \frac{1}{4\pi\epsilon_0}\frac{Q_1 Q_2}{\overrightarrow{r}^2} \tag{2.21}$$

where Q_i is the electric charge of each object, $\overrightarrow{r}$ the distance between the two objects, and ϵ_0 the vacuum permittivity.

In AFM, the tip and the sample have in general different electrostatic potentials that lead to CPD. It can be compensated by applying the voltage difference between tip and sample, which leads to development of the Kelvin Probe Force Microscopy. A simple charge plate capacitor with a distance dependent capacitance $C(z)$ can be used to describe the tip and sample in AFM. In the first approximation the attractive forces between the two plates of the capacitor can be estimated as:

$$F_{capacitor} = \frac{\epsilon_0}{2}\frac{AU^2}{z^2} \tag{2.22}$$

where A is the capacitor area, z the tip-sample distance and U is the applied bias. The equation describes a plate capacitor well, however the AFM tip has a conical shape

that has to be taken into account. Assuming a conductive spherical tip with a radius R and a conductive planar surface, the electrostatic force can be written as following [83]:

$$F_{elec} = \frac{1}{2}\frac{\partial C}{\partial z}(U - U_{CPD})^2 = -\pi\epsilon_0\frac{R^2}{z(z+R)}(V - V_{CPD})^2 \tag{2.23}$$

2.2.5.5 Magnetic forces

Magnetic forces can be sensed by the AFM tip when the tip is coated with a magnetic material. This technique is called Magnetic Force Microscopy (MFM). It is used to investigate the magnetic properties of materials. The stray field coming from the sample generates a force on the magnetic tip. The magnetic interactions depend on the tip-sample distance and might have different origins: exchange interaction (quantum mechanic effect for 2 $nm > d$) or the dipole-dipole interaction ($d > 2$ nm). In MFM, the dipole-dipole interaction is the main effect considering the tip-sample distance of the measurements. The dipole-dipole interaction is characterized with a magnetostatic energy E of the tip-sample system as:

$$E = -\iiint_{tip} \vec{H}(\vec{r})\vec{M}dV \tag{2.24}$$

where $\vec{M}$ is the tip magnetization and $\vec{H}(\vec{r})$ the magnetic field above the sample. The force can be obtained by:

$$F_z = -\frac{\partial E}{\partial z} \tag{2.25}$$

are requires the determination of $\vec{M}$ and $\vec{H}(\vec{r})$. The procedure implies a three-dimensional integration over the volume (Eq. 2.24) [85].

When the tip-sample distance is much smaller as compared to the size of the magnetic tip, the measured force is proportional to the stray field and the tip is visible

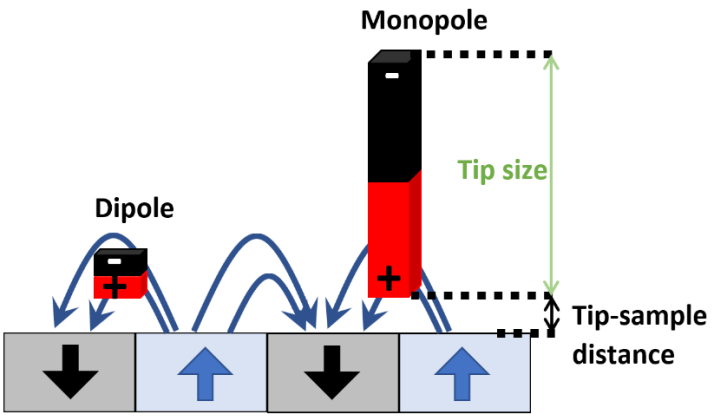

Figure 2.7: — *Schematic of the magnetic tips of different length in the close proximity to the magnetic surface composed of magnetic domains.*

as a monopole at the sample surface (Fig. 2.7). The corresponding Force-Transfer Function (FTF) can be approximated as [86]:

$$FTF \approx -\mu_0 M_{tip} b_x b_y = q_m \tag{2.26}$$

where μ_0 is the vacuum permittivity, M_{tip} the tip magnetization saturation, $b_x b_y$ is the surface of the magnet that is directly facing the sample and q_m the magnet point charge. Thus, for a sharp tip and a stray field decaying rapidly along the z direction (stray field much larger at the bottom tip surface as compared to the top surface of the tip), the force become:

$$F_z = -q_m H_{samp} \tag{2.27}$$

2.2.6 AFM Spectroscopy

Spectroscopy is a powerful measurement tool in the investigation of the local properties of the sample. Similarly to STM, AFM proposes a wide range of spectroscopy in order to investigate different interactions. Here, the force-distance curves, the bias sweep and excitation spectroscopy will be discussed.

2.2.6.1 Force-Distance Spectroscopy

Force-distance spectroscopy is based on recording the response of the cantilever as a function of the tip-sample distance. The z-scanner is used to approach the tip towards the sample, whereas all the other directions are constant [83]. In contact mode, the force-distance curves allow to locally probe the elasticity of the material. The stiffness measurements can be performed by indenting the tip into the probed surface. The backward and forward curves show hysteresis and the fitting of the force-distance curve enables to extract the elastic modulus of the sample. Generally, the force-distance curves can give a wide range of information such as recovering the complete tip-sample interaction energy, evaluating the interaction potential between tip and sample or finding the optimal force region before scanning.

In our case, for non-contact AFM and intermittent AFM measurements the force-distance curve is shown in figure 2.8. The cantilever is excited at its fundamental resonance frequency while the cantilever oscillation is fixed and the CPD is compensated. The force signal is tracked until the tip 'touches' the sample surface, which is visible as a linear increase of the frequency shift Δf and the rapid rise of excitation voltage. At close tip-sample distance, the cantilever might be sensitive to lateral force gradient while at far distances to normal axial forces. This increase, might be due to attractive forces or by a change of force interaction.

We use force-distance curves to find the 'real' sample surface in order to avoid tip crashing during scanning or other spectroscopy experiments. The 'real' surface is defined at the position where the force and the dissipation saturate, the PLL is not able to properly adjust the phase (Fig. 2.8). When the 'real' surface is found we can apply different bias voltages to the sample surface and study the various cantilever responses. The force extraction procedure is described in chapter 4.

2.2.6.2 Bias-Sweep Spectroscopy

Bias spectroscopy mode is particularly sensitive to electrostatic forces. Experimentally the tip is kept at a constant distance and a bias voltage sweep is applied between tip and sample. The cantilever oscillation amplitude is set constant. During the sweep several channels are simultaneously recorded, namely the frequency shift and the excitation voltage needed to keep the oscillations constant. The changes in the electrostatic forces between the tip and the sample are induced by the applied voltage and influence the measured frequency shift and the excitation voltage.

The typical bias-sweep experiment protocol is the following. The tip is positioned at a starting distance d far from the sample surface. The bias is then swept forward and backward with a certain ΔV corresponding to the resolution that we want to obtain (number of points in the spectra). When the bias sweep is finished the tip is moved closer to the sample surface with a defined step Δz and the bias-sweep spectra is acquired. The procedure is repeated until the tip stops at the distance close to the surface. The experiment can be also performed by changing other parameters like the magnetic field, lateral tip position or the sample temperature. In that case the tip-sample distance is kept constant. The extraction of the CPD value is an advantage of bias-sweep spectroscopy mode. The CPD value is equal to the bias voltage for which the frequency shift or excitation voltage signals have a minimum value.

2.2.6.3 Dissipation Images

In those type of measurement the tip scans the large surface area at constant tip-sample distance d. The mode enables to acquire dissipation and frequency shift images when a specific tip-sample bias is applied. Additionally, other parameters might also vary, i.e., magnetic field. The contrast obtained during imaging doesn't necessary correlate with the topography. It can originate from the cantilever damping due to single electron

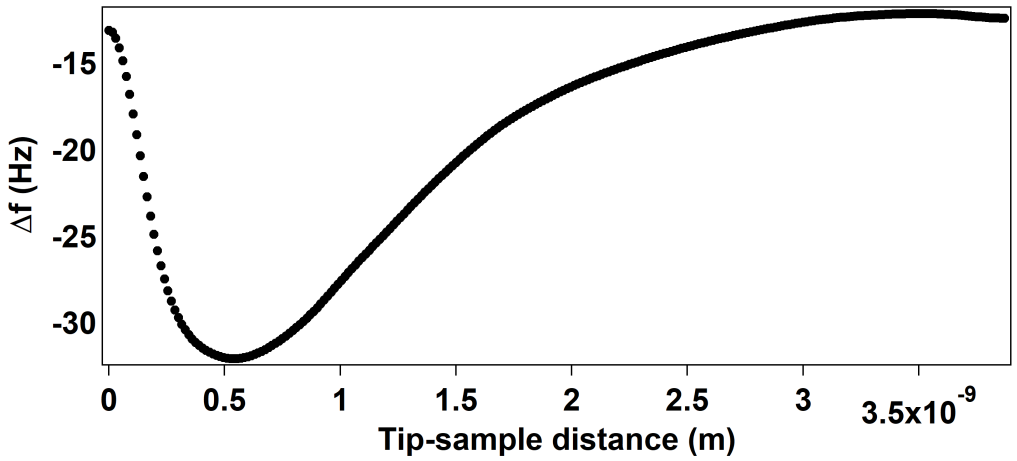

Figure 2.8: — *Typical force-distance curve obtained by p-AFM. Here $\Delta f(Hz)$ is the frequency shift which is proportional to the force.*

excitation, like for example Coulomb rings arising from charging events. Those type of dissipation mechanisms are described in details in chapter 3.

During the imaging the cantilever dynamics is controlled by the PLL and the average errors of the measurements can be extracted from the phase and the amplitude channels. The PLL settings such as proportional and integral gains have to be adjusted depending on the scanning speed and sensor force sensitivity. If the feedback loop is too fast compared to the cantilever decay time, the cantilever cannot accommodate perfectly which in turn might lead to the saturation of the PLL. Inversely when the PLL feedback is too slow the recorded data might miss informations. It is therefore important to adjust the PLL parameters to have a good compromise between the feedback speed and the cantilever response.

Concerning dissipation images, the error induced by the PLL can be determined from the oscillation amplitude A_{osc} signal. The deviation from the amplitude setpoint and the recorded amplitude can be used to estimate the overall error of the excitation image. Similar analysis is possible for the Δf signal. The error is estimated from the phase maps, where the difference between the setpoint and the reference phase can be used to determine the error of the Δf maps.

2.3 Summary

In summary different detection techniques involved in my work were described. It consists of the description of the two different SPM methods and their different characteristics. They have the advantage to be non-invasive, meaning that they are keeping the sample intact during the measurement. From different SPM modes, different information can be extracted down to the nanoscale range. The nanometric resolution can be obtained with pAFM, whereas atomic resolution is possible with STM. Both methods allow for spectroscopy measurements. Additionally, AFM allows for the measurements of non-conductive sample.

3

Non-Contact Friction

In today's electronic circuits the density of components is steadily increasing. These close packed components are not in direct contact, yet they can exhibit different friction mechanisms called Non-Contact (NC) friction. The intrinsic friction as well as the influence of each component can have a huge impact on the overall device performance. To investigate such mechanisms, we use AFM cantilever in NC, dynamic mode. The oscillating tip can be used to sense energy loss effects and investigate distance and voltage dependent frictional response.

NC friction is an ongoing research topic. Friction and energy loss can only be possible if the final state (E_f) of an object is changed as compared to initial state by non-continuous processes that will lead to $E_i \neq E_f$.

The frictional drag force between an AFM tip and a substrate has gained a lot of attention and can be successfully measured in ultrasensitive experiments. According to fluctuation-dissipation theorem random forces that can excite a particle would also cause friction if the particle is being dragged [87]. This friction force can be the main limiting effect in the development of new technologies such as quantum computing seriously constraining quantum bit coherence times, for instance. Reduction of charge and force fluctuations in those systems means reduction of friction as well.

In this section, I discuss different NC friction mechanisms as well as their influence on cantilever dynamics.

3.1 AFM Cantilever Internal Losses

In order to understand the different loss mechanisms in the sample, it is important to understand the dissipation mechanisms occurring in the sensor itself. AFM sensor can be described using the damped harmonic oscillator model. Damping causes the amplitude of oscillation of the cantilever decay in time, making the oscillation energy decrease, until it reaches a thermodynamic equilibrium when the oscillation is stopped.

The decay time (τ) and the equilibrium fluctuations ($x(t)$) contain information about the dissipative processes. The equation of motion can be written as follows [88, 89]:

$$m_{eff}\frac{d^2x}{dt^2} + \Gamma\frac{dx}{dt} + \omega_0^2 x = F_0(\omega_0 t, \Phi) + F_{ext}(t) \tag{3.1}$$

where m_{eff} is the effective mass, Γ is the friction coefficient, ω_0 is the angular resonance frequency, $F_{ext}(t)$ the external force, $F_0(\omega_0 t, \Phi)$ the driving force and Φ a phase shift. The non-conservative friction force (F_{fric}) is proportional to the friction coefficient and the velocity (v) of the oscillator:

$$F_{fric} = \Gamma \times v \tag{3.2}$$

The friction coefficient can also be described as a sum of all possible dissipation channels sensed by the probe:

$$\Gamma = \sum_{i=0}^{N} \Gamma_i = \Gamma_0 + \Gamma_1 + \Gamma_2 + ... + \Gamma_N \tag{3.3}$$

where N is the N-th channel and Γ_0 the friction coefficient of the free cantilever (the non-perturbed system). This friction coefficient can be determined from the spring constant k and the decay time τ by:

$$\Gamma_0 = \frac{k}{\omega_0 \cdot Q} \tag{3.4}$$

where $Q = \tau \cdot \omega_0/2$ is the quality factor of the cantilever. The free cantilever dissipation Γ_0 combines all the internal losses of the cantilever and the main origins are: thermoelastic dissipation, damping due to bulk losses of the sensor, damping due to surface losses of the sensor, losses due to acoustic emission, dissipation due to clamping of the sensor and viscous damping due to the presence of gases and liquids around the sensor. In addition to that, it can be added the internal cantilever damping of the cantilever in presence of an external magnetic field.

In the case of the p-AFM, the experiments that are going to be discussed in the next chapters allow to neglect the last three dissipation losses. Indeed, the measurements are operated in UHV with a vacuum of $p = 10^{-9}$ $mbar$ to $p = 10^{-11}$ $mbar$ making the viscous damping due to gases or liquids and acoustic damping negligible. The dissipation due to clamping of the sensor are optimized by using rigid metallic clamping (see Chap. 4) which allows to avoid the glue. Thus, additional internal losses from loosely clamping are also negligible.

The first three cantilever losses and the effect of a magnetic field on the internal dissipation losses are discussed in the next subsections in order to understand their origin and the methods used to optimized them.

3.1.1 Thermoelastic Dissipation

The thermoelastic dissipation is related, as its name suggests, to the energy losses due to the elastic deformation in the material structure caused by temperature fluctuations.

In AFM systems, the cantilever is oscillating inducing a non-constant strain field in the sensor. It has the consequence of changing its internal energy in a way that the compressed regions become hot and external regions cold. This lack of thermal equilibrium in the sensor creates a heat flow due to the induced temperature gradient that leads to energy dissipation.

This effect is well described by the Zener model, where thermoelastic damping in beams undergoing flexural vibrations is studied. In this model the thermoelastic internal friction (Q^{-1}) is given by [88–90]:

$$Q^{-1} = \frac{\alpha^2 T E}{\rho c_P} \frac{\omega_f \tau}{1 + (\omega_f \tau)^2} \tag{3.5}$$

where α is the thermal expansion coefficient, E the Young modulus, ρ the mass density, c_P the specific heat capacity, ω_f the angular frequency of oscillations and τ the relaxation time. Cantilevers are very thin objects compared to bulk material, leading to a drastic reduction of the thermal conductivity due to phonon-boundary scattering for thickness of order of microns at temperature below $T = 30\ K$. At room temperature, $Q_{RT}^{-1} \approx 10^{-4}$ while at $T = 5\ K$ it is equal to $Q_{5K}^{-1} \approx 10^{-6}$ [91]. Hence, at low temperature this dissipation channel can be neglected and other dissipation mechanism such as bulk or surface losses dominate. Nevertheless, some experiments showed that at room temperature it is most likely the dominant dissipation mechanism [92].

3.1.2 Damping Due To Bulk And Surface Losses

Bulk and surface materials are not perfect structures and have defects. The scattering of elastic waves on the surface or bulk defects while oscillating the cantilever is an important loss mechanism. The oscillating tip induces a stress field that is time dependent and not constant. This stress field is changing the energy landscape around the defect with different energy domains that are also varying with the oscillations. Hence, the quality of the crystallographic structures of the material used in cantilever fabrication is important in order to reduce these bulk and surface effects.

Silicon is the most common cantilever material and it exhibits very high-quality factors under UHV conditions (between 10 000 up to 500 000). In AFM different vibrating modes are used during measurements. Usually, they are the first and the second eigen mode. They both exhibit different stress fields due to their different oscillating shapes, see figure 3.1. The resonance peak of each mode should be represented as single Dirac-like feature where its width (Δf) should be proportional to $1/Q$. That means, the sharper the peak, the less dissipation is present. The energy loss is directly proportional to the quality factor of a sensor which can also be written as follows [88, 89]:

$$Q = \frac{f_0}{\Delta f} = \frac{1}{\epsilon_T} \tag{3.6}$$

where f_0 is the resonant frequency and ϵ_T is the energy loss factor.

In the case of silicon, bulk and surface losses are dominant at temperature below $T = 160\ K$. In order to reduce the losses, experiments show that annealing the

cantilever under UHV at $T \approx 800\ K$ for 12 hours enables to improve Q (a $Q \approx 10^6$ can be reached) [93]. The process leads to the removal of oxides layers and/or weakly bound molecules as well as all the static charges that may be present at the surface and in the bulk of the cantilever.

3.1.3 External Magnetic Field Internal Losses Effect

Under an external magnetic field, the cantilever can experience internal damping. The cantilever deflection on the x and y axes is described as follow [94]:

$$\frac{d^2y}{dx^2} = \frac{m_B(x)}{EI} \tag{3.7}$$

where E is the Young modulus, $m_B(x)$ the total bending moment and I the moment of inertia of the cantilever. m_B and I and given by:

$$m_B(x) = \frac{\rho}{2}(x - L)^2 \tag{3.8}$$

where ρ is the force per unit length and L the cantilever length,

$$I = \frac{wh^3}{12} \tag{3.9}$$

where w is the width and h the thickness of the cantilever. Considering a clamped cantilever end at $y(0) = 0$ and $dy(0)/dx = 0$, the general deflection expression is:

$$y(x) = \frac{\rho x^2}{24EI}(4xL - L^2 - x^2) \tag{3.10}$$

For a conventional silicon based cantilever and analogy with paramagnetism, the force per unit area is a function of the form: $\rho \propto B^2$, where B is the external applied magnetic field and equal to:

$$\rho = \frac{w\beta}{2\mu_0}\int_z^{z+h}\frac{dB^2}{dz}dz \tag{3.11}$$

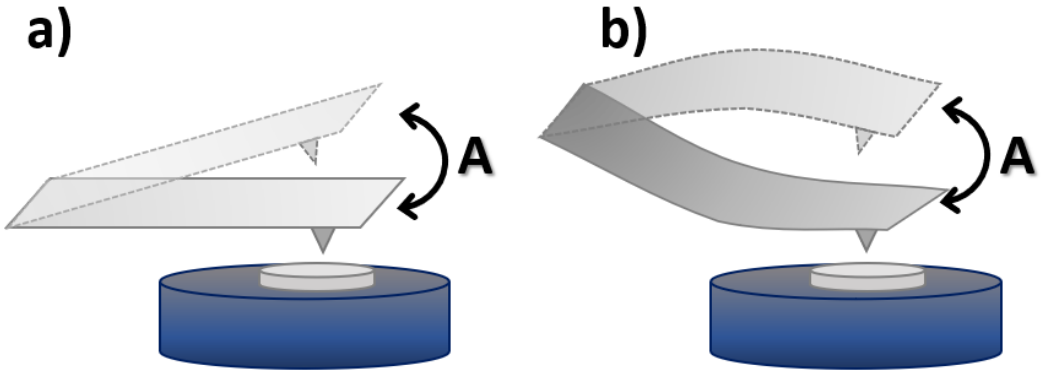

Figure 3.1: — *Schematic of the two first vibrating modes of a rectangular cantilever.* ***a)*** *first vibrating mode.* ***b)*** *second vibrating mode.*

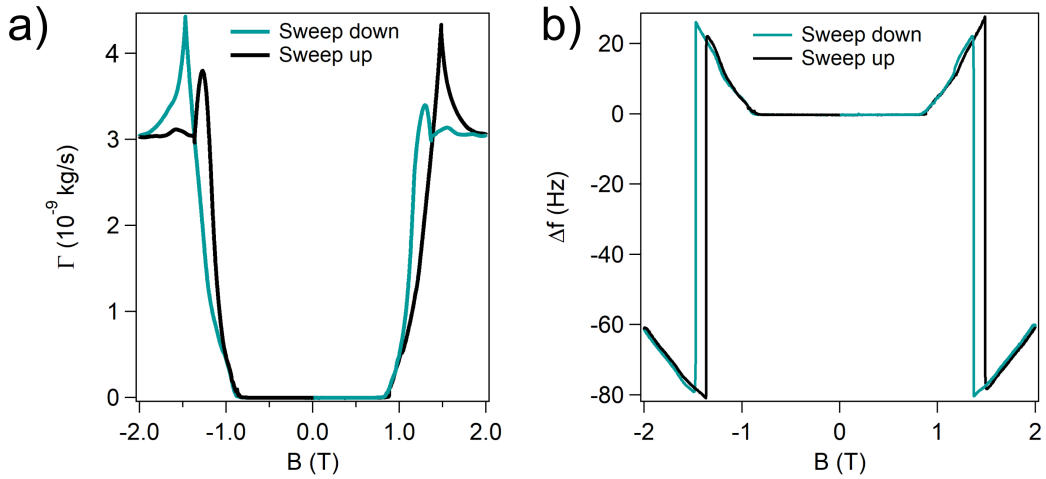

Figure 3.2: — *Magnetometry measurement of a free silicon cantilever. The black curve is the sweep up and the blue curve the sweep down curves.* ***a)*** *dissipation spectrum and* ***b)*** *corresponding* Δf *curves.*

where β is the magnetic coefficient of the cantilever and μ_0 the magnetic vacuum permittivity. For uncoated silicon cantilever $\beta \approx 186$ [94]. The magnetic effect acting on the cantilever is often visible as a decrease of the noise level in the experiment for small field ($\pm 1\ T$ depending the cantilever properties). At large B-field, the dissipation usually reaches a saturation as shown in figure 3.2. Such effect most presumably occurs due to the creation of Eddy currents in the cantilever structure and must be taken into account since it affects the experimental results.

3.1.4 Minimum Detectable Force And Friction

The understanding of the internal losses of a cantilever is important in order to explain the minimum detectable force, which is given in the previous chapter in equation 2.5 [88, 90]:

$$F_{min,i} = \sqrt{\frac{2k_B T k_i \Delta f_i}{\pi f_i Q_i}} \tag{3.12}$$

where the i is referring to each vibrating mode of the cantilever. This equation is showing the importance of Q in the reduction of the sensitivity of the sensor and it is also indicating the force limit. Indeed, the higher Q the lower F_{min} can become.

Experimentally the quality factor is determined in decay time measurements (described in Chap. 4). The decay time of the cantilever is recorded for each oscillating mode. The quality factor can be extracted with the relation:

$$Q_i = \pi f_i \tau_i \tag{3.13}$$

where τ is extracted with an exponential fit to the experimental data. The second mode usually has a lower Q compared to first mode (see Chap. 4), presumably due to more complicated oscillation shape.

Besides the minimum force the quality factor can also determine the minimum dissipated power loss of the free cantilever (P_0) [89]:

$$P_{0,i} = \frac{\pi k_i A_i^2}{eQ_i} = \Gamma_{0,i}\frac{2\pi^2 A_i^2 f_i}{e} \tag{3.14}$$

where A is the oscillation amplitude of the cantilever, e is the electron charge and Γ_0 is the free cantilever damping. The dissipated power ($P_i(d)$) and damping ($\Gamma_i(d)$) of the cantilever interacting with the sample surface at a specific distance d are given by [88, 89]:

$$P_i(d) = P_{0,i} \cdot \left(\frac{A_{exc,i}(d)}{A_{exc,0}} - \frac{f_i(d)}{f_{0,i}}\right) \approx P_{0,i} \cdot \left(\frac{A_{exc,i}(d)}{A_{exc,0}} - 1\right) \tag{3.15}$$

$$\Gamma_i(d) = \Gamma_{0,i} \cdot \left(\frac{A_{exc,i}(d)}{A_{exc,0}} - \frac{f_i(d)}{f_{0,i}}\right) \approx \Gamma_{0,i} \cdot \left(\frac{A_{exc,i}(d)}{A_{exc,0}} - 1\right) \tag{3.16}$$

where $A_{exc}(d)$ and $f_i(d)$ are the cantilever excitation and the cantilever oscillation frequency at a distance d and the suffix 0 refers to the free cantilever. The second term of equations 3.15 and 3.16 can be approximated to 1 due to usually negligible change of the resonant frequency compared to the resonance frequency of the sensor.

3.2 Main Mechanisms Of Energy Dissipation In AFM

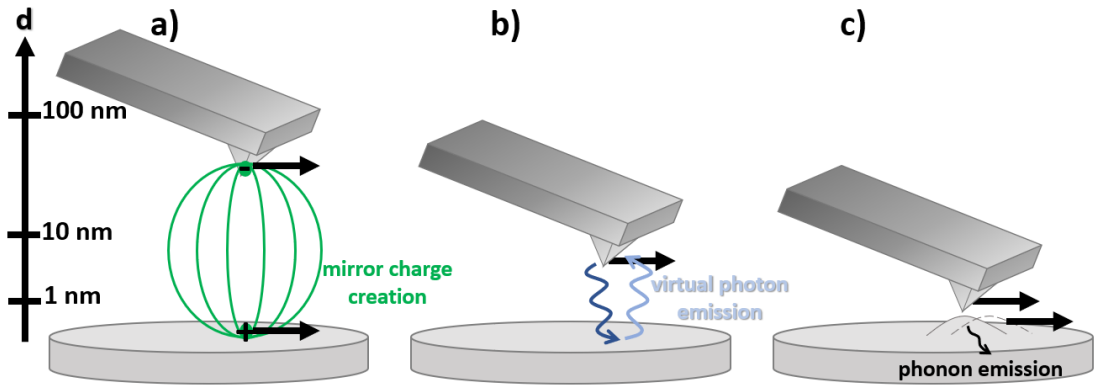

Figure 3.3: — *Schematic of the three main dissipation mechanisms.* ***a)*** *Joule dissipation, where the electronic deformation is dragged by the moving tip, the energy is lost by the creation of electron-hole pairs in metal. Dissipation originates from local current induced when the charged tip oscillates over a resistive medium.* ***b)*** *van der Waals dissipation, where the friction arises from the surface charge fluctuation.* ***c)*** *Phononic friction, where the surface atomic deformation is dragged by the moving tip and the energy is lost to the creation of phonons. The scale bar d, is showing the distance dependence of each contribution.*

The dissipation between two moving bodies separated by a distance d is mainly due to electromagnetic interactions [87–89]. Hence, the NC friction is related to an asymmetry of the reflection coefficient along the direction of motion.

In AFM, the cantilever can induce dissipation when oscillating in close vicinity of a sample surface. Different mechanisms were established, all dependent on tip-sample distance, reflecting the nature of the dissipation. It has also been demonstrated that the oscillating tip can push a finite system into an energy level crossing due to single electron charging or discharging in quantum dot like entities or quantum systems. This later energy dissipation mechanism is a hysteric process, with not so obvious distance dependence, but rather reflects a quantum character of the system.

In this section the main mechanisms of energy dissipation will be discussed starting from long range tip-sample distance d ($d < 100\ nm$), mid-range ($10\ nm < d < 100\ nm$) and short range ($d < 10\ nm$).

3.2.1 Joule Dissipation

Joule dissipation is named after British physicist James Prescott Joule. He studied the nature of heat and developed the first law of thermodynamics, the conservation of energy theory. Moreover, he also formulated the equation describing the relation between the electrical current flow through a resistor and related dissipated power also known as Joule's law. Nowadays, Joule is also known as the energy unit.

The macroscopic Joule's law states that *the amount of heat per second is equivalent to the electric power* (P) *absorbed or power loss* and can be written as follow:

$$P = I^2 \cdot R \tag{3.17}$$

where I is the electrical current flowing through a resistor and R is the resistance.

In NC AFM, this power loss is also present when an electric field or bias voltage is applied between tip and sample. The charge at the end of the cantilever creates a mirror charge in the sample, that is being dragged by the cantilever oscillations creating a displacement current (see Fig. 3.3 a)). This motion of the mirror charge faces the resistance of the crystal that induces Joule type of dissipation [87–89].

The induced displacement current can be obtained by considering the tip sample system as a capacitor with a plate and sphere geometry for the surface and the tip, respectively. Due to the oscillations of the cantilever, the capacitance varies accordingly. The displacement current (D) can be written as follows:

$$D(t) = \frac{\partial C}{\partial t} \times U = \frac{\partial C}{\partial z}\frac{\partial z}{\partial t} \times U \tag{3.18}$$

where C is the capacitance representing the system, z the tip oscillation amplitude and U is the applied bias. In analogy to equation 3.17, the power loss in such system (P_J) can be formulated as follow:

$$P_J = D(t)^2 \times R_{samp} \tag{3.19}$$

where R_{samp} is the resistance of the sample in the current path.

In bias voltage sweep measurements, Joule dissipation is characterized by a parabolic dissipation shape due to the square power dependence visible in equation 3.17. For a sphere and plane system the dissipation curve ($\Gamma(V)$) can be fitted using the power law relation [95]:

$$\Gamma(V) \propto A(V - V_0)^c \tag{3.20}$$

where A is a fitting constant, V is the applied bias voltage, V_0 the CPD voltage and c is a constant. In case of Joule dissipation $c = 2$ [96].

In many experiments discussed in the Thesis, the tip-sample distance is large enough to claim that Joule dissipation is the dominant energy loss mechanism. In that case the dissipated power for a capacitively coupled tip and sample is expressed as follow (see Sup. Mat. S3:1):

$$< P >= \frac{1}{2} R A^2 \omega^2 (V_B - \Delta\phi)^2 (\frac{\partial C}{\partial z})^2 \tag{3.21}$$

and the corresponding frequency shift (see Sup. Mat. S3:1):

$$\Delta f = \frac{f_0}{4k} (\frac{\partial^2 C}{\partial z^2})(V_B - \Delta\phi)^2 \tag{3.22}$$

3.2.2 Van Der Waals Friction

The van der Waals friction is closely related to the van der Waals force. In NC friction the two objects are separated by a distance d large enough to prevent any tunnelling of electrons or other particles through the barrier, yet small enough to allow long-range electro-magnetic interactions, which is present in the gap between the two bodies. When a fluctuating electromagnetic field is created due to thermal or quantum fluctuations in the sample, those fluctuations give rise to the van der Waals interactions that is also responsible of the heat transfer. If the bodies are in motion, the fluctuations give rise to a friction which is called the van der Waals friction [87].

The friction arises from dragging thermal and quantum fluctuations of the current that will be slightly shifted compared to the originally fluctuating current. In AFM, this shift is due to the fact that the original current comes from the oscillating tip (inducing an displacement current under the tip) and the drag occurs in the sample surface. The cantilever oscillates freely while on the sample surface the image charge is facing the sample lattice structure, defects, deformation, geometry, etc. (see Fig. 3.3 b)). The friction then arises from the asymmetry of the reflection coefficient along the motion direction (x-direction). Indeed, if one body emits radiations, these waves are Doppler-shifted in the rest frame of the second body which will result in a different reflection coefficient. The exchange of Doppler-shifted photons is the origin of van der Waals friction.

The van der Waals friction is not as well established as van der Waals force. The theory is still ongoing. In addition to that, measuring van der Waals friction is challenging even with an ultra-sensitive sensor, because the other contributions to dissipation are usually larger. However, with the right configuration and proper choice of parameters should enable to measure such frictional effects with the p-AFM.

3.2.3 Phononic Dissipation

At small d, the two objects are in very close proximity, but not in contact yet. This has the effect of creating a very local surface deformation, when the sample surface and the cantilever are attracted to each other. The oscillating tip is then dragging back and forth the induced surface deformation which result in dissipation [88, 89].

The tip-sample attraction creates a non-uniform force field on the sample surface and the in-plane tip oscillations induce a time-dependent stress field which produces longitudinal acoustic waves. The surface phonons face a dragging of elastic deformation that will induce the dissipation, as presented in figure 3.3 c).

The theory for a spherical tip oscillating above an elastic plane surface predicts a friction coefficient (Γ_{ph}) dependence on the static force ($F(d)$) as follows [96]:

$$\Gamma_{ph} \propto F^2(d) \tag{3.23}$$

According to the Lifshitz theory [97], the elastic stress caused by van der Waals interactions leads to a static force $F(d) \propto d^{-2}$, which results in friction coefficient [98]:

$$\Gamma_{ph} \propto d^{-4} \tag{3.24}$$

In bias sweep experiment the dissipation curve exhibits higher order exponent. Experimentally observed phonon dissipation is expected to vary with a power four ($c = 4$) when using equation 3.20 as a fitting curve [95, 99].

3.2.4 Single Electron Tunnelling

Apart from provoking conventional forms of energy dissipation as described in the previous paragraphs, the external perturbations caused by an oscillating tip might push a finite quantum system towards a transition level crossing with subsequent fluctuations and relaxations leading to energy dissipation due to electrostatic interactions [100]. Thus, it is possible to charge and discharge electrons on quantum dots or quantum dot-like entities using the AFM probe.

In fact, the origin of single electron charging comes from the discreteness of the electron charge. In quantum dots (QD), for example, the tunnelling transfer of one electron into the QD from the back electrode increases the electrostatic energy of the system. When a gate voltage is applied to the system the energy levels of the QD can be shifted. Hence, when one energy level of the QD lies in the gate voltage window an electron can tunnel between the QD and the back electrode. Experimentally, the single electron tunnelling events are observed as jumps (in conductance or AFM energy dissipation) or drops (in capacitance or AFM force). This phenomenon is called Coulomb blockade [101].

The AFM measurements allow to induce single electron charging in quantum or QD systems [100, 102–104] by positioning the AFM tip near the sample surface (where the electrostatic forces are dominant, $d \geq 10\ nm$) and oscillating the cantilever while applying a bias voltage between tip and sample. The oscillating tip is gating the sample

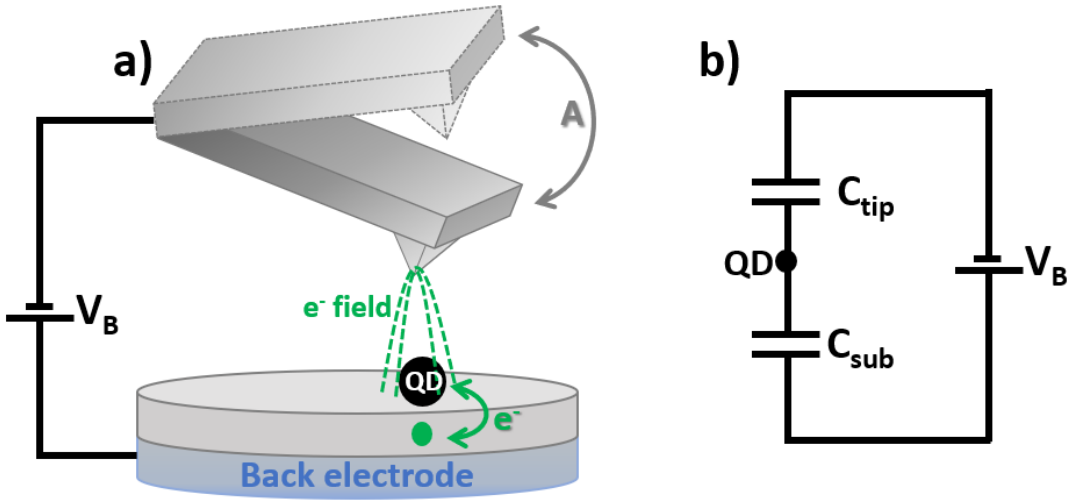

Figure 3.4: — *Schematic of the electron charging with AFM system.* ***a)*** *typical sample setup for electron charging with AFM. The sample is composed of a back electrode substrate that is a host to an electron reservoir. On top of it there is an insulating support that is used as electron tunnel barrier and on top the QD is deposited. The AFM tip is oscillating over the QD, which induces the charging and discharging of the QD by single electrons.* ***b)*** *typical equivalent capacitance circuit of the system.*

with an AC electric field (see Fig. 3.4 a)). If the quantum system is near to resonance with the Fermi energy of the system, the cantilever oscillations can periodically push an electron into and out of the quantum state of the QD. The QD charging energy is equal to $E_C = e^2/C_{dot}$, where C_{dot} is the quantum dot capacitance. This change can be sensed by the AFM cantilever by resolving the quantum dot interaction with the oscillating cantilever.

Indeed, the QD response to the oscillating tip shows characteristic features on the driven feedback system. The in and out electron tunnelling in the QD occurs as a phase shift in the driving force and detected by the feedback system. The phase shift depends on the driving frequency evolution compared to the tunnelling rate of electrons (ω/γ, where ω is the resonance frequency and γ is the finite tunnelling rate of a charge) and results in an in- and out-phase component of the force (F) acting on the AFM cantilever [105, 106]:

$$F \propto \frac{1 + i\omega/\gamma}{1 + (\omega/\gamma)^2} \tag{3.25}$$

The equation explains the enhanced dissipation when an electron tunnel in and out of a QD.

The acting forces can be calculated by representing the AFM and sample system as a capacitance circuit [107, 108] (Fig. 3.4 b)), where C_{tip} is a geometric capacitance describing the tip and sample and C_{sub} is the substrate capacitance. Considering the free energy of the system that consists of the electrostatic charging energy, the work

(W) done by the backgate voltage can be expressed as:

$$W = \frac{q^2}{2C_\sum} - \frac{C_{tip}}{C_\sum} qV_B - \frac{1}{2}\frac{C_{sub}C_{tip}}{C_\sum} V_B^2 \tag{3.26}$$

where $V_B = V - V_{CPD}$ is the backgate voltage, and $C_\sum = C_{tip} + C_{sub}$ is the system total capacitance. The force is obtained by derivation the work with respect to corresponding tip-sample distance z. The electrostatic force becomes:

$$F = -\frac{\partial W}{\partial z} = \frac{1}{C_\sum^2}\frac{\partial C_{tip}}{\partial z}(\frac{q^2}{2} - C_{sub}qV_B + \frac{1}{2}C_{sub}^2 V_B^2) \propto \Delta f \tag{3.27}$$

where the first component of the equation describes the interactions between the charge in a QD and its image charge in the tip, the second component represents the interactions between the charge in the QD and the polarized charge. This term is responsible for the detection of the charge in the QD. The last component represents the electrostatic background due to the back electrode as well as the interactions between the polarized charge in the tip and the back electrode. This equation represent the coupling force between the tip and the QD-sample system, since tunnelling rate is a stochastic process it is important to indicates that it has a time dependency. This time dependency is the reason of the observed phase shift in the detection driving force. When an electron is entering the QD, a dephasing (Φ in Eq. 3.1) is induced between the tip oscillation and the electron tunnelling.

For quantum systems, especially QD or QD-like objects, the substrate capacitance can be composed of two elements: a parasitic capacitance [108] (C_{par}) that describes the overall geometry of the sample and a quantum capacitance (C_Q) that takes into consideration the possible quantization. The later capacitance is directly proportional to the DOS ($\rho(\eta)$) of the sample as follows:

$$C_Q \propto q^2 \rho(\eta) \tag{3.28}$$

where $\eta = E_F/k_B T$ and E_F is the Fermi energy and k_B is the Boltzmann constant. Hence, the investigation of the quantum capacitance enables to study of the electronic properties of the sample with AFM probe.

Experimentally, the single electron charging is represented as a peak in the dissipation spectra and drop in the corresponding frequency shift curve [100, 102–104, 107].

3.3 Summary

In summary non-contact friction has been discussed in details. The cantilever internal dissipation main mechanisms were explained in order to differentiate between cantilever energy loss and the tip-sample interaction loss mechanisms.

Three non-contact dissipation main mechanisms were discussed as well as energy loss related to the single electron charging. The main energy loss mechanisms are closely linked to the tip-sample distance and are corresponding to the interactions described

in the previous chapter. The last dissipation mechanism is a direct consequence of the oscillating tip over a quantum system. All of the dissipation mechanisms exhibit very distinct dissipation features that enable to experimentally distinguish them.

4

Pendulum AFM

Since its development, AFM undergoes many different modifications in order to implement and increase its resolution or sensitivity. The p-AFM is part of this development. It enables an increase in dissipated power sensitivity by changing its geometry in order to use very soft cantilevers.

In the minimum detectable force formula only few parameters can be modified to decrease its value: the quality factor, that we discussed in the previous chapter, the temperature (T), the resonance frequency (f) and the spring constant (k). The temperature is an easy parameter to change, yet the frequency and the spring constant are more difficult. In the conventional configuration AFM, the cantilever is positioned parallel to the sample surface and oscillates perpendicularly above it. This configuration might lead to the snapping of the tip onto the sample surface when the interacting forces are getting too strong compared to the cantilever stiffness ($\partial F/\partial z \geq k$ where $\partial F/\partial z$ is the force gradient). To address this issue another configuration was developed, namely: p-AFM, where the cantilever is positioned perpendicularly and oscillate parallelly, like a tiny pendulum, over the sample surface.

The p-AFM configuration was not developed to improve on the spatial resolution. Its power resides on its ultra-high sensitivity and it is then used as a spectroscopy instrument. It is combined with UHV conditions and low temperatures. These two conditions are also relevant parameters in order to study fundamental properties of materials. They basically result in a significant reduction of thermal fluctuations and no contaminants on the sample surface.

Here, I describe p-AFM setup and its working principle.

4.1 P-AFM System

The p-AFM is a home built system that operates in UHV at cryogenics temperatures (from room temperature to $T = 3.5\ K$) with the possibility to apply a magnetic field

($B = \pm 7\ T$) [109].

The setup is composed of three chambers: the load lock (LL), the preparation and the microscope chambers (see Fig. 4.1 a) and b)) and all the chambers are connected to each other using gate valves.

The first chamber enables the transfer of samples from the laboratory room (ambient conditions) to the p-AFM system or to take back the sample from the system to the laboratory. It operates in high vacuum in order to facilitates the transfer from LL to the preparation chamber without breaking the preparation chamber vacuum. This vacuum is made using a rotary and a turbo pump (blue and green rectangles in Fig. 4.1 a)). When the sample is in the LL and the vacuum is stable, the sample can be transferred into the preparation chamber using a manipulator.

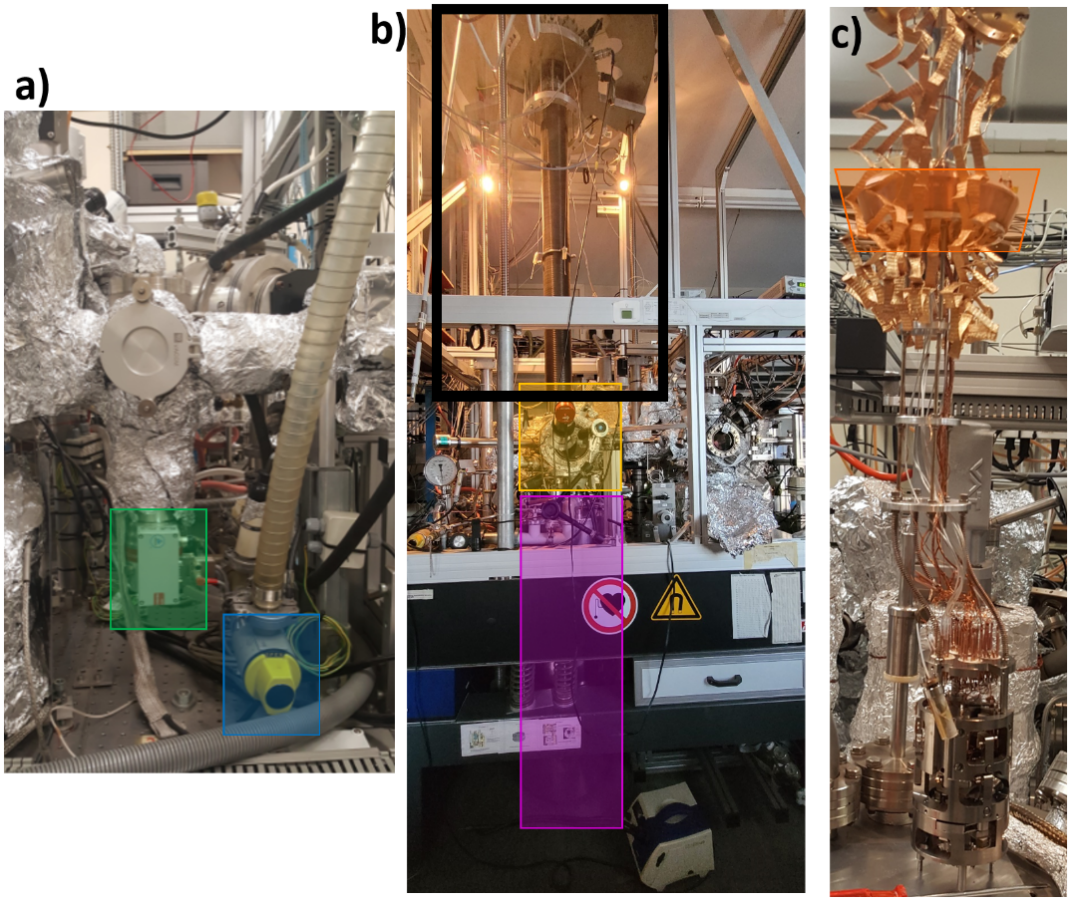

Figure 4.1: — *Different chambers of pendulum AFM microscope.* ***a)*** *LL chamber, the green rectangle shows the turbo pump and the blue rectangle is the rotary pump valve.* ***b)*** *front picture of the microscope chamber where the yellow rectangle corresponds to the top chamber while the pink rectangle marks the cryostat. The black rectangle shows the crane system. Preparation chamber is connected to the microscope chamber via valve separation.* ***c)*** *microscope picture taken when the system was vented. The orange cone shows the conical block that is used for the cooling.*

The second chamber is the preparation chamber. It is sealed off with gate valves meaning that it can be operated separately from the LL and the microscope chamber. It is operating in UHV created by means of different pumps, rough vacuum- and turbo pumps to generate a high vacuum ($p \leq 10^{-7}\ mbar$) and the UHV is obtained by using the ionic pump and titanium sublimation pump, which enable reaching a vacuum of $p = 10^{-11}\ mbar$. The same pumping system is present in the microscope chamber. The samples and the cantilevers can be prepared under UHV conditions. The preparation chamber is equipped with a heater that can reach up to $T = 1500\ K$ and an argon ion sputtering gun. These two setups can be used to prepare the sample surface by cycles of sputtering and annealing. The heater allows annealing the cantilevers in order to lower its internal and bulk losses as described in the previous chapter. When the samples and the cantilevers are prepared, they can be transferred into the microscope chamber using a manipulator.

The last chamber is the microscope chamber and it is composed of two stages, top chamber and cryostat (yellow and pink rectangles in Fig. 4.1 b) respectively). The top chamber is equipped with large windows that enable to optically access the microscope during the sample and the cantilever transfer. The cryostat does not have windows to prevent any disturbing light on the photodiode. A superconducting magnet is residing inside the cryostat. The microscope is also equipped with a heater system to perform temperature dependent measurements. To bring the microscope from measurement to transfer position a crane system is used (black rectangle in Fig. 4.1 a)). The microscope is attached at the end of the crane with the help of a rod. The rod is equipped with a conical block (orange cone in Fig. 4.1 c)) that is designed to fit with the cone of the cryostat. When the two cones are perfectly nested, the cooling process starts.

The microscope resides in the microscope chamber and is composed of different elements.

The p-AFM uses a laser beam deflection method and the laser light is fed into the UHV chamber with a fibre. The laser light is brought into the system with an optical fibre and the spot position at the end of the cantilever with a set of mirrors. The mirrors also allow to optimize the light on the PSD (see Fig. 4.2 a)). Two laser sources are used: a red light to position the spot on the cantilever and perform a first alignment and an infrared light for the measurements to reduce the noise of the laser. The alignment at cryogenic temperature is made in two steps, the first step consists of the RT alignment. Before cooling down to $T = 5\ K$, the microscope is cooled with nitrogen ($T = 77\ K$) to pre-cool the microscope walls. The pre-cooling causes a drift in the microscope. The microscope shrinks during this process due to temperature effects. The drift causes misalignment of the laser beam that has to be corrected. This realignment procedure is repeated when cooled down to $T = 5\ K$, however it is a smaller effect as compared to $T = 77\ K$. The alignment is done by several piezo-motors.

The sample holder is mounted on a piezo-tube that can move in the z direction, which is used to approach or retract the sample from the cantilever, as presented in figure 4.2. The other piezo-motors responsible for the x and y directions are also

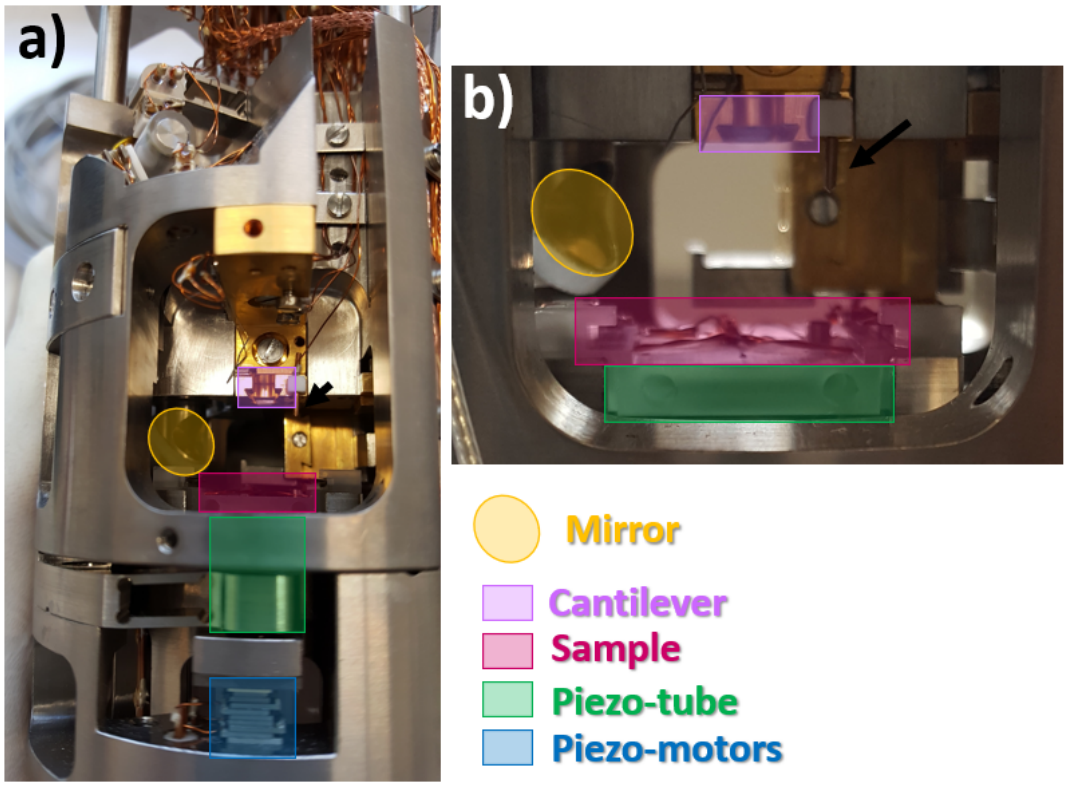

Figure 4.2: — ***a)*** *photo of the microscope. The coloured items are explained in the legend at the bottom of the image. The cantilever as well as the sample position are visible. The different piezoelectric components are visible, as well as one mirror which is used to bring the light onto the cantilever* ***b)*** *zoom-in the microscope in order to see better the sample and cantilever positions in the microscope. The black arrow show the STM contact.*

connected to the piezo-tube (Fig. 4.2 a)). The cantilever is mounted facing the sample holder and is immobile as visible in figure 4.2 b).

To ensure the alignment of the cantilever in the microscope chamber, a pre-alignment is made outside of the chamber directly after mounting of the sensor in the holder. Figure 4.3 a) shows the setup. The pre-alignment also gives information about the cantilever mounting. A red laser is focused on the cantilever (to reproduce the alignment process) and the diffraction pattern is visible on the laboratory wall. To ensure proper cantilever alignment the diffraction pattern must be visible in target. The red dot in the target corresponds to a very good mounting and alignment. If the tip is too high or too low this can give $\pm y$ shift compared to the optimal position of the target. It is also important to mount the cantilever straight.

The microscope system is mounted on four active damping control units to reduce the external vibration noise produced in the building, as visible in figure 4.1 b). The sample holder is the so called *Omicron* holder. It is a rectangular plate with a handle

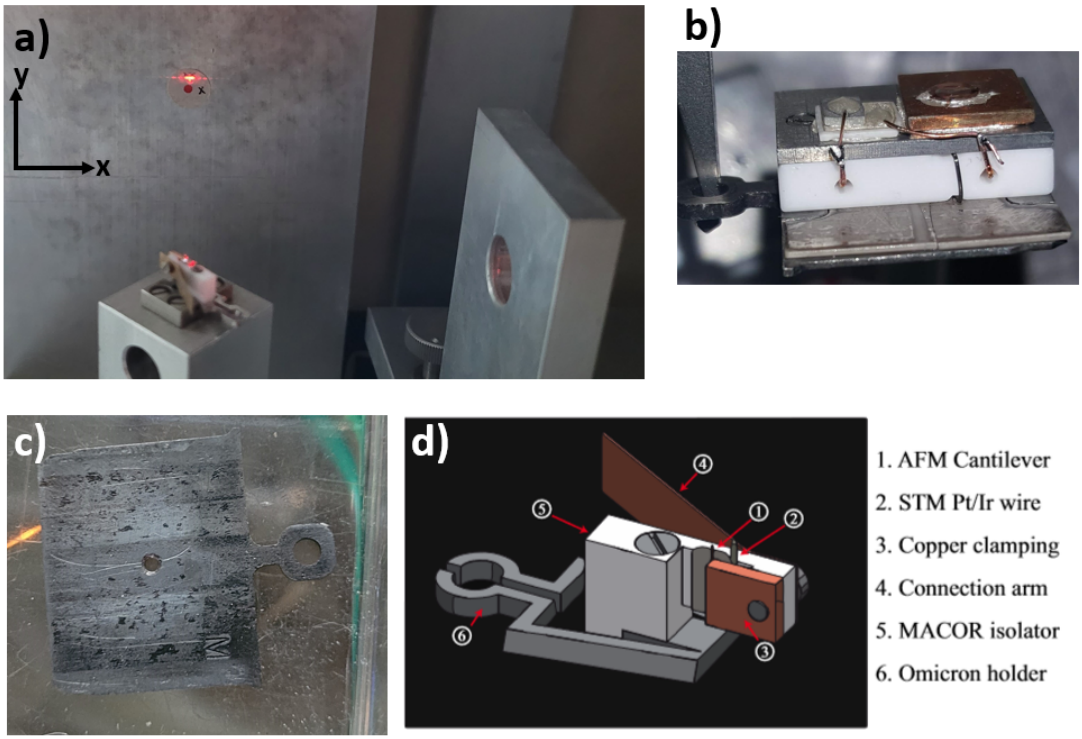

Figure 4.3: — *Cantilever pre-alignment setup.* ***a)*** *pre-alignment setup where a red laser light is focused on the cantilever in order to evaluate if the sensor can be brought into the microscope chamber. The reflection diffraction pattern is also visible.* ***b)*** *modified sample holder that enables to have additional contacts. Two contacts are possible in the p-AFM system.* ***c)*** *normal sample holder.* ***d)*** *cantilever holder. Different components are described in the attached legend.*

in order to move it into the system. It is presented in figure 4.3 c). The experiments carried out in this thesis where made using figure 4.3 b) holder. It is composed of a ceramic isolator and a metallic plate to support the sample. The wires on its side serve as electric contacts for *in-situ* experiments. Only two contacts are allowed within the system. The cantilever holder is presented in figure 4.3 d). It is composed of a holder (with an *Omicron* design) (6), a MACOR ceramic isolator (5) mounted on top of it with a molybdenum screw (resists very high temperatures). The cantilever is clamped to the ceramic plate using a copper block (3). An STM wire can be mounted on this holder if needed, as visible in figure 4.3 d). The copper block ensures the electrical contact with the connection arm (4) via a second molybdenum screw.

4.2 P-AFM Geometry

Pendulum geometry AFM means that the cantilever is oscillating like a tiny pendulum over the sample surface (see Fig. 4.4). This configuration has the advantage of avoiding the snapping of the tip into contact. Thus, we can use very soft and ultra-sensitive

sensors as well as not averaging over the z direction as it is constant. The ultra-sensitive sensors enable to decrease the minimum detectable force sensed by AFM and it is the reason why it is mostly used for spectroscopy measurements [109].

However, such a geometry implies some differences in the interpretation of the acting forces on the cantilever. To understand it, let's first describe the acting forces in conventional AFM. In conventional AFM the normal forces are parallel to the cantilever oscillations, whereas in the p-AFM they are perpendicular to it. Therefore, in conventional AFM it is possible to directly use the equation of an externally driven harmonic oscillator model. In this case, the internal damping force can be compensated by the external driving force [110–112]. The equation of motion becomes [112]:

$$m_{eff}\frac{\partial^2 z(t)}{\partial t^2} = -k_{eff}z(t) + F(z(t), \Phi) \tag{4.1}$$

where $z(t)$ is the time dependent tip position (tip-sample position), k_{eff} is the effective spring constant, $F(z(t), \Phi)$ is the distance dependent interaction force and $\Phi = \omega t$ is the phase. When taking into account the AFM oscillation configuration, $z(t)$ can be written as follows: $z(t) = z_0 + A_i sin(\omega_i t)$, if the sample surface is taken as a reference. Inserting the new form of $z(t)$ in equation 4.1 and integrating it over one oscillation cycle $2\pi/\omega_i$ while rewriting ω as $\omega = 2\pi f$ we can obtain the average frequency shift (Δf):

$$\Delta f_i = \frac{f_{0,i}}{\pi A k}\int_0^{2\pi} sin(\Phi_i) \times F(z_0 + Asin(\Phi_i))d\Phi_i \tag{4.2}$$

where k the spring constant, A is the oscillation amplitude, $f_{0,i}$ is the resonance frequency of every mode and z_0 is the surface distance reference. The equation explains the measured frequency shift of every resonance mode. The equation holds for conventional AFM and it is true only if A is constant and if the dissipative forces are compensated by the external driving force. In the case of the p-AFM, the motion of the cantilever is not perpendicular to the plane surface, hence, the lateral forces also produce a frequency change. It is evident that the force field sensed with the p-AFM is different compared to conventional AFM geometry.

4.3 P-AFM Sensors

The p-AFM is a home build setup and the non-standard geometry makes it difficult to find commercially available cantilevers. All cantilevers are designed for conventional geometry AFM. When operated in pendulum geometry the tip is not facing the sample surface directly. Thus, pendulum AFM uses cantilevers with symmetric or asymmetric tips with Advanced Tip at the End of Cantilever (ATEC). Both sensors are schematically shown in figure 4.4. In case of rectangular cantilever with symmetric tip the frequency of the sensor is given by the equation of motion of the vibrating lever with the formula [113, 114] (see Sup. Mat. S4:1):

$$\omega = \omega_0\sqrt{1 + \frac{3b_1 N}{b_0 L k} + \frac{3}{b_0^2 k}|\frac{\partial F_x}{\partial x}|} \tag{4.3}$$

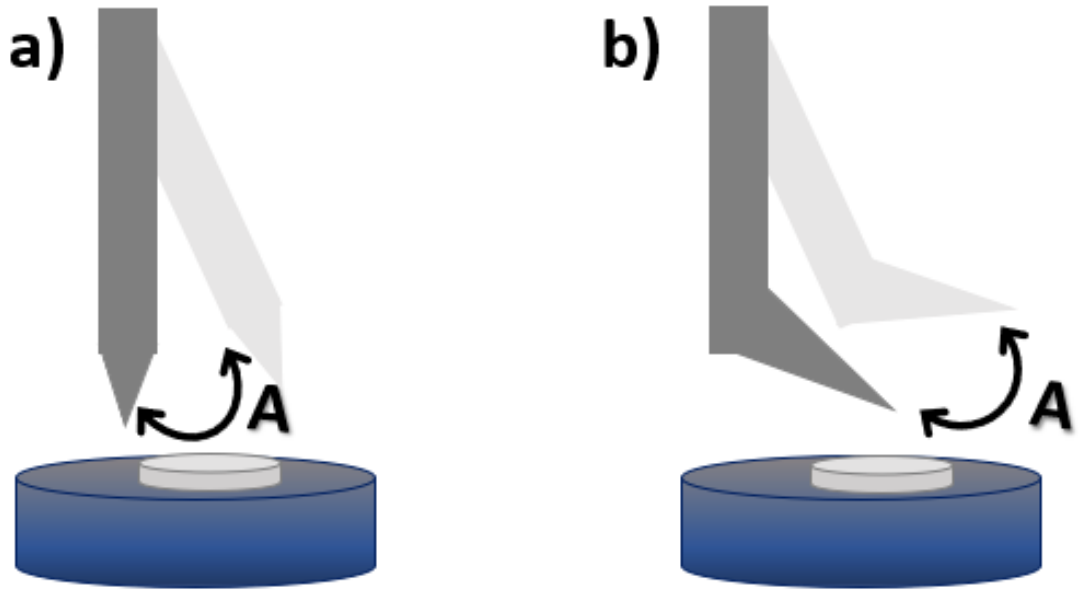

Figure 4.4: — *Schematic of the cantilever in the p-AFM configuration.* ***a)*** *tipless symmetric cantilever.* ***b)*** *normal cantilever with an asymmetric tip at its end. This asymmetric tip enables to have the very end of the tip facing the sample surface during the oscillations.*

where ω_0 refer to the free cantilever, $b_0 = 3.516$ and $b_1 = 0.221$ are the constants, N is the external attractive axial force and L is the cantilever length. The last term in equation 4.3 shows that the lateral force gradient might affect the frequency ω of the cantilever, where F_x is the lateral force [113, 114]. Due to the directional dependence of the interaction, lateral gradient force might be positive or negative meaning that ω can have arbitrary values. Since the frequency of the sensor might change the sign, FM-AFM imaging with this kind of tips is almost impossible. Although imaging is not the advantage of the p-AFM, knowledge about the topography the surface is necessary in order to understand the spectroscopy data. In order to improve on imaging problem, we use asymmetric tips with advanced tips at the end of cantilever.

4.3.1 Asymmetric Tip

The asymmetric tips of ATEC-Cont cantilevers (Advanced Tip at the End of the Cantilever for CONTact mode) has been used in the p-AFM measurements and are shown in figure 4.5 a). These probes were developed to optimize the AFM topography imaging in the contact mode. In the pendulum geometry the asymmetry of the tip enables to establish stable frequency shift feedback. Another advantage is that only the front part of the tip is directly facing the sample surface, see figure 4.4 b).

The ATEC-Cont levers are usually designed with a length of $l = 450\ \mu m$, a width of $W = 50\ \mu m$ and a thickness equal to $t = 2 - 3\ \mu m$. The tip height is $h = 15 - 20\ \mu m$ with an advance angle equal to $\theta = 60°$, which are the origin of the tip asymmetry (see Fig. 4.5 a)) [112]. These cantilevers have a very high-quality factors equal to

$Q \approx 25000$, which after annealing might reach values of $Q \approx 10^6$. The nominal spring constant is equal to $k \approx 0.2\ N/m$ [115].

To find the relation between the lateral and the normal forces components acting on the oscillator, the linear harmonic oscillator approximation can be used. This approximation is possible if the cantilever angle (α), that corresponds to the angle between the real cantilever length L and effective length l_{eff} is small enough and if the condition $sin(\alpha) \approx 0$ is fulfilled. The model simplification consists of a rigid tip with no tip apex deformation.

The effective length is longer than the actual length of the cantilever by an amount of $b = h \times tan(\theta)$ the cantilever angle α can be estimated with respect to the asymmetric tip and the effective length as follows:

$$\alpha = tan^{-1}(\frac{h}{l+b}) \tag{4.4}$$

$$l_{eff} = \sqrt{(l+b)^2 + h^2} \tag{4.5}$$

When the cantilever is oscillating, the clamped lever undergoes a bending moment for any forces acting normal to the sample surface as well as lateral forces (see Fig. 4.5

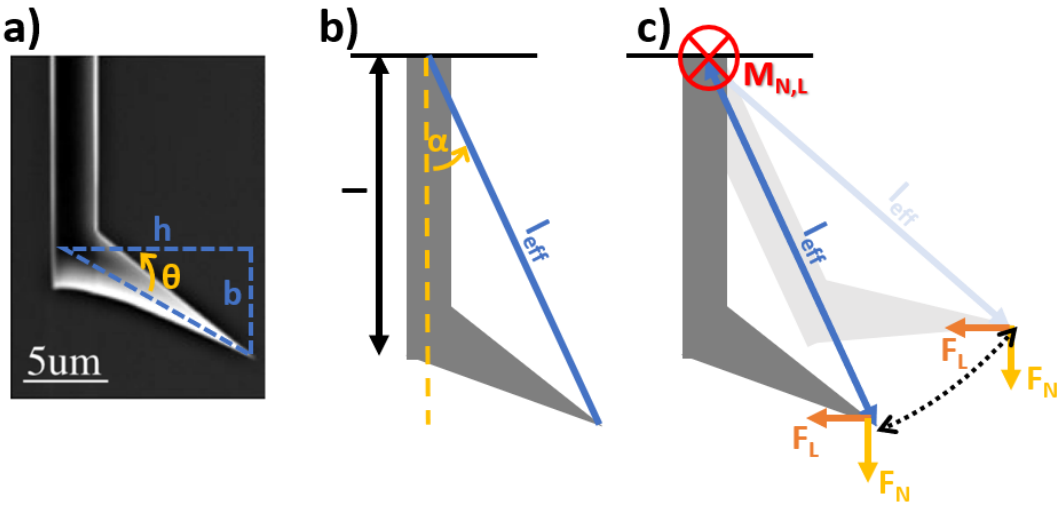

Figure 4.5: *—**a)** Scanning Electron Microscope image of the ATEC-Cont cantilever with the advanced tip at its end. The geometric quantities are showed in blue dashed line, where the tip tilt angle θ is visible as well as the tip height b and length h. **b)** schematic of the cantilever shown in gray where length l and effective length l_{eff} are identified. The angle α corresponds to the angle between the actual cantilever and the effective length. **c)** forces and momentum acting on the driven cantilever. During oscillations tip has an arc trajectory with radius l_{eff}.*

c)). In equilibrium position, we can write:

$$\begin{aligned} |M_N| &= |M_L| \\ F_N \times l_{eff} \times sin(\alpha) &= F_L \times l_{eff} \times cos(\alpha) \\ F_L = F_N \times (\frac{h}{l + h \times tan(\theta)}) &= F_N \times C \end{aligned} \tag{4.6}$$

where M_N is the normal moment, M_L is the lateral moment, F_N the normal forces and F_L are the lateral forces. Usually, for any given h, l and α the coefficient C after F_N is smaller than 1, meaning that due to geometrical reasons the sensitivity to normal forces is reduced compared to the lateral forces. Table 4.1 is showing the influence of the tip length on C. It's clearly visible that this coefficient is very small for both stiff and soft tips. It can also be noticed that C_{soft} is larger than C_{stiff} meaning that for ultra-sensitive levers the acting normal forces have more effects on the cantilever as compared to stiff levers. The α angles are calculated with equation 4.4.

Constants	h (μm)	l (μm)	b (μm)	$\alpha(^\circ)$	C
Soft tip (long tip)	20	450	6.4	1.87	0.044
Stiff tip (short tip)	15	450	4.8	2.5	0.033

Table 4.1: — *Comparison of α and C coefficients for short and long tips in the ATEC-Cont tip sizes.*

In experiments, the cantilever is resonantly driven, meaning that the motion of the tip will follow an arc trajectory (Fig. 4.5 c)), with a radius equal to $r = L_{eff}$. Due to the asymmetry of the tip, its motion is not symmetric and has a perpendicular deviation (dz) in addition to the lateral deviation (dx). The lateral deviation is the amplitude defined in the PLL loop as A_{osc} and it is larger than the perpendicular deviation. In p-AFM ultra-sensitive levers are used, making this perpendicular deviation not negligible. It has an influence on the frequency shift measurements as visible in the equation 4.2.

As described in the previous section the frequency shift in the pendulum geometry depends on lateral as well as normal forces. In order to evaluate each component in the frequency shift, their unit vector from the reference system can be used, see figure 4.5 c). Indeed, the two vectors are orthogonal to each other and it is then allowed to consider these forces independently and add them up: $\Delta f = \Delta f_L + \Delta f_N$. The two components can be written as follows:

$$\Delta f_L = \frac{f_0, i}{\pi A_L k} \int_0^{2\pi} sin(\Phi_i) \times F(x_0 + A_L sin(\Phi_i), z_0) \times cos(\alpha) d\Phi \tag{4.7}$$

$$\Delta f_N = \frac{f_0, i}{\pi A_N k} \int_0^{2\pi} sin(\Phi_i) \times F(x_0, z_0 + A_N sin(\Phi_i)) \times sin(\alpha) d\Phi \tag{4.8}$$

where A_L and A_N are the lateral and the normal amplitudes respectively and the factors $sin(\alpha)$ and $cos(\alpha)$ are responsible for the reduction of the force sensitivity for

the normal and the lateral amplitude components. If we compare equations 4.7 and 4.8 for the situation of the symmetric lever, the tip perpendicular component vanishes over the oscillation cycle due to perfect symmetry. Hence $\alpha = 0$ makes equation 4.8 equal to zero ($F_N \approx 0$) and the lateral components become dominant. Similarly, in the limit of $\alpha = 90°$, the lateral component vanishes and equation 4.7 reduces to equation 4.2.

4.3.2 Cantilever Calibration

In order to correctly interpret the cantilever frequency shift and dissipation signals, cantilever calibration is mandatory which includes determination of the quality factor, the amplitude or the exact spring constant.

The quality factor is obtained independently for both oscillation modes. To do so, the driven oscillations are stopped and the amplitude signal decay time (τ) is recorded. Typical curves are shown in figure 4.6 a) for the first and the second oscillation modes. The decay time is then fitted with an exponential law: $f(x) = Ae^{-\frac{x}{\tau}}$, where A is a fitting constant, x is the time and $f(x)$ are the experimental data. After obtaining the decay time τ, it is possible to calculate the quality factor Q and the minimum detectable force F_{min}. The actual spring constant k as well as the thermal noise x_{rms} for each mode is also determined. This last step is called '*thermal noise calibration*' or '*phase calibration*'.

This calibration is very important because it allows calibrating the actual amplitude of oscillations and properly set calibration factor of the PLL in the units of nm/V. This calibration method relies on measurement of the standard deviation of the cantilever phase signal for different oscillation amplitudes.

To understand this, the Brownian motion of the harmonic oscillator has to be considered. Indeed, when a harmonic oscillator is driven by a periodic force at its resonance frequency its thermal fluctuations induce random forces that have to be taken in consideration as well. The oscillation of the driven cantilever can be modelled using a superposition of different sinusoidal signals with fixed parameters as follows [116]:

$$x(t) = x_0 sin(\omega_0 t) + A(t) sin(\omega_0 t + \phi(t)) \tag{4.9}$$

where x_0 is the driven oscillation amplitude, $A(t)$ is the time-dependent thermal noise amplitude and $\phi(t)$ is the fluctuating phase. Regarding equation 4.8, it is visible that when the driven oscillation stops ($x_0 = 0$), the cantilever is still oscillating due to finite temperature. The oscillation phase of the signal is randomly distributed with homogeneous probability density: $P(\phi) = 1/2\pi$. This probability is amplitude dependent, and it changes every-time x_0 is increased. This change can be measured with a phase sensitive lock-in amplifier.

In the case of stiff sensors, as for example tuning fork, the phase noise is almost negligible and high amplitude stability offers the atomic resolution. In the p-AFM geometry, very small excitation amplitude has to be applied in order to achieve better lateral resolution. The typical oscillation amplitudes are equal to: $x_0 = 50$ Å to

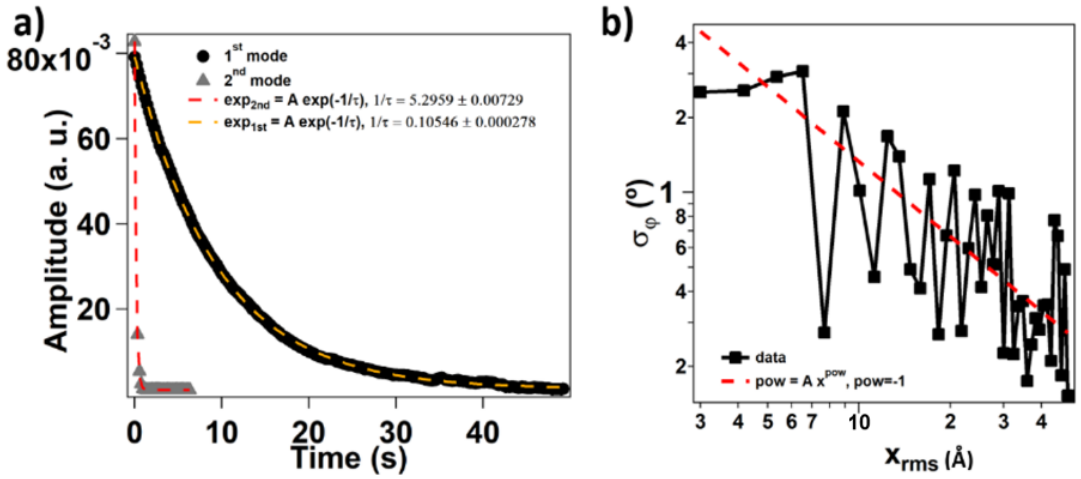

Figure 4.6: — *Experimental decay time and phase noise spectra.* ***a)*** *typical amplitude decay time curves obtained for the first and the second modes in black and gray respectively. The dotted line are the corresponding exponential fitting curves. The decay time is always smaller for the second mode as compared to the first mode.* ***b)*** *typical phase calibration curve where the phase noise is plotted versus oscillation amplitude x_{rms}. The red dotted line is the power law fitting curve.*

$\approx 5\ nm$. Under these conditions and with an annealed cantilever (with a $Q \approx 10^6$) the thermal vibrations are not negligible. The smaller the oscillation amplitude the larger the thermal noise contribution becomes leading to larger phase noise of the signal. We use the phase noise method to calibrate the oscillation amplitudes.

Experimentally, the phase noise is determined in measurement of phase standard deviation for several amplitudes. The amplitudes have a range of $x_0 \in [50\ pm$ to $5\ nm]$. The phase standard deviation is plotted versus rms amplitude (average distance induced by the thermal fluctuations) in a logarithmic scale as shown in figure 4.6 b). The bandwidth of the lock-in amplifier is set to be wider than the bandwidth of the signal. The phase noise σ_ϕ is linked to the amplitude x_0 of the input signal. To calibrate the amplitude a comparison between the measured phase noise signal and the theoretical phase noise curve is made. If the measured rms amplitude (σ) of the signal is larger than the rms amplitude x_{rms} of the random signal, the standard deviation phase noise σ_ϕ can be numerically approximated by [116]:

$$\sigma_\phi = \frac{a\sigma}{x_{rms}} \tag{4.10}$$

where $a = 42.131°$ is a phase jitter and σ is the thermal noise amplitude equal to $\sigma = \sqrt{\frac{k_B T}{k}}$. If the measured signal is perfectly superimposed with the theoretical curves then the cantilever is perfectly calibrated (see Fig. 4.6 b)). The thermal noise amplitude is obtained thanks to the calculated spring constant k.

It is visible from equation 4.10 that when $\sigma = x_{rms}$, the phase jitter is at its theoretical limit and to overcome it, larger amplitudes have to be set.

4.4 STM Measurements With P-AFM

Simultaneous STM and AFM measurements using the AFM probe was the first improvement idea developed after the development of each technique [117]. The electronic behind both techniques is similar, but in most of the cases the tip has to be changed in order to switch the measurement technique. p-AFM offers the possibility to operate in the STM mode without changing the tip. It is possible to perform STM measurements with the relatively stiff ($k = 40\ N/m$) ATEC-NC gold coated tips. Thus, it is possible to measure in AFM and STM on exactly the same sample spot and to acquire dissipation and DOS spectra at the specific place of interest.

To achieve this, a conductive tip (gold coated tip) is necessary. The AFM feedback (cantilever oscillation amplitude) is stopped and replaced by the STM feedback (tunnelling current) in regulating the tip-sample distance. In order to have a stable tunnel junction, the lateral oscillation of the tip are switched off and for a stable feedback while scanning the lateral deflection must be also negligible.

In STM measurements, the tip operates closer to the sample surface as compared to the NC AFM mode. In comparison, for the p-AFM measurements the typical tip-sample distance is $d > 1\ nm$ while for STM measurements $d \leq 1\ nm$. This small distance is the key parameter in order to reach atomic resolution.

4.5 Summary

In summary, the pendulum AFM system has been described. The cantilever geometry was discussed in detail. I compared the conventional AFM geometry and pendulum geometry in order to understand what is the added value of pendulum geometry AFM in order to understand the interaction force. The ability to operate with the STM line also been discussed as well as the cantilever calibration.

5

Free-Standing Graphene

Graphene attracts great attention due to its high electron mobility, mechanical flexibility and the potential use in electronic applications [118]. Dirac energy spectrum and two-dimensional lattice led to unique conductive and magnetic properties. One of the most spectacular examples of such effects is the creation of pseudo-magnetic fields in strain modulated superlattices in graphene [119, 120]. Although recent experiments reported on ferromagnetism of graphene-based materials which is related to defects [121], graphene traditionally has been thought to show diamagnetism, a very weak paramagnetic contribution was noticed as it possesses a simpler structure as compared to other carbon materials and unique electronic properties. Graphene structures might also behave as effective quantum dots and become a host for charge carriers at low temperatures [122–124].

It has been shown that pendulum geometry AFM is sensitive to different types of energy transfer in the non-contact regime between an oscillating probe and a sample, namely phonon excitation, Joule ohmic dissipation or van der Waals dissipation originating from charge fluctuations between the probing tip and the surface, see chapter 3. In a quantum dot the external perturbations caused by an oscillating tip might push a system towards a transition or a level crossing with subsequent fluctuations and relaxation of the system, eventually resulting in the enhancement of energy loss. Charge relaxation in quantum dot creates a hallmark in an AFM dissipation spectrum in the form of dissipation peak [125]. p-AFM mechanical dissipation measurements on suspended graphene show increased energy losses at discrete separations and voltages up to distances of hundreds of nanometers.

STM measurements reveal the formation of 2 nm wide wrinkles in a loosely clamped graphene. Simultaneously, the frequency modulation topography imaging reveals the presence of static out of plane deformations of larger sizes. In addition to that, the graphene membrane is a Chemical Vapour Deposited (CVD) monolayer that might possess structural defects [126–128]. The electronic properties of such structures on

free-standing graphene sheets are still under study [129, 130].

In this chapter, we will discuss the measurements of frictional energy dissipation between a free-standing graphene surface and a silicon cantilever tip oscillating in the pendulum geometry.

We simultaneously acquired the tip oscillation frequency shift Δf and the dissipation signal Γ. As a function of a tip-sample distance, we observed a remarkable train of dissipation maxima that extend as far out as a hundred of nanometers above the surface. We interpret the enhanced dissipation losses at discrete separations and voltages to the presence of van Hove singularities in Quantum Capacitance (C_Q) of 1D-like nanostructure in loosely clamped graphene. The presence of the confined states leads to the enhancement of the density of states in the deformed graphene region. The magnetic field measurement and tight-binding calculations confirmed the presence of the another several nanometers large length scale ($\approx 70\ nm\ to\ 500\ nm$). Calculations and experiments showed linear dependence of dissipation peaks versus magnetic field. We found this behaviour to be related to the linear energy dispersion of graphene. The calculations suggest and confirmed by experiments, that the accidental 2 nm size nanostructures in graphene sheets don't significantly alter the magnetic field dependence.

5.1 Sample Geometry And Characterisation

The sample consists of a CVD grown graphene deposited on a copper substrate patterned with holes of a diameter equal to 6.5 μm, see figure 5.3 d). The structure of the graphene was characterized by means of contact AFM topography images and indentation measurements as presented in figure 5.1 as well as with atomic scale STM topography images and STS measurements as shown in figure 5.3.

The configuration with free-standing graphene membranes leads to the presence of wrinkles in the membranes. The elastic properties of the graphene membranes were thus investigated. The characterisation was made at room temperature (RT) by indentation (curves in Sup. Mat. S5:1) with an AFM tip positioned at the centre of the membranes. We followed the procedure given by Lopez-Polin *et. al.* [131], where the force versus indentation curves were approximated by Schwering-type equation:

$$F(\delta) = \pi\sigma_0\delta + \frac{E_{2D}}{a^2}\delta^3 \tag{5.1}$$

where F is the measured lading force, δ the membrane indentation, σ_0 is the pre-tension accumulated in the membrane, a is the membrane radius and E_{2D} is the 2D elastic modulus. In order to compare with 3D materials and express the Young modulus E_Y in GPa, we divided E_{2D} by the interatomic spacing of graphite ($a_s = 0.34\ nm$).

Our results of the Young modulus values are equal to $E_{2D} = 60\ N/m$ and $E_Y = 0.2\ TPa$. These values are five times smaller compared to high quality exfoliated graphene ($E_g \approx 1\ TPa$). The obtained values suggest partially relaxed suspended

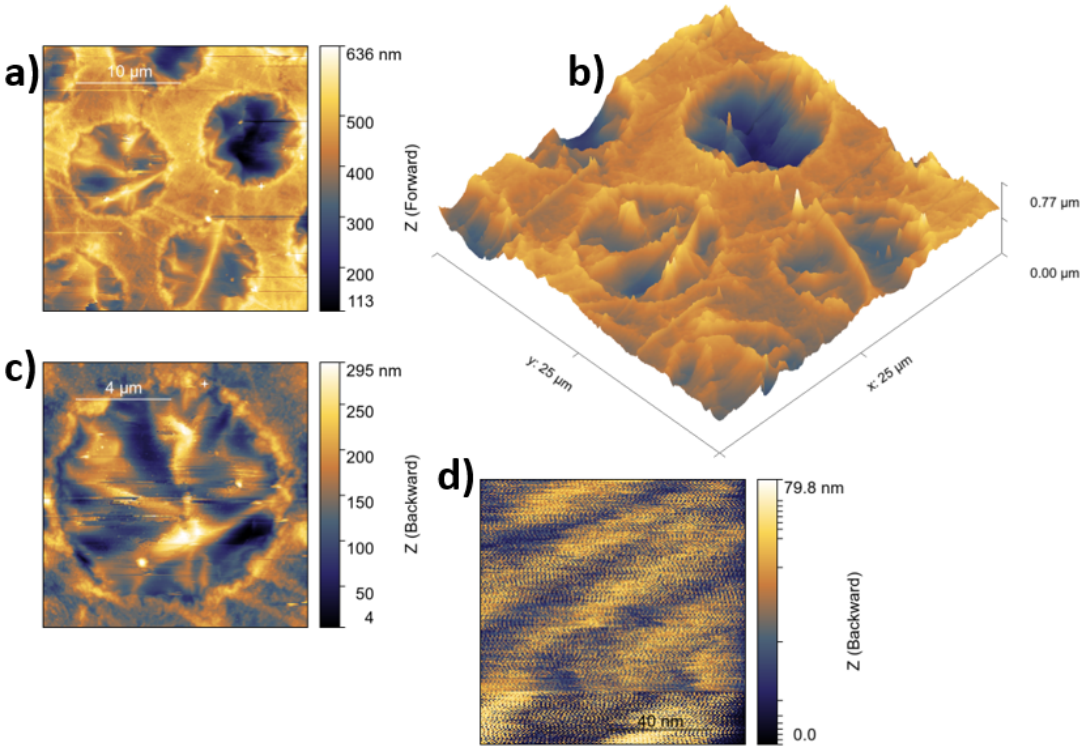

Figure 5.1: — *Contact AFM topography images of the free-standing graphene membranes.* ***a)*** *large scale AFM image of the sample surface, where different membranes are visible.* ***b)*** *3D representation of a) where the corrugation of the sample surface is better visible. Different micro metric wrinkles are visible with random orientations.* ***c)*** *zoom-in image of one membrane.* ***d)*** *shows the formation of hundred nm size wrinkles in the membranes. The resolution limit of the air AFM microscope is* 10 *nm.*

graphene sheets [131–133]. The in-plane stiffness of graphene E_{2D} measured in the experiment can be approximated as [134]:

$$E_{2D}^{-1} = E_{latt}^{-1} + E_{flex}^{-1} + E_{wrink}^{-1} \tag{5.2}$$

where $E_{latt} = 340\ N/m$, E_{flex} and E_{wrink} are contributions to the stiffness from three different mechanisms - stretching of carbon-carbon bonds, flexural phonons and static wrinkles. The substantial softening of the graphene suggests the presence of static wrinkles which are visible in the AFM topography images, see figure 5.1.

The mechanics of graphene membranes with similar size and exactly the same in-plane stiffness equal to $20\ N \cdot m^{-1} < E < E_{2D} = 100\ N/m$ was studied in details and the results concluded that the softening of the graphene is due to the wrinkle contribution E_{wrink}, see equation 5.2 [134]. At low temperatures, the flexural phonons are strongly suppressed whereas at RT their influence is visible as membrane thermal oscillations, visible as a telegraph noise in the frequency shift (Δf) spectrum.

The effect of flexural phonons is demonstrated in figure 5.2, where the Δf signal in and out of the graphene membrane is plotted versus the sample bias voltage. At the membrane centre, the AFM tip experiences telegraph noise due to dynamic out

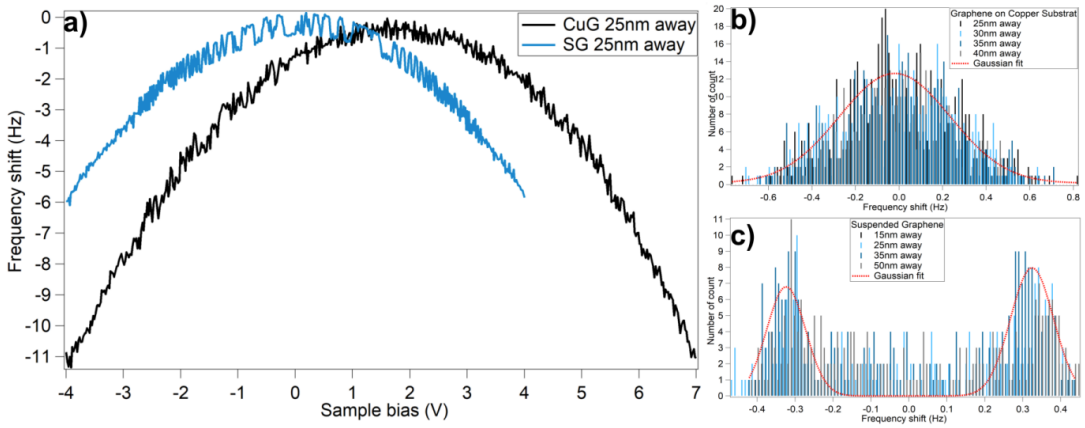

Figure 5.2: — *Telegraph noise.* ***a)*** *frequency shift versus sample bias spectra taken in the middle of the graphene membrane and outside of the membrane at a tip-sample distance of* $d = 25\ nm$*. The frequency noise over the supported graphene shows random noise, whereas the suspended graphene shows telegraph noise* ***b)*** *Gaussian distribution of the noise on the supported graphene.* ***c)*** *noise distribution of the graphene membrane showing a bi-modal distribution. The red line is the Gaussian fit for both spectra.*

of plane deformations, whereas graphene deposited on copper shows regular Gaussian, random type noise. At low temperatures, the flexural phonons are suppressed and we don't observe telegraph noise in the Δf spectra. Thus, we concluded that the softening of the graphene membranes is exclusively due to static wrinkles.

The static wrinkling of the graphene membranes of sizes spanning from few to dozens of nanometer and the presence of 1D-like structure are the scope of this chapter. The small-scale structures are essential for electronic confinement, whereas the large scale structures dominate the magnetic response.

Small scale wrinkles are well resolved by STM and the topography image is shown in figure 5.3 e). The relaxation of the membrane leads to the formation of quasi-1D wrinkles with the width equal to about $W = 2\ nm$. We do not observe similar wrinkle formation on copper supported graphene. Instead, the STM reveals flat topography Moiré resolved image (Fig. 5.3 a)). The STS conductance spectra on suspended graphene are shown in figures 5.3 b) and 5.3 c) and they reveal the broadening of the Charge Neutrality Point (CNP) region, in analogy to transport experiments on strained graphene [135] where wrinkles of uniaxially strained graphene induce spatial redistribution of the scalar potential most likely due to the presence of electron-hole puddles [136] that shift the CNP. This effect is visible as a broadening of the charge neutrality point compared to the unstrained STS curve (Fig. 5.1 b) and c)). The highest and lowest CNP are marked by arrows in figure 5.1 c) and corresponds to the edge points of the plateaus that have width of $\Delta V \approx 0.3\ V$. Graphene deposited on copper (Cu) showed typical "V"-shape conductance spectrum [135, 137] with well-defined CNP. Additionally, the out of plane deformations modify the transport properties introducing distinct anisotropy in the electrical resistance along and across the wrin-

kles [138]. Moreover, conductance measurements across the membranes in graphene revealed Coulomb blockades signatures [139], indicating charge carrier confinement similar to quantum dots [140] and indicates ballistic transport along the Gaussian folded structures.

In this study, the origin of the electron confining structures is not clear. The tight binding calculations reveal confined structures with larger dimensions as compared to the observed nano-wrinkles. They might come from the CVD growth process and the presence of disordered domains in the graphene flakes. The AFM experiments confirm the 1D shape of these confining objects, discussed in the next paragraphs. Hence, the confining object will be referred as 1D quantum dot (1D-QD).

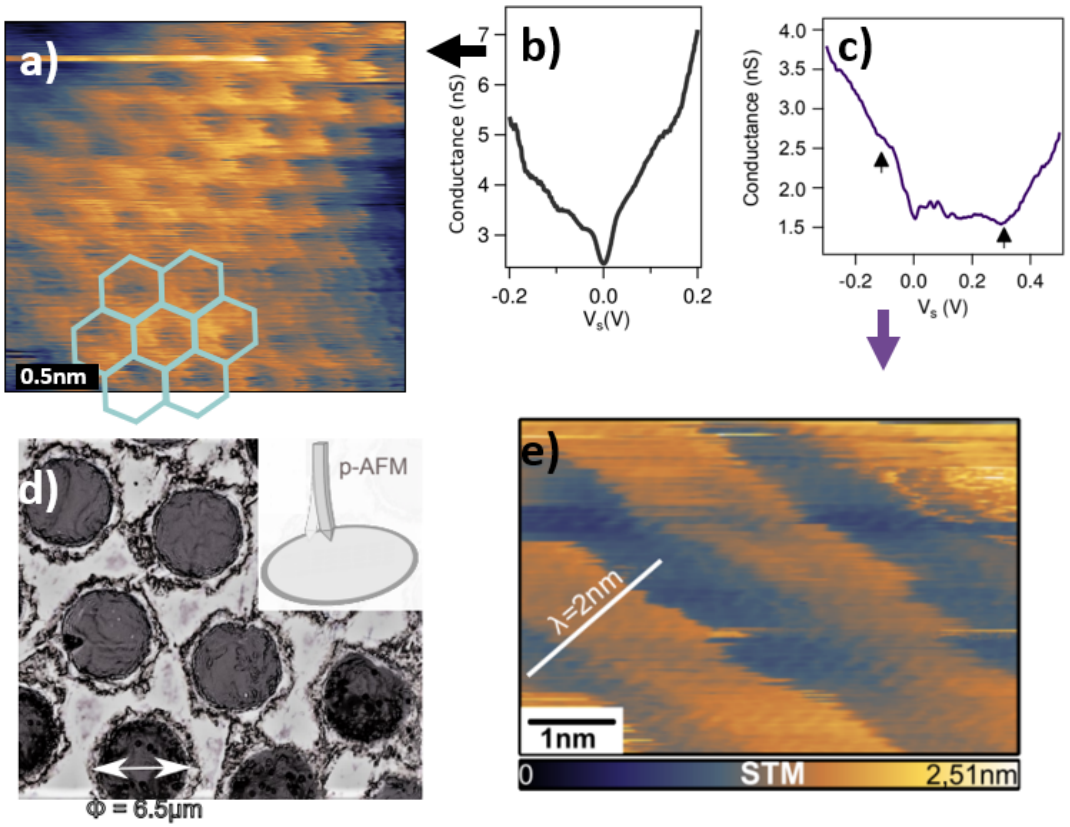

Figure 5.3: — *STM and STS characterization.* ***a)*** *STM topography image of chemical-vapour-deposited graphene on copper surface. The honey-comb graphene lattice is superimposed with STM topography image.* ***b)*** *STS conductance spectrum of graphene with "V"-shape behaviour characteristic for flat graphene.* ***c)*** *STS conductance spectrum taken on 1D-QD graphene. The observed broadening of the CNP is characteristic for deformed graphene. The arrows indicate the highest and the lowest CNP.* ***d)*** *optical microscopy image of the membranes of* 6.5 *µm in diameter suspended on hole patterned copper substrate. The inset shows schematic of the experiment with the p-AFM sensor oscillating on top of the sample.* ***e)*** *STM image of the ripples presents on the graphene membrane. The tunnelling current and sample voltage were equal to* $I = 120\ pA$, $V_S = 10\ mV$.

5.2 Dissipation Measurements

To perform dissipation measurements, we switch to p-AFM mode, were the cantilever is oscillating with a fixed amplitude ($A = 5\ nm$) at a fixed tip-sample distance ($d = 80\ nm$) while a bias (V_S) is applied to the graphene gating Cu substrate. The frequency shift (Δf) as well as the energy dissipation (Γ) of the cantilever are monitored using the PLL (see Chap. 2).

To investigate the energy loss mechanisms, we performed dissipation and force spectroscopy over 2 nm wide graphene wrinkles area. The measurements consist of sweeping the bias from $-10\ V < V_S < 10\ V$ on the sample and record simultaneously the Γ and the Δf measured spectra. The typical p-AFM voltage-dependent spectrum is presented in figure 5.4 a). The Δf curve exhibits a parabolic dependence due to the capacitive coupling of the oscillating tip and the underlying surface. In addition to that, several irregularities are visible at various V_S. The kinks are followed by a non-monotonic dissipation signal shown in blue in figure 5.4 a). Every kink in Δf is followed by a peak in the Γ spectrum. The amount of dissipated energy is in the order of tens of millielectronvolts per cycle, indicating a single electron tunnelling process. It can also be noted that the dissipation spectrum is symmetric with respect to the CPD and the dissipation peaks at highest intensity (n=3 and 5) appear to split.

Figure 5.4 b) shows the distance and voltage dependence of the damping coefficient $\Gamma(d)$ of the cantilever. The map reveals a slight rise of the dissipation at the CPD and it is presumably due to the presence of electron-hole puddles close to the CNP, since $V_S = V_{CPD}$ the oscillating tip drives the carriers in opposite directions and collision between them give rise to frictional dissipation [3]. Apart from that, most of the dissipation features are voltage dependent and are the scope of this study. The positions of the dissipation peaks are marked by arrows and the white dashed line located at $d = 80\ nm$ marks the tip-sample position at which the spectrum shown in figure 5.4 a) is taken. The dissipation peaks are visible at relatively large distance ($d > 100\ nm$) at non-zero V_S. This indicates that the dissipation is not force but voltage controlled [104]. The position of the dissipation peaks shifts linearly towards higher voltage with increasing d due to the decrease of the capacitive coupling between tip and sample. This can be understood by considering that AFM data are influenced by the voltage drop across the vacuum gap and the Cu backgate, which is divided by three capacitances [108]. The total capacitance seen by the tip is given by the equivalent capacitance circuit shown in figure 5.4 d). The tip-surface (C_{TIP}) and the graphene membrane-Cu gate (C_{PAR}) are geometric capacitances. The third capacitance C_Q stands for quantum capacitance, which is a consequence of the Pauli expulsion principle, which requires an extra energy for filling the quantum well (QW) with electrons. It is calculated using this equation [2]:

$$C_Q = \frac{4e^2}{\pi\hbar v_F} \sum_n \frac{\eta}{\sqrt{\eta^2 - x_n^2}} \Theta(\eta - x_n) \propto \rho(\eta) q^2 \tag{5.3}$$

where $\eta = E_F/k_BT$, $x_n = E_n/k_BT$, $E_n = n\pi\hbar v_F/W$, $\Theta(...)$ is the Heaviside unit step function, $q = ne$ the electron charge, k_B the Boltzmann constant, T the temperature

and ρ the DOS. To simulate the frequency shift data, we assume a structure with two length scales: L_x - across and L_y - along the 1D-QD. The simulated quantum capacitance for $L_x = 2\ nm$ wide and $L_y = 75\ nm$ long graphene 1D-QD is shown in figure 5.4 c) as a function of chemical potential V_{CH}, where $V_S = \alpha \cdot V_{CH} \cdot C_Q$, where α is the lever arm and C_Q the quantum capacitance. It is important to note that these values of L_x and L_x are not fixed. Different values can be used if a ratio of 8 can be

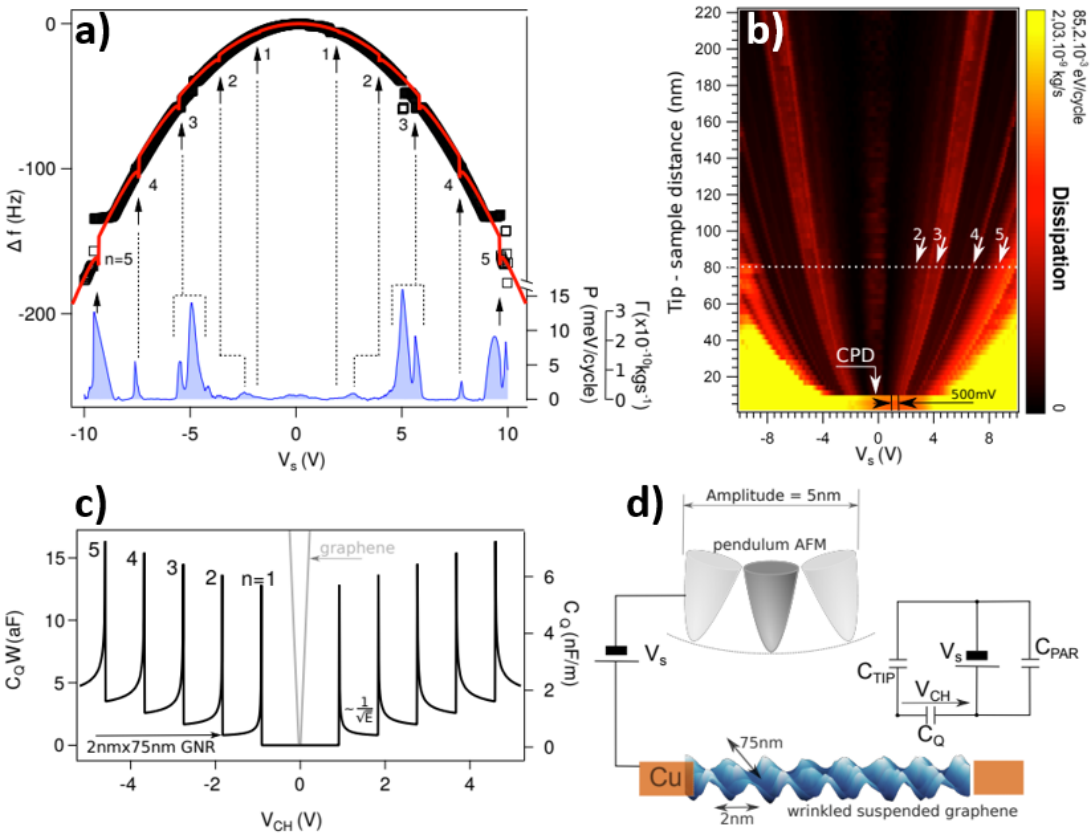

Figure 5.4: — *Voltage dependent frequency shift and dissipation spectra at $d = 80\ nm$ over the 1D-QD graphene.* ***a)*** *frequency shift (Δf)) measurement with a parabolic background (in black) and its fit (in red). The Δf spectrum shows singularities marked by arrows and subsequent numbers n=1, 2, ... at biases when single electron charging of the 1D-QD occurs. Every charging event is accompanied by rise of dissipation (Γ) signal as shown in the blue spectrum. The fit allows estimating the tip-sample capacitance (C_{TIP}) and the quantum capacitance (C_Q).* ***b)*** *Γ map of the graphene 1D-QD plotted versus distance- and tip- sample voltage V_S. The lighter contrast represents large dissipation features marked by arrows in a).* ***c)*** *C_Q versus the chemical potential V_{CH} of the graphene 1D-QD (black) and 2D flat graphene are shown [1–3]. Each van Hove singularity has the characteristic 1D DOS decay $1/\sqrt{V_{CH}}$.* ***d)*** *schematic of the tip-sample geometry and the equivalent electrical circuit. The voltage drop is divided across the three capacitors C_{TIP}, C_Q and C_{PAR}, where the later stands for coupling of the tip to the bulk material.*

applied between them (see Sup. Mat. S5:3).

The usual value of C_Q is in the order of few nF per meter and the simulations revealed a 1D-QD that has a C_Q in the order of few aF. They shows van Hove singularities at specific energies given by quantization conditions: $E_n = n\pi\hbar v_F \cdot \sqrt{L_x^{-2} + L_y^{-2}}$, where n is the quantum number. The formulation of C_Q presented in equation 5.3 was used to reproduce the experimentally observed Δf spectrum (the red curve in Fig. 5.4 a)). The parameters of the model are $C_{TIP} = 2.5\ aF$ and $\alpha = 0.44 - 0.48$ indicating comparable values for C_{TIP} and C_Q.

To reproduce the Δf data, a capacitance model (Fig. 5.4 d)) was used (see Chap. 3) to describe the system. The tip-sample capacitance C_{TIP} was estimated using the spherical tip over a plane surface using this formula: $C_{TIP} = \frac{2\pi R^2}{d} = 2.5\ aF$ with a tip radius equal to $R = 60\ nm$. The sample is described by the two other capacitance $C_{SUB} = C_{PAR} + C_Q$. We assumed that C_{PAR} is a classical geometric capacitance between the 1D-QD and the underlying Cu support. The yellow curve in figure 5.5 is the simulated data with $C_{PAR} = 0$, meaning that the 1D-QD are free-standing and by no means coupled to the bulk of the support. To properly reproduce the data, the 1D-QD must be electronically coupled to the support then $C_{PAR} \neq 0$. We assume that this type of coupling is equivalent to inducing an additional frequency shift to the cantilever $\Delta f_{PAR} = -1.45[\frac{Hz}{V^2}] \cdot V_S^2$ that was added to the total $\Delta f(Hz)$ signal. The influence of C_{PAR} is substantial and at large tip-sample voltages, the Δf signal due to C_{PAR} might be five time larger as compared to $C_{PAR} = 0$ situation. The influence of C_{PAR} is substantial yet does not suppress the presence of the van Hove singularities

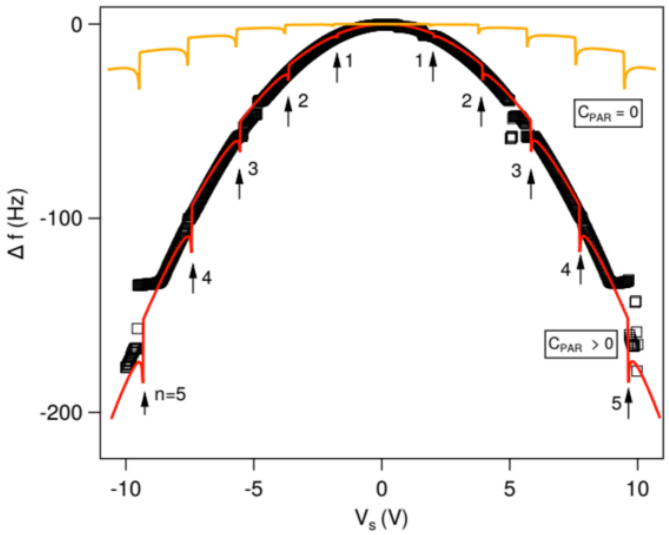

Figure 5.5: — *Voltage dependent frequency shift spectra at $d = 80\ nm$ distance over the surface. The Δf parabola shows some singularities at the biases when single electron charging occurs due to van Hove singularities in the quantum capacitance C_Q. The black points are the experimental data, while the red line is the simulated Δf fit. The fit allows estimating the tip-sample and the quantum capacitance as well as the parasitic capacitance.*

peak nb	E_{max}	$1/\Delta Q$	$2\Delta\omega$	$\Delta\omega$	ΔQ	γ
1	0.48759	5.52809e-6	9.90984	4.95492	180894	8.96315e05
2	0.82348	9.33627e-06	23.2234	11.6117	107109	1.2437e06
3 (1)	23.4714	2.66104e-04	224.56	112.28	3757.92	4.2140e05
3 (2)	9.1259	1.03466e-04	73.2311	36.6155	9665.05	3.53891e05
4	2.6333	2.98552e-05	9.63038	4.81519	33494.9	1.61284e05
5	9.1438	1.03669e-04	294.797	147.399	9646.13	1.42182e05

Table 5.1: — *Table with tunnelling rates $\gamma(Hz)$ for different dissipation peaks. $\Delta\omega$ is the height of the kink in the frequency shift spectra, $E_{max}(meV/cycle)$ is the maximum of the dissipation peak.*

measured on the Δf spectra. The capacitance C_Q, was calculated using the equation 5.3. The lever arm $\alpha = C_{TIP}/(C_{TIP} + \bar{C_Q}) = 0.485$ was analytically estimated using the mean value of the substrate capacitance $\bar{C_Q}$. Under assumption $E_n > E_F$ and for n=5 states (see Fig. 5.4 a)), equation 5.3 reduces to:

$$\bar{C_Q} = \frac{16e^2}{\pi\hbar v_F}\sum_{n=1}^{5}\frac{1}{n} = 2.283 \cdot \frac{16e^2}{\pi\hbar v_F} \tag{5.4}$$

The force was calculated according to equation 3.20 (see Chap. 3) and Δf fitting curve is presented as follow:

$$\Delta f(d) = \frac{f_0^2}{kA}\int_0^{1/2} F[d + Acos(2\pi f_0 t)]cos(2\pi f_0 t)dt + \Delta f_{PAR} \tag{5.5}$$

The experimental data are shown in black and the fitting in red in figure 5.4 a). It can be noted that even if C_{PAR} is substantial it still does not hinder the observation of the quantization effect. It slightly diminishes the quantum effect but the single electron charging of the 1D-QD leaves clear hallmarks in the dissipation spectra. This means that the dissipation probed by the p-AFM tip is proportional to the number of bands and to the scattering in the bulk.

The increased response of the dissipation to single electron charging is due to its sensitivity to the tunnelling rate [100, 106], while the Δf is sensitive to the force averaged over many oscillations cycles (see Sup. Mat. S5:2). The tunnelling rate γ is given by:

$$\frac{\omega}{\gamma} = \frac{1/\Delta Q}{\Delta\omega/\omega} \tag{5.6}$$

where ω is the resonance frequency of the cantilever, $\Delta\omega$ is the decrease of the resonance frequency due to the softening of the cantilever spring constant and ΔQ is the change of the quality factor due to damping. All the values are given in table 5.1. To extract $\Delta\omega$, the parabolic background has been subtracted from the experimental data and the corresponding error uncertainty is equal to 10%. Depending on the peak versus voltage position, table 5.1 shows a drop of the tunnelling rates between $\gamma = 200\ kHz - 1\ MHz$ making the local current in the sample in the range of $j = e\gamma = 30\ fA - 200\ fA$.

5.3 Magnetic Field Measurements

The magnetic field (B) effect was examined by applying a perpendicular external B spanning from $B = -2\ T$ to $B = 2\ T$. The tip was at a distance $d = 150\ nm$ above the surface. The B-effect on the dissipation peaks is shown in figure 5.7, considering the symmetric shape of the curve only the positive V_S side is presented. The increase of d (compared to Fig. 5.4 a)) leads to the rise of the lever arm and is equal to $\alpha = 0.6$ making the kinks in Δf less pronounced. In addition to the dissipation peaks, new features are observed. First, a series of dissipation peaks n=3, 4 are split for $B < 0.5\ T$ and the splitting disappears at larger B (Fig. 5.6). Second, the vanishing of the dissipation peaks for $B > 1\ T$ (see Fig. 5.6). Accordingly, constant height p-AFM dissipation images revealed Coulomb rings (Fig. 5.6 b)) at the corresponding dissipation $V_S = -7.8\ V$ and will be discussed in the next section. They are associated with single electron charging of the graphene 1D-QD. Under B-field the Coulomb rings vanish in agreement with the spectra observations (see Fig. 5.6). Finally, for $B < 1.25\ T$ the dissipation maxima move towards smaller V_S as B-field rises. All these observations suggest that the charging/discharging of the 1D-QD can be tuned by B.

To corroborate the effect of the B on the electron confinement we first concentrate on linear dependence of the dissipation peaks versus V_S and B as visible in figure 5.6 c). In figure 5.6 a) the Γ spectra are shown for different B-fields. A vertical offset is applied to the data for clarity. As B rises, the number of dissipation peaks is reduced ($B = 0\ T$ the split disappear) and a shift to lower energies is observed. The linear trend is clearly visible in figure 5.6 c) and it is marked by the white arrows. The high intensity contrast marked by arrows corresponds to the dissipation peaks visible in figure 5.4. The intensity map for tip-sample distance $d = 150\ nm$ is shown in figure 5.6 c). Another B map was recorded at $d = 400\ nm$ and is presented in Sup. Mat. S5:4. In both cases linear dependence of B is observed, however for larger distances the linear trend appears at larger sample voltages. A tight-binding calculation was performed by Ali Koshravi from SISSA and is presented in Sup. Mat. S5:3. The tight-binding calculations suggests the presence of 75 nm scale structures.

In order to qualitatively explain the dissipation versus the B dependence behaviour we used the Bohr-Sommerfeld (BS) model, where the de Broglie's wave of electrons moving inside the potential well is reflected from the 1D-QD walls interface with an additional magnetically induced shift in the phase. The quantization condition allowed us to calculate the energy of the n-th state and thus C_Q and finally to reproduce the Δf, as shown in figure 5.7 (red curves). The BS phase accumulation model is written as follow [141–143]:

$$2 \cdot k_v \cdot W + \Phi_B = 2\pi n \tag{5.7}$$

where Φ_B is the Peierls phase [144, 145] and k_v the wave-vector. For $B = 0\ T$, we assumed that the wave-function leakage is negligible (infinity rigid quantum well assumption).

The Peierls phase is a line integral of the vector potential $\overrightarrow{A}$ from m to n site of the

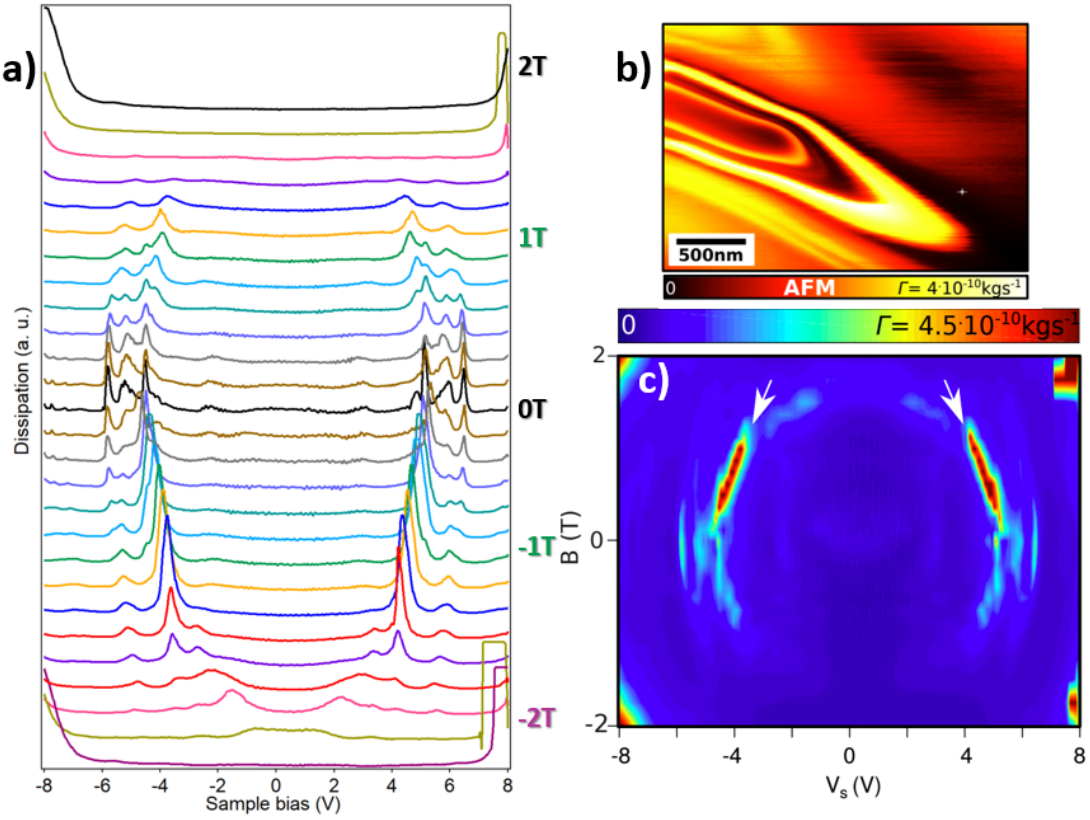

Figure 5.6: — *Energy dissipation as a function of B in the range of $-2\ T \leq B \leq 2\ T$ on the suspended graphene membranes at $d = 150\ nm$.* ***a)*** *dissipation spectra for different magnetic field with a step field $\Delta B = 0.25\ T$, the offset is applied for visualization. As B rises, the amount of dissipation features is reduced and a linear shift towards small tip-sample voltage is observed.* ***b)*** *constant height ($d = 50\ nm$) and constant bias ($V_S = -7.8\ V$) AFM dissipation image of the 1D-QD. It shows Coulomb rings-like features with an elliptical shape oriented in the same direction as the 1D-QD (Fig. 5.3 e)). The spatial extension of the Coulomb rings radii is due to the large tip-sample separation.* ***c)*** *Γ is the intensity map versus V_S and B. The bright features marked by arrows correspond to the high dissipation features shown in figure 5.4 b).*

graphene lattice and is essentially equal to magnetic flux quanta:

$$\Phi_B = \frac{e}{h} \oint_m^n \overrightarrow{A} \cdot d\overrightarrow{l} = \frac{e}{h} \int \overrightarrow{B} \cdot d\overrightarrow{S} \tag{5.8}$$

where $S = L_x \cdot L_y \cdot cos(\Theta)$ is the effective area of the 1D-QD and Θ the 1D-QD curvature. In our simulations we fixed the values $L_x = 2.2\ nm$ and the 1D-QD length $L_y = 75\ nm$ which was the only free parameter in the fitting. It can be noted that these values are much smaller than the membrane size ($R_{membrane} = 3.25\ \mu m$). Thus, the Φ_B depends solely on B and its values are shown in the right hand side in figure 5.8.

Moreover, the linear shift of the dissipation peaks under B is explained by the linear

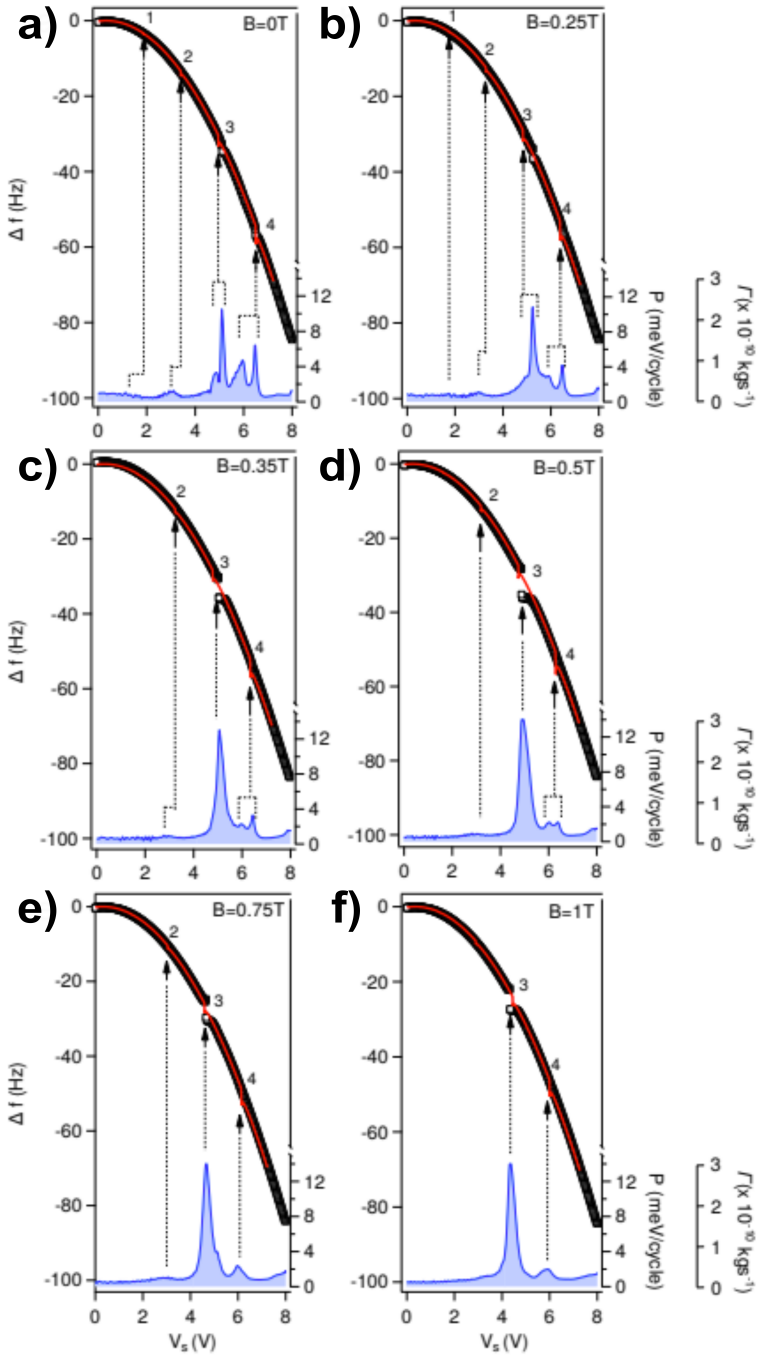

Figure 5.7: — *Voltage dependent frequency shift and dissipation spectra at* $d = 150\ nm$ *and under different* B *in the range of* $0\ T \leq B \leq 1\ T$. ***a) - f)*** *experimental* Δf *parabola in black with the fit to data in red. The* Δf *shows singularities marked by arrows at the biases when the single electron charging event occur in the 1D-QD graphene. Every* Δf *discontinuity is accompanied by rise of dissipation signal as shown in the bottom blue colour curves. For* B *in the range of* $B \leq 0.5\ T$ *the splitting of n=3 and n=4 dissipation peaks are visible. The splitting vanishes when larger magnetic fields are applied.*

dispersion relation of graphene: $E = \hbar k v_F$ and gives V_S equal to:

$$V_S = \frac{\hbar v_F}{2e\alpha}\left(\frac{2n\pi}{\sqrt{L_x^2 + L_y^2}} - BLcos(\Theta)\right) \tag{5.9}$$

the linearity of the function with B field is in excellent agreement with the experiment (see Fig. 5.6 c)). The linear shift does not depend on L_x but on the curvature angle Θ [145].

The curvature significantly changes the DOS [145], we can thus speculate that the splitting of the dissipation peaks (n = 3, 4 in figure) observed for small B might be due to wrinkle-like formation or the presence of surface distortion as visible in figure 5.3. Unlike square and triangular lattices, graphene honeycomb lattice in spanned by two different sets of triangular Bravai's lattices A and B. The presence of curvature and the associated lattice distortion breaks the spatial symmetry and leads to different degree of localization of the wave-functions on both A and B sublattices leading to the visible energy dissipation splitting for $B < 0.5\ T$ in figure 5.7. However, the wave-functions between A and B sublattices still have a strong overlap [145] and applying

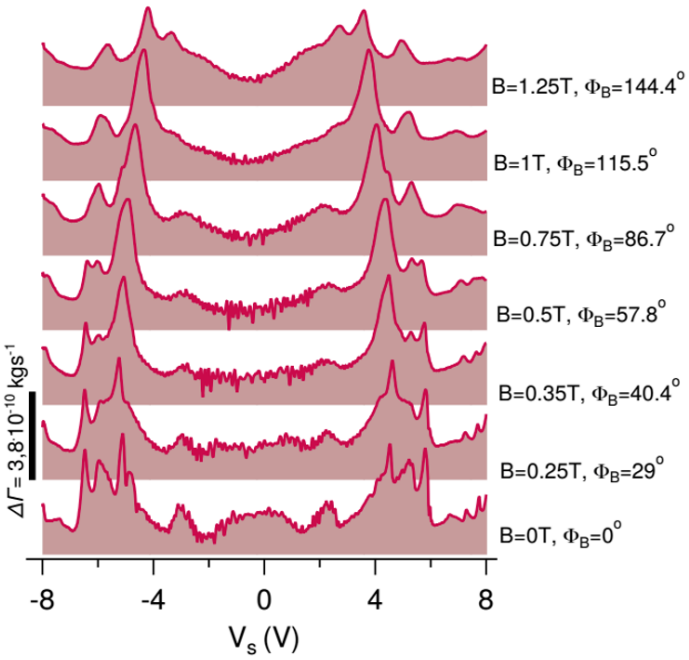

Figure 5.8: — *Energy dissipation versus bias voltage under B in the range of $0\ T \leq B \leq 1.25\ T$. The tip is at constant distance ($d = 150\ nm$). The bottom curve with the well pronounced dissipation peaks is for $B = 0\ T$. A constant vertical shift is applied to the curves for visibility and the scale bar length is $\Delta\Gamma = 3.6 \cdot 10^{-10} kg.s^{-1}$. The B and the corresponding Φ_B are given on the right side of every spectrum. As the B rises, the amount of dissipation features is reduced and the linear shift towards small tip-sample voltages is observed. The effect is better visible on the maps of figure 5.6 c). For better visibility of the dissipation logarithmic scale has been applied to every spectrum.*

a perpendicular $B > 0.5\ T$ brings together neighbouring electronic states of A and B sublattices and thus leads to observed lack of energy splitting at those B.

The last observable features on the B map are the vanishing of the dissipation peaks at large B ($B > 0.5\ T$). This vanishing is related to the lateral confinement by the 1D-QD that suggests a competition between the finite size of the 1D-QD confinement and the magnetic quantization. Indeed, when the magnetic length $l_B = \sqrt{\frac{\hbar}{eB}}$ becomes comparable to L_x it can be expected to enter magnetic quantization regime with the Landau function entirely residing on the 1D-QD. For $L_x = 2\ nm$ 1D-QD that would imply a critical B two orders of magnitude larger than that used in our experiment ($B_c \approx 150\ T$). Thus, it is reasonable to claim that B of about $B = 1\ T$ is too weak to close the Landau orbits and to enter magnetic quantization regime as it was reported for the case of nanoribbons [145]. On the other hand, in nanometric sized graphene QD realized by electrostatic gating the continuous transition from spatial to magnetic confinement was observed with a clear emergence of highly degenerated Landau levels for the critical B_c equal to $B_c \approx 0.6\ T$ [124]. Our results suggest that in the 1D-QD graphene the quasi-1D character and the charge confinement is destroyed due to the softening of the potential well by the external B.

As a last remark before closing the discussion about B dependence, we noticed that to reproduce the experimental results by tight-binding calculations, the effective size of the graphene flake is larger and equal to 75 nm. Sizes of L_x and L_y must satisfy a ratio of 8 between them (see Supp. Mat. S5:3) in order to reproduce linear shift of the dissipation peaks versus B field. Thus, we concluded that the magnetic response is rather due to domain boundaries present in CVD graphene than the tip-induced deformations. According to tight-binding calculations only the presence of larger graphene structures allows for the graphene magnetic response - here it is most probably L_y. The presence of the electrostatic gating and the interaction between induced E- and B- fields is yet to be studied.

5.4 Coulomb Rings

Figure 5.9 shows constant height ($d = 50\ nm$) dissipation image resembling the well known Coulomb rings (CR) - structures characteristic for single electron charging phenomena upon tip gating of the underlying quantum entity [100,140]. The elliptic shape of the dissipation might suggests the existence of two length scales - short and long across and along the 1D-QD, respectively. The existence of two length scales was recently confirmed in graphene nano-ribbons, where not only the width, but also the length can give confinement [146]. AFM detection of CR depends on the tip sample distance and thus capacitance and thus the lever arm $\alpha = \frac{C_{TIP}}{C_{TIP}+C_{SUB}} < 1$. The large d and $\alpha < 1$ causes significant spacial extension of the rings.

The B dependence of the CR is shown in figure 5.9 for B spanning from $B = 0\ T$ to $B = 2\ T$ and steps of $\Delta B = 0.25\ T$. The B images are showing that the interpreted vanishing of the peak might rather be related to a shift of the ring center induced

by the B-field. The elliptical shape remains at each field validating the confinement across and along the 1D-QD.

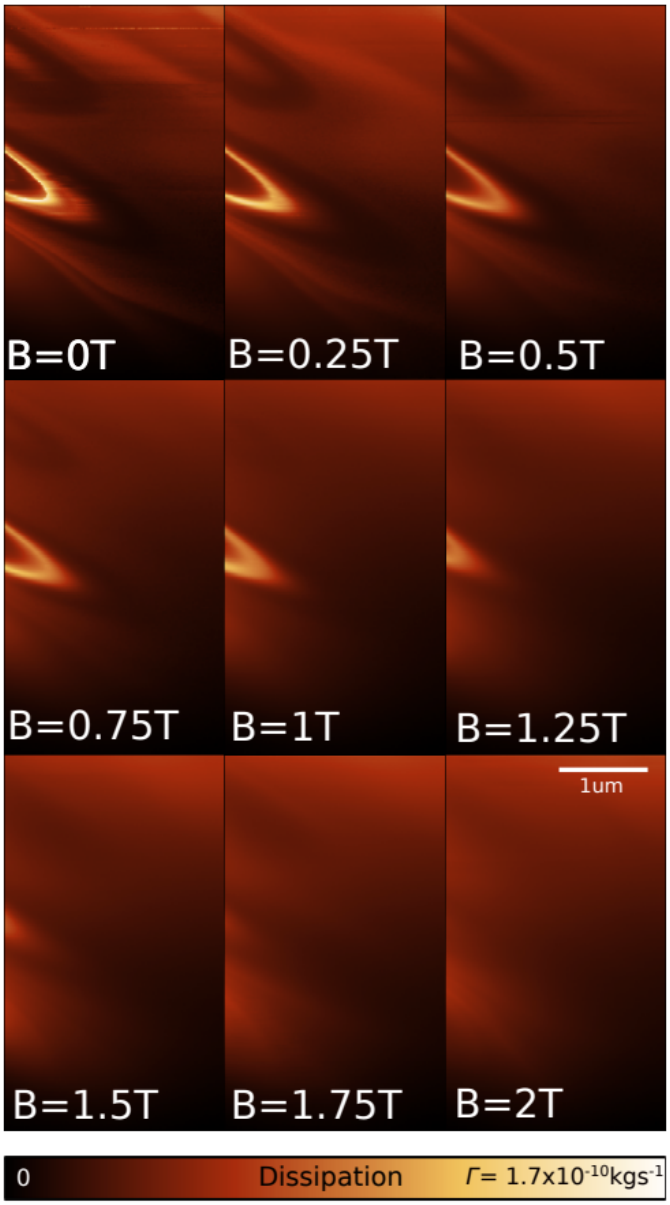

Figure 5.9: — *Constant height $d = 50$ nm and constant bias voltage $V_S = -7.8$ V AFM images. Visible CR are characteristic for single electron charging phenomena upon tip gating of the underlying quantum entity. The elliptic shape points to quasi-1D character of the nanostructure. The dissipation intensity of rings depends on the applied magnetic field and CR vanish for $B > 1.25$ T.*

5.5 Summary

Our low temperature p-AFM dissipation spectroscopy experiments on free-standing graphene 1D-QD showed multiple mechanical dissipation features. The detailed analysis showed that force and dissipation are sensitive to quantum capacitance C_Q of quasi-one-dimensional graphene, in particular to the presence of van Hove singularities. We attributed the existence of dissipation peaks to occupy/deoccupy of the electronic states via single electron tunnelling mechanism. We found that dissipation is highly sensitive to the external B. At moderate B the wave-function acquires an additional Peierls phase that shifts the confined states to the lower energies. As expected for linear dispersion relation of graphene, the electronic states and corresponding dissipation peaks dependence on B is linear. Finally, we have demonstrated that quantum effects leave clear hallmark in energy dissipation spectroscopy performed by p-AFM.

6

Magic-Angle Twisted Bilayer Graphene

Twisted bilayer graphene at the magic angle twist (MATBG, with a twist angle of $\theta \approx 1.08°$) or twisted bilayer graphene (TBG) has gained a lot of interest in the twistronic physics. Indeed, that angle twist leads to formation of flat energy bands close to the Fermi level [147] and allows the investigation of exotic quantum phases such as superconductivity [31,38,39,148], ferromagnetism [36,37], super-lattice induced correlated insulating states (SIS) [**?**,31,38,40] and Mott-insulators phase transition [31,38,40,149]. The recent advances in fabricating such devices enabled to obtain high quality MATBG, that revealed interesting features such as van Hove singularities [150], Hofstadter butterfly spectrum [37] or spin-orbit coupling [151].

When two layers of graphene are stacked on top of each other, a superlattice structure is created, called Moiré pattern inducing a mini-Brillouin zone (mBZ). This mBZ modulates the electronic properties of the sample and can be filled with four electrons. The density to fill one Moiré unit cell is noted $\pm n_s$, when the carrier density (n) is equal to n_s, the mBZ is filled. The other filling with holes/electrons ($\pm 1/4$, $\pm 2/4$ and $\pm 3/4$) defines the filling factors (FF) and indicate the filling status of the mBZ. Conductance measurements showed that every FF has a signature in the spectra. Indeed, they are represented as a drop of the conductance [31, 39, 152] and as peaks in the resistance [31, 40, 153, 154] curves. However, such measurements require very clean samples due to their detection method that average over the total device. SPM on the other hand, allows the investigation of local surface spots and thus the angle distribution doesn't need to be as homogeneous in order to detect interesting features in the spectroscopy or imaging experiments.

Recent capacitance measurement experiment revealed that half filling (2/4 electrons in the mBZ also noted $n_s/2$) is characterized by a drop in capacitance and represented as a peak in the energy loss [40, 155]. Here, we measure the dissipation and the force (Δf) on a TBG. Strikingly, in the present non-contact realization, this is done without the tip touching the sample and oscillating at the extremely low frequency of 13 kHz. Moreover, SIS are detected above an encapsulated device, therefore the tip

literally does couple to the existing subsurface phenomena. The measurements reveal the presence of enhanced dissipation for 1/2, also for ±1/4, ±3/4 and 4/4.

In this chapter, we report on low temperature p-AFM measurements on TBG to detect the series of super-lattice induced insulating states in TBG by purely mechanical means. A very brief introduction of the twisted bilayer graphene band structure and magic angle physics is given based on reference [156].

It is known that the superlattice density n_s depends on the twist angle θ as following: $n_s = \frac{8\Theta^2}{\sqrt{3}a^2}$, where a is the lattice constant of graphene [31]. Since the electronic properties of TBG are extremely sensitive to the homogeneity of the twist angle the cautious control of the stacking process is crucial [157]. Owing to the local character of the measurement, the sharp tip of p-AFM is able to confirm high quality of TBG devices and to determine a narrow twist angle distribution over micrometer distances equal to $\Delta\Theta = 1.06° \pm 3$ %. The dissipation spectra and the constant height dissipation images were acquired, showing the existence of few hundred nanometer domains of different local doping, which is confirmed by a spacial variation of charge neutrality point (CNP).

Application of magnetic fields leads to strong oscillation of the energy dissipation signal which is enhanced for fractional 3/4 band filling. The magnetic field induced oscillations appear at different B-fields and show few B-field periodicities. We discriminate two types of magneto-oscillations. The oscillations observed at larger magnetic fields with small periodicity are identified as originating from quantum interference effects occurring at boundaries between domains of different doping. The phenomena is commonly known as Aharonov-Bohm effect. The observed oscillations with larger periodicity, localized near zero B-field are consistent with recent SQUID on tip measurements, which supports the presence of orbital magnetism reported recently in TBG devices at 3/4 band filling [158, 159].

6.1 Twisted Bilayer Graphene

2D materials have very interesting properties and we saw that these properties can be drastically different from the bulk materials and that's the reason why they attract a lot of attention since two decades. Moreover, their properties can be tuned even further when they are stacked on top of each other, where proximity effects can be induced from one layer to another [151]. More interesting properties arise when those layers are stacked and twisted. The properties of the twisted materials can significantly modify the band structure and the electronic interactions at low energies. When two 2D materials are stacked and twisted on top of each other, a visual long-range modulation of the atom density is visible. This superstructure is called Moiré pattern. It originates from the spatial interference of two periodic lattices that are misaligned. The apparent Moiré pattern is determined by the shortest wavevectors that connects the reciprocal vectors of the different layers. In the reciprocal space, the two reciprocal lattices or Brillouin zones (BZ) are rotated by the same angle θ with respect to the origin (see Fig. 6.1). The difference between the BZ of the two layers induces a mBZ that can be

carried out of the six corners of the BZ as shown in figure 6.4. The mBZ has a reduced momentum and consists of multiples states at different energies also referred to mini bands.

The TBG physics is controlled by the ratio between the interlayer hopping amplitude noted w and the energy at which the Dirac cones from the two layers intersect and is noted as ζ:

$$\zeta = \frac{w}{\hbar v_{F0} |\overrightarrow{K}| \theta} \tag{6.1}$$

where v_{F0} is the Fermi velocity of a graphene monolayer, $|\overrightarrow{K}|$ the momentum at the K points and θ is the twist angle. This ratio describes how strong the interlayer hopping is compared to the intrinsic Dirac nature of the bands. Small ζ represents large θ ($w << \hbar v_{F0} |\overrightarrow{K}| \theta$), meaning that the Dirac cones are far apart in the momentum space to affect their low energy dispersion states. Big ζ represents small θ, at those twist angles a dramatic drop of the Fermi velocity is observed. It is the result of the interlayer hybridization and the Fermi velocity can be written as follows:

$$v_F = v_{F0}(1 - 9\zeta^2) \tag{6.2}$$

For some values of α, the Fermi velocity of the twisted system in the mBZ corners K_s and K'_s drops to zero. The corresponding angles are the so-called magic angles. The first magic angle is related to $\alpha = 1/3$ and equal to a twist angle $\theta = 1.08°$. The states at those magic angles are close to zero energy and result in the flattening of the entire bands in a window of few meV. These bands are fourfold degenerated, two valleys and two spins. The total density needed to fill them is equal to four times the mBZ area, also equivalent to four electrons per Moiré unit cells: $n_s = 4/A_m$, where

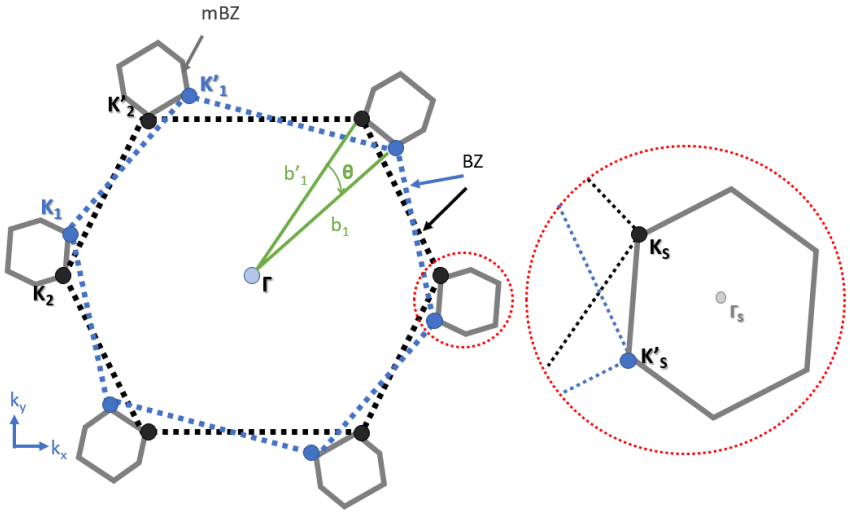

Figure 6.1: — *Illustration of the reciprocal space, where the original BZ of the two graphene layers (in blue and black) are twisted on top of each other and the mBZ is shown in gray. The inset is a zoom in of the mBZ showing the different K corners.*

$A_m = \frac{\sqrt{3}}{2}/(\frac{a}{\theta})^2$. That leads to the density to fill the mBZ n_s equal to:

$$n_s = \frac{8\theta^2}{\sqrt{2}a^2} \tag{6.3}$$

where $a = 0.246\ nm$ is the graphene lattice constant.

6.2 Sample Geometry

The sample consists of a p-doped silicon substrate used as a backgate where a 300 nm layer of silicon dioxide (SiO_2) and a 10 nm thick hBN layer has been deposited on top of it, both serve as an insulating barrier. On top of that resides the TBG that is protected from top by 10 nm thick hexagonal boron nitride (hBN) layer, see figure 6.2. The sample is shaped as a rectangle surrounded by eight gold wires. The inset of figure 6.2 shows the p-AFM topography image where the entire device is visible. For the measurements, two wires were contacted and kept grounded (marked with the orange arrows).

The equivalent capacitance model of the system is presented schematically in figure 6.2 left bottom. The system can be described by different capacitances and the resistance, which represents the dissipative part.

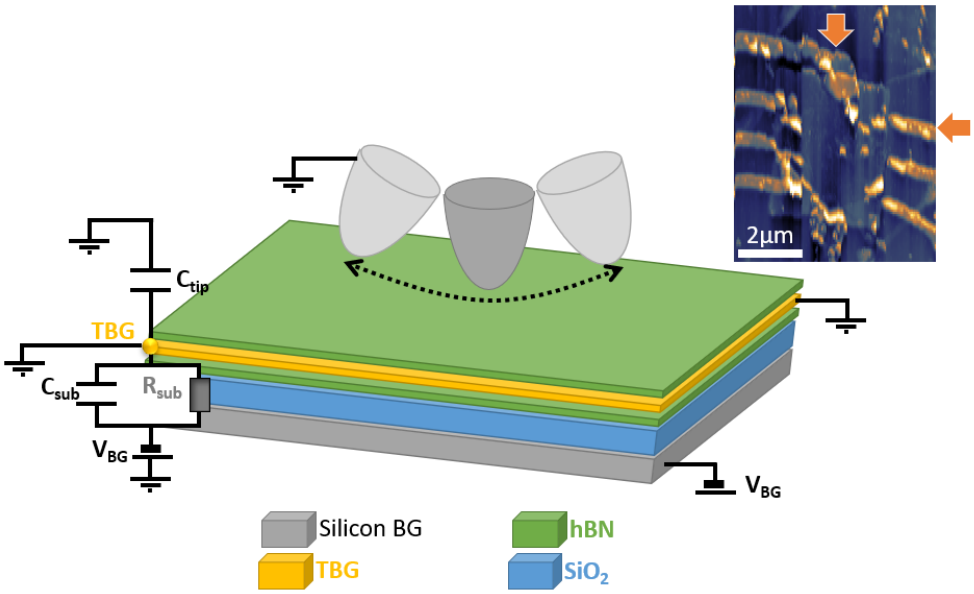

Figure 6.2: — *Schematic of the sample side view and capacitance circuit. The inset is a p-AFM image of the sample surface. The orange arrows points out the gold contacted wires.*

6.3 Dissipation Measurements

The cantilever is oscillating with a fixed amplitude of $A_{exc} = 1\ nm$, at a fixed tip-sample distance $d = 150\ nm$, while a backgate voltage is applied to the silicon substrate. The cantilever and the graphene are both grounded, see figure 6.2 d. The frequency shift (Δf) as well as the energy dissipation (Γ) of the cantilever are monitored using the PLL (see Chap. 2).

To investigate the energy loss mechanisms, we performed dissipation and force spectroscopy measurements over the grounded area, to reduce any electrostatic effects that could induce artefacts in the measurements. The backgate voltage (V_{BG}) was swept from $-50\ V < V_{BG} < 60\ V$ and simultaneously recording the Γ and the Δf spectra. The typical p-AFM voltage-dependent spectrum is presented in figure 6.3. The Δf exhibits a double parabolic dependence due to different capacitive coupling between the silicon substrate and the TBG and is presented in Sup. Mat. S6:1. The first parabola describes the silicon backgate and the second parabola describes the TBG. The later one has a CPD shift of $V_{CPD} \approx 8\ V$ and is attributed to scattering due to disorder. The corresponding disorder density can be calculated using this shift and it is equal to $n_D = 5 \times 10^9\ cm^{-2}$. That value corresponds well to already reported results by Cao *et. al.* [31]. In addition to that, few singularities are visible at various V_{BG}. The kinks in frequency spectrum are followed by very sharp dissipation peaks, as shown in the inset.

The p-AFM tip oscillating at hundred nanometer distance from the TBG device is coupled capacitively to the underlying TBG and is sensitive to the series of SIS in both electron and hole doped regions. SIS are detected via mechanical energy loss of the cantilever sensor. Owing to large tip-sample distance, the dominant dissipation mechanism is Joule dissipation (see Chap. 3) which is linked to the creation of local, displacement currents by an oscillating tip and reads as follows (see Sup. Mat. S3:1):

$$P = \frac{1}{2} R A^2 \omega^2 (\Delta\phi)^2 (\frac{\partial C}{\partial z})^2 \tag{6.4}$$

where A, ω are the cantilever oscillation amplitude and frequency, respectively. $\Delta\phi$ is defined by tip and sample potential and is equal to the difference of their work functions. Joule dissipation consists of two dissipation channels: resistive (R) and capacitive $\frac{\partial C}{\partial z}$. Therefore, the observed series of SIS are due to both, the rise of sample resistivity in the current path and an abrupt change of system capacitance, which involves quantum capacitance (C_Q) of TBG. The resistive part produces wide and less pronounced dissipation peaks as observed for $n_s/4$ and $n_s/2$ band filling, whereas the capacitance change leads to creation of much sharper spikes ($3n_s/4$ and n_s). It does so, due to charge injection into flat energy bands, or else, due to the presence of van Hove singularities in the electronic density of states. The crossing of Fermi energy with van Hove singularity results in change of thermodynamic compressibility $\partial n/\partial\mu$ of TBG, which reflects the ability of TBG to absorb an amount of charge n when changing chemical potential μ. This process leads to a rapid change of quantum capacitance:

$$C_Q = Aq^2 \cdot \partial n/\partial\mu \tag{6.5}$$

where q is the elementary charge, A is the lateral device area probed by the tip. The frequency shift of the cantilever signal can be approximated by (see Sup. Mat. S3:1):

$$\Delta f = \frac{\omega_0}{8\pi k}(\Delta\phi)^2 \frac{\partial^2 C}{\partial z^2} \tag{6.6}$$

where ω_0 and k are eigenfrequency and stiffness of the cantilever.

Since Δf solely depends on system capacitance (while other parameters are fixed) the charge injection into the flat energy bands results in Δf change, as observed for $3n_s/4$ and n_s band filling (see inset Fig. 6.3 and Sup. Mat. S6:1). Particularly at full filling the change of Δf is in agreement with already reported huge rise of thermodynamic compressibility [160].

The dissipation curves exhibit a series of peaks that are symmetric with respect to the TBG CPD. It is worth to mention that the presented data were corrected with respect to raw data in order to account for creation of depletion region for the hole side. The original data showed broadening of the negative voltage side as compared to electron side. The depletion capacitance correction is described more in detailed in Sup. Mat. S6:2. Indeed, the system can be described as a MOS transistor with a metal - oxide - semiconductor structure. In the accumulation phase, the capacitance behaves like a plate capacitor $C_i = \epsilon_i/d$, where ϵ_i is the permittivity of the considered material and d its thickness. When a positive backgate voltage is applied the holes (majority charges) are accumulated in the p-doped silicon layer and TBG is doped

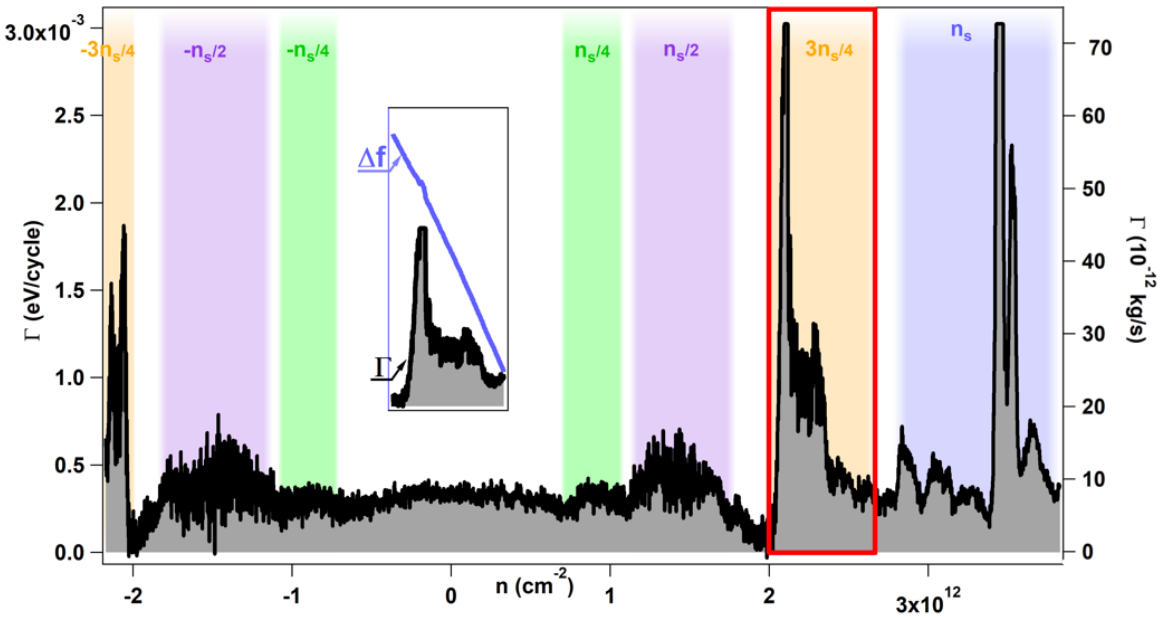

Figure 6.3: — *Dissipation spectrum taken on TBG, where all different FF are identified and coloured in green, violet, orange and blue for $n_s/4$, $n_s/2$, $3n_s/4$ and n_s, respectively. The backgate voltage was converted to charge density n. The inset shows the corresponding Δf spectrum where a tiny drop is visible at the corresponding dissipation peak.*

with electrons. Conversely, when the voltage becomes negative, the holes are sucked out from the backgate region which create a depletion region that induces the drop of the total capacitance value C. The p-AFM system can be schematized using a capacitance circuit as presented in figure 6.2 d, hence the depletion can be corrected by adding a depletion capacitance in the model that allows to symmetrize the data and obtain the correct position of the dissipation peaks (see Sup. Mat. S6:2). The peaks were analysed by converting the backgate voltage into doping using the relation: $n = \frac{C_{ox} \cdot V_{BG}}{q}$, where $C_{ox} = \epsilon_0 \epsilon / t_{SiO_2}$ is the SiO_2 oxide capacitance and ϵ_0 is the vacuum permittivity, ϵ is SiO_2 permittivity and $t_{SiO_2} = 300\ nm$ the thickness of the oxide layer and q the electron charge. Figure 6.3 shows the corrected data with the identification of the peaks. Indeed, the position of the peaks exactly corresponds to the different FF where $n_s = 2.83 \times 10^{12}\ cm^{-2}$ is the position of full filling peak. This value was used to calculate the corresponding twist angle using equation 6.3. We determined the twist angle equal to $\theta = 1.10°$. This is slightly above the magic angle, nevertheless small enough to have flat bands.

6.4 Angle Distribution

Due to the local character of the method, it is perfectly suited to determine the twist angle at different sample positions over the large area of TBG. Other techniques already reported the presence of angle domains related to relaxation that occurs in TBG after twisting [154]. The p-AFM is able to resolve and investigate the angle distribution over the surface by performing dissipation measurements at different positions on the device. 55 subsequent dissipation spectra were acquired along the $1\mu m$ long red line and for each spectrum both the twist angle θ and CPD shift from charge neutrality point were determined. Figure 6.4 a) is a topography image of the device taken at $T = 5\ K$. The black crosses mark the positions of different measurements points (the distance between them is $\Delta d = 20\ nm$). The twist angle θ (green) and CPD (black) measured along the line profile shown in a) are presented in figure 6.4 b). It shows the evolution of the angle and the CPD along that line and reveals a very small angle variation. Although the sample indicates a good twist angle homogeneity, a presence of charge disorder leads to considerable variation of the CPD. Indeed, the CPD data set has both negative and positive values, suggesting the presence of p- and n- doped regions on the surface. Thus, the data suggest the presence of domains of different local doping, as expected for van der Waals heterostructures supported on SiO_2 substrates [161]. A weak cross correlation (10 %) as a function of displacement was noticed between θ and CPD values, meaning both observables are not inherently linked. Figure 6.4 c) is the histogram of the angle distribution measured on the TBG sample. The present red dotted line is a Gaussian fit that reveals an average angle equal to $\theta = 1.06°$ with an angle distribution of 3 % with respect to the average value indicating a decent twist angle homogeneity.

To investigate those domains further, Γ and Δf constant height images were acquired simultaneously at the place shown in figure 6.4 a). The tip was positioned at a distance $d = 150\ nm$ away from the sample surface and different V_{BG} was applied to the sample

corresponding to different FF, $V_{BG} = 24\ V$ and $V_{BG} = 31.4\ V$ for $n_s/4$ and $n_s/2$ respectively. Thus, the contrast is solely due from the position change of the Γ peak due to local variation of θ and the CPD value. Since the twist angle is homogeneous in the sample, the majority of the contrast originates from the CPD shift. Both maps, presented in figure 6.5, shows the corresponding dissipation and force for $n_s/4$ and $n_s/2$ fillings. The maps revealed the presence of domains marked with white dotted lines in figure 6.5 a) with sizes of few hundred nanometers, well visible on Δf (Fig. 6.5 c) and d)). In addition to the domains, circular features are also present in the Γ maps already reported in AFM measurements [100, 102, 103] and known as Coulomb blockade (CB) (black arrows in Fig. 6.5 a)). Indeed, local probe measurements of single electron charging is visible as spatially extended Coulomb rings separating the different charge states of the quantum-dot-like entity. It is not clear whether the source of CB could be a point defect in graphene or hBN. It could also be an imperfection introduced into TBG during stacking process. It was demonstrated that out of plane deformed graphene might behave as an effective quantum dot [140]. No significant change of contrast of hundred nanometers domains was observed between images taken

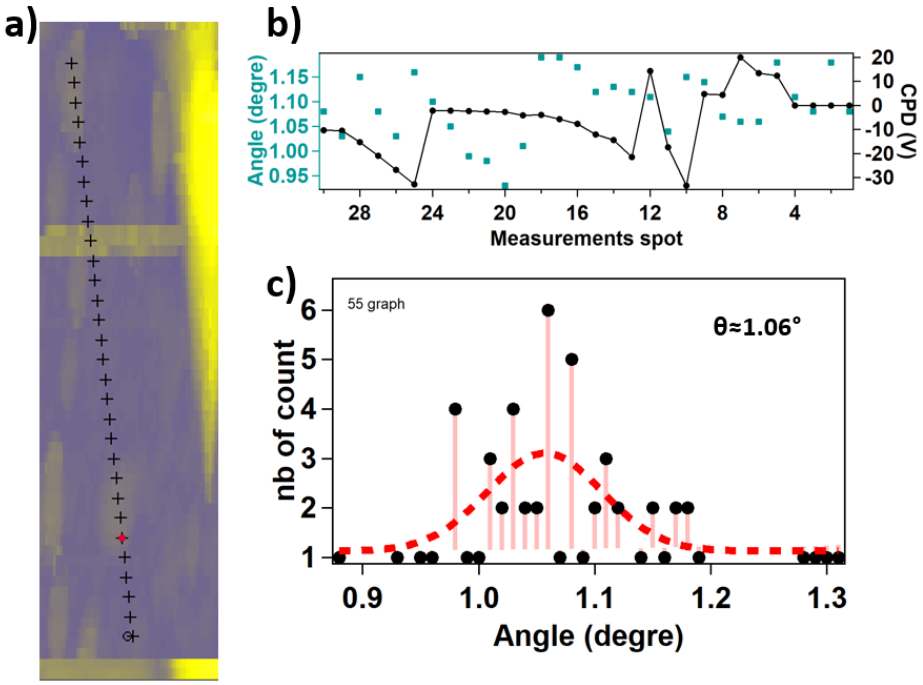

Figure 6.4: — *Twist angle distribution.* ***a)*** *p-AFM topography image of the sample at $T = 5\ K$. The dimensions of the image are 200 $nm \times 1\ \mu m$. The black crosses show different measurement positions with a distance of 20 nm between them.* ***b)*** *corresponding line profile data. In blue the twist angles at different places are shown and in black points show the CPD variation which depends on local doping of TBG.* ***c)*** *histogram over 55 measurement points, were the number of counts is plot versus the twist angle found over the device. The red dotted line is the Gaussian fit used to determine the angle distribution.*

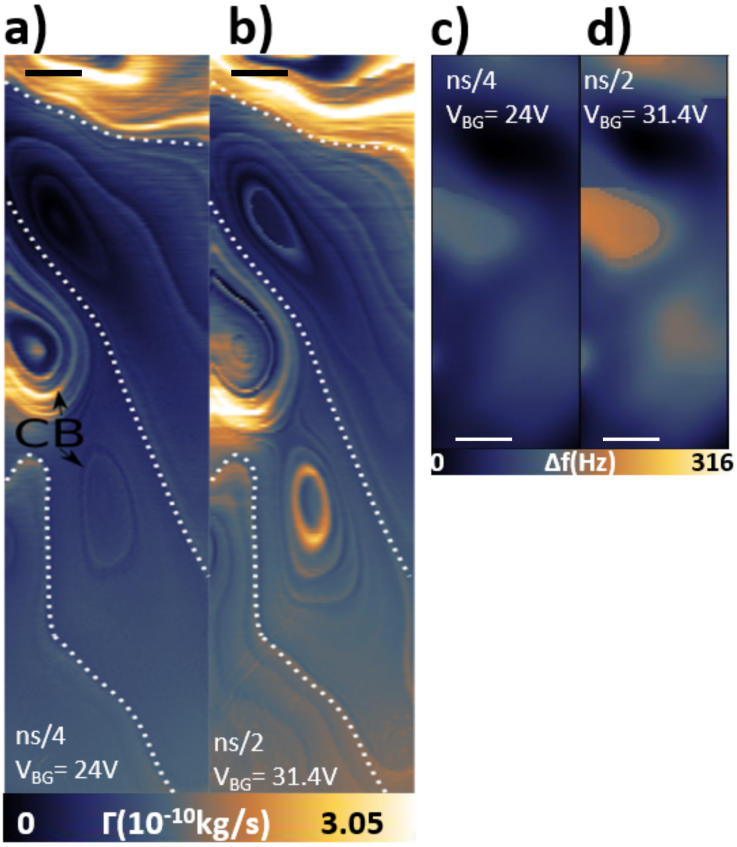

Figure 6.5: — *Constant high p-AFM images taken at the same position as in figure 6.4 a) at a* $d = 150\ nm$. ***a)*** Γ *map over the sample surface of* $n_s/4$ *filling taken at a* $V_{BG} = 24\ V$. *The white dashed lines are highlighting the different domains and the black arrows point to Coulomb rings.* ***b)*** Γ *map over the sample surface for* $n_s/2$ *filling taken at a* $V_{BG} = 31.4\ V$. ***c)*** *and* ***d)*** *corresponding* Δf *constant height images taken for* $n_s/4$ *and* $n_s/2$, *respectively. The scale bars are* 50 nm.

at different V_{BG}, whereas CB rings show strong voltage dependence, which suggests different origins of both features.

6.5 Magnetic Field

Next, we applied an external magnetic field in direction perpendicular to the sample surface. Figures 6.6 a) - b) and 6.6 c)-d) are constant height Γ images for $n_s/2$ and $n_s = 3/4$, respectively. The images were taken at different sample spots as compared to figure 6.5. While images in figure 6.6 a) and c) show the data for $B = 0\ T$, the data in 6.6 b) and d) are taken with applied external B-field equal to $B = 2\ T$. All data show the presence of hundred nanometers sized domains that are highlighted with white dashed lines. Furthermore, we noticed that the domain contrast, especially for $3n_s/4$ filling, is enhanced under application of B-fields (see Fig. 6.6 c) and d)). The Γ intensity map with few superimposed dissipation spectra versus charge density n and

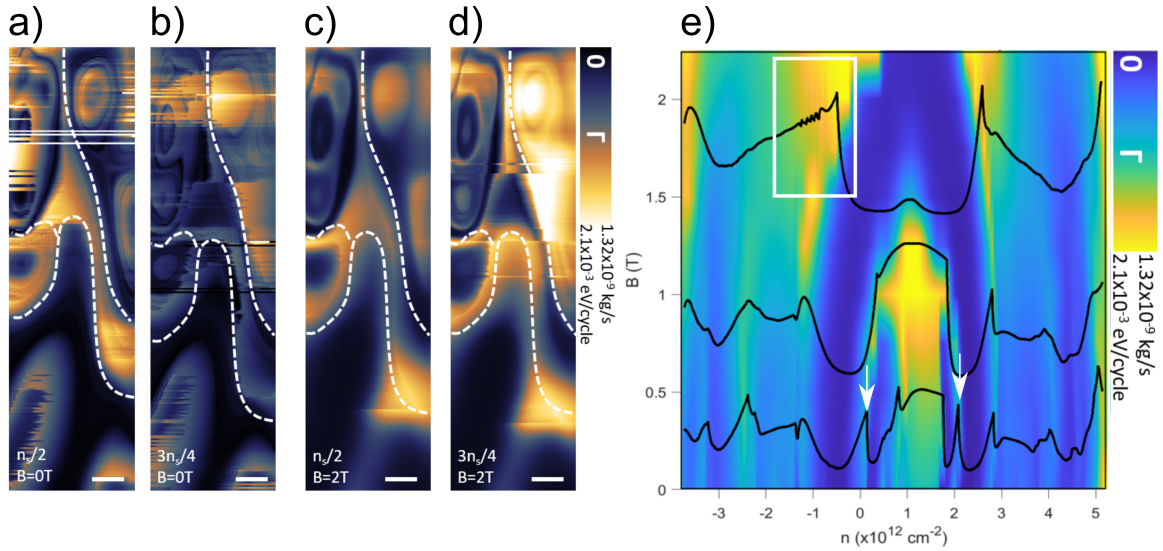

Figure 6.6: — *Constant height ($d = 150\ nm$) dissipation images and spectra versus n and B-field while the TBG was kept grounded.* ***a)*** *to* ***b)*** *Γ contrast for different FF, $n_s/2$ and $3n_s/4$ respectively under different B conditions.* ***a)*** *and* ***c)*** *are without B-field and* ***b)*** *and* ***d)*** *are with an external B-field of $B = 2\ T$ applied perpendicular to the sample surface. Hundred nanometer size domains are visible and marked with dashed lines. Slight rise of Γ intensity was noticed under B application. The scale bar is 50 nm.* ***e)*** *Γ intensity map and spectra (black curves) are shown versus n and B-field. The white arrows point out satellite peaks surrounding the CNP. The application of an external B-field about $B \approx 1.5\ T$ leads to the emergence of magneto-oscillations (white rectangle).*

B-field is plotted in figure 6.6 e) and also shows increase of Γ versus B_{ext}-field. The observed enhancement of dissipation contrast at CNP for $B = 1\ T$ is presumably due to increased electron-hole scattering when an external B-field drives charges in the opposite direction. At charge densities $n_s/2 < n < 3n_s/4$ and for non-zero B-field we observed the oscillations in Γ signal (marked with white rectangle in Fig. 6.6 e)), which we further analysed in details, yet before we discuss it, we would make an important comment about dissipation behaviour versus B-field.

Until now, we reported on the measurements with the grounded cantilever positioned over the grounded TBG device. In the presence of small electric field in order of $mV/\mu m$ applied in plane of the TBG sample, Γ contrast evolution versus B-field is different. Figures 6.7 a) and b) are the dissipation images for $n_s/2$ taken under zero B-field applied and under a B-field equal to $B = 2\ T$, respectively. This spectrum was recorded in a partially grounded area which leads to the presence of a small electric field. In contrast to the case of grounded TBG, the application of magnetic fields leads to strong Γ contrast reduction. The hundred nanometer size domains vanish, whereas we observe some remnant contrast of CB rings, which again confirms that both features are of different origin. The dissipation spectra versus V_{BG} under external B-field are shown in figure 6.7 d). Here, we point out that Γ contrast reduction versus B-field

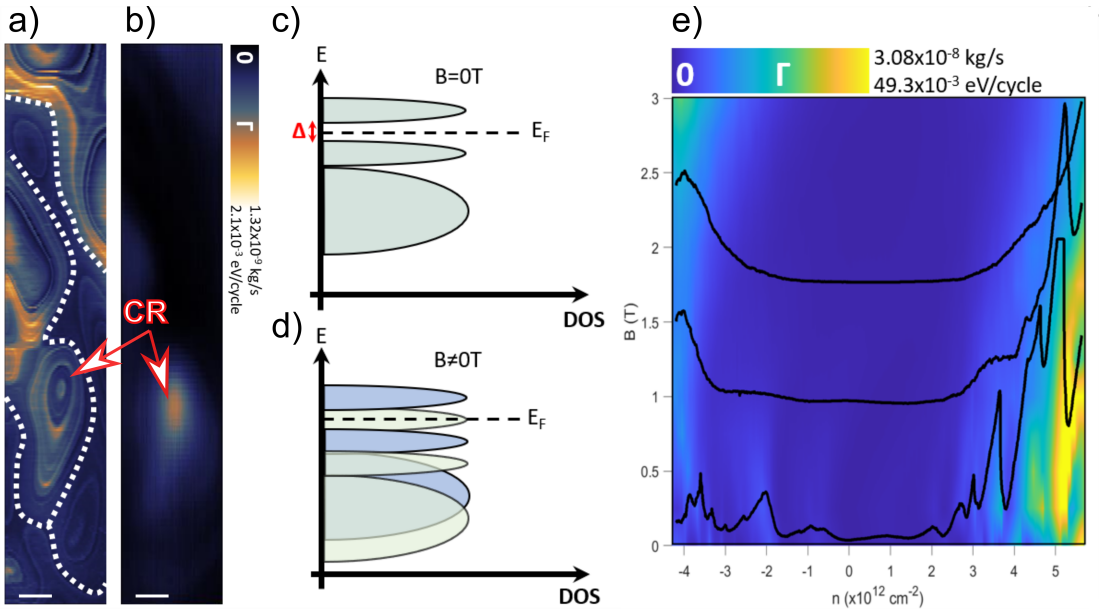

Figure 6.7: — *Constant height* ($d = 150\ nm$) *dissipation images and spectra versus* n *and* B*-field while small in-plane voltage equal fractions of* mV *was applied to the TBG device.* ***a)*** Γ *contrast for* $n_s/2$ *without external* B*-field. Hundred of nanometer size domains (white dashed lines) as well as CB features are visible (red arrows).* ***b)*** $B = 2\ T$ *dissipation image of* $n_s/2$ *filling. Although, the hundred of nanometer size domains contrast disappeared, some contrast from the CB remain. The scale bar is* $50\ nm$. ***c)*** *schematic of the possible mechanism of energy closing gap due to* B*-field induced Zeeman shift.* ***d)*** Γ *intensity map and spectra (black curves) are shown versus* n *and* B*-fields larger than* $B = 2\ T$ *leading to disappearance of the dissipation peaks.*

was observed only in the presence of small in-plane electric field applied to MATBG. The external magnetic field provides Zeeman energy $2\mu_B B \approx 0.2\ meV$ needed to at least partially close the correlated insulator energy gap, hence the vanish of dissipation peaks characteristic for different SIS and overall Γ contrast reduction (see Fig. 6.7 c) and d)).

Indeed, the charge redistribution under application of in-plane electric fields builds an electric field between the graphene layers which in turn modifies the interlayer interaction. Based on the results we concluded that in-plane polarization weakens the interlayer coupling leading to slight reduction of energy gap. Further application of relatively weak magnetic fields of the order of $B = 2\ T$ introduced Zeeman shift which fully close the energy gap and recovers a normal metal state. Cao *et. al.* [40] reported that application of B-fields of few Tesla lead to Zeeman shift of the order of few hundred of μeV that suppress the half-filling states. Our results support this scenario.

In the partially grounded area, the FF seems to be B dependent. Indeed, increasing the B-field shifts them to larger V_{BG} values. It can be noted low dissipation intensity close to CPD value. On the contrary, the dissipation map recorded in the grounded area shows large dissipation peaks in the proximity of CPD. The peaks are surrounded

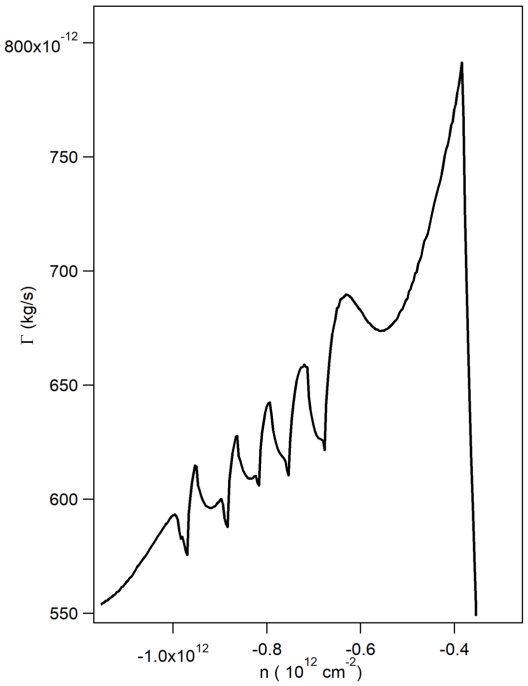

Figure 6.8: — *Zoom-in the dissipation spectra shown in figure 6.7 b) for B-field ranging from* $0.9\ T \leq B \leq 2\ T$*, where oscillation are visible for* $-3n_s/4$ *and* $-n_s/2$ *FF.*

from either side with two satellite peaks (see white arrows in Fig. 6.7 e)). In this region the FF seems to be B independent.

To conclude with this part, the Γ maps recorded in the partially grounded area showed in figures 6.5 and 6.6 without and with B-field, respectively, are in good agreement with figure 6.7 a) and explain why the domains disappear. In agreement to that on the grounded area, the Γ maps does not disappear with B as shown in the figures in Sup. Mat. S6:3.

As a last remark, interesting features under B-field are observed for the grounded area experiments. First, the CPD is surrounded by two peaks that are not $n_s/4$ (white arrows in Fig. 6.6 e)). They are often mentioned as secondary Dirac points [162] or satellite peaks [163]. Their presence is claimed to be either due to good alignment between top-graphene-bottom hBN layer or due to proximity induced spin-orbit coupling in MATBG. In our case and our sample geometry none of those conditions are valid and the presence of these peaks in not yet understood. Nevertheless, it can be noticed that as the B-field increases the dissipation also rises. At large B-field the dissipation peaks merge and approach the CPD value until they vanish completely. Interestingly the merging of those two dissipation peaks is followed by the emergence of oscillations for $\pm 3n_s/4$ and $\pm n_s/2$ FF as visible in figure 6.8.

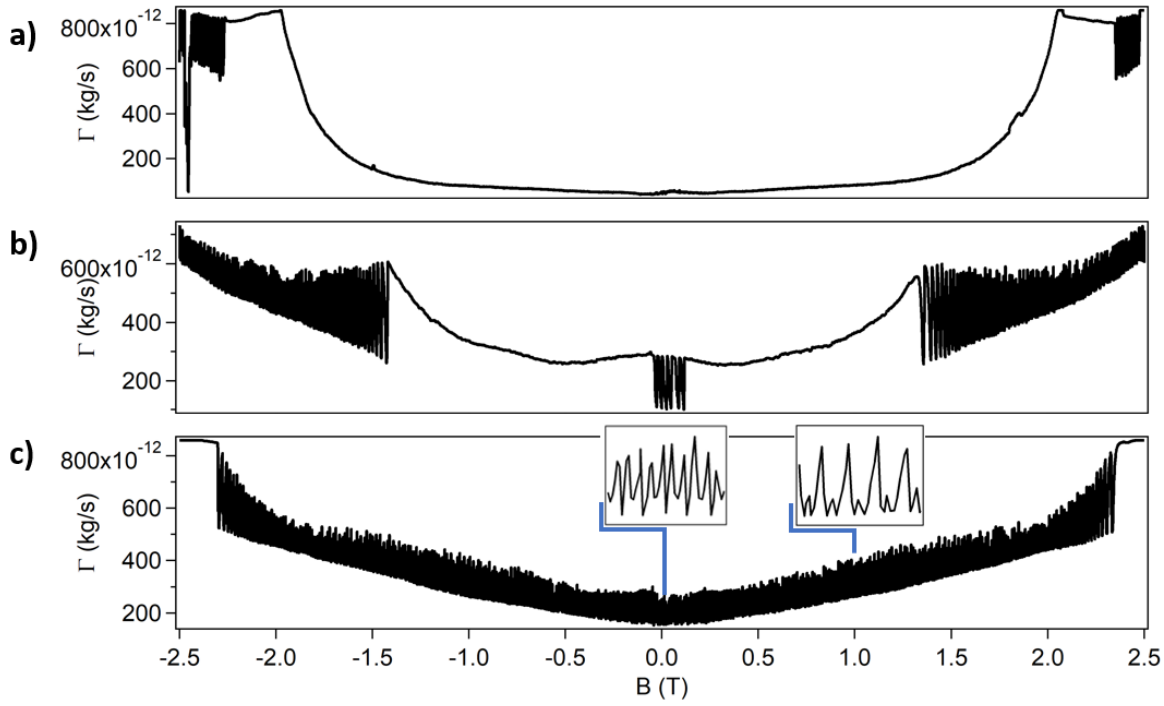

Figure 6.9: — *Dissipation spectra under magnetic sweep for different FF.* ***a)*** $n_s/2$ *FF sweep.* ***b)*** $3n_s/4$ *FF sweep.* ***c)*** $3n_s/4 \leq n \leq n_s$. *The insets represent the characteristic oscillations for large (top right) and low (top left) B sweeps.*

6.6 Quantum Magneto-Oscillations

The magneto-oscillations visible in figures 6.6 e) and 6.8, the energy dissipation of the grounded TBG was further studied under varying B-field. The tip-sample distance ($d = 150\ nm$) and V_{BG} were set constant while the B-field was swept from $-2.5\ T < B < 2.5\ T$. The sweep rate was equal to $0.007\ T/min$. The different insulating FF were investigated meaning $n_s/4$, $n_s/2$, $3n_s/4$ and n_i for $3ns_4 < n_i < n_s$.

The corresponding charge concentrations were equal to $0.9{\cdot}10^{12}\ cm^{-2}$, $1.4{\cdot}10^{12}\ cm^{-2}$, $2.1{\cdot}10^{12}\ cm^{-2}$ and $2.3{\cdot}10^{12}\ cm^{-2}$, respectively (see Fig. 6.3). The recorded dissipation Γ versus B spectra are shown in figure 6.9. Strikingly, the dissipation signal shows oscillations that are strongly enhanced for $3n_s/4$ and $3n_s/4 < n_i < n_s$. Analogous magneto-oscillations are also observed in $\Delta f(B)$ spectra and those data are shown in Sup. Mat. S6:4 as well as the $n_s/4$. Whereas $n_s/2$ spectrum shows only residual oscillations, the data for $3n_s/4$ are characterized by two different types of oscillations, namely those localized at large B-field ($B > |2T|$) and those present at low B-field ($B < |0.1T|$). Further increase of band filling to $3n_s/4 < n_i < n_s$ results in continuous magneto-oscillations all along the $\Gamma(B)$ spectrum, as shown in figure 6.9 c). The insets show at least two different periodicities at $B = 0T$ and $B = 1T$.

Next, we analysed the Fast Fourier Transformed (FFT) dissipation spectra and the FFT spectra are shown in figure 6.10 for band fillings equal to $3n_s/4$ (a) to c)) and $3n_s/4 < n_i < n_s$ (d) to e)), respectively. Both FF revealed a distribution of

periodicities as seen in figure 6.9 c) and e), with $1/B$ aperiodic character which excludes the presence of Shubnikov-de-Haas oscillations due to emergence of apparent Fermi surface as previously reported in bilayer graphene [31, 164]. Next, the FFT analysis was performed separately for low B-regions (Fig. 6.10 a) and 6.10 d) for $3n_s/4$ and $3n_s/4 < n_i < n_s$, respectively) and high B-regions (Fig. 6.10 c) and 6.10 f) for $3n_s/4$ and $3n_s/4 < n_s < n_s$, respectively). A distinction between oscillations periodicity for high (marked with green arrows) and low (marked with black arrow) B-regions is visible. At low B-regions the oscillations have periodicity $\Delta B_{low} \approx 16\ mT$ (Fig. 6.10 a)), whereas FFT spectrum taken at high B-regions and shown in figure 6.10 c) shows two peaks localized at $\Delta B_{high} \approx 5\ mT$ and $8\ mT$. A separation of high and low B-field oscillations visible in figure 6.9 b) as well as their different periodicities suggest their different origin. At $3n_s/4 < n_i < n_s$ FF (Fig. 6.10 e)-f)) similar peaks that are marked with green and black arrows are again visible. Moreover, the additional peaks appear (marked with triangles) and since their frequencies roughly match $16\ mT - 5\ mT$ and $16\ mT - 8\ mT$, those are presumably due to beat interference between oscillations present at high and low B-regions. We have to make a one remark before closing the results section. Although, $\Gamma(B)$ spectrum for $n_s/2$ filling (Fig. 6.9 a)) is in most parts smooth, a tiny oscillations are visible at $B = 0T$ and at large B-fields, which indicates that although the tip mostly senses $n_s/2$ domains underneath, a minute amount of domains with $3n_s/4$ filling is present in the tip proximity. Therefore, despite the decent twist angle homogeneity measured across micrometer distance, somewhere on the 'horizon' of the tip shadow potential must be domains of different angle twist. Hence, the effective sample area probed by the oscillating pendulum tip at $d = 150nm$ distance must be in the order of few hundred nanometers.

The magneto-oscillation experiments enables to distinguish two different types of magneto-oscillations characterized by different periodicities, with distribution falling in between $\Delta B = 5\ mT - 15\ mT$. The rise of dissipation signal (also domain contrast) observed at $3n_s/4$ FF and at high B-fields suggests that oscillations origin is related to the presence of hundred nanometer sized domains of different doping. The presence of positive and negative CPD domains leads to formation of local p-n junctions. Further application of B-fields creates a directional edge currents flowing at the junction boundaries and the quantum mechanical interference at domain boundaries leads to magneto-oscillations. Thus, the oscillations in high B-regions are originating from simple Aharonov-Bohm effect in analogy to oscillations reported in high-mobility GaAs two-dimensional electron gas [165, 166] and recently reported in graphene based quantum Hall systems [167]. The period of Ahoronov-Bohm oscillations should satisfy well the standard formula:

$$\Delta B \cdot S = \frac{h}{e} \tag{6.7}$$

where $\frac{h}{e}$ is the magnetic flux quanta and S is the surface area enclosed by circulating channels inside the graphene domain. According to the expression the periodicity $\Delta B = 10\ mT$, results in domain sizes roughly equal to $S = 600\ nm$, which is in agreement with observed domains by p-AFM. The decreasing oscillation amplitude with increasing magnetic field (Fig. 6.9 b)) indicates the vanishing coupling between

edge states as they move further apart from each other at higher magnetic fields.

We will make one remark before closing. Larger periodicity $\Delta B = 15\ mT$ oscillations present at very narrow B-field window near zero ($-100\ mT < B < 100\ mT$) are consistent with recent SQUID on tip measurements [158, 159] which reported the emergence of orbital magnetism in TBG devices at 3/4 band filling. p-AFM data are in agreement with the measured width of the hysteresis loop of Hall resistance, which has been found to be slightly below $\pm 100\ mT$ (see Fig. 1A in [158]), as well as with the evolution of the coercive field versus n (see Fig. 2C therein). According to Tschirhart

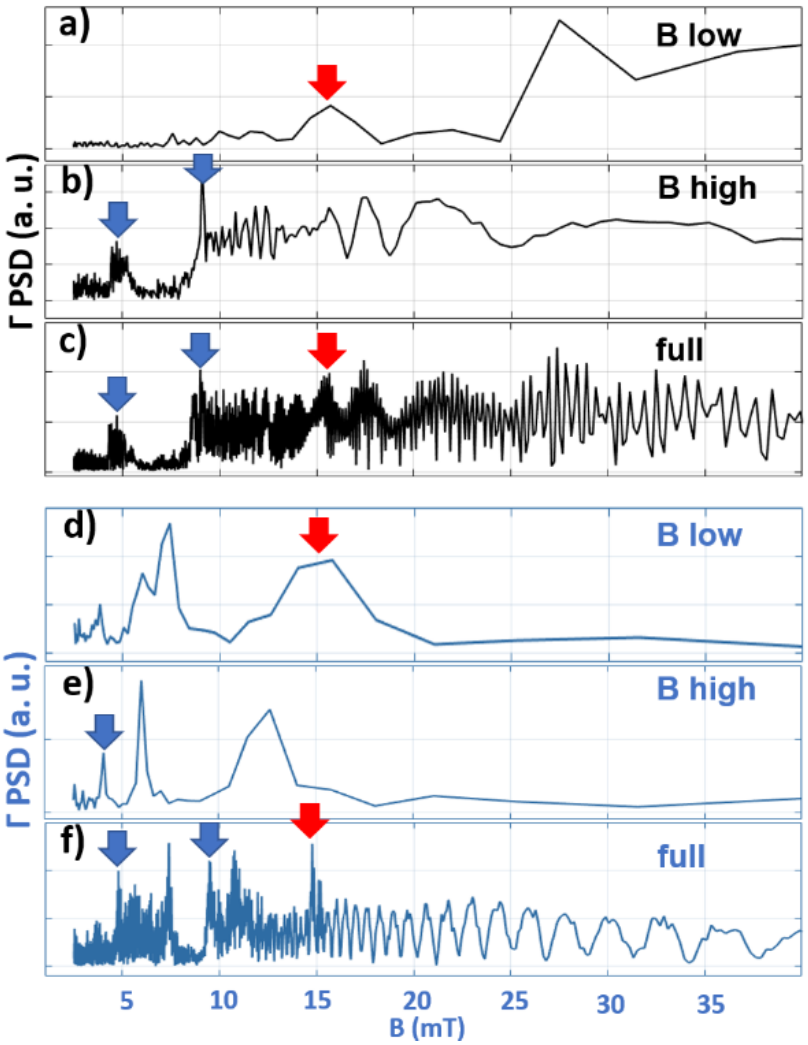

Figure 6.10: — *FFT of the $\Gamma(V)$ curves showed in figure 6.9 for $3n_s/4$ and $3n_s/4 < n < n_s$ for **a-c** and **d-f** respectively. **a)** and **d)** low B-field FFT analysis in a range of $-0.1\ T < B < 0.14\ T$. The red arrow points out the most prominent feature of the spectrum. **b)** and **e)** large B-field FFT analysis in the range of $\pm 2\ T < B < \pm 2.5\ T$. The blue arrows mark the dominant magnetic field period of the spectra. **c)** and **f)** full spectrum FFT ($-2.5\ T < B < 25\ T$). The arrows show the same peaks in all the spectrum.*

et. al. [158], when two materials of opposite Chern number are put in contact the emergence of chiral edge states is expected at the interface [168]. The observation of magneto-oscillations present at B-field as low as $B < 100\ mT$ and localized at $3n_s/4$ band filling supports the scenario of chiral edge currents present at domain boundaries, as observed by SQUID measurements

6.7 Summary

Low temperature p-AFM mechanical dissipation detected the series of SIS in TBG as a function of carrier density and magnetic field. It does it without literally touching the crystal and strikingly couples to the subsurface effect in the encapsulated quantum device. The mechanism of dissipation rise at different band filling was discussed and is consistent with the creation of local currents below the oscillating tip as well as a rapid change of quantum capacitance of TBG device. Due to the local detection the p-AFM could quantify the twist angle and doping at various sample spots and concluded charge disorder to be dominant. Spatially resolved dissipation images showed the existence of hundred nanometers domains. Application of magnetic fields leads to magneto-oscillations of the dissipation signal which is enhanced at $3n_s/4$ band filling. We identify those oscillations as originating from Aharonov-Bohm quantum interference effect at domain's boundaries of different doping. Another type of oscillations near $-100\ mT < B < 100\ mT$ magnetic field were found and presence of those is in agreement with scenario of Chern domain walls. Finally, we have demonstrated that mechanical oscillators can address quantum effects in energy dissipation.

7

Molybdenum Disulfate

The emergence of atomically thin materials also called 2D materials opened up a wide range of possibilities due to their extraordinary properties as compared to their bulk. Transitional metal dichalcogenides or TMDs are part of them. Over the last decade, they demonstrated great properties such as spin-orbit coupling [169], very large exciton binding energy [170] or stable trion excitation [171]. The potential applications for them makes their investigation explode especially in the area of new generation of low-dimensional transistors [45], photo-emitting [172] or spintronics devices [173]. Although, it would open up a very interesting possibility to study and control magnetism at an atomic scale [174], the presence of a magnetic 2D material is missing or they are very complex to fabricate. Moreover, different magnetic atomic layers of van der Waals heterostructure might be manipulated in very diverse ways, namely by stacking or twisting. The possibility to achieve magnetism with TMDs materials is crucial not only because of their properties but also due to their manipulation capability, that is nowadays well established.

Molybdenum disulfate (MoS_2) is a natural candidate, indeed it's spin-orbit coupling [175] makes it suitable for spintronic devices. During the past years, its electrical [176, 177] and optical [178, 179] properties has been heavily studied. It is important to notify that the pristine bulk MoS_2 is a non-magnetic material. However, recent theoretical and experimental studies revealed the possibility to induce a magnetic moment in the MoS_2 monolayer. The magnetic moment can be induced by defects and zigzag edge of the flake [180–182]. It has been reported that adsorption of transition metal ad-atoms onto the surface can lead to ferromagnetic state [183]. An adsorption of H or F atoms results in creation of local magnetic moments that eventually results in anti-ferromagnetic coupling of them [184]. Beside adsorption, stress is another way to induce magnetic moment onto MoS_2 monolayer. The calculations revealed that strain itself cannot induce magnetism in the perfect monolayer and the presence of a defect is mandatory [185, 186].

More recently, it has been shown that the mobile electrons in a semi-conductor can lower their energy and align their spin due to Pauli exclusion principle [187]. This phenomenon can induce a ferromagnetic phase due to the alignment of all the electron spins. This behaviour was already reported in TBG [188] and MoS_2 [189]. Thus, a phase transition is expected between a ferromagnetic phase (FMP) at low electron densities to paramagnetic phase (PMP) for high electronic densities.

p-AFM already demonstrated to be an excellent tool in the investigations of phase transitions [190]. The study of the temperature driven phase transition from superconducting to normal metal phase of the Nb surface [95] is a good example. Each phases dissipate differently, that lead to dramatic change of the dissipation curves. Similar effect can be expected for single monolayer MoS_2 when electron concentration is changed from low to high resulting in FMP to PMP transition.

In this chapter, we report on low temperature ($T = 5\ K$) force and energy dissipation experiments over single monolayer of MoS_2. A doping driven phase transition between a FMP to a PMP over the surface is observed and survives up to $T = 77\ K$. The experiment was performed with a homemade magnetic tip with a high coercivity. The experiments where carried out with the application of an external magnetic field.

7.1 Sample Geometry And Tip Characterization

The sample was fabricated by Dr. Mehdi Ramezani from Prof. Dr. Christian Schönenberger group from the University of Basel. It is composed of a silicon substrate, the backgate is a made out of a graphite flake and the tunnelling barrier is a 20 nm think hBN film. On top of that, the MoS_2 monolayer and graphene flake are deposited and capped with a top 4 nm thick hBN film. The device was contacted and grounded by the means of the graphene flake that serves as a gate. The sample is presented in figure 7.1, where a) is an optical microscope image showing the different layers and b) is the p-AFM image. On the p-AFM image only a fragment of the device is visible. The method of fabrication is described elsewhere: [191, 192]. During all the experiments presented in this chapter, the monolayer MoS_2 and the tip were kept grounded.

The MoS_2 sample was first measured using a non-magnetic ATEC-cont cantilever with and without external perpendicular magnetic field (B_{ext}-field). These measurements were used as a reference to the measurements performed with magnetic tip.

Figure 7.2 a) shows the typical Γ and Δf spectra obtained on MoS_2. It is important to note that PMMA polymer clusters were distributed randomly on the sample surface (high features on the AFM and the optical microscope images). Hence, scanning over the surface during the topography and the excitation image favoured the grabbing of PMMA material on the tip. It effects on the Γ spectrum is showed in Sup. Mat. S7:1. The typical parabolic like Δf is obtained versus backgate voltage V_{BG}.

To complete the characterization of the MoS_2 monolayer an external magnetic field (B_{ext}) was applied. The internal damping of the cantilever and the interaction with the sample lead to the saturation of the dissipation signal at $B = 4\ T$. The expected Shubnikov de Haas oscillations [44, 193] were not observed due to the low B_{ext}-field

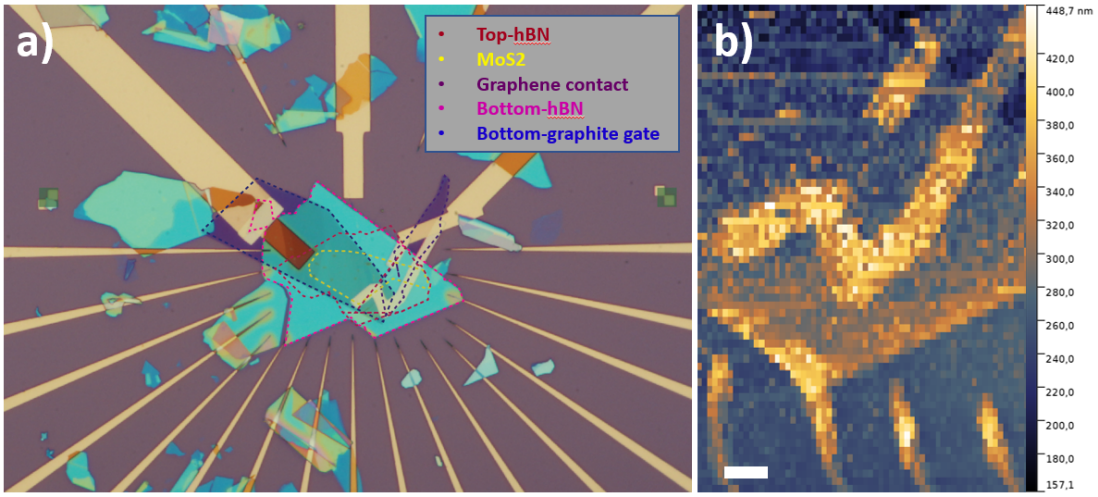

Figure 7.1: — *Optical and AFM images of the sample.* ***a)*** *optical image of the stacked MoS_2 device, where all the different layers are marked with coloured dotted lines and described in the attached legend.* ***b)*** *p-AFM 64 × 64 pixel image taken at room temperature, where the MoS_2 monolayer is located nearby the zigzag wire. The scale bar is $2\mu m$.*

value. The corresponding Γ and Δf are shown in figure 7.2 b).

The magnetic field dependent experiments showed that Δf signal is varying in the range of only few hundred mHz. A drastic reduction of the dissipation features was noticed when increasing B_{ext}-field. This effect was also observed in Γ maps, where constant height dissipation images were recorded over MoS_2 at different B_{ext}-field as presented in figure 7.2 c) to e). The maps revealed a decrease of the dissipation intensity in the middle of the flake (also the PMMA contrast) followed by an big increase of the dissipation at the edges. One can speculate a spin valley Hall-like effect. The supposed effect is separating the charges from different valleys that experience opposite Lorentz-like forces moving them in opposite directions perpendicular to the tip-induced drift current [194]. It is important to note, that only the MoS_2 edges show this increase of dissipation intensity in B_{ext}-field.

The actual experiment was performed with a homemade magnetic tip. The magnetic cantilever is a tipless Arrow TL cantilever with a ferromagnetic cobalt samarium ($SmCo_5$) particle glued at its very end, see Sup. Mat. S7:2. In terms of force sensitivity, Arrow TL has a smaller spring constant ($k = 0.06\ N/m$) with a large quality factor ($Q = 215568$) as compared to the ATEC-cont cantilever. After gluing the magnet the tip was sharpened using a focus ion beam, see figure 7.3 a). The tip was characterized by means of magnetometry method, where a sweep of magnetic field $B = \pm 3\ T$ was applied. Figures 7.3 b) and c) show the Δf and Γ channels, respectively. A hysteresis loop is clearly visible on both spectra, which is characteristic for a ferromagnetic magnet. The coercive field is found to be equal to $B_c \approx 0.4\ T$, see figure 7.3 c). This implies that the magnet have a strong magnetic field that can magnetize the sample locally. This is a very important parameter for the experiments in order to see any magnetic effect on the sample since MoS_2 is not a magnetic material. Moreover, it enables

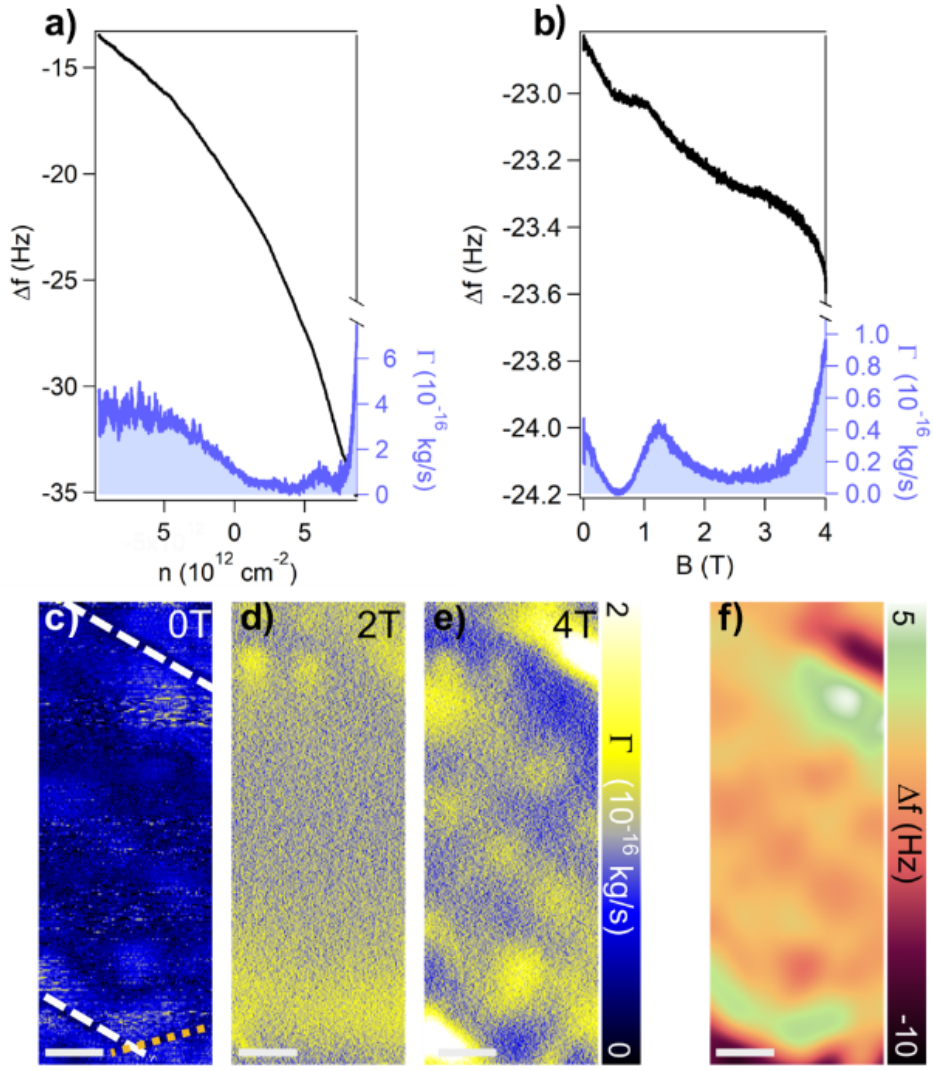

Figure 7.2: — *Characterization of MoS_2 device with nonmagnetic tip at $T = 5\ K$.* ***a)*** *typical $\Gamma(V)$ and $\Delta f(Hz)$ spectra recorded on MoS_2.* ***b)*** *Γ and Δf data versus the magnetic field from $B = 0\ T$ to $B = 4\ T$. No Shubnikov de Haas oscillations are visible.* ***c)*** *to* ***e)*** *constant height dissipation images recorded at one edge of the MoS_2 flake. The white dotted lines show the MoS_2 edge while the orange dotted lines are the top hBN edge. Images were taken at different magnetic field: $B = 0\ T$, $B = 2\ T$ and $B = 4\ T$.* ***f)*** *corresponding Δf image, which is the same for each B-field applied, meaning the tip-sample distance remains unchanged when B-field is applied. The scale bar is equal to 200 nm.*

us to do external magnetic field measurements with an reasonable B_{ext}-field range of operation where the magnetic properties of the cantilever are invariant. The magnetic moment of the tip was determined by fit the formula to the Δf data [195, 196]:

$$\frac{\Delta\omega}{\omega_0} = \frac{m_{tip} H H_k}{2k_0 L_e^2 (H + H_k)} \tag{7.1}$$

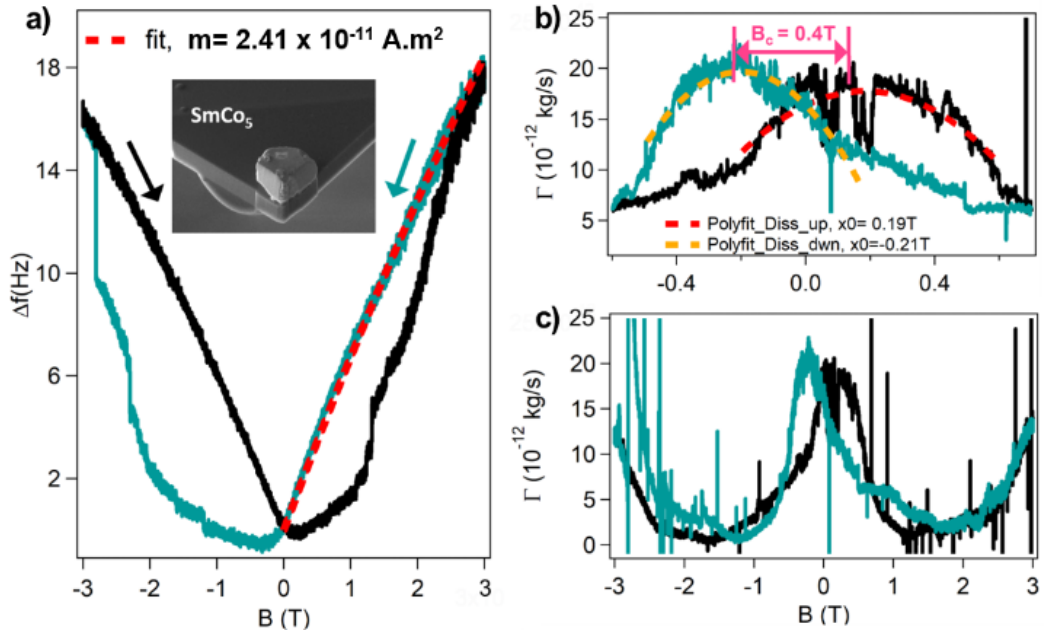

Figure 7.3: — *Cantilever image and magnetometry data.* ***a)*** *Δf data versus magnetic field for the free cantilever at $T = 5\ K$. The black curve is the sweep forward and the blue curve is the sweep downward. The red dashed line is the fit of the data, that allows to find the magnetic moment of the tip equal to: $m = 2.5 \times 10^{-14}\ A \cdot m^2$. The inset is a Scanning Electron Micrograph of the magnet glued on the ARROW TL cantilever. The bottom end of the cantilever was sharpened using Focused Ion Beam.* ***b)*** *zoom in Γ magnetometry curve where the hysteresis that allows to extract the coercive field equal to: $\Delta B \approx 0.4\ T$ is better visible.* ***c)*** *$\Gamma(V)$ full magnetometry spectrum.*

where $m_{tip} = M_s V$ is the tip magnetic moment, $M_s = 7.8 \times 10^6\ A \cdot m$ is the saturation magnetization, $V = 3.081 \times 10^{-18}\ m^3$ is the magnet volume, $k_0 = 0.06\ N/m$ is the cantilever spring constant, $\omega_0 = f_0/2\pi = 1.04\ kHz$ is the cantilever frequency in the zero field, H is the magnetic field in Oe and $H_k = 2K_u/M_s$ with K_u being the uniaxial anisotropy. The fit to the data is shown as the red dotted line in figure 7.3 b) and revealed a magnetic moment equal to $m_{tip} = 2.41 \times 10^{-11} A \cdot m^2$. Thus, we can determine a magnetic force with the formula [86]: $F = q_m H_{sample}$, where $q_m = -\mu_0 M_s d_x d_y = -9.03 \times 10^{-3}\ nN/A \cdot m^{-1}$ is the magnet point charge, d_x and d_y are the longitudinal and lateral dimensions of the tip facing the sample. $\mu_0 = 4\pi \times 10^{-7}\ kg \cdot m \cdot A^{-2} s^{-2}$ is the vacuum permittivity and H_{samp} the sample stray field. In chapter 4, we demonstrated that the static normal force acting on cantilever in pendulum geometry is given by (see Sup. Mat. S4:1):

$$F = \frac{2}{3} \frac{b_0 L k_0}{b_1 \omega_0} \Delta\omega \tag{7.2}$$

thus the:

$$|H_{samp}| = |\frac{F}{q_m}| \tag{7.3}$$

where H_{samp} is the sample magnetic strength. In this work, the magnetic moment

of MoS_2 is assumed to be homogeneous, thus $H_{samp} = M_{samp}$, where M_{samp} is the magnetization of MoS_2, see figure 7.4 a).

7.2 Dissipation Measurements

The cantilever is oscillating with a fixed amplitude $A_{exc} = 5\ nm$, at a fixed tip-sample distance $d = 100\ nm$ while the backgate voltage (V_{BG}) was applied to the graphite backgate from $-4\ V$ to $10\ V$. The backgate voltage was converted into doping using: $n = \frac{C_{ox}V_{BG}}{q}$, where $C_{ox} = \frac{\epsilon_0(\epsilon_{hBN}/2)}{t_{hBN}}$ is the oxide capacitance and q is the electron charge. The cantilever and the MoS_2 are both grounded as presented in figure 7.4 a). The energy dissipation as well as the Δf are monitored using the PLL. First, the topography measurements were performed in order to find a proper measurement position on the device. The large quality factor of the cantilever ($Q = 215568$) made the image process difficult for the PLL to adjust reasonably the phase to image, thus the Q-controller mode was used. This mode consists of artificially reduce the quality factor of the cantilever inducing the reduction of its decay time facilitating the PLL to adjust to it and enables the acquisition of images with correct quality [197]. The spectroscopic measurement were made with the first oscillation mode and without the Q-control.

We performed Γ and Δf spectroscopy over the MoS_2 flake. The frequency-shift was converted into force using equation 7.2 and converted into M_{samp} with equation 7.3. The non-corrected/converted data are presented in Sup. Mat. S7:3 and the resulting curves are presented in figure 7.4 b). Forward (low n to high n sweep, FWD) and

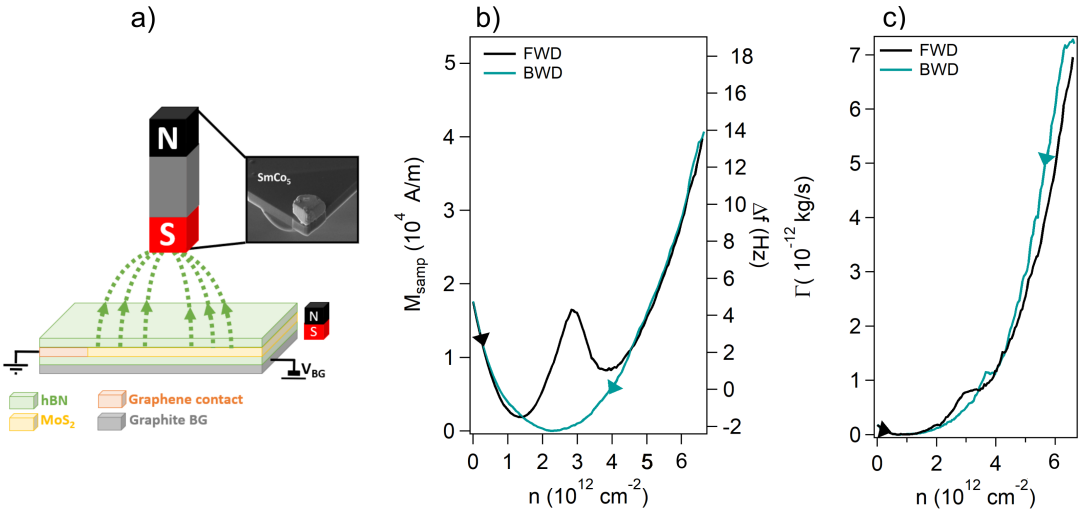

Figure 7.4: — *Voltage dependent $\Delta f/M$ and Γ spectra at $d = 100\ nm$ over MoS_2.* ***a)*** *schematic of the tip-sample geometry assuming a monopole approximation of the tip. The green dotted lines are the magnetic field coming from the sample.* ***b)*** *M_{samp} vs n FWD and BWD spectrum over MoS_2 at $d = 100\ nm$ distance in black and blue, respectively. The M curves are calculated based the Δf curves.* ***c)*** *corresponding Γ spectrum.*

backward (high n to low n sweep, BWD) sweeps revealed an hysteresis. Indeed, the two curves show different trend. In addition to that, a part of the hysteresis was located at the negative doping side. A correction was made in order to have all the hysteresis in the positive doping side and the corrected doping became: $n_{corr} = n + \Delta n$, where $\Delta n = 1.13 \times 10^{-12}\ cm^{-2}$ corresponding to a doping offset, for the rest of this chapter $n = n_{corr}$.

The Δf curves (FWD and BWD) shows the typical Joule related parabolic background that is due to the capacitive coupling between the tip and the backgate electrode. The FWD curves shows a peak at $n_c = 2.86 \times 10^{12}\ cm^{-2}$ in addition to the parabolic background. This suggest that the peak is not induced by any capacitance coupling coming from the tip and the sample and might be related to other physical phenomena. The dissipation spectrum is also showing similar features in the dissipation spectrum, a peak is visible at $n_c = 2.86 \times 10^{12}\ cm^{-2}$ in the FWD spectrum but it is shifted to higher doping in the BWD sweep ($n_c^{BWD} = 3.66 \times 10^{12}\ cm^{-2}$). Moreover, the dissipation and the noise level is enhanced after n_c indicating a physical change between the low and high doping region.

Figure 7.5 shows the distance dependent frequency shift $\Delta f(d)$ (a) and b)) and damping coefficient $\Gamma(d)$ (c) and d)) versus backgate voltage. The backgate voltage sweeps are performed in both directions: FWD (a and c) and BWD (b and d). The FWD maps reveal neither no distance dependent shift nor intensity change of the peak. Moreover, the peak persists at relatively large distance ($d > 100\ nm$). The hysteresis, is very well defined and is d independent.

It can be noted that n_c value is close to the doping concentration at which the

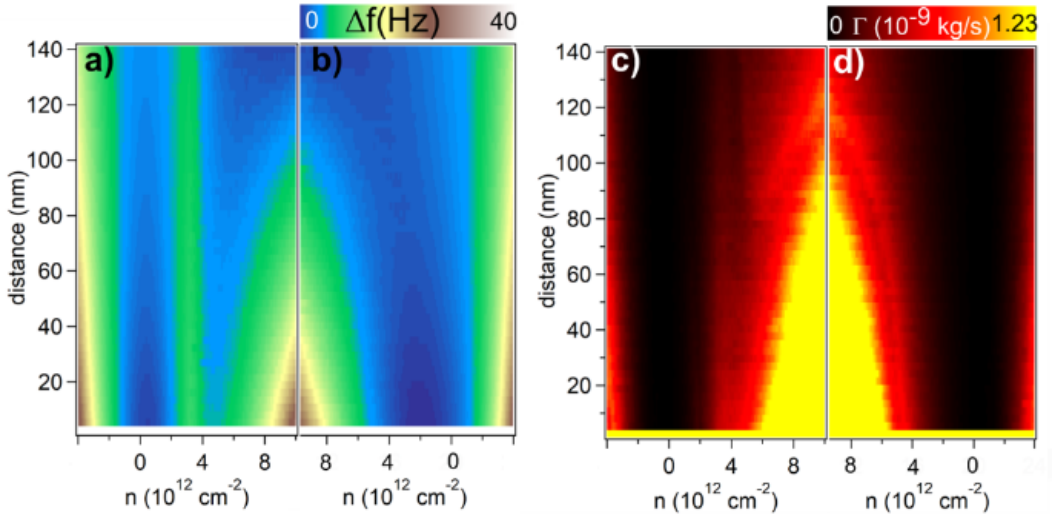

Figure 7.5: — *Tip-sample distance and backgate voltage dependent force and dissipation maps.* ***a)*** *V_{BG} forward (FWD) sweep Δf map and* ***b)*** *the corresponding backward (BWD) sweep Δf map. The transition peak is visible only in forward sweep direction.* ***c)*** *corresponding FWD sweep Gamma map and* ***d)*** *the Γ BWD sweep map.*

first-order FMP to PMP phase transition was observed in a monolayer MoS_2 with photoluminescence technique [189] ($n_c = 3 \times 10^{12}\ cm^{-2}$). They observed an abrupt change of the photoluminescence intensity, whereas in our measurement the change rather show a very distinct peak.

A ferromagnetic phase to a paramagnetic phase transition can be explained based with simple considerations. The band structure of MoS_2 monolayer is related to its graphene-like lattice structure with molybdenum and sulfur sub-lattices [198]. Like graphene, the band edges are located at the K and K' points. The spin-orbit coupling present in MoS_2 provoke a spin degeneracy. Hence, in each valley the two conduction and valence bands are split in two bands (spin-up and spin-down). The upper valence band has the same spin as the lower conductance band and vice-versa for the two other bands [171]. When MoS_2 is magnetized, here by the tip magnet, the minima of the lower conduction bands are getting shifted due to the Zeeman splitting. Thus, the first electrons filling the band via the backgate contact populates the lowest band energy (see Fig. 7.6 a)). As the filling goes, the inter- and intra-valley exchange interaction pulls to lower energies the same spin polarized bands as presented in figure 7.6 b). At low doping, the conductance bands gap is very large thus the electrons only lies in the lower covalent band, see the left schematic in figure 7.6 b), which corresponds to a strongly correlated system. A spontaneous alignment of the electron spin is thus induced leading to ferromagnetism. At a critical doping n_c, the bands structure is getting drastically modified with the filling of the upper bands. For high doping, the gap between the two bands is strongly reduced and the system enter a non-interacting free spin regime favouring paramagnetism, as schematized in the right part of figure 7.6 c).

The above can be translated into the coupling of a magnetic mechanical oscillator to the magnetic quantum spin system. At the low doping regions, in correlated electronic regime, all the spins are aligned towards the same direction, thus the cantilever oscillations do not disturb the system resulting in a low and quasi-constant dissipation with low noise level. For high doping, the spins are oriented in a disordered manner and they are getting disturbed by the tip oscillations. They try to align with the cantilever macroscopic magnetic momentum resulting in the increasing of the dissipation with n.

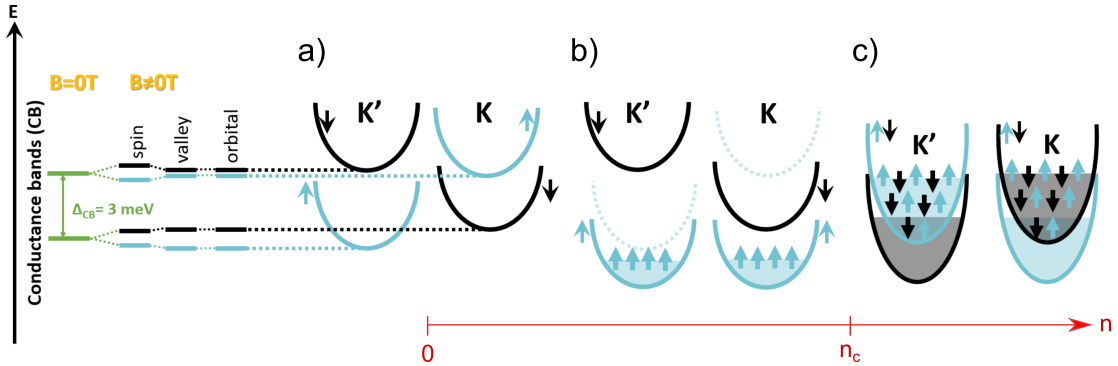

Figure 7.6: — *Schematic of the electronic band structure in the FMP and the PMP regions with respect to the doping.*

The observed asymmetry in the data excludes the simple geometric capacitive effects as an origin of the peak. Instead, it is a strong hint for the first-order phase transition. This hysteric behaviour is discussed in the last section.

7.3 Magnetic Field Dependence

To understand the origin of the peak, an external magnetic field (B_{ext}) was applied ranging from $B_{ext} = -0.2\ T$ to $B_{ext} = 0.2\ T$. Since the applied B_{ext}-field is lower than the coercive field of the cantilever (Fig. 7.3 b)) we can exclude the change of tip magnetization during the measurements. The doping sweep parameters remains the same and the tip-sample distance is equal to $d = 60\ nm$. The BWD sweep of $B_{ext} = 0\ T$ was removed from all the curves (M and Γ) which is equivalent to remove the Joule dissipation contribution, the original data are in Sup. Mat. S7:4. Thus, only the ferromagnetic and the paramagnetic contributions remain. Figure 7.7 shows the resulting dissipation (Fig 7.7 a)) and magnetization (Fig. 7.7 b)) curves. The FMP is showing no reaction whereas the PMP rise exponentially with n. As expected, in the PMP it is sensitive to B_{ext}-field. Indeed, the application of an external B_{ext}-field increases the disorder in the sample inducing an increase of the dissipation and magnetization. For both channels the transition peak is clearly visible at $n_c = 2.86 \times 10^{12}\ cm^{-2}$. Figure 7.7 a), shows an additional peak at $n = 3.66 \times 10^{12}\ cm^{-2}$ corresponding to shifted peak in the BWD spectrum (see Fig. 7.4 c)). This peak is less defined as compared to n_c and is B_{ext}-field dependent, visible on the reduction of its intensity. For positive B_{ext}, the dissipation and the magnetization increases. In fact, the external magnetic field polarizes the sample (see Fig. 7.7 c) and d)). The magnetization and the dissipation increase indicates a stiffening of the cantilever. This happens when the attractive forces are dominant. Figure 7.7 c) schematizes the phenomena. The MoS_2 has it own polarization, the attractiveness of the forces in presence indicates that MoS_2 and the tip apex poles are opposite magnetic pole as described in figure 7.7 c). Inversely, when B_{ext} is negative the polarization of MoS_2 is reversed and the new configuration is shown in figure 7.7 d) resulting to repulsive forces inducing a softening of the cantilever. The negative M gives hint on the tip magnetization, it suggests that M_{tip} is smaller than M_{ext}. Thus, the magnetic forces induced by B_{ext} are larger than the tip explaining the negative M and Γ.

To investigate further the magnetic properties of MoS_2, the magnetization is expressed in Bohr magnetron units (μ_B) by:

$$M = n_{3D}\mu_B \tag{7.4}$$

where $n_{3D} = n_{2D}/d_{MoS_2}$ is the three dimensional density of states of MoS_2 with d_{MoS2} the monolayer thickness and n_{2D} the doping concentration in the 2D layer. Using equation 7.4 we can define the molar magnetization of MoS_2 as: $M_{mol} = M/n_{3D}$, the resulting curves are presented in figure 7.8 a). In addition to that B_{ext} was expressed in H as the magnetic strength by: $B_{ext} = \mu_0 \times H$. Magnetization cuts versus B_{ext} for different n where made, the typical behaviour in each phase is presented in figure

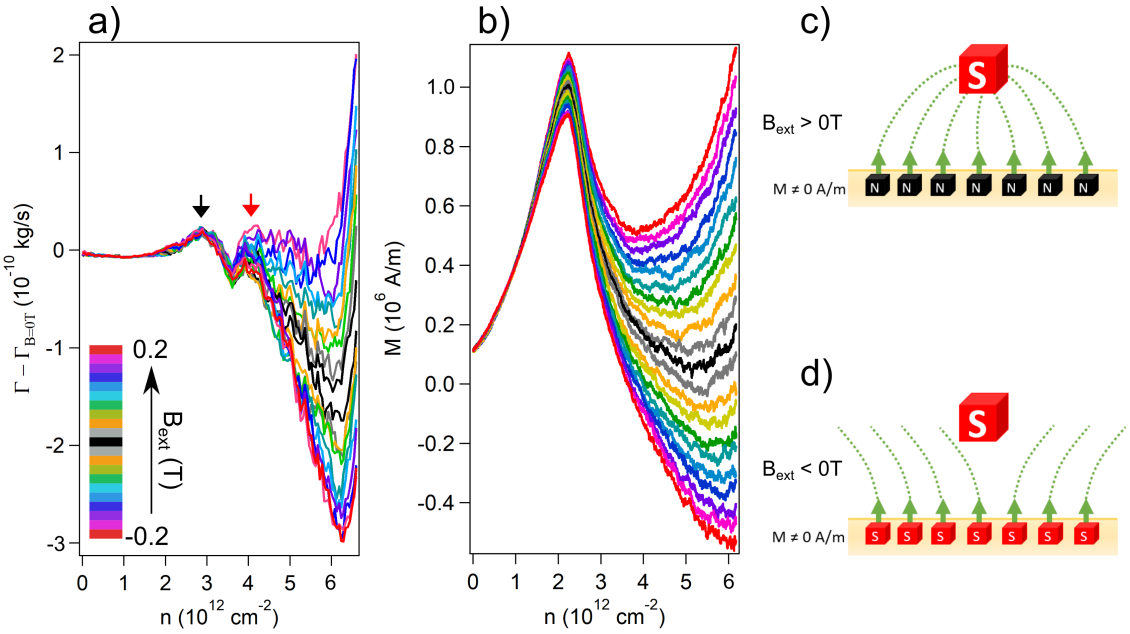

Figure 7.7: — *Magnetization and energy dissipation dependence versus n under an external magnetic field.* ***a)*** *dissipation curves after subtraction of backward dissipation* $\Gamma_{B=0T}$*. The ferromagnetic state is located below* n_c*, whereas the paramagnetic state exists at larger doping. The black arrow point out* n_c *whereas the red arrow points out the peak localized at* $n \approx 3.6 \times 10^{12} cm^{-2}$*.* ***b)*** *magnetization curves after subtraction of the backward force for* $B = 0\ T$*. The procedure allows to remove electrostatic force contribution from the data.* ***c)*** *schematic of the polarization of the sample when* $B_{ext} \geq 0$ *with respect to the tip polarization. The poles in the tip and sample are opposite leading to attractive forces.* ***d)*** *schematic of the polarization of the sample when* $B_{ext} < 0$ *with respect to the tip polarization. The poles in the tip and sample are the same leading to repulsive forces.*

7.8 b). They exhibit a linear behaviour with B_{ext}. The change of the slope between each phase is very distinct. The linear trend of M_{mol} versus H is a great hint for a first-order phase transition. Indeed, theory predicted [199] that for a first-order phase transition the spin susceptibility χ must be linear with respect to the magnetic field. It is a direct consequence of the negative cubic non-analyticity of the free energy that depends on the magnetization fraction M according to [199]:

$$F(M) = aM^2 + bM^4 + c|M|^3 \tag{7.5}$$

where a, b and c are constants. The first two terms are the Ginzburg-Landau parameters, which describe the second order phase transition, while the third term is the non-analytic correction that can lead to a first-order phase transition if the coefficient c is negative.

The Pauli paramagnetism formalism defines the spin susceptibility as follow [200]:

$$\chi = \frac{dM_{samp}}{dH_{ext}} \tag{7.6}$$

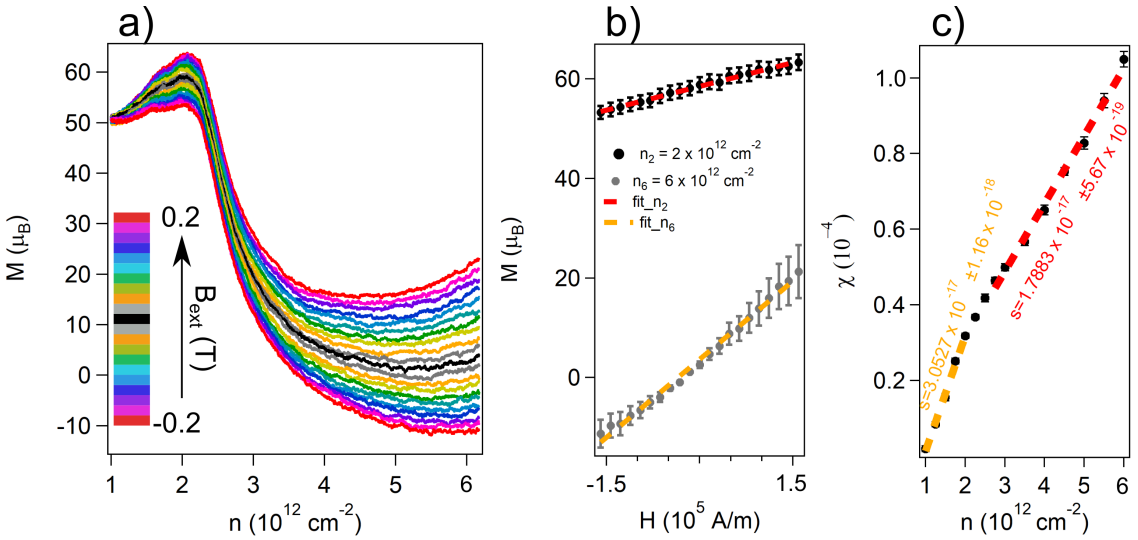

Figure 7.8: — *Spin susceptibility of MoS_2.* ***a)*** *M_{mol} data versus n, the dotted line correspond to the n_{cuts} presented in b) at $n_2 = 2 \times 10^{12}$ cm^{-2} and $n_6 = 6 \times 10^{12}$ cm^{-2} in black and gray, respectively.* ***b)*** *M_{mol} versus B_{ext} for n_2 and n_6 in black and gray respectively. The dotted lines are the corresponding linear fit for each cut. The data shows a linear dependence with B_{ext}.* ***c)*** *extracted χ from b) slopes versus n.*

where M_{samp} is the sample magnetization and H_{ext} is the external magnetic field strength. Using equation 7.6, we can determine that the slope of figure 7.8 b) is directly proportional to χ. Figure 7.8 c) shows the extracted χ from figure 7.8 b) slopes. In a non-interacting system, the susceptibility in the paramagnetic phase is expected to be constant. In our case, the susceptibility in the paramagnetic phase is non-constant indicating a strongly correlated electron system [201,202]. In addition to that, a distinct change of slope between the FMP and the PMP is visible, represented by the orange and red dotted lines in the FMP and the PMP phase respectively. The converging point is situated at n_c.

The paramagnetic spin magnetic susceptibility is defined as: $\chi_{para} = \mu_0 \mu_B^2 \mathcal{D}_{3D} = \mu_0 \mu_B^2 \mathcal{D}_{2D}/d_{MoS_2}$, where μ_B is the Bohr magnetron, $\mathcal{D}_{3D} = \mathcal{D}_{2D}/d_{MoS_2} = 2m^*/\pi\hbar^2 = 3 \times 10^{37}\ m^{-2}.J^{-1}$ the 3D and 2D density of states and $d_{MoS_2} = 0.62\ nm$ the monolayer thickness. Its first approximation using the sample properties and parameters give a value of $\chi_{para} \approx 5.23 \times 10^{-6}\ N/T^2.m$. This value agrees with the extracted χ from the experiments (Fig. 7.8 c)).

7.4 Time And Doping Dependent Measurements

Hysteric behaviour on first-order phase transition is a known effect. It comes from the difference of transition point that can be assimilated as a thermodynamic variable [203]. Indeed, in such transition a latent energy (E_l) has to be absorbed or dissipated by the system to enable the transition. The low to high energy transition needs to absorb E_l that is induced smoothly by increasing the doping concentration. The

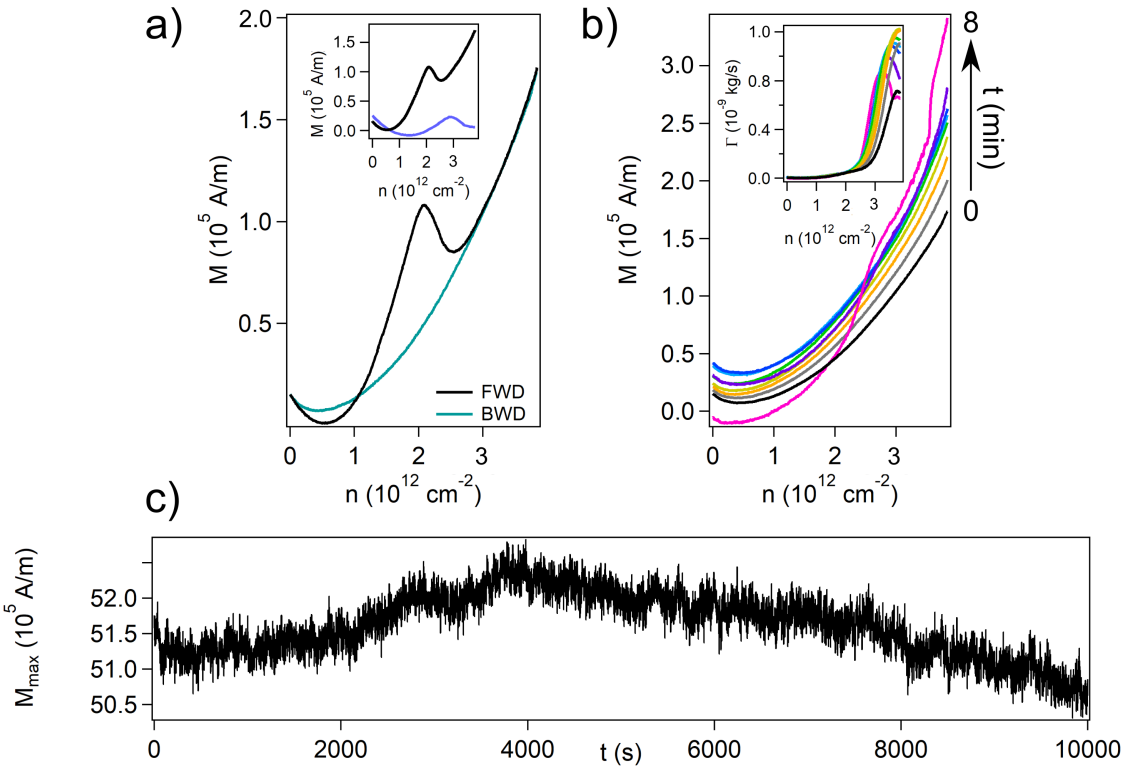

Figure 7.9: — *Time experiments.* ***a)*** *FWD and BWD magnetization curves versus doping at $T = 77\ K$ in black and blue respectively. The inset shows the $T = 5\ K$ and $T = 77\ K$ FWD curves versus doping.* ***b)*** *BWD time dependent M measurements. The time step between each curve is $\Delta t = 1\ min$ and the inset shows the corresponding Γ BWD curves.* ***c)*** *long term recording over n_c for $t = 3\ h$ to observe its evolution, so significant change are visible.*

high to low transition is more complex, the system needs to dissipate E_l. In our case this transition shows some complexity. Analogous to the water liquid to solid phase transition, the water can stays liquid even below its critical temperature also knows as super-cooling water. Only the application of an external energy enables to freeze the water. In our case, a similar effect is happening. The BWD curve shows no dissipation peak indicating its incapacity to recover the transition peak, thus its inability to dissipate fully E_l. To address it, experiments were performed at tip-sample distance $d = 20\ nm$ and temperature $T = 77\ K$. The backgate voltage sweep range is now from $V_{BG} = -4\ V$ to $V_{BG} = 6\ V$.

The typical FWD and BWD experimental curve taken at $T = 77\ K$ are displayed in figure 7.9 a) in black and blue respectively. In analogy to low temperature $T = 5\ K$ experiment, the phase transition peak appears at $n = 2.07 \times 10^{12}\ cm^{-2}$. The acquisition time of a single spectra is $t = 4\ min$. A time dependent experiment was made to verify whether a change of the waiting time between subsequent sweeps could potentially recover the transition peak in the BWD sweep. The BWD measurements consist of

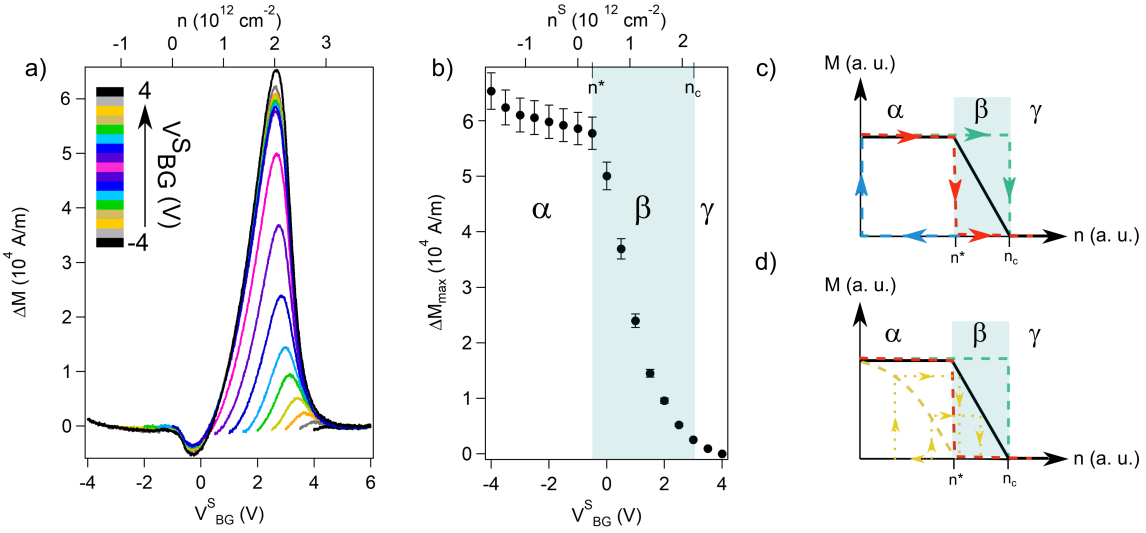

Figure 7.10: — *Initial doping driven experiments.* ***a)*** *ΔM versus n and V_{BG} evolution when the starting V^S_{BG} is changed from $V^S_{BG} = -4\ V$ to $V^S_{BG} = 4\ V$ with a step of $\Delta V^S_{BG} = 0.5\ V$ after each sweep.* ***b)*** *ΔM_{Max} evolution versus V^S_{BG} and its corresponding n^S. The blue rectangle highlight the region where ΔM_{max} is drastically reduced with respect to V^S_{BG}. Three different regions can thus be distinguished: α, β and γ corresponding to the FMP, transition and PMP regions.* ***c)*** *thermal activation simple model, the red dotted line correspond to the system in a thermal equilibrium, the green dotted line is for the thermal excited state and the black curve represent the actual system when the system is thermally activated from a local to a global minimum state are the FWD sweeps. The dotted blue curve is the represent the BWD sweep.* ***d)*** *Similar model as c) but it take in consideration the new starting V_{BG}, visible as the yellow dotted lines.*

applying different waiting time t between subsequent BWD sweeps. The time range was changing from $t = 0\ min$ to $t = 8\ min$ with a time step of $\Delta t = 1\ min$. The curves show a slight offset on the M curves after each sweep but no significant changes in the shape of the curve. Nevertheless, at $t = 7\ min$ a tiny rise of M is observable around $n \approx 3.5 \times 10^{12}\ cm^{-2}$ and after $t = 8\ min$ it was even more defined. The dissipation shows no changes over time, see figure 7.9 b) inset. However, no recovery of the FWD curve was observed. In addition to that, the tip was positioned for $t \approx 3\ h$ at the peak position in order to observe its evolution with time, see figure 7.9 c). No significant changes were observed. Thus, we concluded that the time effect is not the main hysteresis mechanism.

We further looked at the impact of the backgate voltage and the doping concentration on the observed phenomena. The background has been removed by subtracting the FWD and the BWD (ΔM) spectrum to remove the electrostatic contribution and keeps the magnetic response (the FWD and the BWD spectrum are in Sup. Mat. S7:5). In figure 7.10 a), the ΔM FWD backgate/doping dependent measurement are shown. The initial backgate voltage V^S_{BG} between subsequent spectra was changed from $V^S_{BG} = -4\ V$ to $V^S_{BG} = 4\ V$ with a step of $\Delta V^S_{BG} = 0.5\ V$. The change of the

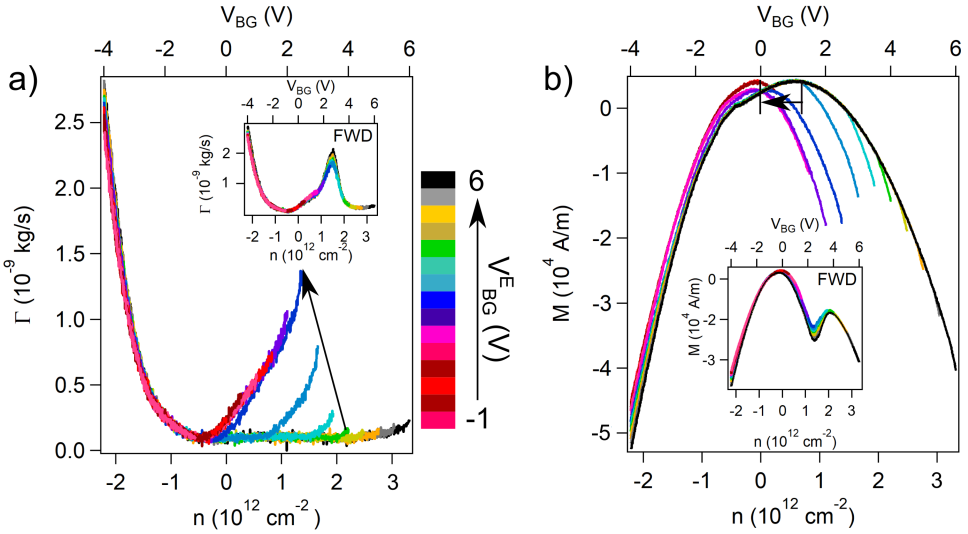

Figure 7.11: — *Doping driven experiments.* ***a)*** *Γ versus n and V_{BG} BWD evolution with different ending voltage V^E_{BG} from $V^E_{BG} = 6\ V$ to $V^E_{BG} = -1\ V$ with a step of $\Delta V^E_{BG} = 0.1\ V$.* ***b)*** *corresponding M spectrum. The insets of both figures are the FWD curves.*

starting voltage for each sweep induces the change of the transition peak intensity as well as its position. The position of the transition peak varies from $V_{BG} = 2.8\ V$ to $V_{BG} \approx 3.5\ V$ and then vanishes after crossing the phase transition. Figure 7.10 b), shows the intensity evolution of the transition peak (ΔM_max) versus V^S_{BG}. When the sweep is performed in both FMP and PMP regions (α region), the peak has a maximum intensity, whereas it disappears when only PMP region is swept (γ region). Thus, we concluded that in order to see the ferromagnetic to paramagnetic phase transition the system must be depleted inducing the removal of all electrons from the bands and start to fill the bands from zero. The minimum V^S_{BG} that have to be applied to see the peak transition with the maximum intensity is equal to about $V^S_{BG} = -0.5\ V$. This is a strong hint for the first-order phase transition type of scenario. A second-order phase transition is expected to be 'smooth', hence the gate would not need to fill the bands from zero. At any density we would initiate the measurement it should be possible to see the transition peak. Figure 7.10 c) shows a simple thermal activation model of the phase transition. Indeed, if we consider a simple sweep ($-4\ V < V_{BG} < 6\ V$), the thermal equilibrium of the system seems to play an important role. The blue curve schematizes the BWD while the red, green and black curves the FWD sweep, corresponding to the system in thermal equilibrium, out of equilibrium and thermally excited from a local to a global minimum state respectively. The observed drop of M corresponds to the phase transition at n_c. For the thermal equilibrium system (red dotted curve) the drop is abrupt from high $M = M_{max}$ to $M = 0$ as expected from a first-order phase transition. Now, if we consider thermal fluctuations (green dotted curve), it is visible that n_c is shifted to higher n. In experiments, we can reasonably assume that there is a combination of both limits. This case is represented by the black curve where the drop at n_c is not as sharp but rather try to find its 'real' local

minimum situated in between both limits. This simple model explains the observed n_c shift as well as the gradual vanishing of ΔM_{max} visible in figures 7.6 a) and b). This model does not take in consideration the change of V_{BG}^S. Figure 7.10 d) does. The light blue curve represents the new BWD curve when considering different starting sweeps. The FWD M curves looks very similar to figure 7.10 c) but this model confirms the thermally excited model as an possible explanation of the experimental observations. The dissipation spectra shows the same behaviour and are presented in Sup. Mat. S7:6. Thus, the experiment let us conclude that the observed hysteresis is rather doping driven than time driven.

Figures 7.11 a) and b) show the BWD sweeps Γ and M data, respectively. The ending backgate voltage between subsequent sweeps was changed from $V_{BG}^E = 6\ V$ to $V_{BG}^E = -1\ V$ with a step of $\Delta V_{BG}^E = 0.5\ V$. When the sweeping voltage is large enough to involve both phases the BWD curves does not show any sign of transition. The M curves have a parabolic shape where the maximum point is located at $V_{BG} \approx 1.22\ V$. In addition to that, the Γ shows very low dissipation. Around the transition voltage $V_{BG}^E \approx 3.5\ V$ a tiny rise of the dissipation is visible and the M parabola, the maximum point is shifted closer to the position obtained in the FWD sweep. Indeed, the BWD sweep parabola always showed one maximum located at $V_{BG} \approx 1.22\ V$ while the FWD is characterized by a double parabola with maximum located in both regions at $V_{BG}^{FMP} \approx 0\ V$ and $V_{BG}^{PMP} \approx 4\ V$. For the backgate voltage sweep performed only in the FMP region, the FWD and the BWD curves are identical. We also note that the background of both Γ and M curves have the same shape as their corresponding FWD curves presented in the insets of each figure. Again, the data confirmed a clear difference between the two phases, however transition from high to low doping density is not able to recover the peak characteristic for the phase transition.

As a last remark, we can notice that the dissipation peak at the phase transition in the Γ spectrum is more pronounced and better defined for $T = 77\ K$ as compared to the low temperature $T = 5\ K$ experiments. It is reasonable to assign this phenomenon to the presence of disorder and thermal effects. The increase of temperature increased the thermal instabilities favouring more disorder in the systems which leads to a higher dissipation.

7.5 Summary

In conclusion, we fabricated high quality MoS_2 device and measured its magnetization and dissipation response with low temperature p-AFM with magnetic tip and external magnetic field. The measurements revealed a doping driven phase transition from ferromagnetic to paramagnetic phase. Each phase has very distinct behaviour under magnetic field. Based on the simple model we determined the magnetic susceptibility which tends to have a quasi-linear dependence versus doping. The susceptibility is discontinuous and not constant indicating a strongly correlated 2D electron system. The observed hysteresis with the doping suggests a first-order ferromagnetic to

paramagnetic phase transition, in agreement with previous findings and theoretical predictions.

Conclusion

"Quantum mechanics describes nature as absurd from the point of view of common sense. And yet it fully agrees with experiments. So I hope you can accept nature as She is - absurd."

Richard P. Feynman

In conclusion to this Thesis, we demonstrated that p-AFM is a powerful tool that allows to investigate the quantum properties of 2D materials.

Pendulum geometry of the p-AFM allows to increase the AFM sensitivity. The cantilever is suspended perpendicularly to the sample surface and oscillates like a tiny pendulum. The main advantage of this configuration is the increased force sensitivity due to low cantilever stiffness and at the same time the tip avoids snapping into the sample surface. The p-AFM technique is rather used as a spectroscopic tool designed to study energy loss or dissipation mechanisms on different surfaces. Since it is important to know how and where energy leaks, the investigations of the nanoscale energy loss are among few priorities in nanoscience. Over the Thesis, I demonstrated p-AFM ability to perform local (single curve) and non-local (constant height maps) spectroscopy studies. In many situations, pendulum tip coupled to a quantum device can be schematized with a capacitance circuit, with a quantum capacitance present. Hence, p-AFM revealed itself as a very powerful and a very sensitive tool to investigate quantum effects on 2D materials.

In the different chapters, we saw that different physical phenomena, quantum or not, show very distinct behaviour and we are able to recognize and analyse them. In this work, we studied two different graphene systems: free-standing monolayer graphene sheet and twisted bilayer graphene at the magic angle twist (MATBG) as well as a monolayer of MoS_2. In these three cases the different dissipation mechanisms were found, all of them leave a different footprint in the dissipation and force spectra.

The free-standing graphene shows the presence of peaks in the dissipation spectrum followed by dips in the frequency shift. This is characteristic for the single electron

charging and discharging events due to the AFM cantilever oscillations over an effective quantum dot. The AFM capacitance model allows to determine the tip-sample capacitance C_{TIP} that shifts the position of the charging peaks, the effect which is related to the lever arm. The sample capacitance C_{SUB} allows to explain the origins of the peaks. This later capacitance is composed of two capacitances and the quantum capacitance is one of them. The experiment showed that for small objects ($\approx 60\ nm$) the p-AFM is sensitive to van Hove singularities that are present in quantum capacitance. Those peaks are the result of quantum size effect and are directly related to the electronic density of states ρ of graphene as given by the formula: $C_Q = \rho q^2$. In our sample, the quantization originates from small structures presents on the sample surface. The graphene sheet shows the existence of nanometer size surface deformations as well as presence of domains created during the growth process. The quantum entity has a 1D-shape which is confirmed with the constant height dissipation maps that shows Coulomb rings elongated along one specific direction. The presence of an external perpendicular magnetic field shifts the position of the peaks to lower energies in a linear manner. Such behaviour is due to the linear energy dispersion of graphene and the introduction of a Peierls phase by magnetic field. The magnetic field dependence is qualitatively well described with a Bohr-Sommerfeld phase accumulation model. A more detailed tight binding calculations were also performed and are in good agreement with our experiments.

The second studied sample was the so-called MATBG. The dissipation spectrum revealed the presence of dissipation peaks corresponding to different filling factors and labelled: $n_s/4$, $n_s/2$, $3n_s/4$, n_s for one, two, three and four electrons filling the energy bands. Those peaks are related to the electron entering the mini-Brillouin zone (mBZ) of the MATBG. The measured phenomena is a result of the specific geometry of the sample that consists of two layers of graphene stacked and twisted on top of each other. The twist angle creates a mBZ that can be filled with four electrons. This mBZ induces flat bands that are the origin of correlated insulating state of the MATBG. The peaks in the dissipation had two distinct origins. The first case for $n_s/2$ and $3n_s/4$ band filling is similar to the case of free-standing graphene. In this case the dips are observed in the frequency shift spectrum and are related to presence of van Hove singularities in the density of states. In the second case the rise of dissipation is related to resistive loses. The dissipation spectrum related to Joule loses show less sharp peaks with a Gaussian-like shape. At the same time no features are visible in the frequency shift curve. We performed two types of experiments: a local experiment, that permits to study the angle distribution of the sample by acquiring a single dissipation spectrum at a certain spot of the device, and a constant height dissipation maps that scans over the sample surface over a large surface area. Both type of experiments exhibit the presence of angle domains within the sample. The presence of domains of different doping are believed to be the origin of quantum oscillations observed when a perpendicular magnetic field is applied. Those oscillations of dissipation and force are visible for specific band filling. Two different type of oscillations were found. The first are the Aharonov-Bohm oscillations, that are due to the presence of the hundred nanometer size domains. At the domain's edges the magnetic field induces charge hopping between neighbouring domains. Those oscillations were observed for $n_s/2$ and

$3n_s/4$ bands fillings at large B and they are $1/B$-aperiodic. The second oscillations are only observed at $3n_s/4$ and are most probably related to the ferromagnetic nature of this filling. They appear at $B = 0\ T$ and have a larger period compared to Aharonov-Bohm oscillations. For densities larger than $3n_s/4$ band filling, the two oscillations coexist.

The last measured sample is not a graphene based material but a monolayer of MoS_2. The dissipation and the frequency shift spectra show the presence of a phase transition between a ferromagnetic phase existing at low doping to a paramagnetic phase present at large doping. Such phase transition was predicted by theory and later confirmed experimentally. Our measurements are consistent with these studies. The acquisition of forward and backward dissipation and force spectra show an asymmetry with respect to doping. The phase transition is only visible when sweeping from low to large doping. Magnetic field measurements showed a linear magnetic susceptibility, which confirms a first-order phase transition scenario.

Hence, we demonstrated that quantum effects in various samples leave a clear hallmark in a dissipation and force spectra. The quantum effects are very robust and shows the versatility of the p-AFM technique. The possibility to access the information about sample density of states only with capacitively coupled pendulum tip is another advantage of this technique. The key parameter here is the quantum capacitance - that p-AFM is sensitive to - and it helps us to understand the different quantum effects that we encountered.

Bibliography

[1] John, D., Castro, L. & Pulfrey, D. Quantum capacitance in nanoscale device modeling. *Journal of Applied Physics* **96**, 5180–5184 (2004).

[2] Fang, T., Konar, A., Xing, H. & Jena, D. Carrier statistics and quantum capacitance of graphene sheets and ribbons. *Applied Physics Letters* **91**, 092109 (2007).

[3] Crossno, J. *et al.* Observation of the dirac fluid and the breakdown of the wiedemann-franz law in graphene. *Science* **351**, 1058–1061 (2016).

[4] Sze, S. M. & Kwok, K. N. *Physics of semiconductor devices* (Wiley-Interscience, New Jersey, 2007).

[5] Marchiori, R. 8 - mathematical fundamentals of nanotechnology. In Da Róz, A. L., Ferreira, M., de Lima Leite, F. & Oliveira, O. N. (eds.) *Nanostructures*, 209–232 (William Andrew Publishing, 2017). URL https://www.sciencedirect.com/science/article/pii/B9780323497824000085.

[6] Frêne, J. Histoire des techniques. *Mécanique and Industries* **2**, 263–282 (2001). URL https://www.sciencedirect.com/science/article/pii/S1296213901011150.

[7] Hutchings, I. M. Leonardo da vinci s studies of friction. *Wear* **360-361**, 51–66 (2016). URL https://www.sciencedirect.com/science/article/pii/S0043164816300588.

[8] Singer, I. L. Friction and energy dissipation at the atomic scale: A review. *Journal of Vacuum Science and Technology A* **12**, 2605–2616 (1994). URL https://doi.org/10.1116/1.579079. https://doi.org/10.1116/1.579079.

[9] Robbins, N. O. & Krim, J. Energy dissipation in interfacial friction. *MRS Bulletin* **23**, 23–26 (1998). URL https://doi.org/10.1557/S088376940003058X.

[10] Kisiel, M., Samadashvili, M., Gysin, U. & Meyer, E. Non-contact friction. *NanoScience and Technology* **97**, 93–110 (2015).

[11] Greenwood, J. A. & Williamson, J. B. P. Contact of nominally flat surfaces. *Proceedings of the Royal Society of London. Series A, Mathematical and Physical Sciences* **295**, 300–319 (1966). URL http://www.jstor.org/stable/2415421.

[12] Binnig, G., Quate, C. F. & Gerber, C. Atomic force microscope. *Phys. Rev. Lett.* **56**, 930–933 (1986). URL https://link.aps.org/doi/10.1103/PhysRevLett.56.930.

[13] Novoselov, K. S. *et al.* Two-dimensional atomic crystals. *Proceedings of the National Academy of Sciences* **102**, 10451–10453 (2005). URL https://www.pnas.org/content/102/30/10451. https://www.pnas.org/content/102/30/10451.full.pdf.

[14] Novoselov, K. S., Mishchenko, A., Carvalho, A. & Neto, A. H. C. 2d materials and van der waals heterostructures. *Science* **353**, aac9439 (2016). URL https://www.science.org/doi/abs/10.1126/science.aac9439. https://www.science.org/doi/pdf/10.1126/science.aac9439.

[15] Mermin, N. D. & Wagner, H. Absence of ferromagnetism or antiferromagnetism in one- or two-dimensional isotropic heisenberg models. *Phys. Rev. Lett.* **17**, 1133–1136 (1966). URL https://link.aps.org/doi/10.1103/PhysRevLett.17.1133.

[16] Mermin, N. D. Crystalline order in two dimensions. *Phys. Rev.* **176**, 250–254 (1968). URL https://link.aps.org/doi/10.1103/PhysRev.176.250.

[17] Peierls, R. Bemerkungen uber umwandlungstemperaturen. *Helv. Phys. Acta* **7**, 81–83 (1934).

[18] Peierls, R. Quelques proprietes typiques des corps solides. *Ann. Inst. Henri Poincare* **5**, 177–222 (1935).

[19] Hu, Y. & Wang, B. Vibrational stability of graphene. *AIP Advances* **3**, 052101 (2013).

[20] Novoselov, K. S. *et al.* Nucleation, growth and the intermediate layer in ag/si(100) and ag/si(111). *Surface Science* **147**, 197–200 (2005). URL https://doi.org/10.1038/nature04233.

[21] Zinke-Allmang, M. Thin film growth dynamics analyzed by ion scattering. *Nuclear Instruments and Methods in Physics Research Section B: Beam Interactions with Materials and Atoms* **64**, 113–119 (1992). URL https://www.sciencedirect.com/science/article/pii/0168583X9295448Z.

[22] Novoselov, K. S. *et al.* Two-dimensional gas of massless dirac fermions in graphene. *Nature* **438**, 433–450 (1984). URL https://www.sciencedirect.com/science/article/pii/0039602884904655.

[23] Geim, A. K. & Grigorieva, I. V. Van der waals heterostructures. *Nature* **499**, 419–425 (2013).

[24] Yu, Q., Luo, Y., Mahmood, A., Liu, B. & Cheng, H.-M. Heterostructures as high-performance electrocatalysts. *Electrochem. Energ. Rev.* **2**, 373–394 (2019).

[25] Meyer, J. C. *et al.* The structure of suspended graphene sheets. *Nature* **446**, 60–63 (2007). URL https://doi.org/10.1038/nature05545.

[26] Lopez-Polin, G., Gomez-Navarro, C. & Gomez-Herrero, J. The effect of rippling on the mechanical properties of graphene. *Nano Materials Science* **4**, 18–26 (2022).

[27] Deng, S. & Berry, V. Wrinkled, rippled and crumpled graphene: an overview of formation mechanism, electronic properties, and applications. *Materials Today* **19**, 197–212 (2016). URL https://www.sciencedirect.com/science/article/pii/S1369702115003119.

[28] Partoens, B. & Peeters, F. M. From graphene to graphite: Electronic structure around the k point. *Phys. Rev. B* **74**, 075404 (2006). URL https://link.aps.org/doi/10.1103/PhysRevB.74.075404.

[29] Moon, P. & Koshino, M. Energy spectrum and quantum hall effect in twisted bilayer graphene. *Phys. Rev. B* **85**, 195458 (2012). URL https://link.aps.org/doi/10.1103/PhysRevB.85.195458.

[30] Fang, S. & Kaxiras, E. Electronic structure theory of weakly interacting bilayers. *Phys. Rev. B* **93**, 235153 (2016). URL https://link.aps.org/doi/10.1103/PhysRevB.93.235153.

[31] Cao, Y. *et al.* Unconventional superconductivity in magic-angle graphene superlattices. *Nature* **556**, 40–50 (2018). URL https://doi.org/10.1038/nature26160.

[32] Suárez Morell, E., Correa, J. D., Vargas, P., Pacheco, M. & Barticevic, Z. Flat bands in slightly twisted bilayer graphene: Tight-binding calculations. *Phys. Rev. B* **82**, 121407 (2010). URL https://link.aps.org/doi/10.1103/PhysRevB.82.121407.

[33] Trambly de Laissardière, G., Mayou, D. & Magaud, L. Localization of dirac electrons in rotated graphene bilayers. *Nano Letters* **10**, 804–808 (2010). URL https://doi.org/10.1021/nl902948m. PMID: 20121163, https://doi.org/10.1021/nl902948m.

[34] Bistritzer, R. & MacDonald, A. H. Moiré bands in twisted double-layer graphene. *Proceedings of the National Academy of Sciences* **108**, 12233–12237 (2011). URL https://www.pnas.org/content/108/30/12233. https://www.pnas.org/content/108/30/12233.full.pdf.

[35] Shen, C. *et al.* Correlated states in twisted double bilayer graphene. *Nature physics* **16**, 520–525 (2020).

[36] Sharpe, A. L. *et al.* Emergent ferromagnetism near three-quarters filling in twisted bilayer graphene. *Science* **365**, 605–608 (2019).

[37] Yu, S. *et al.* Hofstadter subband ferromagnetism and symmetry-broken chern insulators in twisted bilayer graphene. *Nature Physics* **17**, 478–481 (2021).

[38] You, Y.-Z. & Vishwanath, A. Superconductivity from valley fluctuations and approximate so(4) symmetry in a weak coupling theory of twisted bilayer graphene. *npj Quantum Materials* 4–16 (2019).

[39] Yankowitz, M. *et al.* Tuning superconductivity in twisted bilayer graphene. *Science* **363**, 1059–1064 (2019).

[40] Cao, Y. *et al.* Correlated insulator behaviour at half-filling in magic-angle graphene superlattices. *Nature* **556**, 80–84 (2018).

[41] Wang, Q. H., Kalantar-Zadeh, K., Kis, A., Coleman, J. N. & Strano, M. S. Electronics and optoelectronics of two-dimensional transition metal dichalcogenides. *Nature Nanotechnology* **7**, 699–712 (2012).

[42] Kuc, A., Heine, T. & Kis, A. Electronic properties of transition-metal dichalcogenides. *MRS Bulletin* **40**, 577–584 (2015).

[43] Li, X., Zhang, F. & Niu, Q. Unconventional quantum hall effect and tunable spin hall effect in dirac materials: application to an isolated mos_2 trilayer. *Phys. Rev. Lett.* **110**, 066803 (2013).

[44] Pisoni, R. *et al.* Interactions and magnetotransport through spin-valley coupled landau levels in monolayer mos_2. *Phys. Rev. Lett.* **121**, 247701 (2018).

[45] Radisavljevic, B., Radenovic, A., Brivio, J., Giacometti, V. & Kis, A. Single-layer mos2 transistors. *Nature Nanotechnology* **6**, 147–150 (2011). URL `https://doi.org/10.1038/nnano.2010.279`.

[46] Winer, W. Molybdenum disulfide as a lubricant: A review of the fundamental knowledge. *Wear* **10**, 422–452 (1967). URL `https://www.sciencedirect.com/science/article/pii/0043164867901871`.

[47] Yu, L., Ruzsinszky, A. & Perdew, J. P. Bending two-dimensional materials to control charge localization and fermi-level shift. *Nano Letters* **16**, 2444–2449 (2016). URL `https://doi.org/10.1021/acs.nanolett.5b05303`. PMID: 26938458, `https://doi.org/10.1021/acs.nanolett.5b05303`.

[48] Kuc, A., Zibouche, N. & Heine, T. Influence of quantum confinement on the electronic structure of the transition metal sulfide ts_2. *Phys. Rev. B* **83**, 245213 (2011). URL `https://link.aps.org/doi/10.1103/PhysRevB.83.245213`.

[49] Splendiani, A. *et al.* Emerging photoluminescence in monolayer mos2. *Nano Letters* **10**, 1271–1275 (2010). URL `https://doi.org/10.1021/nl903868w`. PMID: 20229981, `https://doi.org/10.1021/nl903868w`.

[50] Li, X., Zhang, F. & Niu, Q. Unconventional quantum hall effect and tunable spin hall effect in dirac materials: Application to an isolated mos_2 trilayer. *Phys. Rev. Lett.* **110**, 066803 (2013). URL `https://link.aps.org/doi/10.1103/PhysRevLett.110.066803`.

[51] Li, Z. *et al.* Tailoring mos2 exciton–plasmon interaction by optical spin–orbit coupling. *ACS nano* **11**, 1165–1171 (2017).

[52] Wang, L., Kutana, A. & Yakobson, B. I. Many-body and spin-orbit effects on direct-indirect band gap transition of strained monolayer mos2 and ws2. *Annalen der Physik* **526**, L7–L12 (2014).

[53] Roldán, R., Cappelluti, E. & Guinea, F. Interactions and superconductivity in heavily doped mos 2. *Physical Review B* **88**, 054515 (2013).

[54] Binnig, G. & Rohrer, H. Scanning tunneling microscopy. *Surface Science* **126**, 236–244 (1983). URL `https://www.sciencedirect.com/science/article/pii/0039602883907161`.

[55] Gysin, U., Rast, S., Kisiel, M., Werle, C. & Meyer, E. Low temperature ultrahigh vacuum noncontact atomic force microscope in the pendulum geometry. *Review of Scientific Instruments* **82**, 023705 (2011). URL `https://doi.org/10.1063/1.3551603`. `https://doi.org/10.1063/1.3551603`.

[56] Nahas, Y. *et al.* An experimental uhv afm-stm device for characterizing surface nanostructures under stress/strain at variable temperature. *Review of Scientific Instruments* **84**, 105117 (2013). URL https://doi.org/10.1063/1.4826555. https://doi.org/10.1063/1.4826555.

[57] Edwards, H., Taylor, L., Duncan, W. & Melmed, A. J. Fast, high-resolution atomic force microscopy using a quartz tuning fork as actuator and sensor. *Journal of Applied Physics* **82**, 980–984 (1997). URL https://doi.org/10.1063/1.365936. https://doi.org/10.1063/1.365936.

[58] Volcke, C. *et al.* Stm tip functionalisation : A route to chemical contrast imaging. *Physicalia Magazine* **27**, 415–422 (2005).

[59] Young, R., Ward, J. & Scire, F. The topografiner: An instrument for measuring surface microtopography. *Review of Scientific Instruments* **43**, 999–1011 (1972). URL https://doi.org/10.1063/1.1685846. https://doi.org/10.1063/1.1685846.

[60] van de Leemput, L. E. C. & van Kempen, H. Scanning tunnelling microscopy. *Reports on Progress in Physics* **55**, 1165–1240 (1992). URL https://doi.org/10.1088/0034-4885/55/8/002.

[61] Della Pia, A. & Costantini, G. *Scanning Tunneling Microscopy*, 2301–2313 (Springer Netherlands, Dordrecht, 2012). URL https://doi.org/10.1007/978-90-481-9751-4_45.

[62] thinkSRS. About lock-in amplifiers (2010). URL https://www.thinksrs.com/downloads/pdfs/applicationnotes/AboutLIAs.pdf.

[63] Baratoff, A., Binnig, G., Fuchs, H., Salvan, F. & Stoll, E. Tunneling microscopy and spectroscopy of semiconductor surfaces and interfaces. *Surf. Sci.* **168**, 734–743 (1986).

[64] Vázquez de Parga, A. L. & Miranda, R. *Scanning Tunneling Spectroscopy*, 2313–2321 (Springer Netherlands, Dordrecht, 2012). URL https://doi.org/10.1007/978-90-481-9751-4_111.

[65] Cocco, A. & Masin, S. C. The law of elasticity. *Psisologica* **31**, 647–657 (2010).

[66] Giessibl, F. J. Advances in atomic force microscopy. *Rev. Mod. Phys.* **75**, 949–983 (2003). URL https://link.aps.org/doi/10.1103/RevModPhys.75.949.

[67] Rast, S., Wattinger, C., Gysin, U. & Meyer, E. The noise of cantilevers. *Nanotechnology* **11**, 169 (2000).

[68] Collins, I. Phase-locked loop (pll) fundamentals. *Analog dialogue* **52** (2018).

[69] Rajabifar, B., Jadhav, J. M., Kiracofe, D., Meyers, G. F. & Raman, A. Dynamic afm on viscoelastic polymer samples with surface forces. *Macromolecules* **51**, 9649–9661 (2018). URL https://doi.org/10.1021/acs.macromol.8b01485. https://doi.org/10.1021/acs.macromol.8b01485.

[70] Labuda, A. *et al.* Tapping mode afm imaging in liquids with bluedrive photothermal excitation. *Microscopy Today* **26**, 12–17 (2018).

[71] Voigtländer, B. *Amplitude Modulation (AM) Mode in Dynamic Atomic Force Microscopy*, 209–229 (Springer International Publishing, Cham, 2019). URL https://doi.org/10.1007/978-3-030-13654-3_13.

[72] Garcıa, R. & Perez, R. Dynamic atomic force microscopy methods. *Surface science reports* **47**, 197–301 (2002).

[73] Albrecht, T. R., Grütter, P., Horne, D. & Rugar, D. Frequency modulation detection using high-q cantilevers for enhanced force microscope sensitivity. *Journal of Applied Physics* **69**, 668–673 (1991). URL https://doi.org/10.1063/1.347347. https://doi.org/10.1063/1.347347.

[74] Albrecht, T. R., Grütter, P., Horne, D. & Rugar, D. Frequency modulation detection using high-q cantilevers for enhanced force microscope sensitivity. *Journal of Applied Physics* **69**, 668–673 (1991). URL https://doi.org/10.1063/1.347347. https://doi.org/10.1063/1.347347.

[75] Oatley, C. W. & Appleton, E. V. The measurement of contact potential difference. *Proceedings of the Royal Society of London. Series A - Mathematical and Physical Sciences* **155**, 218–234 (1936). URL https://royalsocietypublishing.org/doi/abs/10.1098/rspa.1936.0095. https://royalsocietypublishing.org/doi/pdf/10.1098/rspa.1936.0095.

[76] Loeb, L. B. The contact potential difference or volta potential. In *Static Electrification*, 32–58 (Springer, 1958).

[77] Ellner, M. *et al.* The electric field of co tips and its relevance for atomic force microscopy. *Nano Letters* **16**, 1974–1980 (2016).

[78] Moll, N., Gross, L., Mohn, F., Curioni, A. & Meyer, G. The mechanisms underlying the enhanced resolution of atomic force microscopy with functionalized tips. *New Journal of Physics* **12**, 125020 (2010).

[79] Jarvis, S. P., Sweetman, A. M., Kantorovich, L., McGlynn, E. & Moriarty, P. Pauli's principle in probe microscopy. In *Imaging and Manipulation of Adsorbates Using Dynamic Force Microscopy*, 1–24 (Springer, 2015).

[80] Wang, X., Ramírez-Hinestrosa, S., Dobnikar, J. & Frenkel, D. The lennard-jones potential: when (not) to use it. *Phys. Chem. Chem. Phys.* **22**, 10624–10633 (2020). URL http://dx.doi.org/10.1039/C9CP05445F.

[81] Dalgarno, A. & Davison, W. *The Calculation of Van Der Waals Interactions*, vol. 2 of *Advances in Atomic and Molecular Physics* (Academic Press, 1966). URL https://www.sciencedirect.com/science/article/pii/S006521990860216X.

[82] Hamaker, H. C. The london-van der waals attraction between spherical particules. *Physica* **4**, 1058–1072 (1937).

[83] Meyer, E. Atomic force microscopy. *Surface science* **41** (1992).

[84] Sarid, D. *Scanning Force Microscopy: with applications to electric, magnetic and atomic foces*. QH212.S32S27 (Oxford SERIES IN OPTICAL AND IMAGING SCIENCES, 1994).

[85] Grutter, P. *et al. Magneticforce microscopy.* Ph.D. thesis, University of Basel (1989).

[86] Hug, H. J. *et al.* Quantitative magnetic force microscopy on perpendicularly magnetized samples. *Journal of Applied Physics* **83**, 5609–5620 (1998).

[87] Volokitin, A. I. & Persson, B. N. J. *Theory of noncontact friction*, 393–438 (Springer Science & Business Media, 2007).

[88] Gnecco, E. & Meyer, E. *Non-contact friction*, 224–240 (Cambridge University Press, 2015).

[89] Kisiel, M. *et al. Dissipation at large scale separations*, 609–627 (Springer, 2015).

[90] Gysin, U. *et al.* Temperature dependence of the force sensitivity of silicon cantilevers. *Phys. Rev. B* **69**, 045403 (2004). URL `https://link.aps.org/doi/10.1103/PhysRevB.69.045403`.

[91] Reid, S. *et al.* Mechanical dissipation in silicon flexures. *Physics letters A* **351**, 205–211 (2006).

[92] Sun, Y., Fang, D. & Soh, A. K. Thermoelastic damping in micro-beam resonators. *International Journal of Solids and Structures* **43**, 3213–3229 (2006).

[93] Yang, J., Ono, T. & Esashi, M. Energy dissipation in submicrometer thick single-crystal silicon cantilevers. *Journal of Microelectromechanical systems* **11**, 775–783 (2002).

[94] Kumar, M., Arinero, R., Bergez, W. & Tordjeman, P. Thermo-magnetic behaviour of afm–mfm cantilevers. *Measurement Science and Technology* **26**, 085002 (2015).

[95] Kisiel, M. *et al.* Suppression of electronic friction on nb films in the superconducting state. *Nature Materials* **10**, 119–122 (2011). URL `https://doi.org/10.1038/nmat2936`.

[96] Volokitin, A., Persson, B. & Ueba, H. Giant enhancement of noncontact friction between closely spaced bodies by dielectric films and two-dimensional systems. *Journal of experimental and theoretical physics* **104**, 96–110 (2007).

[97] Dzyaloshinskii, I. E., Lifshitz, E. M. & Pitaevskii, L. P. The general theory of van der waals forces. *Advances in Physics* **10**, 165–209 (1961).

[98] Dorofeyev, I., Fuchs, H., Wenning, G. & Gotsmann, B. Brownian motion of microscopic solids under the action of fluctuating electromagnetic fields. *Physical review letters* **83**, 2402 (1999).

[99] Persson, B. Surface resistivity and vibrational damping in adsorbed layers. *Physical Review B* **44**, 3277 (1991).

[100] Cockins, L. *et al.* Energy levels of few-electron quantum dots imaged and characterized by atomic force microscopy. *Proceedings of the National Academy of Sciences* **107**, 9496–9501 (2010).

[101] Beenakker, C. W. Theory of coulomb-blockade oscillations in the conductance of a quantum dot. *Physical Review B* **44**, 1646 (1991).

[102] Miyahara, Y., Roy-Gobeil, A. & Grutter, P. Quantum state readout of individual quantum dots by electrostatic force detection. *Nanotechnology* **28**, 064001 (2017).

[103] Stomp, R. *et al.* Detection of single-electron charging in an individual inas quantum dot by noncontact atomic-force microscopy. *Physical review letters* **94**, 056802 (2005).

[104] Yildiz, D., Kisiel, M., Gysin, U., Gürlü, O. & Meyer, E. Mechanical dissipation via image potential states on a topological insulator surface. *Nature materials* **18**, 1201–1206 (2019).

[105] Brink, M. *Imaging single-electron charging in nanostructures by low-temperature scanning force microscopy.* Ph.D. thesis, Cornell University (2006).

[106] Zhu, J., Brink, M. & McEuen, P. L. Single-electron force readout of nanoparticle electrometers attached to carbon nanotubes. *Nano letters* **8**, 2399–2404 (2008).

[107] Klein, L. J. & Williams, C. C. Single electron tunneling detected by electrostatic force. *Applied Physics Letters* **79**, 1828–1830 (2001).

[108] Luryi, S. Quantum capacitance devices. *Applied Physics Letters* **52**, 501–503 (1988).

[109] Gysin, U., Rast, S., Kisiel, M., Werle, C. & Meyer, E. Low temperature ultrahigh vacuum noncontact atomic force microscope in the pendulum geometry. *Review of Scientific Instruments* **82**, 023705 (2011). URL `https://doi.org/10.1063/1.3551603`. `https://doi.org/10.1063/1.3551603`.

[110] Giessibl, F. J. Forces and frequency shifts in atomic-resolution dynamic-force microscopy. *Physical Review B* **56**, 16010 (1997).

[111] Giessibl, F. J. & Bielefeldt, H. Physical interpretation of frequency-modulation atomic force microscopy. *Physical Review B* **61**, 9968 (2000).

[112] Raman, A., Reifenberger, R. & Tung, R. *Cantilever dynamics and nonlinear effects in atomic force microscopy*, 361–395 (Springer, 2009).

[113] Söngen, H., Bechstein, R. & Kühnle, A. Quantitative atomic force microscopy. *Journal of Physics: Condensed Matter* **29**, 274001 (2017).

[114] Samadashvili, M. *Non-contact friction studied with ppendulum AFM.* Ph.D. thesis, University of Basel (2014).

[115] Advanced tip at the end of the cantilever contact mode. `https://www.nanosensors.com/advanced-tip-at-the-end-of-the-cantilever-contact-mode-afm-tip-ATEC-CONT`.

[116] Rast, S., Gysin, U. & Meyer, E. Phase noise induced due to amplitude fluctuations in dynamic force microscopy. *Phys. Rev. B* **79**, 054106 (2009). URL `https://link.aps.org/doi/10.1103/PhysRevB.79.054106`.

[117] Hapala, M., Ondracek, O., M. Stetsovich, Svec, M. & Jelinek, P. *Simultaneous nc-AFM/STM measurements with atomic resolution*, 29–49 (Springer, 2015).

[118] Castro Neto, A. H., Guinea, F., Peres, N. M. R., Novoselov, K. S. & Geim, A. K. The electronic properties of graphene. *Rev. Mod. Phys.* **81**, 109–162 (2009). URL `https://link.aps.org/doi/10.1103/RevModPhys.81.109`.

[119] Levy, N. *et al.* Strain-induced pseudo–magnetic fields greater than 300 tesla in graphene nanobubbles. *Science* **329**, 544–547 (2010).

[120] Banerjee, R. *et al.* Strain modulated superlattices in graphene. *Nano letters* **20**, 3113–3121 (2020).

[121] Wang, Y. *et al.* Room-temperature ferromagnetism of graphene. *Nano letters* **9**, 220–224 (2009).

[122] Halbertal, D. *et al.* Nanoscale thermal imaging of dissipation in quantum systems. *Nature* **539**, 407–410 (2016).

[123] Jung, S. *et al.* Evolution of microscopic localization in graphene in a magnetic field from scattering resonances to quantum dots. *Nature Physics* **7**, 245–251 (2011).

[124] Gutiérrez, C. *et al.* Interaction-driven quantum hall wedding cake–like structures in graphene quantum dots. *Science* **361**, 789–794 (2018).

[125] Langer, M. *et al.* Giant frictional dissipation peaks and charge-density-wave slips at the nbse2 surface. *Nature materials* **13**, 173–177 (2014).

[126] Wood, J. D., Schmucker, S. W., Lyons, A. S., Pop, E. & Lyding, J. W. Effects of polycrystalline cu substrate on graphene growth by chemical vapor deposition. *Nano letters* **11**, 4547–4554 (2011).

[127] Murdock, A. T. *et al.* Controlling the orientation, edge geometry, and thickness of chemical vapor deposition graphene. *ACS nano* **7**, 1351–1359 (2013).

[128] Lee, S.-M., Kim, J.-H. & Ahn, J.-H. Graphene as a flexible electronic material: mechanical limitations by defect formation and efforts to overcome. *Materials Today* **18**, 336–344 (2015).

[129] Hussain, S. *et al.* Physical and electrical properties of graphene grown under different hydrogen flow in low pressure chemical vapor deposition. *Nanoscale research letters* **9**, 1–9 (2014).

[130] Jauregui, L. A., Cao, H., Wu, W., Yu, Q. & Chen, Y. P. Electronic properties of grains and grain boundaries in graphene grown by chemical vapor deposition. *Solid State Communications* **151**, 1100–1104 (2011).

[131] Lopez-Polin, G. *et al.* Increasing the elastic modulus of graphene by controlled defect creation. *Nature Physics* **11**, 26–31 (2015).

[132] Traversi, F. *et al.* Elastic properties of graphene suspended on a polymer substrate by e-beam exposure. *New Journal of Physics* **12**, 023034 (2010).

[133] Zhang, X. & Beyer, A. Mechanics of free-standing inorganic and molecular 2d materials. *Nanoscale* **13**, 1443–1484 (2021).

[134] Nicholl, R. J. *et al.* The effect of intrinsic crumpling on the mechanics of free-standing graphene. *Nature communications* **6**, 1–7 (2015).

[135] Shioya, H., Russo, S., Yamamoto, M., Craciun, M. F. & Tarucha, S. Electron states of uniaxially strained graphene. *Nano letters* **15**, 7943–7948 (2015).

[136] Somanchi, S. *et al.* From diffusive to ballistic transport in etched graphene constrictions and nanoribbons. *Annalen der Physik* **529**, 1700082 (2017).

[137] Parga, A. V. D. & Miranda, R. *Graphene spintronic*, 124 –155 (Woodhead Publishing, 2014).

[138] Zhu, W. *et al.* Structure and electronic transport in graphene wrinkles. *Nano letters* **12**, 3431–3436 (2012).

[139] Wu, Y. *et al.* Quantum wires and waveguides formed in graphene by strain. *Nano letters* **18**, 64–69 (2018).

[140] Qiao, J.-B. *et al.* Bound states in nanoscale graphene quantum dots in a continuous graphene sheet. *Physical Review B* **95**, 081409 (2017).

[141] Echenique, P. & Pendry, J. Theory of image states at metal surfaces. *Progress in Surface Science* **32**, 111–159 (1989).

[142] Smith, N., Brookes, N., Chang, Y. & Johnson, P. Quantum-well and tight-binding analyses of spin-polarized photoemission from ag/fe (001) overlayers. *Physical Review B* **49**, 332 (1994).

[143] An, J. *et al.* Quantization condition of quantum-well states in cu/co (001). *Physical Review B* **68**, 045419 (2003).

[144] Wakabayashi, K., Fujita, M., Ajiki, H. & Sigrist, M. Electronic and magnetic properties of nanographite ribbons. *Physical Review B* **59**, 8271 (1999).

[145] Chung, H.-C., Chang, C.-P., Lin, C.-Y. & Lin, M.-F. Electronic and optical properties of graphene nanoribbons in external fields. *Physical Chemistry Chemical Physics* **18**, 7573–7616 (2016).

[146] Talirz, L. *et al.* Band gap of atomically precise graphene nanoribbons as a function of ribbon length and termination. *ChemPhysChem* **20**, 2348–2353 (2019).

[147] Tarnopolsky, G., Kruchkov, A. J. & Vishwanath, A. Origin of magic angles in twisted bilayer graphene. *Physical review letters* **122**, 106405 (2019).

[148] Lian, B., Wang, Z. & Bernevig, B. A. Twisted bilayer graphene: a phonon-driven superconductor. *Physical review letters* **122**, 257002 (2019).

[149] Cao, Y. *et al.* Tunable correlated states and spin-polarized phase in twisted bilayer-bilayer graphene. *Nature* **583**, 215–220 (2020).

[150] Chung, T.-F., Xu, Y. & Chen, Y. P. Transport measurements in twisted bilayer graphene: electron-phonon coupling and landau level crossing. *Physical review B* **98**, 035425 (2018).

[151] Island, J. O. *et al.* Spin-orbit-driven band inversion in bilayer graphene by van der waals proximity effect. *Nature* **571**, 85–89 (2019).

[152] Codecido, E. *et al.* Correlated insulating and superconducting below the magic angle. *Science advances* **5**, eaaw9770 (2019).

[153] Polshyn, H. *et al.* Large linear-in-temperature resistivity in twisted bilayer graphene. *Nature Physics* **15**, 1011–1016 (2019).

[154] Uri, A. *et al.* Mapping the twist-angle disorder and landau levels in magica-angle graphene. *Nature* **581**, 47–52 (2020).

[155] Tomarken, S. L. *et al.* Electronic compressibility of magic angle graphene superlattices. *Physical review letters* **123**, 046601 (2019).

[156] Cao, Y. *et al. Study Of electronic correlation and superconductivity in twisted graphene superlattices*. Ph.D. thesis, Massachusetts Institute of Technology (2020).

[157] Lu, X. *et al.* Superconductors, orbital magnets and correlated states in magic-angle bilayer graphene. *Nature* **574**, 653–657 (2019).

[158] Tschirhart, C. *et al.* Imaging orbital ferromagnetism in a moiré chern insulator. *Science* **372**, 1323–1327 (2021).

[159] Grover, S. *et al.* Chern mosaic and berry-curvature magnetism in magic-angle graphene. *Nature Physics* 1–8 (2022).

[160] Zondiner, U. *et al.* Cascade of phase transitions and dirac revivals in magic-angle graphene. *Nature* **582**, 203–208 (2020).

[161] Rhodes, D., Chae, S. H., Ribeiro-Palau, R. & Hone, J. Disorder in van der waals heterostructures of 2d materials. *Nature materials* **18**, 541–549 (2019).

[162] Ponomarenko, L. A. *et al.* Cloning of dirac fermions in graphene superlattices. *Nature* **497**, 594–597 (2013).

[163] Tiwari, P., Srivastav, S. K., Ray, S., Das, T. & Bid, A. Quantum spin hall effect in bilayer graphene heterostructures. *arXiv: Mesoscale and Nanoscale Physics* (2020).

[164] Oka, T. *et al.* Ballistic transport experiment detects fermi surface anisotropy of graphene. *Physical Review B* **99**, 035440 (2019).

[165] Zhang, Y. *et al.* Distinct signatures for coulomb blockade and aharonov-bohm interference in electronic fabry-perot interferometers. *Physical Review B* **79**, 241304 (2009).

[166] Rosenow, B. & Halperin, B. Influence of interactions on flux and back-gate period of quantum hall interferometers. *Physical review letters* **98**, 106801 (2007).

[167] Ronen, Y. *et al.* Aharonov–bohm effect in graphene-based fabry–pérot quantum hall interferometers. *Nature nanotechnology* **16**, 563–569 (2021).

[168] Hasan, M. Z. & Kane, C. L. Colloquium: topological insulators. *Reviews of modern physics* **82**, 3045 (2010).

[169] Xiao, D., Liu, G.-B., Feng, W., Xu, X. & Yao, W. Coupled spin and valley physics in monolayers of mos 2 and other group-vi dichalcogenides. *Physical review letters* **108**, 196802 (2012).

[170] Chernikov, A. *et al.* Exciton binding energy and nonhydrogenic rydberg series in monolayer ws 2. *Physical review letters* **113**, 076802 (2014).

[171] Mak, K. F. *et al.* Tightly bound trions in monolayer mos2. *Nature materials* **12**, 207–211 (2013).

[172] Yang, X. & Li, B. Monolayer mos2 for nanoscale photonics. *Nanophotonics* **9**, 1557–1577 (2020).

[173] Li, X. & Wu, X. Two-dimensional monolayer designs for spintronics applications. *Wiley Interdisciplinary Reviews: Computational Molecular Science* **6**, 441–455 (2016).

[174] Park, J.-G. Opportunities and challenges of two-dimensional magnetic van der waals materials: magnetic graphene. *arXiv preprint arXiv:1604.08833* (2016).

[175] Kormányos, A. *et al.* Monolayer mos 2: Trigonal warping, the γ valley, and spin-orbit coupling effects. *Physical review b* **88**, 045416 (2013).

[176] Ahmad, S. & Mukherjee, S. A comparative study of electronic properties of bulk mos2 and its monolayer using dft technique: application of mechanical strain on mos2 monolayer. *Nature* (2014).

[177] Yue, Q. *et al.* Mechanical and electronic properties of monolayer mos2 under elastic strain. *Physics Letters A* **376**, 1166–1170 (2012).

[178] Molina-Sanchez, A., Hummer, K. & Wirtz, L. Vibrational and optical properties of mos2: From monolayer to bulk. *Surface Science Reports* **70**, 554–586 (2015).

[179] Ermolaev, G. A. *et al.* Broadband optical properties of monolayer and bulk mos2. *npj 2D Materials and Applications* **4**, 1–6 (2020).

[180] Ataca, C., Sahin, H., Akturk, E. & Ciraci, S. Mechanical and electronic properties of mos2 nanoribbons and their defects. *The Journal of Physical Chemistry C* **115**, 3934–3941 (2011).

[181] Zhao, X., Xia, C., Wang, T. & Dai, X. Effect of structural defects on electronic and magnetic properties of pristine and mn-doped mos2 monolayer. *Solid State Communications* **220**, 31–35 (2015).

[182] Pan, H. & Zhang, Y.-W. Edge-dependent structural, electronic and magnetic properties of mos 2 nanoribbons. *Journal of Materials Chemistry* **22**, 7280–7290 (2012).

[183] Wang, Y., Li, S. & Yi, J. Electronic and magnetic properties of co doped mos2 monolayer. *Scientific reports* **6**, 1–9 (2016).

[184] He, J., Wu, K., Sa, R., Li, Q. & Wei, Y. Magnetic properties of nonmetal atoms absorbed mos 2 monolayers. *Applied Physics Letters* **96**, 082504 (2010).

[185] Scalise, E., Houssa, M., Pourtois, G., Afanas'ev, V. & Stesmans, A. Strain-induced semiconductor to metal transition in the two-dimensional honeycomb structure of mos2. *Nano Research* **5**, 43–48 (2012).

[186] Tao, P., Guo, H., Yang, T. & Zhang, Z. Strain-induced magnetism in mos2 monolayer with defects. *Journal of Applied Physics* **115**, 054305 (2014).

[187] Li, J. *et al.* Spontaneous valley polarization of interacting carriers in a monolayer semiconductor. *Physical Review Letters* **125**, 147602 (2020).

[188] Sharpe, A. L. *et al.* Evidence of orbital ferromagnetism in twisted bilayer graphene aligned to hexagonal boron nitride. *Nano Letters* **21**, 4299–4304 (2021). URL `https://doi.org/10.1021/acs.nanolett.1c00696`. PMID: 33970644, `https://doi.org/10.1021/acs.nanolett.1c00696`.

[189] Roch, J. G. *et al.* First-order magnetic phase transition of mobile electrons in monolayer mos 2. *Physical review letters* **124**, 187602 (2020).

[190] Kisiel, M. *et al.* Noncontact dissipation reveals critical central peak in srtio3. *arXiv preprint arXiv:1506.01306* (2015).

[191] Jurg Handschin, C. *et al. Quantum transport in encapsulated graphene P-N junctions.* Ph.D. thesis, University of Basel (2017).

[192] Wang, L. *et al.* One-dimensional electrical contact to a two-dimensional material. *Science* **342**, 614–617 (2013). URL `https://www.science.org/doi/abs/10.1126/science.1244358`. `https://www.science.org/doi/pdf/10.1126/science.1244358`.

[193] Pisoni, R. *et al.* Gate-tunable quantum dot in a high quality single layer mos2 van der waals heterostructure. *Applied Physics Letters* **112**, 123101 (2018).

[194] Mak, K. F., McGill, K. L., Park, J. & McEuen, P. L. The valley hall effect in mos2 transistors. *Science* **344**, 1489–1492 (2014).

[195] Gysin, U. *et al.* Magnetic properties of nanomagnetic and biomagnetic systems analyzed using cantilever magnetometry. *Nanotechnology* **22**, 285715 (2011).

[196] Stipe, B., Mamin, H., Stowe, T., Kenny, T. & Rugar, D. Magnetic dissipation and fluctuations in individual nanomagnets measured by ultrasensitive cantilever magnetometry. *Physical Review Letters* **86**, 2874 (2001).

[197] Hölscher, H. & Schwarz, U. Q-controlled amplitude modulation atomic force microscopy in liquids: An analysis. *Applied physics letters* **89**, 073117 (2006).

[198] Mak, K. F., Lee, C., Hone, J., Shan, J. & Heinz, T. F. Atomically thin mos 2: a new direct-gap semiconductor. *Physical review letters* **105**, 136805 (2010).

[199] Miserev, D., Klinovaja, J. & Loss, D. Exchange intervalley scattering and magnetic phase diagram of transition metal dichalcogenide monolayers. *Phys. Rev. B* **100**, 014428 (2019). URL `https://link.aps.org/doi/10.1103/PhysRevB.100.014428`.

[200] Ashcroft, N. W. & Mermin, N. D. *Physique des solides* (EDP sciences, 2012).

[201] Shashkin, A. *et al.* Pauli spin susceptibility of a strongly correlated two-dimensional electron liquid. *Physical review letters* **96**, 036403 (2006).

[202] Bogoslovskiy, N., Petrov, P. & Averkiev, N. The impurity magnetic susceptibility of semiconductors in the case of direct exchange interaction in the ising model. *Physics of the Solid State* **61**, 2005–2009 (2019).

[203] Kuwahara, H., Tomioka, Y., Asamitsu, A., Moritomo, Y. & Tokura, Y. A first-order phase transition induced by a magnetic field. *Science* **270**, 961–963 (1995).

Supplementary Materials

Supplementary Material For Non-Contact Friction

S3:1. Displacement Durrent and Joule Dissipation

Dissipated power:

$$P = I^2 \cdot R = V_B \cdot I \tag{0.1}$$

where I, R, V_B stand for displacement current, resistance and bias voltage. When a voltage V_B is applied between tip and sample the displacement current induced by the oscillating tip is equal to:

$$i_d = \dot{q}(t) = \dot{C}(V_B - V_{CPD}) = \frac{\partial C}{\partial z}\frac{\partial z}{\partial t}(V_B - V_{CPD}) \tag{0.2}$$

where C is tip-sample capacitance, V_{CPD} is the tip-sample contact potential difference equal to the difference of tip and sample workfunctions $\Delta\phi$. The tip oscillations are equal to: $z(t) = Asin(\omega t + \Phi)$ and the dissipated power reads as follows:

$$P = R \cdot i_d^2 = R(\frac{\partial C}{\partial z})^2(V_B - V_{CPD})^2(\frac{\partial z}{\partial t})^2 \tag{0.3}$$

where $\gamma = R(\frac{\partial C}{\partial z})^2(V_B - \Delta\phi)^2$ is the effective damping coefficient proportional to the resistance of the sample in the current path. The dissipated power is:

$$P = R(\frac{\partial C}{\partial z})^2(V_B - \Delta\phi)^2(-A\omega^2 sin(\omega t + \Phi)) \tag{0.4}$$

and the dissipated power averaged over one period of oscillations:

$$< P >= \frac{1}{2}RA^2\omega^2(V_B - \Delta\phi)^2(\frac{\partial C}{\partial z})^2 \tag{0.5}$$

In the case of a capacitively coupled oscillating cantilever above the sample the energy of the system is given by $E = \frac{1}{2}(\frac{\partial C}{\partial z})(V_B - \Delta\phi)^2$.

The oscillation frequency of the sensor is determined by the effective change of the cantilever stiffness due to force interaction:

$$f = \frac{1}{2\pi}\sqrt{\frac{k + \frac{\partial F}{\partial z}}{m}} \tag{0.6}$$

Taking into account, that frequency is defined as: $\Delta f = f - f_0$, where f_0 is the free cantilever oscillation frequency, we can write:

$$\frac{\Delta f}{f_0} + 1 = \sqrt{1 + \frac{k_{ts}}{k}} \tag{0.7}$$

where $k_{ts} = \frac{\partial F}{\partial z}$. Developing the right side of the equation into series and assuming weak force interaction compared to stiffness $k_{ts} << k$ the frequency shift is given by:

$$\Delta f = -\frac{f_0}{2k}k_{ts} = -\frac{f_0}{2k}(\frac{\partial F}{\partial z}) \tag{0.8}$$

Finally, for capacitively coupled tip and sample:

$$\Delta f = \frac{f_0}{4k}(\frac{\partial^2 C}{\partial z^2})(V_B - \Delta\phi)^2 \tag{0.9}$$

Supplementary Material For Pendulum AFM

S4:1

In pendulum geometry the cantilever Δf induced by the interaction forces depends on both normal axial and lateral force gradient. In this case the lateral force gradient can be neglected, the dominant interactions are the axial forces since $\omega \ll \omega_0$.

In the case of a symmetric tip and a rectangular lever the frequency dependence versus the force is given by the equation of motion of the vibrating lever. In the presence of external axial force N the equation of motion can be approximated as:

$$\frac{d^4}{dz^4}x\left(z\right)+\frac{N}{EI}\frac{d^2}{dz^2}x\left(z\right)=x\left(z\right)\lambda \tag{0.10}$$

where E is the Young modulus, I-th the area moment of inertia, ρ the mass density, $z=ZL$ the lever elongation, L the lever length and $A=\frac{N}{EI}\cdot L^2$ the lever cross-section. Equation 0.10 can be rewrote as:

$$\frac{d^4}{dZ^4}x\left(Z\right)+A\frac{d^2}{dZ^2}x\left(Z\right)-\Lambda x\left(Z\right)=0 \tag{0.11}$$

with $\Lambda=\lambda\cdot L^4$.

The general solution of equation 0.11 as a form of:

$$\begin{aligned}x(Z)=\,&c1\,\cos\left(\sqrt{a+b}Z\right)+c2\,\sin\left(\sqrt{a+b}Z\right)+\\&+c3\,\cosh\left(\sqrt{-a+b}Z\right)+c4\,\sinh\left(\sqrt{-a+b}Z\right)\end{aligned} \tag{0.12}$$

where $a=\frac{1}{2}A$ and $b=\frac{1}{2}\sqrt{A^2+4\Lambda}$.

The oscillations induces a deformation of the lever shape, the corresponding boundary conditions for deflected, slope moment and share force become: $x(0)=\frac{dx}{dZ}_{(x=0)}=0$ and $\frac{d^2x}{dZ^2}_{(x=1)}=\frac{d^3x}{dZ^3}_{(x=1)}=0$ and $x(Z)$ can be expressed as follow:

$$\begin{aligned}x(Z)=\;&c_1\left(\cos\left(\sqrt{a+b}Z\right)+\right.\\&\frac{\left(-\cos\left(\sqrt{a+b}\right)a-\cos\left(\sqrt{a+b}\right)b+\cosh\left(\sqrt{-a+b}\right)a-\cosh\left(\sqrt{-a+b}\right)b\right)\sqrt{-a+b}\sin\left(\sqrt{a+b}Z\right)}{\left(\sqrt{-a+b}\sqrt{a+b}\sin\left(\sqrt{a+b}\right)-\sinh\left(\sqrt{-a+b}\right)a+\sinh\left(\sqrt{-a+b}\right)b\right)\sqrt{a+b}}-\\&-\cosh\left(\sqrt{-a+b}Z\right)-\\&\left.\frac{\left(-\cos\left(\sqrt{a+b}\right)a-\cos\left(\sqrt{a+b}\right)b+\cosh\left(\sqrt{-a+b}\right)a-\cosh\left(\sqrt{-a+b}\right)b\right)\sinh\left(\sqrt{-a+b}Z\right)}{\sqrt{-a+b}\sqrt{a+b}\sin\left(\sqrt{-a+b}\right)b}\right)\end{aligned}$$

At the boundary condition $x=0$ the equation become:

$$\begin{aligned}0=\,&-a^2\cos\left(\sqrt{a+b}\right)\cosh\left(\sqrt{-a+b}\right)+a^2+\\&+a\sqrt{-a+b}\sin\left(\sqrt{a+b}\right)\sqrt{a+b}\sinh\left(\sqrt{-a+b}\right)+\\&+b^2+\cos\left(\sqrt{a+b}\right)\cosh\left(\sqrt{-a+b}\right)b^2\end{aligned} \tag{0.13}$$

This equation can be easily solved numerically and the solution of a and b can be approximated with a fourth order polynomial as follow:

$$b = 3.516 + 0.221 \cdot a + 0.146 \cdot a^2 - 0.003 \cdot a^3 - 0.001 \cdot a^4 \tag{0.14}$$

$$= b_0 + b_1 \cdot a + b_2 \cdot a^2 + b_3 \cdot a^3 + b_4 \cdot a^4 \tag{0.15}$$

In addition to that, the case of $N = 0$, equation 0.13 reduces to the free-oscillating lever [84]:

$$\cos\left(\sqrt[4]{\lambda}L\right)\cosh\left(\sqrt[4]{\lambda}L\right) + 1 = 0 \tag{0.16}$$

The unperturbed system is obtained for $a = \frac{NL^2}{2EI} = 0$ and $b = b_0 = 3.516$ [84]. In the special case of $a \ll 1$ corresponding of a lack of longitudinal elongation of the lever, equation 0.15 reduces to:

$$b = b_0 + b_1 \cdot a = 3.516 + 0.221 \cdot a \tag{0.17}$$

and the eigenvalue λ:

$$\lambda = \frac{{b_0}^2}{L^4} + \frac{b_0\, b_1\, N}{L^2 EI} \tag{0.18}$$

The eigenfrequency of the cantilever in the presence of normal axial force is then equal:

$$\omega = \omega_0 \sqrt{1 + \frac{b_1\, NL^2}{b_0\, EI}} \tag{0.19}$$

The resulting static normal force (N) acting on the cantilever in pendulum geometry is given by:

$$N = \frac{2}{3}\frac{b_0 L k_0}{b_1 \omega_0}\Delta\omega \tag{0.20}$$

where b_i are constants, L the cantilever length, k_0 the cantilever spring constant, ω_0 the cantilever resonant frequency and $\Delta\omega$ the frequency shift.

Supplementary Material For Magnetic Tuning Of Mechanical Dissipation In Quantum Graphene

S5:1. Young Modulus of Graphene - Indentation Graphene Membrane

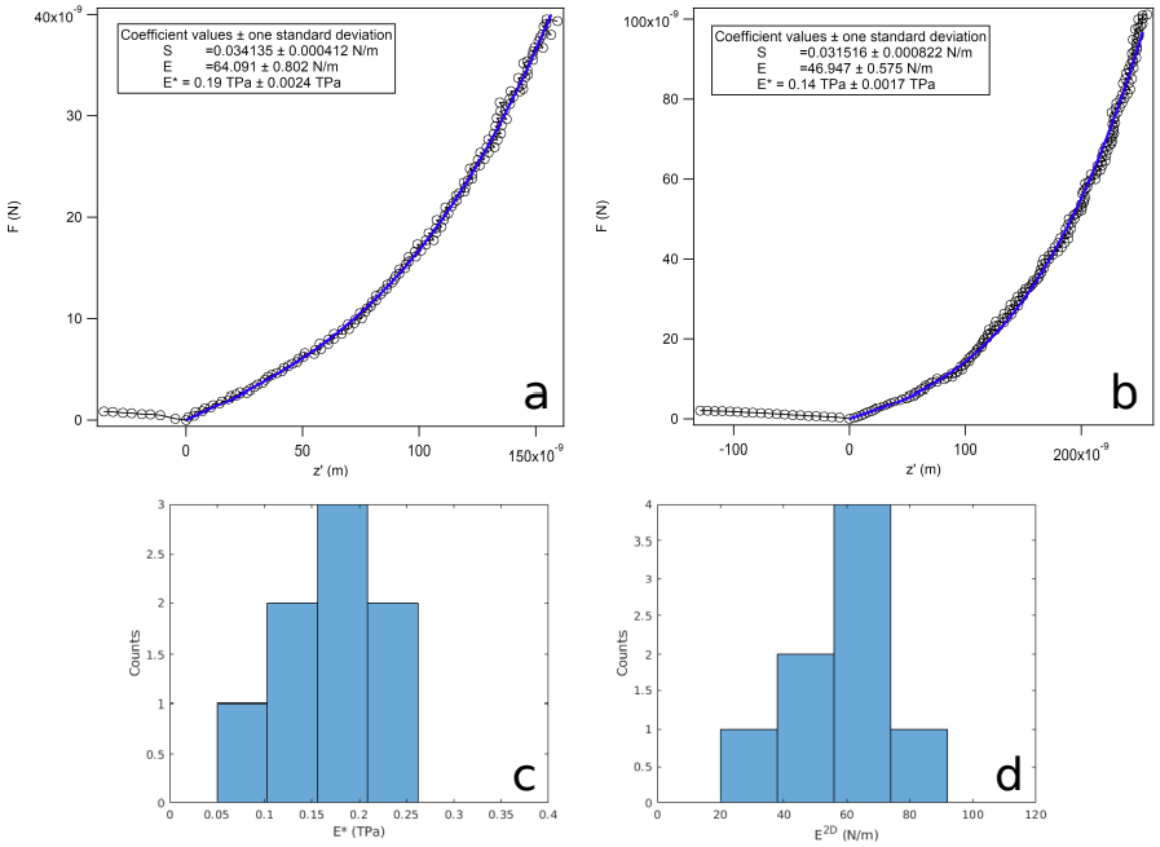

Figure c.1: — ***a)*** *and* ***b)*** *are two loading curves for two different peak forces (40 nN and 100 nN), both taken in the middle of the membrane. Z is the indentation depth and F is the loading force.* ***c)*** *and* ***d)*** *show histograms of the measured E_{2D} and $E = E_{2D}/0.34$ nm of the drumheads. The obtained values are $E_{2D} = 60$ N/m and $E = 0.2\,TPa$. The values are about 5 times smaller compared to the literature data for exfoliated graphene. The pre-tension accumulated in the membranes is equal to about $\sigma_0 = 0.03\ N - m^{-1}$.*

S5:2. Tunnelling rates calculation

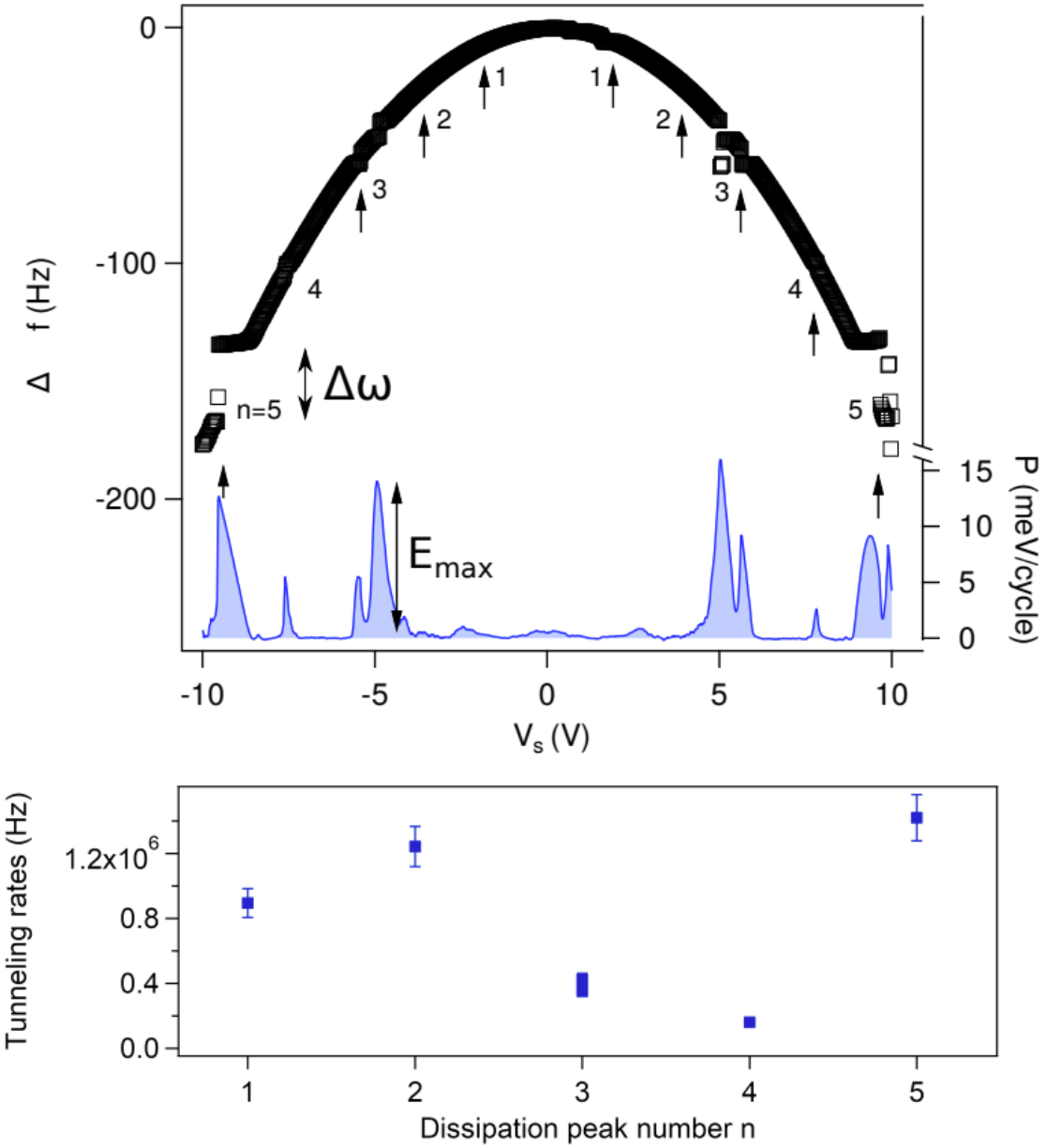

Figure c.2: — *Top: Δf (in black) and the corresponding dissipation (in blue) spectra versus sample voltage V_S. $\Delta\omega$ is the height of the kink in the frequency shift spectra, while E_{max} is the maximum of the dissipation peak. Bottom: The calculated tunnelling rates γ during single electron charging process for different n quantum number.*

S5:3. Tight binding calculations

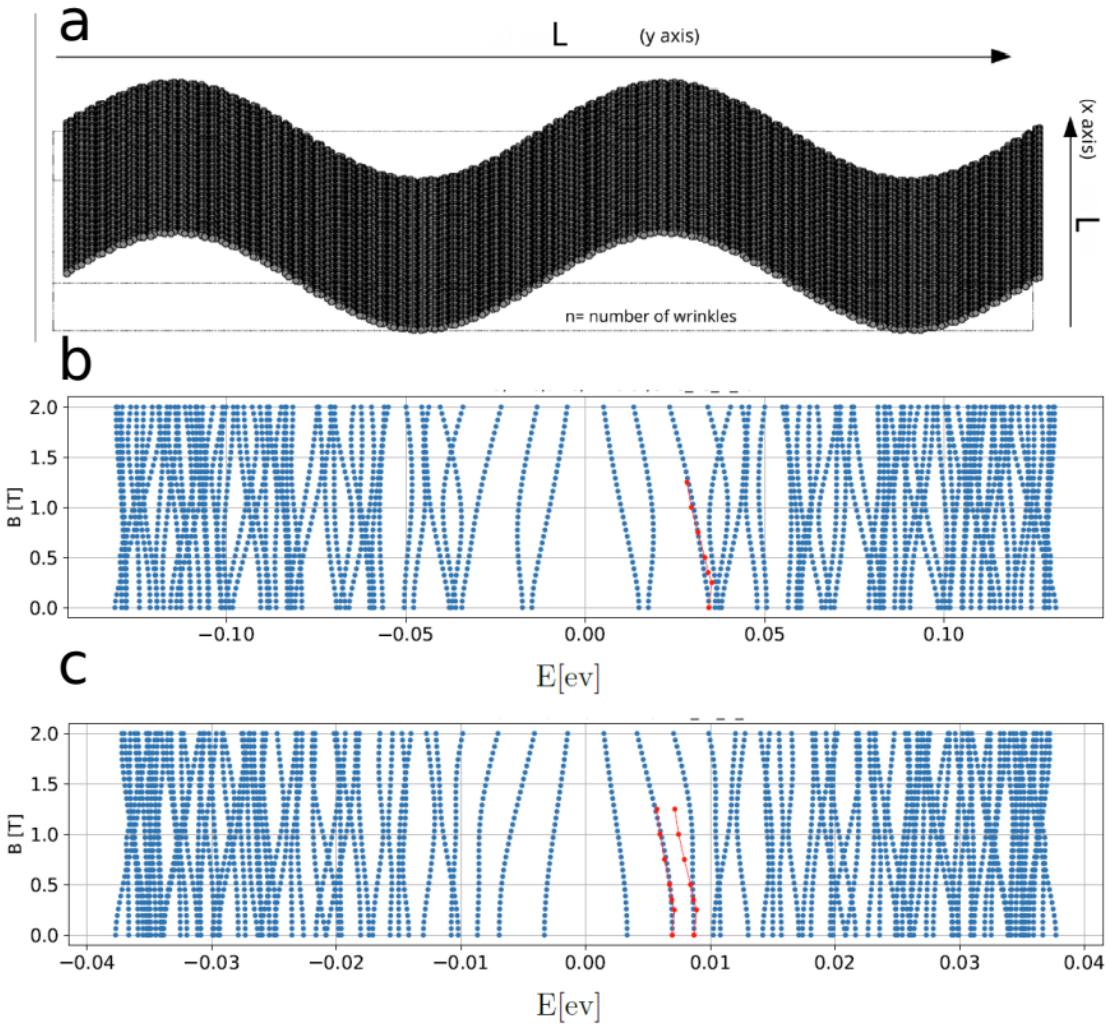

Figure c.3: — *Tight binding calculation results of the $L = L_y = 75\ nm$ graphene flake.* ***a)*** *shows the wrinkled flake shape used in the calculations.* ***b)*** *and* ***c)*** *show energy levels for flat and wrinkled graphene with a square shape and a size of $L = 75\ nm$. The red line is a pick of the experiment. In both cases, wrinkled and flat surface, are in good agreement between calculations and experiments.*

In order to understand the experiments, a tight binding calculation was performed, we consider the graphene flake shown in figure c.3 a) with a square shape, where the characteristic size of the flake is $L = 75\ nm$. The calculation is done in open boundary condition, adding 2 eV on carbon atoms with dangling bond to get rid of edge states. To apply a vertical magnetic field we used a linear gauge varying along the wrinkles (x axis) $A = (B_y, 0, 0)$. The Peierls phase is calculated by centering the gauge in the middle of the flake for symmetry reasons. Figures c.3 b) and c) show the B-field dependent energy structure of graphene flake without and with the wrinkles respectively.

In both cases, we found a good agreement with the experimental data, marked by the red line. The experimental line in counter weighted on the second/third level of our calculation, with a scale ratio of 10^3 to 10^4. By matching the experimental line with the calculated levels. The tight-binding calculation reproduces well the experimental data recorded at two different distances (figure c.5). Moreover, we found a good agreement between the experiments and the calculations for both wrinkled (Fig. c.3 b) and the flat (figure c.3 c) graphene. Thus, we conclude that 2 nm wrinkles in the graphene sheet do not alter importantly either the magnetic field dependence or the effective size $L_y = 75\ nm$.

Knowing that different size of the graphene flakes were calculated and it was found out that a ratio of 8 between L_x and L_y is best describing our measurements in terms of energy. Figure c.4 shows two size calculations, $L_x = L_y = 75\ nm$ and $L_x = 37\ nm$ and $L_y = 300\ nm$ for a) and b) respectively. It is remarkably visible that the effective size of the graphene flake does not change the confinement much. The rectangular shape of the flake is reproducing the energy levels better, especially the kink visible at $B = 0.25\ T$. The calculations revealed that the main parameter that has to be conserved is the coefficient 8 between L_x and L_y.

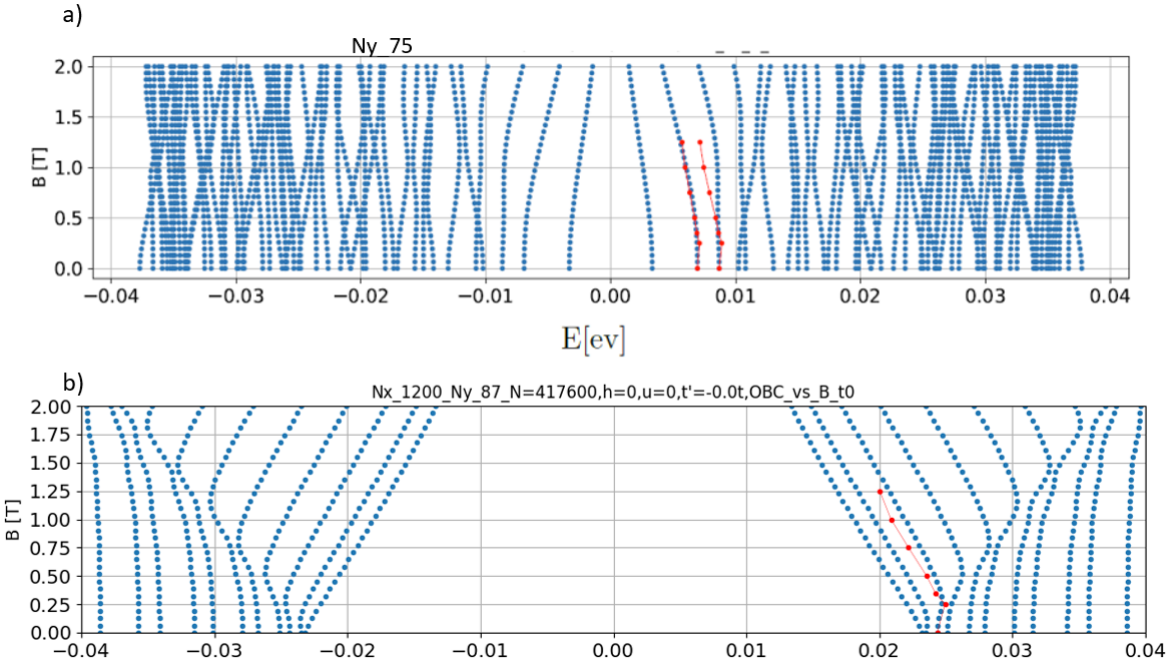

Figure c.4: — *Tight binding calculation results of the different size,* 300 *nm graphene flakes.* ***a*** *and* ***b*** *show energy levels for* $L = L_y = 75\ nm$ *and* $L_x = 37\ nm$ *graphene flakes respectively.*

S5:4. Energy Dissipation at Different Tip-Sample Distances

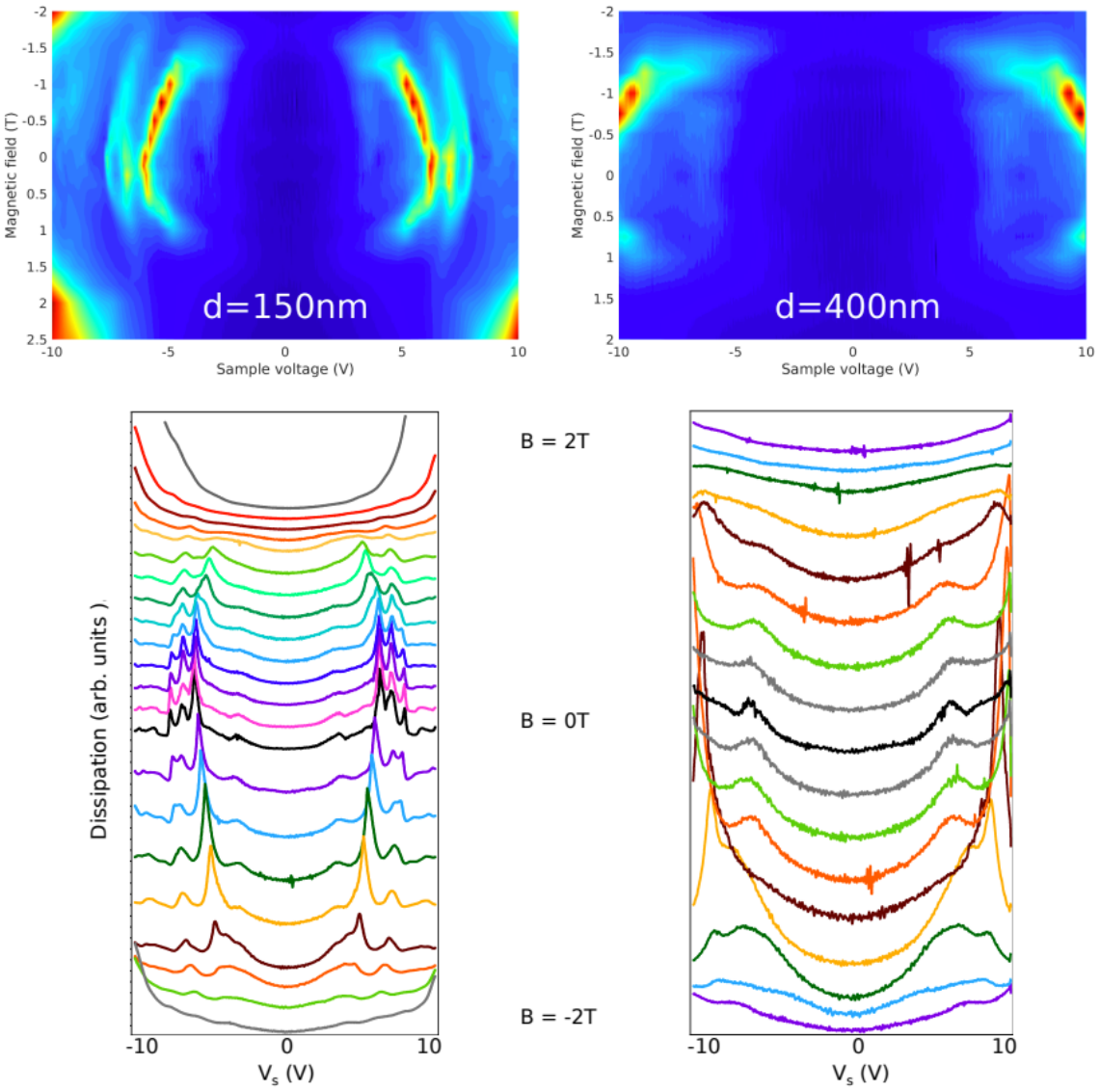

Figure c.5: — *Energy dissipation as a function of B changing in the range of $0\ T \leq B \leq 2\ T$ measured at $T = 5\ K$ on the suspended graphene surface at two different distances. On the left panel the dissipation is obtained at a distance $d = 150\ nm$, whereas on the right panel the dissipation was measured at a distance $d = 400\ nm$. Top images are the dissipation maps and the lower graphs are the corresponding raw data offsetted for better visibility. As the magnetic field rises, the amount of dissipation features is reduced and the linear shift towards small tip-sample voltage is observed.*

Supplementary Material For Twisted Bilayer Graphene At The Magic Angle

S6:1. Frequency Shift Data

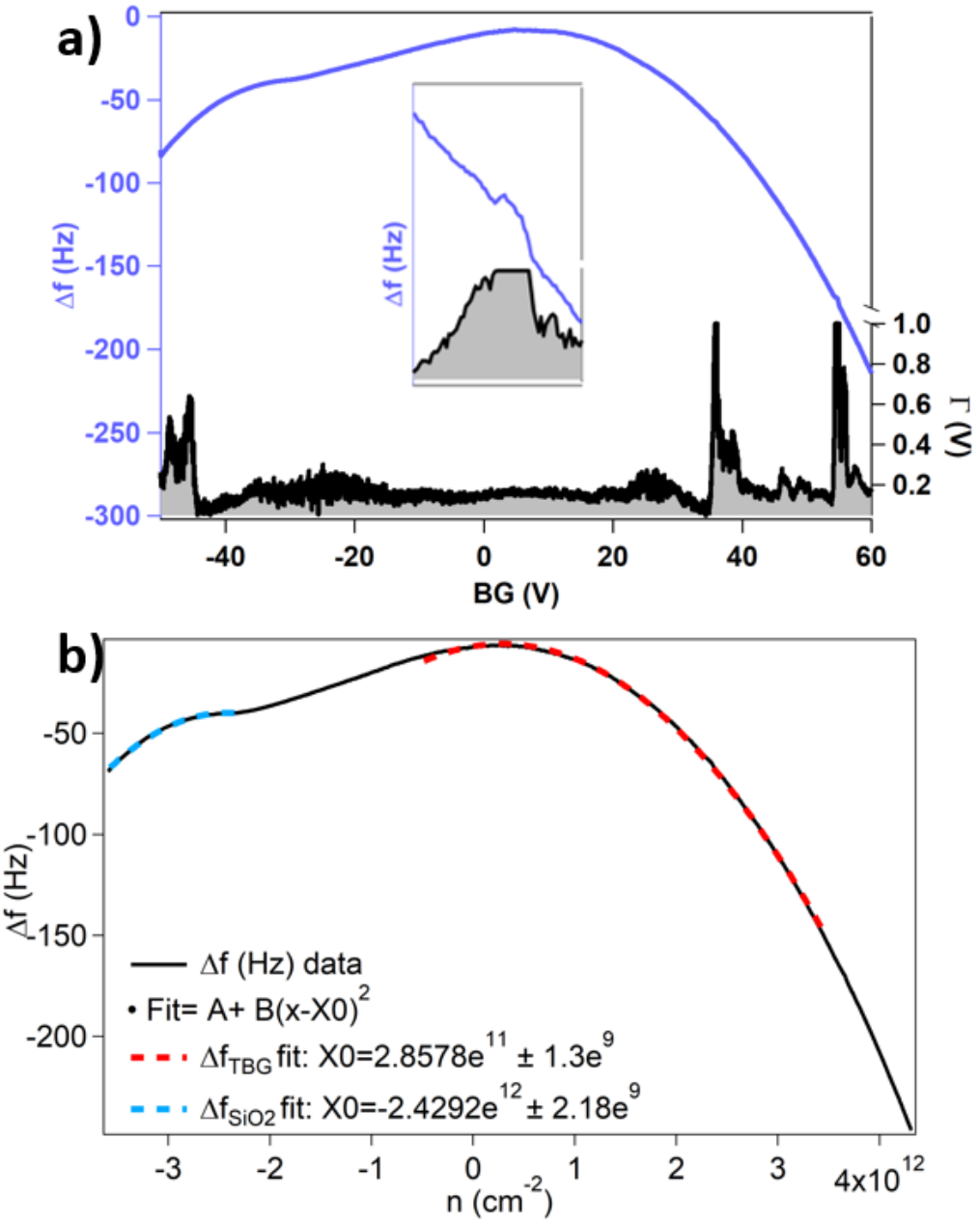

Figure c.6: — Γ *and* $\Delta f(Hz)$ *spectra over TBG in black and blue, respectively. The* $\Delta f(Hz)$ *shows double parabola attributed to the silicon substrate and the TBG respectively.*

S6:2. Depletion Capacitance Correction

Figure c.7 a) shows the capacitance model for a MOS system, were different phases are visible: accumulation, depletion and inversion. In the accumulation phase, the capacitance is big and the capacitor behaves likes a plate capacitor $C_i = \epsilon_i/d$ where ϵ_i is the permittivity of the material and d its thickness. As the voltage increase the depletion region starts to appear. In this region the electrons (holes for p-doped materials) are moved out from metal layers that are depleted, increasing virtually the oxide layer thickness (Fig. c.7 c)), inducing the dropping of the capacitance value. The depletion width is noted W_D and the depletion capacitance C_D emerges and has to be added in the total capacitance C.

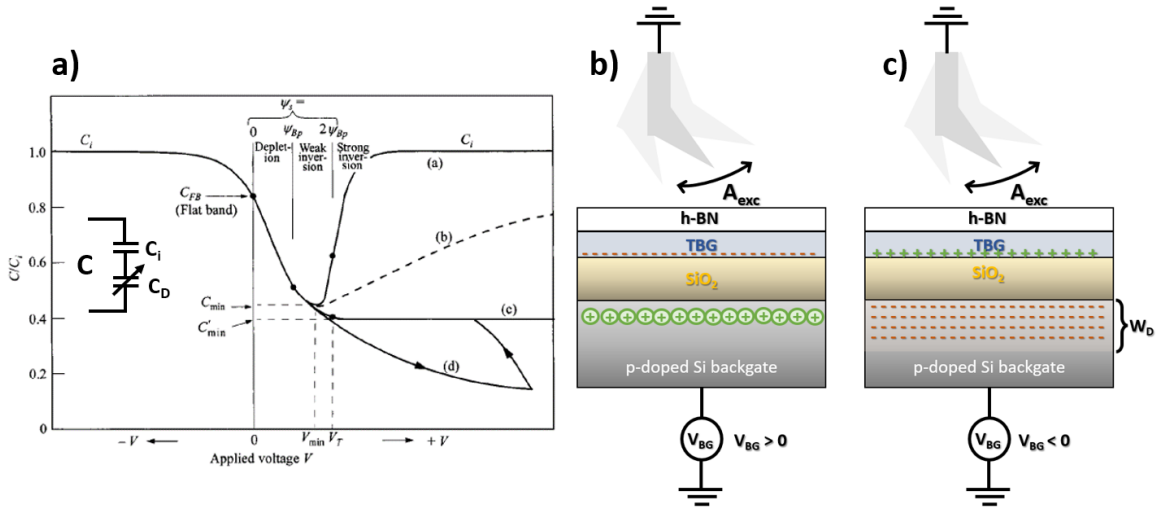

Figure c.7: — ***a)*** *Capacitance model of a MOS system [4] that is the combination of an oxide and voltage dependent semiconductors.* ***b)*** *is the schematic of the accumulation regime where the electrons (-) gets accumulated at the sample surface when a positive voltage is applied.* ***c)*** *is the depletion process schematic, the electrons are pushed away from the surface leaving a holes reside (+) in the surface. The p-AFM cantilever is made of highly n-doped silicon and behaves as a metal due to its doping.*

The backgate is a p-doped silicon wafer, when a positive voltage is applied to it all the electrons gets accumulated under the sample surface (Fig. c.7 b)) but when the voltage becomes negative the holes are sucked out creating a depletion region (Fig. c.7 c)). To overcome this, the depletion width (W_D) and capacitance (C_D) were calculated and corrected using [4]:

$$W_D = \sqrt{\frac{\epsilon_s^2}{C_{ox}^2} + \frac{2\epsilon_s V}{qN_D}} - \frac{\epsilon_s}{C_{ox}} \tag{0.21}$$

$$C_D = \sqrt{\frac{\epsilon_s q P_{po}}{2\psi_s}} = \frac{\epsilon_s}{W_D} \tag{0.22}$$

where $\epsilon_s = 11.7$ is the silicon permittivity, C_{ox} the oxide capacitance, N_D the concentration of donors, P_{po} the carrier concentration of a p-type semiconductor and ψ_s is

the build-in potential.

$$C = \frac{C_i C_D}{C_i + C_D} \tag{0.23}$$

The raw and the corrected dissipation spectra are presented in figure c.8 is a) and b) respectively. The depletion enabled to correct the width and the position of the peaks in the hole part. This correction was used to identify the FF visible in the hole part.

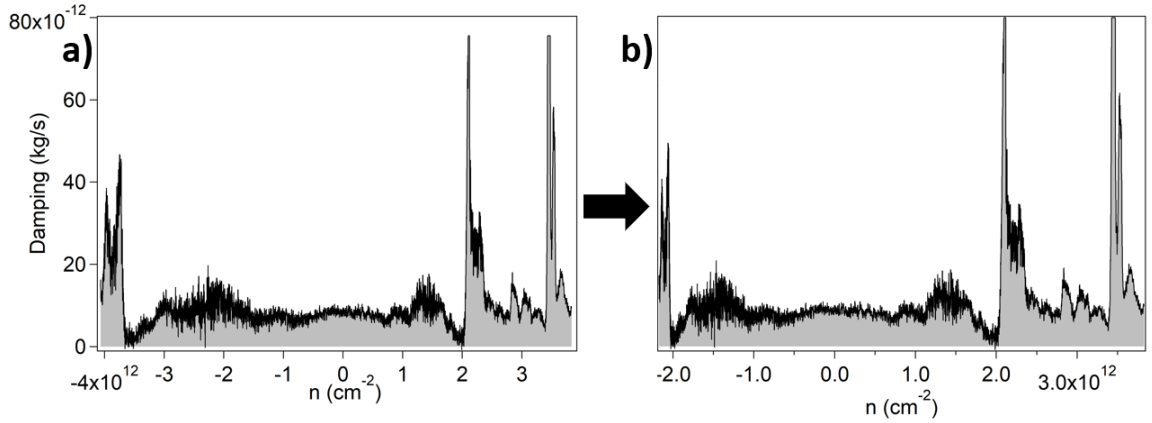

Figure c.8: — ***a)*** *dissipation curve before depletion correction.* ***b)*** *dissipation curve after depletion correction.*

S6:3. Γ Maps For Incompressible Regions Under B-Field

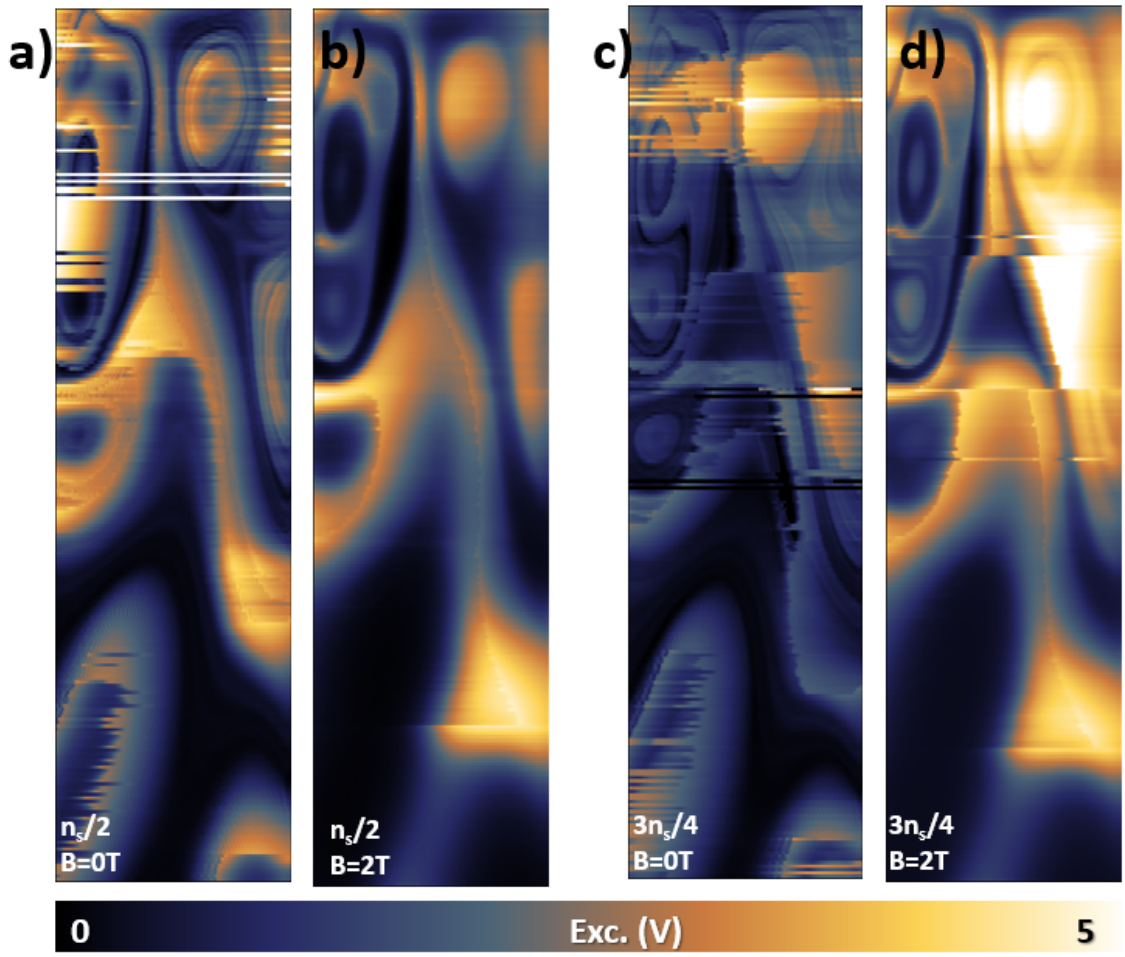

Figure c.9: — *Excitation images taken above the incompressible region, the size of the image is* $200\ nm \times 1\mu m$. ***a)*** *and* ***b)*** $n_s/2$ *maps under* $B = 0\ T$ *and* $B = 2\ T$. ***c)*** *and* ***d)*** $3n_s/4$ *maps taken at* $B = 0\ T$ *and* $B = 2\ T$. *In this case the domains and the Coulomb rings does not vanish when a* B*-field is applied.*

S6:4. Frequency-Shift Magnetic Sweeps

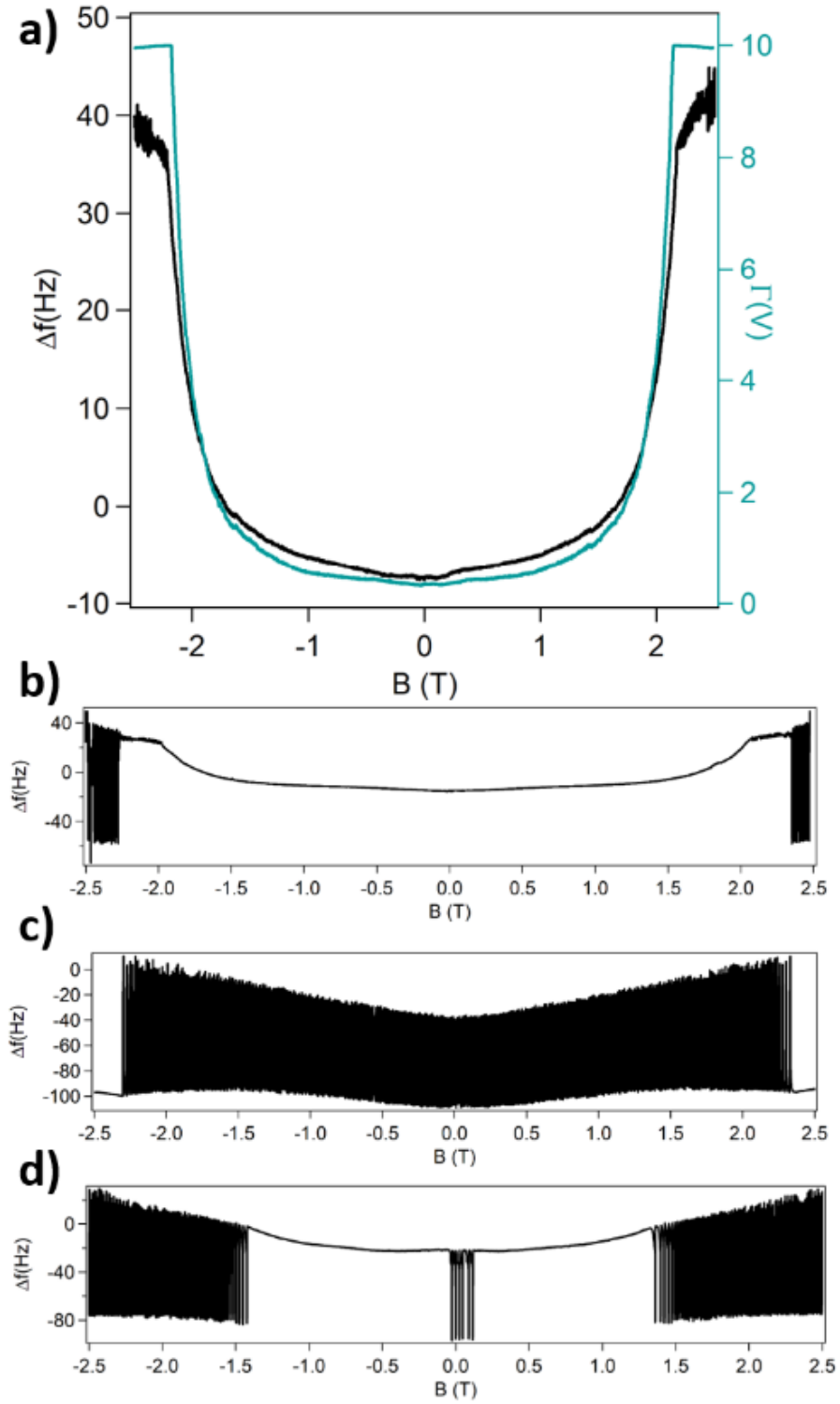

Figure c.10: — Δf *versus magnetic field sweep.* ***a)*** *dissipation and frequency-shift curve for* $n_s/4$ *filling.* ***b)*** *-* ***d)*** Δf *curves for* $n_s/2$, $3n_s/4$ *and* $3n_s/4 < n < n_s$ *FF.*

Supplementary Material For MoS_2 Monolayer

S7:1. PMMA Curves

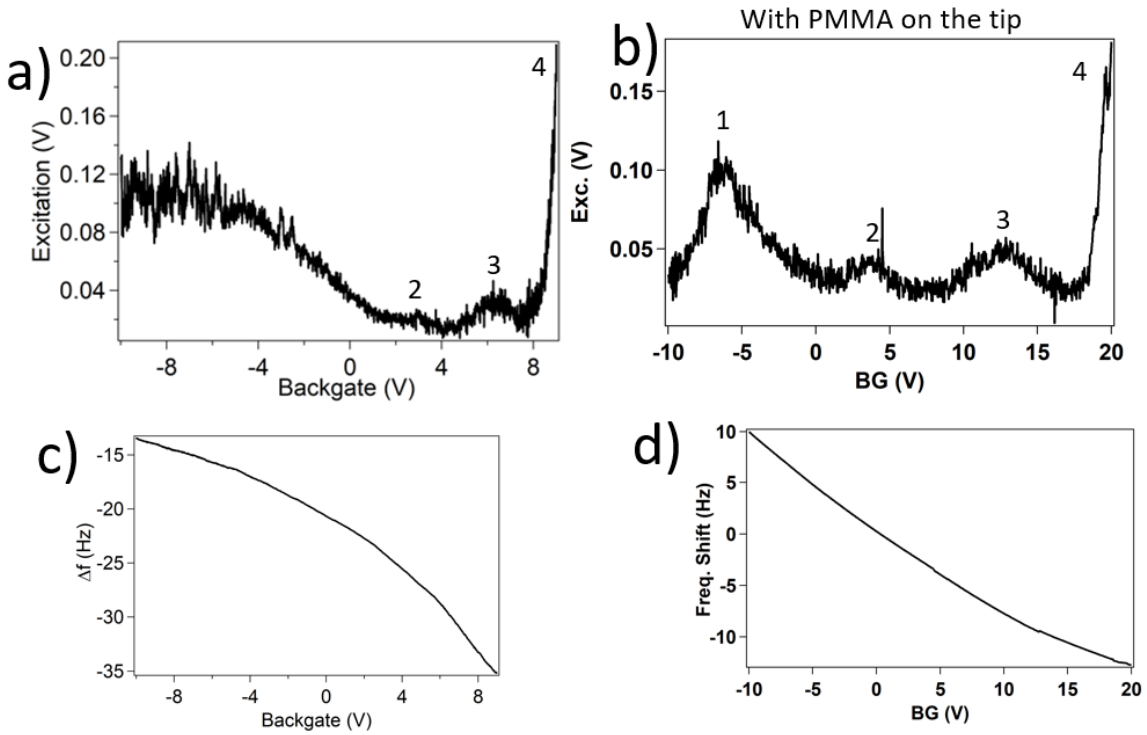

Figure c.11: — *Measurement with nonmagnetic tip over MoS_2.* ***a)*** *and* ***b)*** $\Gamma(V)$ *curves over MoS_2 with and without PMMA on the tip, respectively.* ***c)*** *and* ***d)*** *corresponding $\Delta f(Hz)$ curves where a change of the curvature is visible when PMMA is on the tip.*

S7:2. Magnetic Tip Fabrication

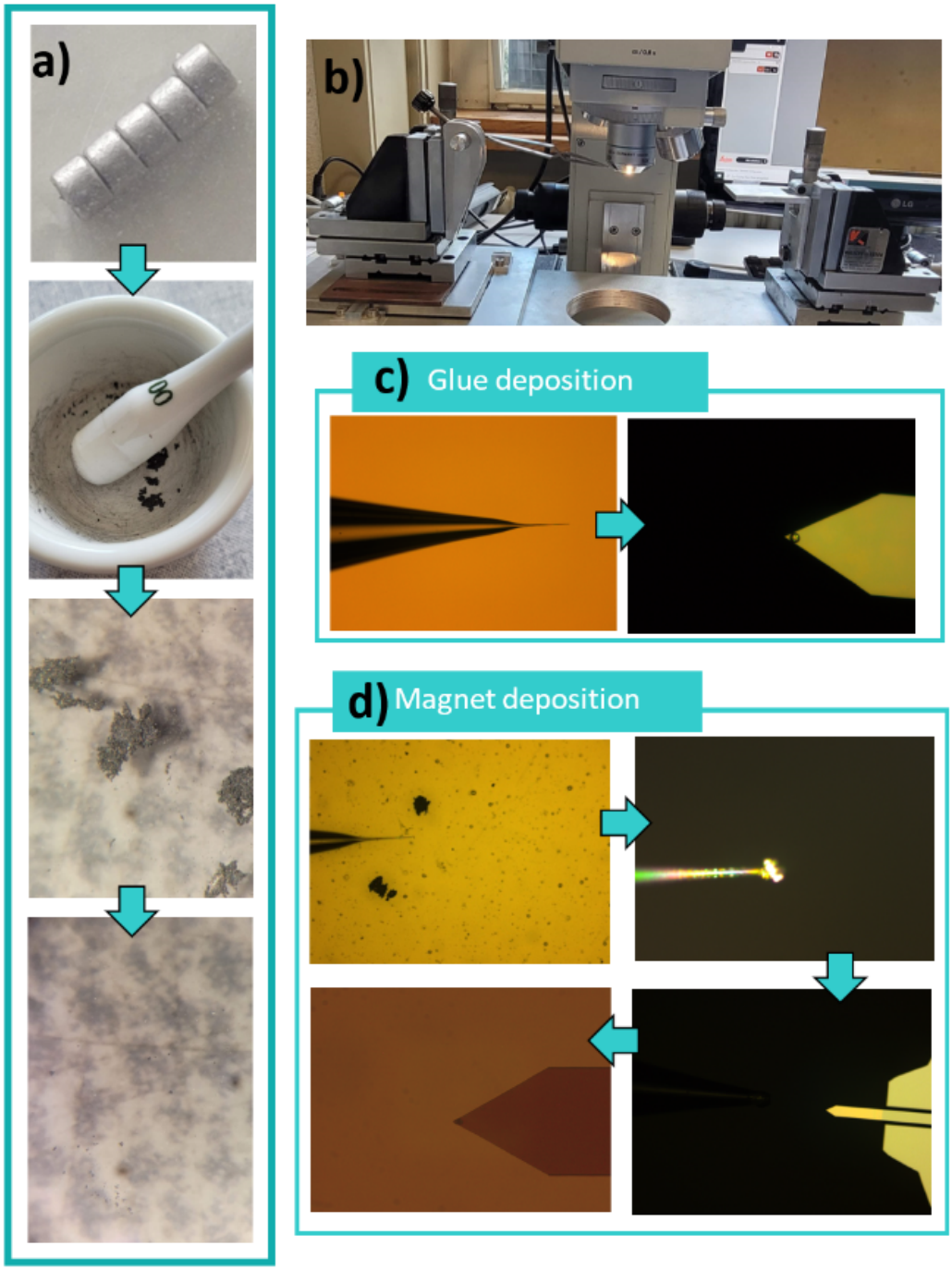

Figure c.12: — *Magnetic tip mounting. The nanomagnet comes from a* $CoSm_5$ *magnet that was crushed into very small pieces. Single-like particles of micrometer size (the smallest we could find) were selected and glued using epoxy glue and very precise manipulator on the ARROW TL cantilever, as shown in the pictures.*

S7:3. Non converted frequency-shift spectrum

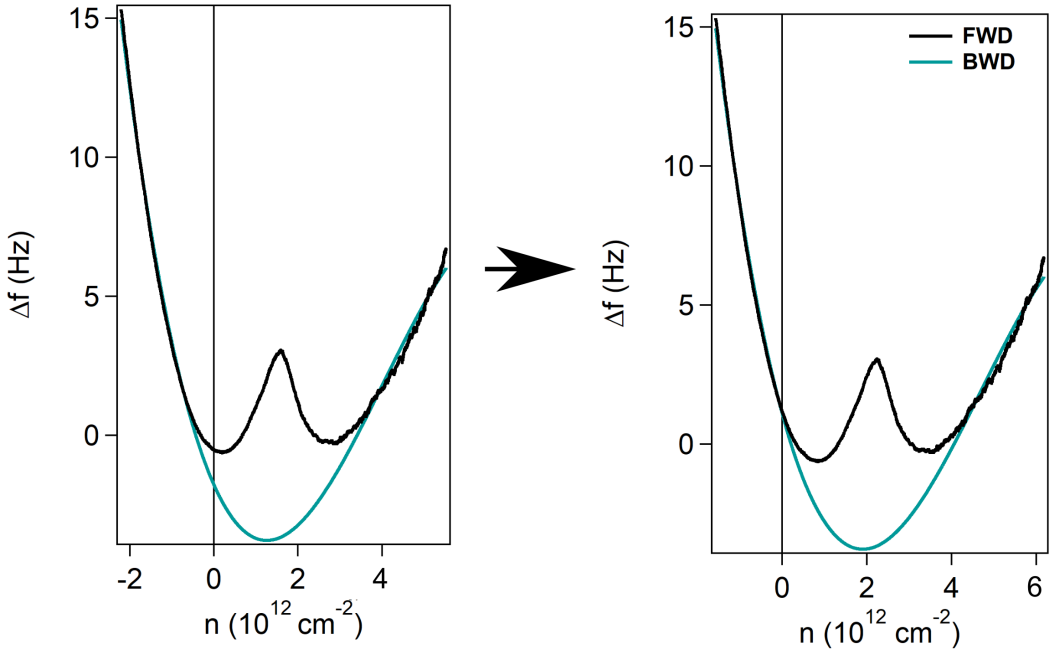

Figure c.13: — *Frequency-shift raw FWD and BWD sweep on MoS_2 doping correction.*

S7:4. Non substracted magnetic field curves

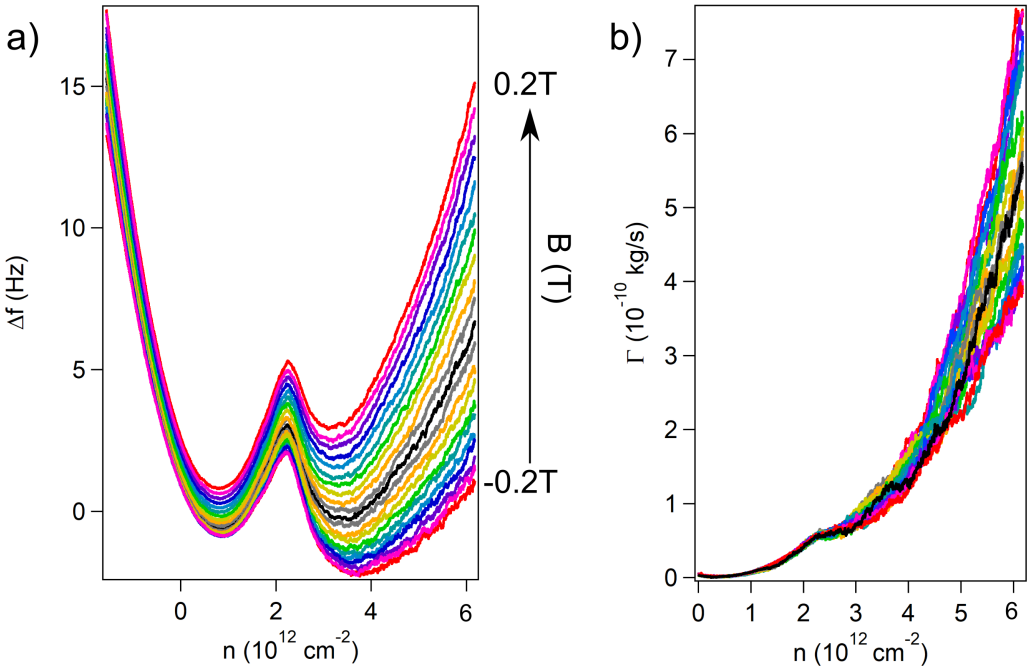

Figure c.14: — *External magnetic field effect on the frequency-shift and dissipation raw data.* ***a)****,* $\Delta f(Hz)$ *spectrum, the vertical offset is coming from the cantilever damping under* B_{ext}*-field.* ***b)*** *corresponding* Γ *curves.*

S7:5. Non substracted doping driven spetrum experiments

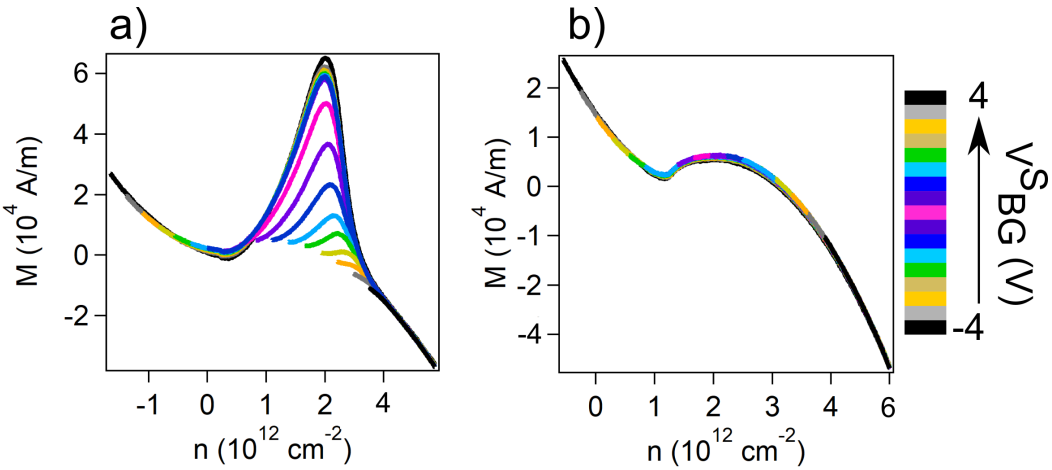

Figure c.15: — *Magnetization at $T = 77\ K$ over MoS_2 sample raw data.* ***a)*** *is the FWD sweeps and* ***b)*** *is the BWD corresponding sweeps for different starting backgate voltage V^S_{BG} ranging from $-4\ V \leq V^S_{BG} \leq 4\ V$ with a step of $\Delta V^S_{BG} = 0.5\ V$.*

S7:6. Dissipation curves for the doping driven experiments

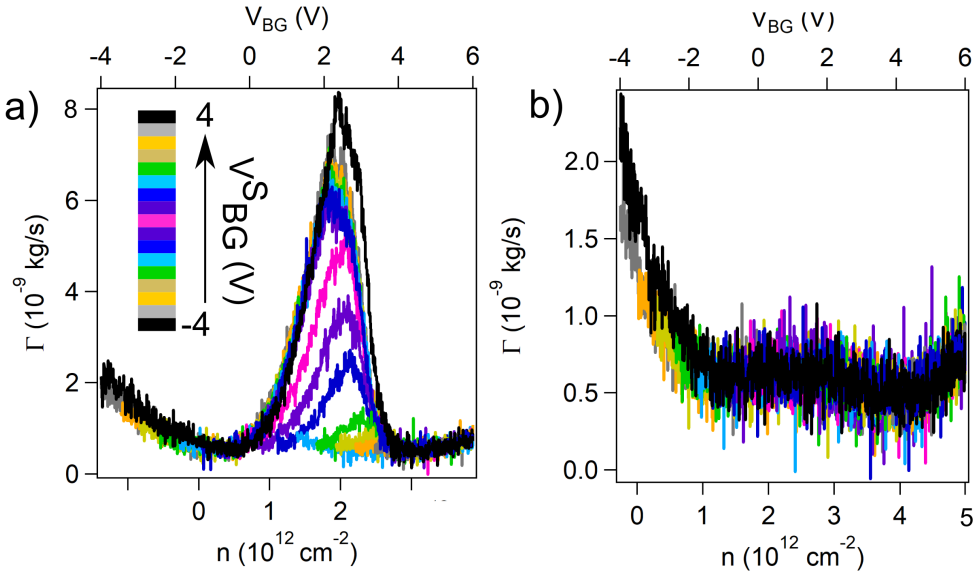

Figure c.16: — *Dissipation curves for different V^S_{BG}.* ***a)*** *FWD sweeps and* ***b)*** *corresponding BWD sweep.*

List of publications & communications

Peer-Reviewed Journal Publications

1. **Ollier, Alexina**; Kisiel, M.; Khosravi, A.; Gysin, U.; Tossati, E. and Meyer, E. Magnetic tuning of mechanical dissipation in quantum graphene. *paper in preparation* (2023).

2. **Ollier, Alexina**; Kisiel, M.; Liu, X.; Gysin, U.; Poggio, M.; Efetov, D. and Meyer, E. Giant energy dissipation on twsited bilayer graphene at the magic angle twist. *paper in preparation* (2023).

3. **Ollier, Alexina**; Kisiel, M.; Gupta, A.; Ramezani, M.; Gysin, U.; Watanabe, K.; Tanaguchi, T; Baumgartner, A. ; Schönenberger, C. and Meyer, E. Magnetic phase transition in MoS_2 detected with AFM. *paper in preparation* (2023).

Presentations

1. Energy dissipation on suspended graphene. **Ollier A.**; Kisiel M..; Pawlak R.; Gysin U. and Meyer, E. *QCQT Lunch Meeting*, 2019–12–03, Basel, Switzerland.

2. Energy dissipation on free-standing graphene. **Ollier A.**; Kisiel M.; Pawlak, R; Gysin U. and Meyer, E. *Nano in the Snow Winter School*, 2020–01–24, Lauenen, Switzerland.

3. Band theory: A small overview. **Ollier A.** *Nano in the Snow Winter School*, 2021–01–22, online.

4. Magnetic tuning of mechanical dissipation in quantum graphene. **Ollier A.**; Kisiel M.; Pawlak R.; Gysin U. and Meyer E. *EMRS*, 2021–05–31, online.

5. Low frequency noise in suspended graphene at RT. **Ollier A.**; Kisiel M.; Gysin U. and Meyer E. *EMRS*, 2021–06–02, online.

6. Energy dissipation on suspended graphene. **Ollier A.**; Kisiel M.; Pawlak R.; Gysin U. and Meyer E. *SPS and OPG Annual Meeting*, 2021–08–31, Innsbruck, Austria

7. Energy dissipation on twisted bilayer graphene at the magic angle twist. **Ollier A.**; Kisiel M.; Gysin U. and Meyer E. *SPS and OPG Annual Meeting*, 2021–09–01, Innsbruck, Austria

8. Giant energy dissipation on twsited bilayer graphene at the magic angle twist. **Ollier A.**; Kisiel M.; Gysin U. and Meyer E. *ICSPM*, 2021–12–09, online.

9. Giant energy dissipation on twsited bilayer graphene at the magic angle twist. **Ollier A.**; Kisiel M.; Gysin U. and Meyer E. *Nano in the Snow Winter School*, 2022–01–28, Zermatt, Switzerland.

10. Giant energy dissipation on twsited bilayer graphene at the magic angle twist. **Ollier A.**; Kisiel M.; Gysin U. and Meyer E. *QCQT Lunch Meeting*, 2022–04–26, Basel, Switzerland.

11. Giant energy dissipation on twsited bilayer graphene at the magic angle twist. **Ollier A.**; Kisiel M.; Gysin U. and Meyer E. *The Capri Spring School on Transport in Nanostructures*, 2022–05–12, Anacapri, Italy.

12. Magnetic tuning of mechanical dissipation in quantum graphene. **Ollier A.**; Kisiel M.; Gysin U. and Meyer E. *EWEG 2D*, 2022–05–25, St Moritz, Switzerland.

13. Magnetic tuning of mechanical dissipation in quantum graphene **Ollier A.**; Kisiel M.; Gysin U.; Khosravi A.; Tosatti E. and Meyer E. *ICTP*, 2022–06–09, Trieste, Italy.

14. Giant energy dissipation on twsited bilayer graphene at the magic angle twist. **Ollier A.**; Kisiel M.; Gysin U. and Meyer E. *NC-AFM 2022*, 2022–08–03, Nijmegen, The Netherland.

15. Magnetic tuning of mechanical dissipation in quantum graphene **Ollier A.**; Kisiel M.; Gysin U.; Khosravi A.; Tosatti E. and Meyer E. *IVC*, 2022–09–13, Sapporo, Japan.

16. Giant energy dissipation on twisteb bilayer graphene at the magic angle twist **Ollier A.**; Kisiel M.; Gysin U. and Meyer E. *Graphene workshop*, 2022–10–20, Budapest, Hungary.

17. Magnetic phase transition in MoS_2 detected with AFM. **Ollier A.**; Ramezani, M.; Kisiel M.; Gupta, A.; Gysin U.; Baumgartner, A., Schönenberger, C. and Meyer E. *QCQT lunch seminar*, 2022–11–29, Basel, Switzerland.

Posters

1. Nanoscale mechanical energy dissipation in quantum systems and 2D-materials. **Ollier A.**; Kisiel M.; Gysin U. and Meyer, E. *SNC*, 2019–06–06, Lausane, Swizerland.

2. Nanoscale mechanical energy dissipation in quantum systems and 2D-materials. **Ollier A.**; Kisiel M.; Gysin U. and Meyer E. *NCAFM*, 2019–07–31, Regensburg, Germany.

3. Nanoscale mechanical energy dissipation in quantum systems and 2D-materials. **Ollier A.**; Kisiel, M.; Gysin U., E. C. and Meyer, E. *SNI Annual Meetingl*, 2019–09–12, Lenzerheide, Swizerland.

4. Magnetic tuning of mechanical dissipation in quantum graphene. **Ollier A.**; Kisiel M.; Pawlak R.; Gysin U. and Meyer. *ICSPM*, 2020–12–11, online.

5. Low frequency noise in suspended graphene at RT. **Ollier A.**; Kisiel M.; Pawlak R.; Gysin U. and Meyer, E. *EMRS 21*, 2021–06–01, online.

6. Giant dissipation on twisted bilayer graphene at magic angle twist. **Ollier A.**; Marcin K.; Gysin U. and Meyer, E. *SNC 21*, 2021–06–24, online.

7. Giant dissipation on twisted bilayer graphene at the magic angle twist. **Ollier A.**; Marcin K.; Gysin U. and Meyer, E. *SNI Annual Meeting*, 2021–09–09, Lenzerheide, Switzerland.

8. Giant energy dissipation on twsited bilayer graphene at the magic angle twist. **Ollier A.**; Kisiel M.; Gysin U. and Meyer E. *2DSPM*, 2022–06–09, San Sebastian, Spain

9. Phase transition of a monolayer MoS_2. **Ollier A.**; Ramezani, M.; Kisiel M.; Gupta, A.; Gysin U.; Baumgartner, A., Schönenberger, C. and Meyer E. *SNI Annual Meeting*, 2022–09–07, Lenzerheide, Switzerland

10. Phase transition of a monolayer MoS_2. **Ollier A.**; Ramezani, M.; Kisiel M.; Gupta, A.; Gysin U.; Baumgartner, A., Schönenberger, C. and Meyer E. *IVC 22*, 2022–09–12, Sapporo, Japan